Tese de Livre Docência:

Modelagem de dados de espalhamento e difração a baixos ângulos

Prof. Dr. Cristiano Luis Pinto de Oliveira
Instituto de Física
Universidade de São Paulo

FICHA CATALOGRÁFICA
Preparada pelo Serviço de Biblioteca e Informação
do Instituto de Física da Universidade de São Paulo

Oliveira, Cristiano Luis Pinto de

Modelagem de dados de espalhamento e difração a baixos ângulos.
São Paulo, 2016.

Tese (Livre Docência) – Universidade de São Paulo. Instituto de Física.
Depto. de Física Experimental.

Área de Concentração: Física da Matéria Condensada.

Unitermos: 1.Teoria do espalhamento; 2. Difração por raios X;
3. Modelagem de dados; 4. Raios X; 5. Espalhamento de raios x a baixos
ângulos

USP/IF/SBI-011/2016

Resumo

Para a investigação da estrutura da matéria diversos métodos experimentais podem ser utilizados. Dentre um número muito grande de técnicas, os assim chamados métodos espectroscópicos são amplamente utilizados para o estudo dos mais variados tipos de sistemas. Uma grande classe de métodos espectroscópicos são os métodos de espalhamento de radiação, particularmente luz visível e raios X, bem como espalhamento de nêutrons. Além das dificuldades de realização deste tipo de experimentos, existem dificuldades iguais ou maiores na correta análise e interpretação dos resultados.

Nesta tese de livre docência apresento uma descrição detalhada de métodos de simulação, análise e modelagem de dados experimentais de espalhamento a baixos ângulos que são utilizados em uma vasta gama de aplicações, permitindo a correta análise e descrição de dados experimentais obtidos, bem como a obtenção de parâmetros estruturais pertinentes.

Métodos inovadores de analise e modelagem de dados de espalhamento foram desenvolvidos e são aplicados na interpretação de diversos sistemas, acoplando fatores de forma e de estrutura. Como resultado informações estruturais inéditas puderam ser obtidas para estes sistemas, demonstrando a potencialidade e aplicabilidade destas técnicas quando combinadas com os métodos desenvolvidos.

Abstract

For the investigation of the structure of matter several experimental approaches can be applied. The so called spectroscopic methods are widely used for the structural characterization of several systems. A large class of such methods is the scattering methods: Light scattering, X-ray scattering and Neutron Scattering. Besides the experimental limitations of these methods, the main difficulties are the correct analysis and interpretation of the experimental data.

In this thesis it is presented a detailed description of different types of simulation, analysis and modeling methods applied to the interpretation of small angle scattering data is presented, on a large set of applications, permitting the correct data analysis and the retrieval of structural parameters.

Innovative modeling and analysis methods were developed and are applied to several systems, combining form factor and structure factors. As a result, novel structural information could be obtained for the studied systems, demonstrating the potential and applicability of these techniques when combined with the developed methods.

Índice

1. Introdução 9

2. Espalhamento a Baixos ângulos 9

3. Infra-Estrutura de pesquisa 12
   3.1 Equipamentos de SAXS de Laboratório 12
   3.2 Desenvolvimento de detetor Bidimensional 15

4. Métodos de Modelagem de Dados Experimentais 16
   4.1 Transformada Indireta de Fourier – Modelagem Independente da forma 17
   4.2 Método de Transformada Inversa de Fourier generalizado – Desacoplando Fator de forma e estrutura 20
   4.3 Modelagem dependente da forma – Assumindo um fator de forma conhecido 22
   4.4 Métodos de Modelagem ab initio 26
   4.5 Deconvolução Quadrática – obtenção do perfil de densidade eletrônica 29
   4.6 Efeitos de tamanho do feixe e resolução do detetor 30
   4.7 Modelagem simultânea de fatores de forma e de estrutura 31
   a) Sistemas hexagonais 31
   b) Sistemas Planares – Deconvolução Gaussiana 34
   c) Método de Deconvolução Generalizado 40

5. Exemplos de Aplicação 43
   5.1 Estudos de Sistemas lamelares 43
   5.2 Estudos em Lipoproteínas 46

6. Considerações Finais e Perspectivas 58

7. Bibliografia 59

8. Apêndice 63
   a. Publicações selecionadas 63

Índice de Figuras

Figura 1 – Representação do processo de espalhamento por uma partícula fixa. Figura tirada de (Oliveira, 2011). 9

Figura 2 – Esquema de uma configuração experimental de SAS. O feixe proveniente de uma fonte é colimado utilizando elementos óticos (fendas, *pinholes*, etc) e incide na amostra. O feixe transmitido é coletado e pelo perfil de espalhamento é possível obter-se informações pertinentes à amostra..... 11

Figura 3 - NANOSTAR com o *upgrade* Xenocs para a fonte e sistema de colimação. A parte indicada pela linha tracejada corresponde ao *upgrade*. 13

Figura 4 – Equipamento XEUSS^{TM} da Xenocs, instalado no IFUSP. 14

Figura 5 – Acima: Esquerda - Peças fabricadas para fazer a adaptação do detetor bidimensional. Podem-se observar os anéis de aço inox nos quais a folha de Mylar será colada. Também notamos a flange que prenderá os anéis na peça quadrada, que por sua vez será presa ao detetor. Direita - Fotografia das peças encaixadas sobre nosso detetor bidimensional. Realizamos a colagem da folha de mylar entre os anéis a fim de iniciar os testes de resistência mecânica da mesma. A janela de Mylar suportou uma pressão de 4 atm sem sofrer danos. Abaixo: Detector montado com sistema de vácuo e pressurizador. Um vacuomanômetro foi utilizado para monitorar a pressão no sistema. Figura tirada de (Sales, 2015) 15

Figura 6 – Curvas teóricas para intensidades de espalhamento e correspondentes funções p(r) para corpos com formas simples. As intensidades foram normalizadas. Figura tirada de (Oliveira, 2011). 17

Figura 7 – Intensidades de SAXS para polímero P105 e o sistema composto Lisozima + P105 para várias temperaturas. A) e B) Intensidade de espalhamento e função p(r) para soluções de P105 (A) à 20, 60, 70 e 80ºC. C) e D) Intensidade de espalhamento e função p(r) para P105+Lisozima à 20, 60, 70 e 80ºC. As intensidades da mistura Lisozima+P105 podem ser compreendidas como composicoes lineares das intensidades da lisozima sozinha e das micelas de P105. Dados tirados de (Oliveira, 2005). 19

Figura 8 – Agregação de Lisozima induzida por calor. Esquerda: Dados experimentais (círculos abertos) e ajustes teóricos (linhas sólidas). Os frames foram coletados com o sistema à 80º, em intervalos de 5 minutos. Direita: curvas de distribuição de distâncias p(r) para cada curva. Figura tirada de (Oliveira, 2011). 19

Figura 9 – Estudos de SAXS para agregação de glucagon em fibras amilóides. Da esquerda para a direita: Serie de dados de SAXS coletados em função da temperatura, curvas de distribuição de pares de distâncias p(r) para cada curva de espalhamento, modelos obtidos através da construção por elementos finitos e uma imagem de TEM obtida para o sistema de fibras amilóides maduras. Figura baseada em (Oliveira *et al.*, 2009). 24

Figura 10 – Construção do modelo. A) Posição dos vértices de um cubo. B) União dos vértices com segmentos de retas. C) Modelo do tipo sólido. D) União dos vértices com subunidades esféricas. E) União dos vértices com DNA. F) Modelo do tipo casca. Figura adaptada de (Alves *et al.*, 2014). 25

Figura 11 – Considerações sobre posições e planos. O vetor n é a normal ao plano definido pelos vetores v_1 e v_2. O vetor v_3 conecta o ponto de referência p_{ref} ao ponto de interesse p_0. (a) Se $v_3 \bullet n = 0$ p0 está no plano, se $v_3 \bullet n < 0$ p_0 está no semi espaço negativo e se $v_3 \bullet n > 0$ p_0 está no semi espaço positivo do plano. (b) p_0 está dentro do tetraedro quando $v_3 \bullet n < 0$ para todos os vetores normais às faces do tetraedro. 25

Figura 12 – Calculo de intensidades teóricas para diversos corpos geométricos. Corpos construídos unindo-se os vértices com segmentos de reta (a) corpos construídos com segmentos tipo DNA nas arestas (b), corpos tipo casca (c) e corpos sólidos (d). Figura tirada de (Alves *et al.*, 2014). 26

Figura 13 – Exemplo de modelagem *ab initio* para dados de SAXS utilizando o programa GASBOR. Esquerda: Estrutura otimizada (esferas sólidas) superposta pela estrutura real conhecida por cristalografia de proteínas (arquivo pdb 6lyz.pdb). Direita: Ajuste dos dados experimentais. Círculos abertos – dados experimentais. Linha sólida – ajuste do modelo. Figura tirada de (Oliveira, 2011)..27

Figura 14 – Complexo hemoglobina-haptoglobina-CD163. (a) estrutura cristalográfica do complexo hemoglobina-haptoblobina (Hp-Hb). (b) cálculo da intensidade teórica de espalhamento para as cristalográficas do complexo em humanos (hHp-Hb) e em suínos (pHp-Hb). O ajuste dos dados do complexo Hp-Hb com o receptor CD163 (hHp-Hb-CD163) e o correspondente modelo foi obtido utilizando o programa CORAL. Figura tirada de (Andersen *et al.*, 2012). 28

Figura 15 – Exemplo de aplicação do método de deconvolução quadrática. A) Dados experimentais de SDS (círculos abertos) e o ajuste obtido pelo método de IFT (linha sólida). B) Função p(r) calculada pelo método de IFT (círculos abertos) e a p(r) teórica obtida pelo método de deconvolução usando o método de Glatter (linha sólida). C) Perfil de densidade eletrônica obtido representado por funções degrau (linhas tracejadas) e por uma representação suave (linha sólida). Figura retirada de (Oliveira, 2011).....29

Figura 16 – Estudo de sílica mesoporosa ordenada em sistemas hexagonais. Esquerda: curvas de SAXS obtidas para diferentes instantes do estudo *in situ*. Direita: Figura de TEM para o sistema final calcinado. Figura tirada de (Sundblom *et al.*, 2009).....32

Figura 17 – Esquerda: Construção do perfil de densidade eletrônica utilizando quatro Gaussianas (G1, G2, G3 and G4) com quatro diferentes amplitudes (-1, -0.3, 1, 0.3). São mostrados com quatro linhas diferentes. O perfil resultante é motrado em linha continua e grossa. Direita: Ajuste de dados experimentais utilizando o modelo de 4 gaussianas. Circulos Abertos: dados experimentais para sistema de lipossomas de fosfatidilcolina de ovo. Linha continua: Intensidade teórica. Linha pontilhada: fator de estrutura. Linha Tracejada: fator de forma $|F(q)|^2$. O perfil de densidade eletronica obtido é mostrado como um inset. Abaixo: Método de ponto de inflexão, executado automaticamente pelo programa de ajuste para determinar o valor de λ_{opt}. Figura tirada de (Oliveira *et al.*, 2012) 39

Figura 18 – (a) Curvas experimentais de SAXS para a fase lamelar com variadas frações de volume do lipídio (φ). As linhas finas para φ=0.582 representam as funções de resolução para as três posições de picos. As linhas tracejadas são os fatores de forma e as linhas pontilhadas os fatores de estrutura obtidos utilizando o procedimento de minimização descrito no texto. (b) Perfis de densidade eletrônica e definição da espessura da membrana δ. Em todos os casos as curvas foram deslocadas para melhor clareza. Figuras tiradas de (Oliveira *et al.*, 2012). 44

Figura 19 – Resultados de SAXS para o sistema Lecitina + Simulsol. Dados experimentais (símbolos) e o respectivo ajuste por modelo teórico (linhas solidas) para composições de mebrana (fração em massa do Simulsol): 30% (a) and 90% (b). Em (a) as curvas foram obtidas em um

equipamento de laboratório (NANOSTAR / IFUSP) e em (b) os dados foram obtidos na linha SWING do Síncrotron Soleil. (c) Perfil de densidade electronica obtida pelo procedimento de amuste, com quantidade variavel de Simulsol. Na figura, r = 0 representa o centro da bicamada e a definição de valores negativos e positivos é dado tendo-se a água como referencia. Inserção: Efeito do cosurfactante na espessura da bicamada. (d) Representação esquemática do efeito do simulsol na flutuação da espessura da bicamada. Figura baseada em (Gerbelli *et al.*, 2013).....45

Figura 20 – Método de deconvolução aplicado à modelagem de SAXS para LDL para diferentes tempos de oxidação por Cobre. a) Fator de Forma ajustado com o método de deconvolução. Dados experimentais (símbolos abertos) e ajuste do modelo (linha solida). b) Perfis de densidade eletrônica obtidos com o método de deconvolução. Figura tirada de (Oliveira, Santos*, et al.*, 2014). 48

Figura 21 – Método de deconvolução aplicado à modelagem de SAXS para HDL para diferentes tempos de oxidação por Cobre. a) Fator de Forma ajustado com o método de deconvolução. Dados experimentais (símbolos abertos) e ajuste do modelo (linha solida). b) Perfis de densidade eletrônica obtidos com o método de deconvolução. Figura tirada de (Oliveira, Santos*, et al.*, 2014). 49

Figura 22 – Método de Transformada de Fourier Generalizado (GIFT) aplicado ao desacoplamento entre fatores de forma e estrutura nos dados de SAXS para LDL. a) Ajuste (linha continua) dos dados experimentais de LDL (círculos abertos) utilizando o método GIFT. O fator de forma obtido neste procedimento linha tracejada foi utilizado no método de deconvolução. b) Curvas de distribuição de pares de distâncias *p(r)* obtidas pelo ajuste do método GIFT. Figura tirada de (Oliveira, Santos*, et al.*, 2014). 50

Figura 23 – Serie de dados de SAXS para os experimentos realizados. (a) Dados à 42ºC. (b) Dados à 60ºC. (c) Dados à 80ºC. Em todos os casos a curva da LDL nativa medida à 22ºC é mostrada para comparação. Esta curva foi deslocada para melhor visualização. Figura tirada de (Oliveira, Monteiro*, et al.*, 2014). 52

Figura 24 – Método GIFT e resultados de deconvolução para a LDL a 42ºC. (a) Dados experimentais de SAXS para diferentes instantes (círculos abertos), ajuste teórico obtido pelo método GIFT (linha sólida), fator de forma desacoplado (símbolos em "X") e o ajuste do fator de forma utilizando o método de deconvolução (linha tracejada). (b) Perfil de densidade eletrônica obtido para cada instante. Figura tirada de (Oliveira, Monteiro*, et al.*, 2014). 54

Figura 25 – Agregação da LDL à 42ºC. Análise por IFT: (a) Intensidade de espalhamento para os agregados (círculos) obtida pelo método GIFT. A curva *p(r)* correspondente é mostrada em (b). Cálculo das frações: (c) intensidade na origem para dados coletados à 42ºC (círculos) indicando um aumento monótono da intensidade. Isto indica um aumento sistemático da contribuição dos agregados. A linha neste gráfico é apenas para guia visual. (d) fração de número dos monômeros de LDL (círculos) e agregados (triângulos abertos). (e) fração de volume monômeros de LDL (círculos) e agregados (triângulos abertos). (f) fração de intensidade dos monômeros de LDL (círculos) e agregados (triângulos abertos). Todas as frações foram calculadas utilizando as equações 62 e 63 com os correspondentes valores de α. As linhas indicadas no gráfico são para guia visual. Modelagem dos agregados: utilizando modelagem *ab initio* tipo *dummy atom* (Seção 4.4) é possível ajustar os dados (linhas sólidas em (a)) e obter os modelos 3D para os agregados, mostrados em (g) para cada instante. Note que as esferas em (g) possuem o diâmetro de 350Å. Figura tirada de (Oliveira, Monteiro*, et al.*, 2014).....55

Figura 26 – Método GIFT e resultados de deconvolução para a LDL a 60ºC. (a) Dados experimentais de SAXS para diferentes instantes (círculos abertos), ajuste teórico obtido pelo método GIFT (linha sólida), fator de forma desacoplado (símbolos em "X") e o ajuste do fator de forma utilizando o

método de deconvolução (linha tracejada). (b) Perfil de densidade eletrônica obtido para cada instante. Figura tirada de (Oliveira, Monteiro, *et al.*, 2014). 56

Figura 27 – Agregação da LDL à 60ºC. Análise por IFT: (a) Intensidade de espalhamento para os agregados (círculos) obtida pelo método GIFT. A curva p(r) correspondente é mostrada em (b). Cálculo das frações: (c) intensidade na origem para dados coletados à 42ºC (círculos) indicando um aumento monótono da intensidade. Isto indica um aumento sistemático da contribuição dos agregados. A linha neste gráfico é apenas para guia visual. (d) fração de número dos monômeros de LDL (círculos) e agregados (triângulos abertos). (e) fração de volume monômeros de LDL (círculos) e agregados (triângulos abertos). (f) fração de intensidade dos monômeros de LDL (círculos) e agregados (triângulos abertos). Todas as frações foram calculadas utilizando as equações 62 e 63 com os correspondentes valores de α. As linhas indicadas no gráfico são para guia visual. Modelagem dos agregados: utilizando modelagem *ab initio* tipo *dummy atom* (Seção 4.4) é possível ajustar os dados (linhas sólidas em (a)) e obter os modelos 3D para os agregados, mostrados em (g) para cada instante. Note que as esferas em (g) possuem o diâmetro de 350Å. Figura tirada de (Oliveira, Monteiro, *et al.*, 2014). 57

Índice de Tabelas

Tabela 1 – Alguns exemplos de expressões semi-analíticas para intensidades de espalhamento calculadas para partículas com formas simples 23

Siglas e abreviações

CD163 – *Cluster of Differentiation 163*

DLS – *Dynamic light Scattering*

DNA – *DeoxyriboNucleic Acid* (ácido desoxirribonucleico)

FAPESP – Fundação de Amparo à Pesquisa do Estado de São Paulo

GIFT – *Generalized Indirect Fourier Transformation*

HDL – *High Density Lipoproteins*

IFT – *Indirect Fourier Transformation*

IFUSP – Instituto de Física da Universidade de São Paulo

INCT-FCx – Instituto Nacional de Ciência e Tecnologia em Fluidos Complexos

LDL – *Low Density Lipoproteins*

LNLS – Laboratório Nacional de Luz Sincrotron

P105 – polímero bloco ($EO_{36}PO_{56}EO_{36}$)

PEG – polímero Polietileno glicol

SANS – *Small Angle Neutron Scattering*

SAS – *Small Angle Scattering*

SAXS – *Small Angle X-Ray Scattering*

SWAXS – *Small/Wide Angle X-Rau scattering*

USP – Universidade de São Paulo

WAXS – *Wide Angle X-Ray Scattering*

Z-scan – Técnica de varredura Z

1. Introdução

Métodos espectroscópicos são amplamente utilizados para o estudo dos mais variados tipos de sistemas. Estes métodos são baseados nas diversas formas de interação que a radiação possui com a matéria, dependendo de sua faixa de energia. Uma grande classe de métodos espectroscópicos são os métodos de espalhamento de luz, particularmente luz visível e raios X, bem como espalhamento de nêutrons. Nestes casos os dados experimentais podem fornecer informações estruturais importantes sobre o sistema como, por exemplo, forma das partículas, arranjo estrutural, variação da densidade de contraste eletrônico, resposta a agentes externos como temperatura, pH, força iônica etc. No entanto, a princip al dificuldade da utilização destes métodos consiste na análise e interpretação dos resultados.

Apresento neste trabalho um conjunto de métodos de simulação, análise e modelagem de dados experimentais de espalhamento a baixos ângulos que são utilizados em uma vasta gama de aplicações, permitindo a correta análise e descrição de dados experimentais obtidos bem como a obtenção de parâmetros estruturais pertinentes. Este conjunto de ferramentas está à disposição da comunidade cientifica para aplicação em estudos de variados tipos de sistemas.

2. Espalhamento a Baixos ângulos

Para compreender experimentos de espalhamento a baixos ângulos pode-se iniciar com uma partícula fixa no espaço. Isso é mostrado na Figura 1 onde uma onda incidente com vetor de onda $\vec{k}_0$ incide nos pontos O e P separados por um vetor $\vec{r}$.

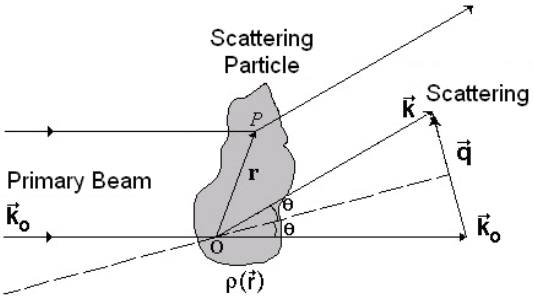

Figura 1 – Representação do processo de espalhamento por uma partícula fixa. Figura tirada de (Oliveira, 2011).

Como o espalhamento é assumido como elástico (primeira aproximação de Born), a onda espalhada com vetor de onda $\vec{k}$ possui o mesmo módulo da onda incidente e então a diferença entre os feixes incidentes e espalhados é dado por:

$$\vec{q} = \vec{k} - \vec{k}_0, \qquad \left|\vec{k}\right| = \left|\vec{k}_0\right|$$
$$\left.\begin{array}{l} q = 2k\sin\theta \\ k = \dfrac{2\pi}{\lambda} \end{array}\right\} \Rightarrow q = \frac{4\pi}{\lambda}\sin\theta \qquad (1)$$

O que fornece a definição do vetor transferência de momento do espaço recíproco, q. A amplitude de espalhamento $f(\vec{q})$ é dada pela transformada de Fourier da densidade de comprimento de espalhamento do centro espalhador, $\rho(\vec{r})$:

$$f(\vec{q}) = \frac{1}{4\pi}\int_V \rho(\vec{r})\exp(-i\vec{q}\cdot\vec{r})d\vec{r} \qquad (2)$$

A quantidade mensurável é a intensidade de espalhamento, *I(q)* que é o modulo quadrático da amplitude de espalhamento,

$$\begin{aligned} I_1(\vec{q}) &= \left|f(\vec{q})\right|^2 = f(\vec{q})\bullet f(\vec{q})^* \\ I_1(\vec{q}) &= \int_V\int_V \rho(\vec{r}\,')\rho(\vec{r}\,'-\vec{r})\exp(-i\vec{q}\cdot\vec{r})d\vec{r}d\vec{r}\,' \end{aligned} \qquad (3)$$

Em geral, assume-se que a particular não está fixa, mas sim que pode assumir qualquer orientação. Desta forma, devem-se realizar médias da intensidade de espalhamento para as possíveis orientações da partícula. Estas operações de promediação permitem a escrita da intensidade de espalhamento média para uma partícula como sendo dada por (Feigin & Svergun, 1987):

$$\begin{aligned} I_1(q) &= 4\pi\int_0^\infty p(r)\frac{\sin(qr)}{qr}dr \\ p(r) &= \frac{r^2}{2\pi^2}\int_0^\infty q^2 I_1(q)\frac{\sin(qr)}{qr}dq \end{aligned} \qquad (4)$$

Sendo que a função *p(r)* é similar à função de Patterson obtida em métodos cristalográficos, mas promediada para todas as orientações da partícula espalhadora.

Um esquema de uma configuração típica de SAS (*Small Angle Scattering*) é mostrado na Figura 2. Quando este método é utilizado com fontes de raios X recebe o nome de SAXS (*Small Angle X-ray Scattering*) e com fontes de nêutrons SANS (*Small Angle Neutron Scattering*).

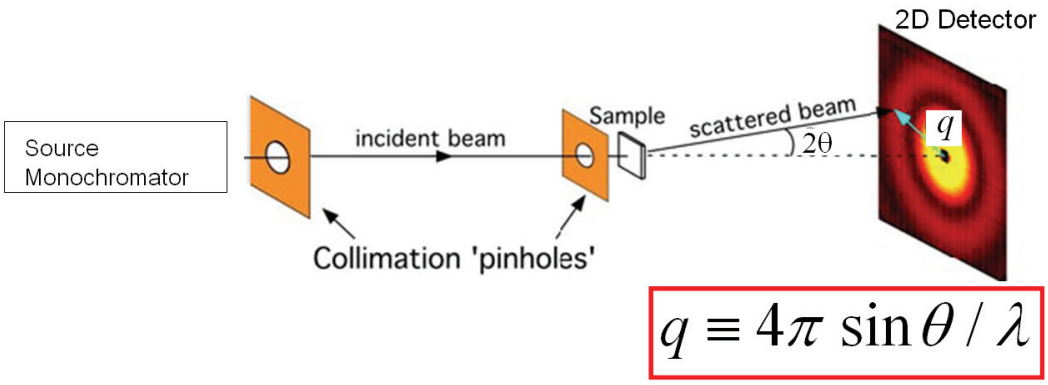

Figura 2 – Esquema de uma configuração experimental de SAS. O feixe proveniente de uma fonte é colimado utilizando elementos óticos (fendas, *pinholes*, etc) e incide na amostra. O feixe transmitido é coletado e pelo perfil de espalhamento é possível obter-se informações pertinentes à amostra.

Para um sistema de partículas em solução, a intensidade espalhada pode ser representada pela seguinte expressão,

$$I(q) = N\langle f^2(\vec{q})\rangle\langle S(\vec{q})\rangle \qquad (5)$$

sendo N o número de partículas iluminadas pelo feixe incidente, $\langle f^2(\vec{q})\rangle = P(q)$ é o fator de forma da particular espalhadora, com $f(\vec{q})$ a amplitude de espalhamento e $\langle S(\vec{q})\rangle$ é o fator de estrutura do sistema. Diferentes variações da expressão (5) podem ser obtidas dependendo do sistema em estudo. O fator de forma fornece informações sobre a forma, dimensões, anisotropia e contrastes de densidade eletrônica da partícula espalhadora. O fator de estrutura fornece informações sobre possíveis interações entre as partículas, estados de oligomerização, agregação, etc.

Os "*brackets*" $\langle\ \rangle$ indicam uma média sobre todas as orientações da partícula. Isso se deve ao fato de termos um sistema de partículas randomicamente orientadas, as quais, quando submetidas a medidas de espalhamento, fornecem um espalhamento isotrópico. Desta maneira uma curva de SAS típica é o resultado da média sobre todas as possíveis orientações da partícula e esta operação diminui enormemente a quantidade de informação do sistema fazendo com que, por exemplo, diferentes tipos de modelos possam ajustar igualmente os dados experimentais.

Partículas com anisotropias bastante distintas, como por exemplo, partículas tipo bastão muito alongadas ou planos com áreas superficiais muito grandes, permitem um desacoplamento do próprio fator de forma em duas componentes (Pedersen, 1997). Assim o fator de forma da partícula 3D, $P(q)_{3D}$, pode ser dado por:

- Partículas tipo bastão, sendo o comprimento muito maior que o raio da seção transversal:

$$P(q)_{3D} = P(q)_{1D} P(q)_{2D} \quad (6)$$

Neste caso $P(q)_{1D}$ é o fator de forma para um bastão infinitamente fino, com comprimento L. Esta expressão foi obtida por Neugebauer (Neugebauer, 1942),

$$P(q)_{1D} = P(q)_{rod} = 2Si(qL)/(qL) - 4\sin^2(qL/2)/(q^2L^2) \quad (7)$$

Onde, $Si(x) = \int_0^x t^{-1} \sin t \, dt$.

- Partículas planares com espessura muito fina e área superficial muito grande

$$P(q)_{3D} = P(q)_{2D} P(q)_{1D} \quad (8)$$

Neste caso $P(q)_{2D}$ é o fator de forma de um plano infinitamente fino. Para um disco circular de raio R infinitamente fino (Kratky & Porod, 1949),

$$P(q)_{2D} = P(q)_{plane} = \frac{2}{q^2R^2}\left[1 - \frac{J_1(2qR)}{qR}\right] \quad (9)$$

Para o caso onde a dimensão de anisotropia é infinita, isto é, bastões com comprimento infinito ou planos infinitos as expressões (2) e (4) se resumem a $1/q$ para o caso de bastões com comprimento infinito e $1/q^2$ para o caso de planos infinitos. Estas formas simplificadas são usualmente utilizadas em modelos de dados de espalhamento e podem ser aplicadas quando as dimensões anisotrópicas são muito maiores do que a resolução dos dados experimentais (Oliveira *et al.*, 2012, Sundblom *et al.*, 2009). No entanto, quando as dimensões não podem ser consideradas infinitas a utilização das expressões (6) e (8) permitem a determinação destas quantidades.

3. Infra-Estrutura de pesquisa

3.1 Equipamentos de SAXS de Laboratório

Coordenei da melhoria e instalação de dois equipamentos de SAXS de laboratório no Instituto de Física da USP, o que torna o IFUSP local de referencia tanto a nível nacional quanto internacional. Sou coordenador dos equipamentos NANOSTAR™-Bruker e XEUSS™-Xenocs. Utilizando recursos do Núcleo de Apoio a Pesquisa em Fluidos Complexos, projeto que participo, foi possível instalar uma nova fonte (fonte *Microfocus* GENIX3D™) e sistema de colimação (*scatterless slits*) no equipamento NANOSTAR. Estes acessórios foram providos pela empresa XENOCS e ocasionou um aumento de 40x no fluxo, quando comparado com a configuração anterior (tubo convencional). As fendas são motorizadas de modo que é possível fazer o alinhamento do sistema e alterações no tamanho do feixe de modo automatizado. O sistema possui um detetor

bidimensional VANTEC2000™-Bruker, cuja compra também foi coordenada por mim através de um projeto FAPESP (#2010/19074-6). Uma foto atual do equipamento é mostrada na Figura 3.

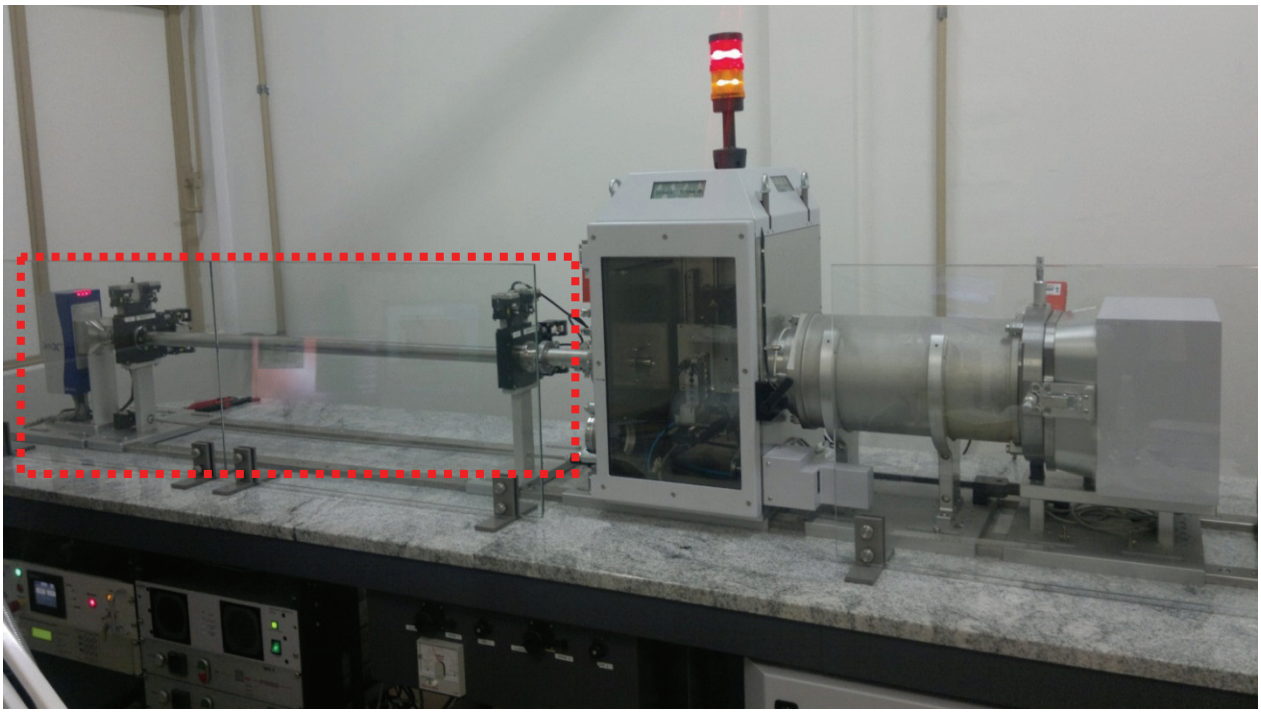

Figura 3 - NANOSTAR com o *upgrade* Xenocs para a fonte e sistema de colimação. A parte indicada pela linha tracejada corresponde ao *upgrade*.

Como resultado deste *upgrade* no equipamento uma séria de experimentos que antes não eram possíveis de serem realizados (devido ao baixo fluxo), estão agora acessíveis. Em particular, estudos de sistemas biológicos como proteínas em solução, sistemas de surfactantes, etc, podem agora ser estudados no equipamento de laboratório. Diversos exemplos serão mostrados ao longo do texto.

Como resultado de outro projeto que participo, um projeto temático FAPESP (#2011/13616-4) no qual sou pesquisador associado, foi possível adquirir um segundo equipamento de SAXS de laboratório, que é mostrado na Figura 4. Este equipamento é em muitos aspectos complementar ao NANOSTAR, pois permite a fácil montagem de acessórios em sua mesa óptica. Além disso, possui fonte *microfocus* e sistema de colimação similar ao instalado no NANOSTAR, provendo o mesmo fluxo de fótons.

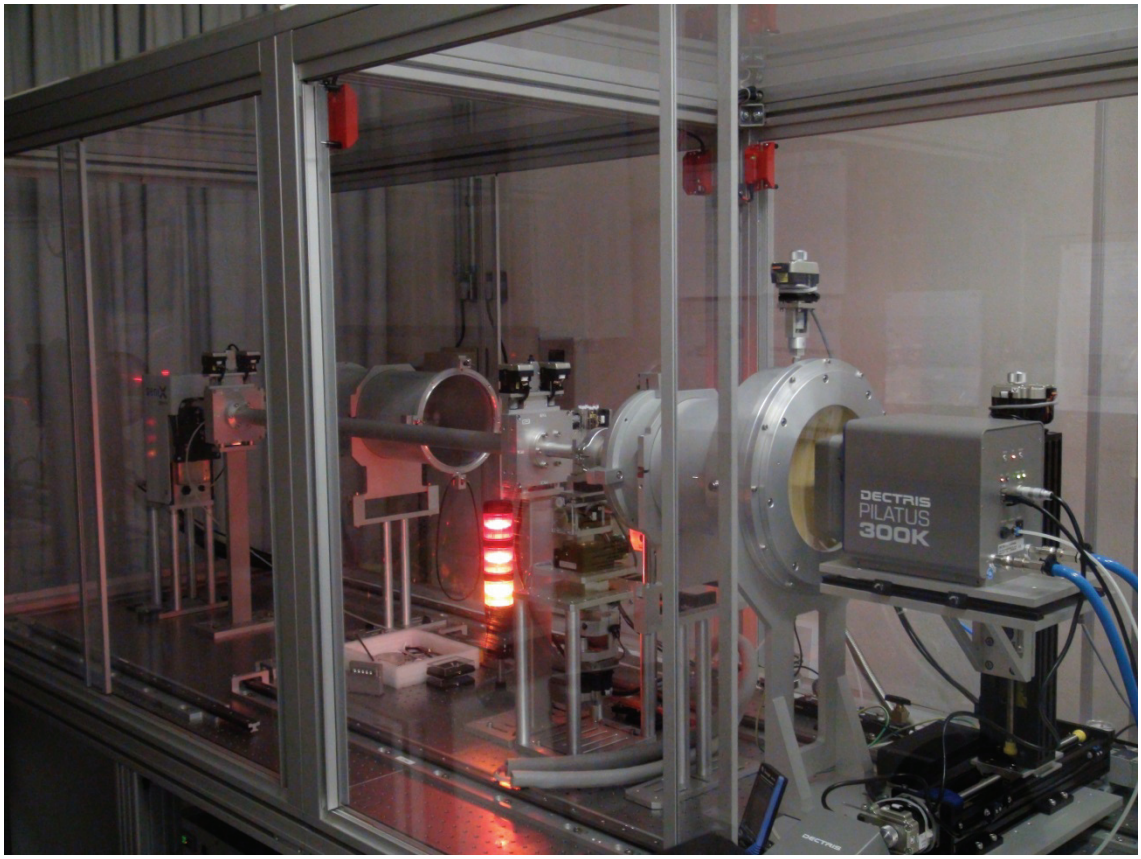

Figura 4 – Equipamento XEUSS™ da Xenocs, instalado no IFUSP.

Para este equipamento um detetor bidimensional PILATUS™ 300k, fornecido pela empresa Dectris, foi adquirido com recursos do Instituto Nacional de Ciência e Tecnologia em Fluidos Complexos (INCT-FCx), do qual também faço parte. Com recursos da FAPESP (#2011/13616-4) adquirimos outro acessório, uma câmara de vácuo com detetor WAXS, que permite a medida simultânea de dados de espalhamento a baixos ângulos (SAXS) e alto ângulo (WAXS). Este é o primeiro equipamento de laboratório no Brasil que permite medidas simultâneas de SAXS-WAXS.

A presença destes dois equipamentos no IFUSP promove uma situação única para a realização de pesquisas. Em muitos casos, a amostra a ser estudada é obtida por processos de síntese e purificação complexos e com baixa eficiência. Deste modo, ao se obter a amostra, a mesma deve ser medida o mais rápido possível para garantir sua integridade e qualidade dos resultados. Equipamentos de laboratório de boa qualidade possibilitam esta oportunidade. Além disso, como mostrarei nos exemplos, apenas em casos onde não é possível realizar os experimentos nos equipamentos do IFUSP, foi necessário submeter projetos ao Laboratório nacional de Luz Sincrotron.

3.2 Desenvolvimento de detetor Bidimensional

O sistema de deteção é um dos mais importantes componentes de qualquer aparato experimental. A qualidade dos dados é conseqüência direta da eficiência e resolução do detetor. Venho trabalhando em um projeto onde é proposto o desenvolvimento de um detetor bidimensional a gás multifilar para deteção de raios X. Este tipo de detetor existe em algumas formas comerciais, mas diversos centros de pesquisa em todo o mundo desenvolvem seus próprios detetores de modo a poderem realizar otimizações nos mesmos bem como eventuais operações de manutenção sem a necessidade de custos adicionais ou de longas esperas.

Oriento um estudante, Eraldo de Sales, que vem trabalhado desde sua Iniciação Científica e agora finaliza um mestrado na adaptação e caracterização de um detetor existente no Departamento de Física Nuclear da Universidade de São Paulo para utilização no estudo de reações com íons pesados, mas que poderia ser adaptado para ser utilizado na detecção de raios X. Neste período de tempo já foi possível realizar-se adaptações necessárias neste detetor para esta nova condição de operação bem como foram realizados diversos testes. Maiores detalhes podem ser encontrados na dissertação de mestrado do estudante (Sales, 2015).

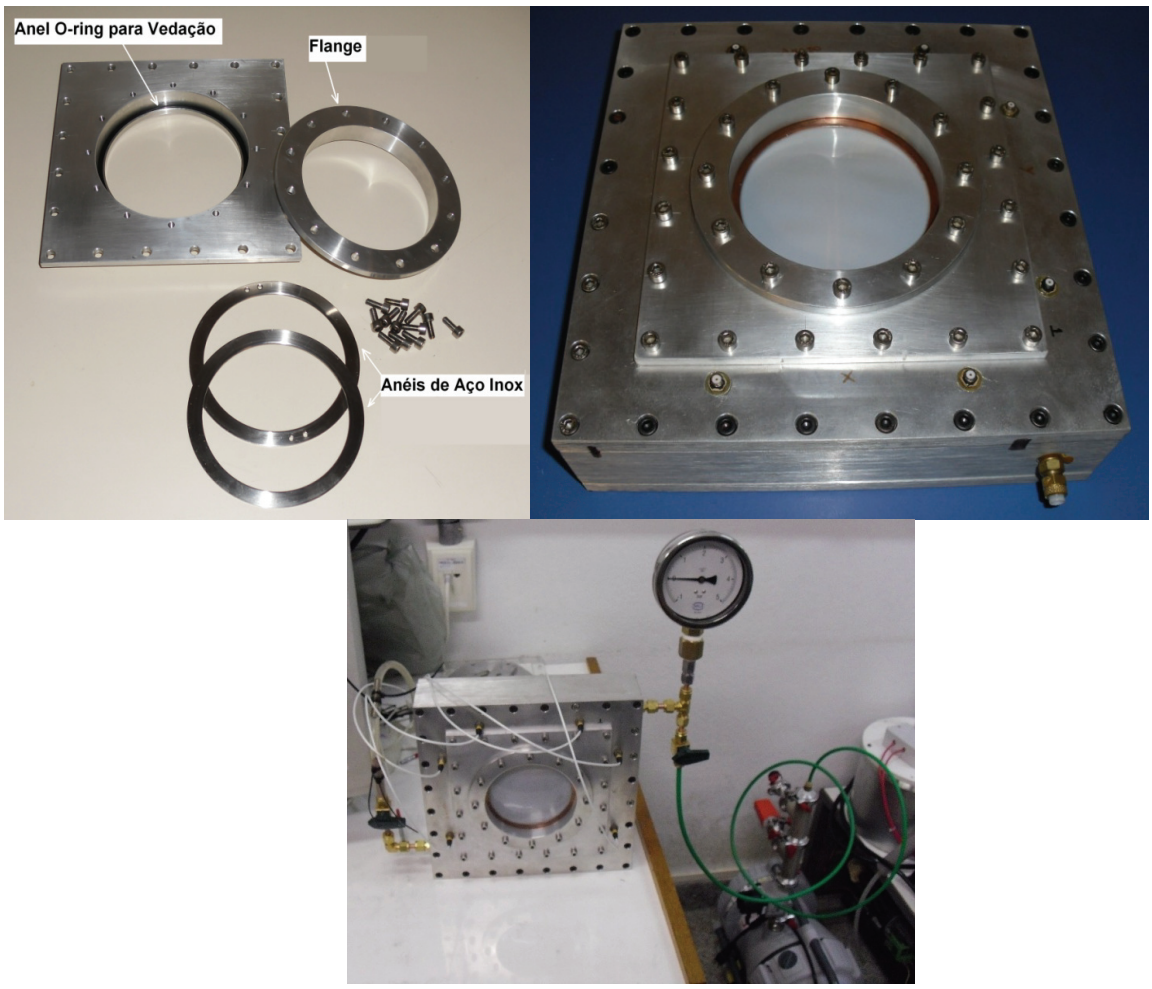

Figura 5 – Acima: Esquerda - Peças fabricadas para fazer a adaptação do detetor bidimensional. Podem-se observar os anéis de aço inox nos quais a folha de *Mylar* será colada. Também notamos a flange que prenderá os anéis na peça quadrada, que por sua vez será presa ao detetor. Direita - Fotografia das peças encaixadas sobre

nosso detetor bidimensional. Realizamos a colagem da folha de mylar entre os anéis a fim de iniciar os testes de resistência mecânica da mesma. A janela de Mylar suportou uma pressão de 4 atm sem sofrer danos. Abaixo: Detector montado com sistema de vácuo e pressurizador. Um vacuomanômetro foi utilizado para monitorar a pressão no sistema. Figura tirada de (Sales, 2015)

4. Métodos de Modelagem de Dados Experimentais

Diferentes metodologias podem ser utilizadas para se obter informações estruturais a partir de dados de espalhamento. Usualmente a informação desejada é a distribuição de contraste densidade de espalhamento $\Delta\rho(r)$, que pode fornecer informações sobre forma, tamanho, polidispersidade, periodicidade, etc. Note que foi a quantidade importante é o ***contraste*** entre a partícula e o meio onde está inserida, o qual pode ser diferente dependendo da radiação utilizada. O procedimento para obter $\Delta\rho(r)$ é chamado "problema inverso de espalhamento", ou seja, obter informação a partir de dados no espaço recíproco. A principal dificuldade decorre do fato de que não temos acesso experimental à amplitude de espalhamento, mas sim à intensidade de espalhamento, $I(q) \propto \langle f^2(\vec{q}) \rangle$. Das características intrínsecas de experimentos e espalhamento, o teste χ^2 (*chi-square*) é uma boa função de minimização para procedimentos de otimização e ajuste de dados (Knoll, 2010, Press, 1992). Dado um número N de pontos experimentais, $I_{exp}(q_i)$, com desvios padrões $\sigma(q_i)$ e a intensidade teórica $I_{teo}(q_i)$ calculada para os mesmos valores de q, a função χ^2 é definida como:

$$\chi^2 = \sum_{i=1}^{N} \frac{\left(I_{\exp}(q_i) - I_{teo}(q_i)\right)^2}{\sigma(q_i)^2} \qquad (10)$$

Uma prática comum é a utilização do χ^2 reduzido, $\chi_R^2 = \chi^2/(N-M)$, sendo N o número de pontos experimentais e M o número de parâmetros independentes no modelo teórico. Um bom ajuste dos dados experimentais ocorre quando as diferenças entre o modelo e os dados experimentais são menores do que os desvios $\sigma(q_i)$. Deste modo, como χ_R^2 é normalizado por (N-M), se N é razoavelmente maior que M o valor de χ_R^2 para um bom ajuste deve ser próximo a 1. Valores consideravelmente maiores que 1 podem provavelmente indicar discrepâncias entre o modelo e os dados experimentais ou incertezas subestimadas. Por outro lado, valores consideravelmente menores que 1 indicam incertezas superestimadas.

Este teste, bem como variações do mesmo, é utilizado para minimização nos processos de ajuste de dados experimentais pela utilização de modelos teóricos, como detalhado a seguir.

4.1 Transformada Indireta de Fourier – Modelagem Independente da forma

Para sistemas bastante diluídos possíveis interações entre partículas espalhadoras podem ser negligenciadas de modo que o fator de estrutura *S(q)* tem valor unitário. Nestes casos a intensidade de espalhamento medida é proporcional à intensidade de uma única partícula, a qual pode ser representada através da transformada de Fourier de uma função do espaço real, *p(r)*:

$$I(q) = N\left\langle f^2(\vec{q})\right\rangle = NI_1(q) \qquad (11)$$

$$I_1(q) = 4\pi\int_0^\infty p(r)\frac{\sin(qr)}{qr}dr$$

$$p(r) = \frac{r^2}{2\pi^2}\int_0^\infty q^2 I_1(q)\frac{\sin(qr)}{qr}dq$$

A função *p(r)*, também conhecida como função de distribuição de distâncias entre pares, tem o significado físico de histograma de distribuição de distâncias no interior de uma partícula. Existem na literatura diversos procedimentos capazes de fornecer esta função a partir de dados experimentais (programas ITP e GIFT (Glatter, 1977, Bergmann *et al.*, 2000, Fritz & Glatter, 2006); programa GNOM (Semenyuk & Svergun, 1991); programa WIFT e WGIFT (Oliveira *et al.*, 2009), entre outros). A forma desta curva fornece informações importantes sobre a forma das partículas espalhadoras, como mostrado na Figura 6. Uma informação direta desta curva é o valor da máxima dimensão da partícula, fornecido pelo valor em *r* no qual esta função vai para zero.

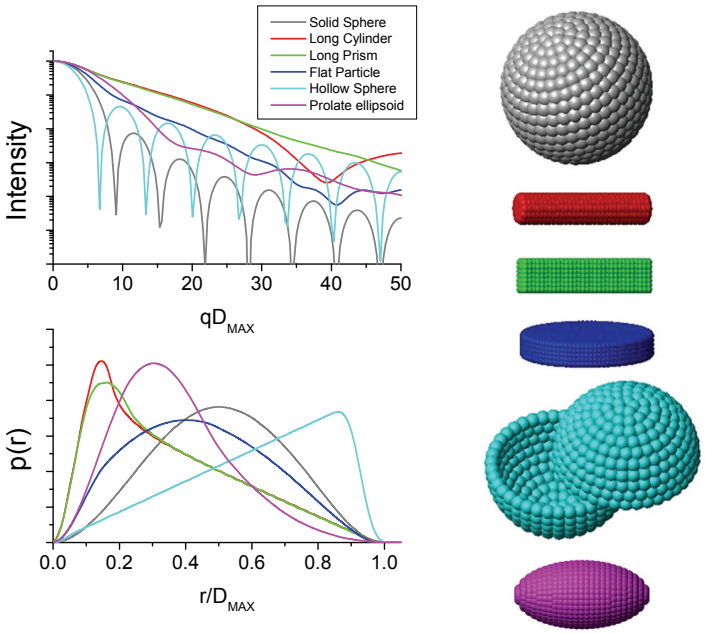

Figura 6 – Curvas teóricas para intensidades de espalhamento e correspondentes funções p(r) para corpos com formas simples. As intensidades foram normalizadas. Figura tirada de (Oliveira, 2011).

Em muitas situações tem-se um sistema composto de populações com formas diferente. Nestes casos, a intensidade espalhada será a soma das intensidades correspondentes a cada população:

$$I(q) = \sum_{i=1}^{N} f_i I_i(q) \qquad (12)$$

Sendo f_i a fração numérica de cada espécie do sistema e $I_i(q)$ a intensidade correspondente a cada forma do sistema. É assumido que as partículas não interagem entre si. Nestes casos a função $p(r)$ calculada será dada por:

$$p(r) = \sum_{i=1}^{N} f_i p_i(r) \qquad (13)$$

Onde $p_i(r)$ é a função de distribuição de pares de distâncias para cada sistema. Caso as partículas possuam formas bastante distintas, é possível inferir as formas de ambas as espécies na curva de espalhamento e da função p(r). Um exemplo de aplicação é mostrado na Figura 7. O polímero P105 (Almeida *et al.*, 2004) forma micelas à temperatura ambiente, como mostrado na figura. Quando colocado junto com a proteína lisozima, tem-se um sistema composto por micelas de P105 e proteínas. Pela análise da função p(r) foi possível identificar a presença de micelas de P105 e lisozima, sem formação de complexo.

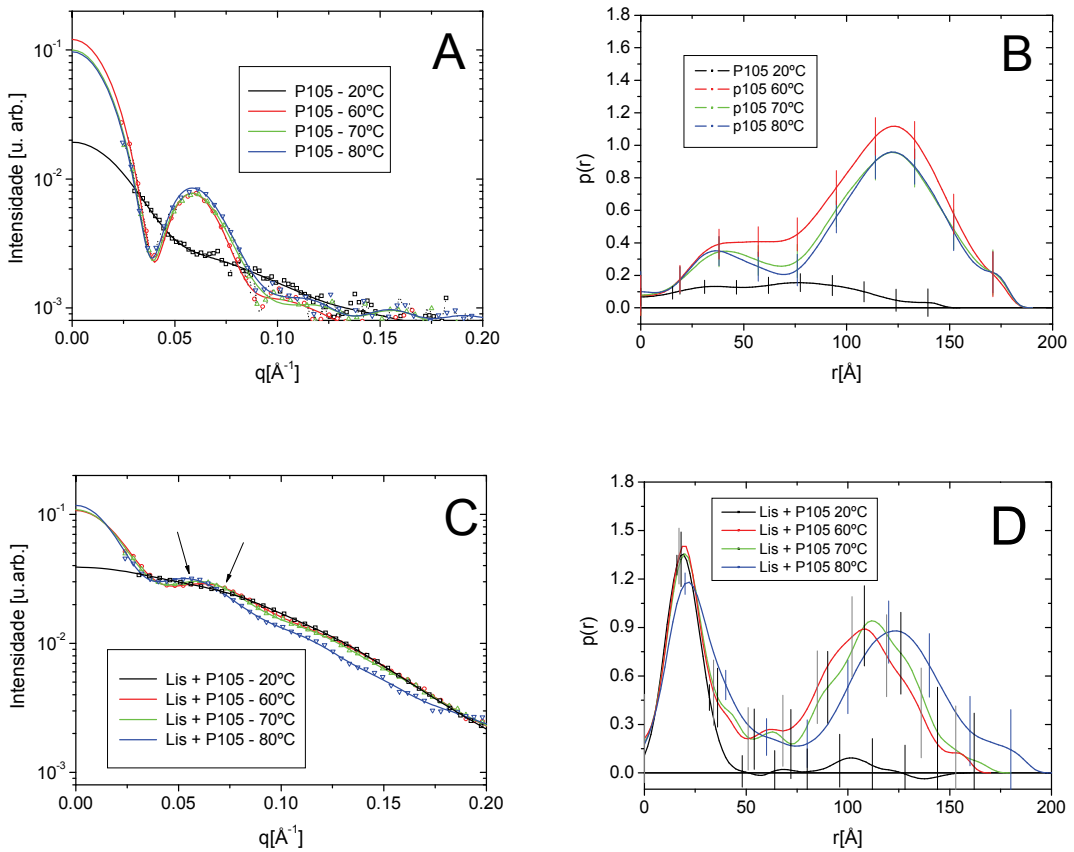

Figura 7 – Intensidades de SAXS para polímero P105 e o sistema composto Lisozima + P105 para várias temperaturas. A) e B) Intensidade de espalhamento e função p(r) para soluções de P105 (A) a 20, 60, 70 e 80ºC. C) e D) Intensidade de espalhamento e função p(r) para P105+Lisozima a 20, 60, 70 e 80ºC. As intensidades da mistura Lisozima+P105 podem ser compreendidas como composicoes lineares das intensidades da lisozima sozinha e das micelas de P105. Dados tirados de (Oliveira, 2005).

Em outras situações a subunidade pode se agregar e compor uma estrutura maior. Pode-se admitir que a partícula de interesse *é* a subunidade e sendo assim o agregado pode ser visto como um *fator de estrutura* deste sistema, uma vez que indica a forma como estas partículas se aglomeram. Um possível procedimento nestes casos consiste em se ajustar a curva toda utilizando o método de IFT e a função *p(r)* assim obtida conterá informações do agregado como um todo (fator de forma + fator de estrutura). Um exemplo é mostrado na Figura 8, onde a agregação de lisozima induzida por calor ao longo do tempo é descrita pelo método de IFT (Oliveira, 2011). Neste caso, apesar de sabermos que a lisozima é a subunidade agregadora base, olhamos para o sistema como um todo.

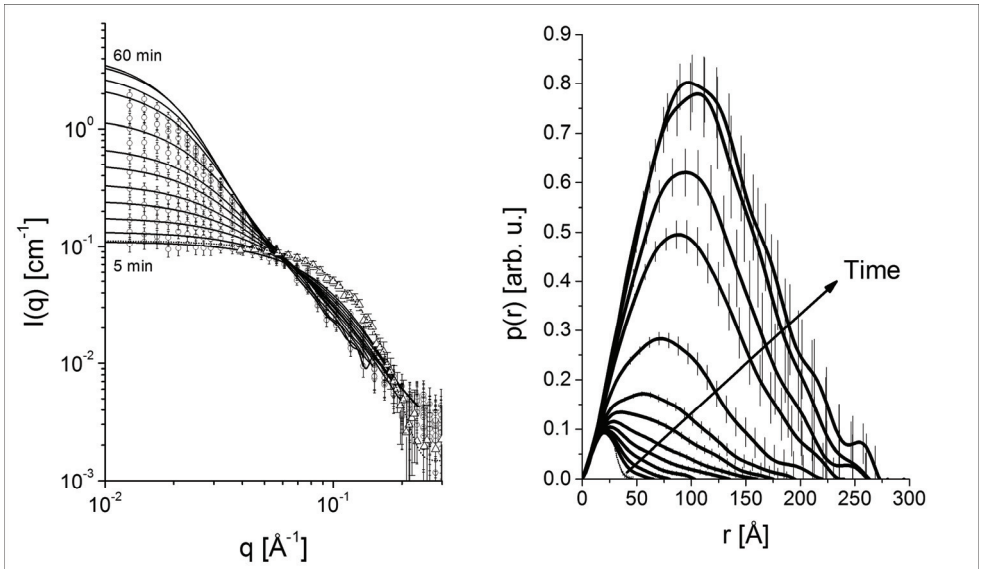

Figura 8 – Agregação de Lisozima induzida por calor. Esquerda: Dados experimentais (círculos abertos) e ajustes teóricos (linhas sólidas). Os frames foram coletados com o sistema à 80º, em intervalos de 5 minutos. Direita: curvas de distribuição de distâncias p(r) para cada curva. Figura tirada de (Oliveira, 2011).

Em outras situações pode-se tentar utilizar a forma da subunidade e explicitamente introduzir o fator de estrutura no sistema. Este procedimento foi proposto por Glatter no programa GIFT (Bergmann *et al.*, 2000) e também por Oliveira no programa WGIFT (Oliveira *et al.*, 2009) e será mais bem detalhado no próximo tópico.

4.2 Método de Transformada Inversa de Fourier generalizado – Desacoplando Fator de forma e estrutura

Neste caso pretende-se ajustar simultaneamente o fator de forma, dado por uma função p(r) *apenas* para a partícula espalhadora e o fator de estrutura *S(q)* do sistema. A intensidade pode ser expressa em função da aproximação de desacoplamento (Kotlarchyk & Chen, 1983),

$$I(q) = k\,P(q)(1+\beta(q)[S(q)-1]) \qquad (14)$$

onde k é uma constante de proporcionalidade (para medidas em escala absoluta, $k = N\Delta\rho^2 V^2$, sendo $\Delta\rho$ o contraste de densidade de espalhamento da partícula e V o volume da partícula); $P(q) = I_1(q) = \langle f^2(\vec{q})\rangle$ é o fator de forma da partícula; $\beta(q) = \langle f(\vec{q})\rangle^2 / \langle f^2(\vec{q})\rangle$ sendo $\langle f(\vec{q})\rangle$ a amplitude de espalhamento promediada em todas as orientações e *S(q)* o fator de estrutura médio do sistema. Aproximações para o termo $\beta(q)$ podem ser obtidas através do ajuste de parte da curva por um modelo de um elipsóide de revolução ou cilindro (Oliveira *et al.*, 2009). O fator de forma é calculado usando a expressão,

$$P(q) = 4\pi \int_0^{D_{\max}} p(r)\frac{\sin(qr)}{qr}\,dr \qquad (15)$$

que é similar ao indicado na equação (3) mas o fato de que a partícula possui uma máxima dimensão finita (D_{max}) é explicitado na integral.

Pode-se utilizar expressões analíticas ou semi-analíticas para descrever o fator de estrutura do sistema. Um exemplo é assumir o sistema como sendo composto por esferas rígidas com raio R_{HS} e fração de volume η, sendo possível obter uma expressão para o fator de estrutura (Kinning & Thomas, 1984) :

$$S_{HS}(q) = \frac{1}{1+24\eta G(2R_{HS}q)/(2R_{HS}q)} \qquad (16)$$

$$G(A) = \frac{a(\sin A - A\cos A)}{A^2} + \frac{\beta(2A\sin A + (2-A^2)\cos A - 2)}{A^3} + \frac{\gamma[-A^4 cpsA + 4\{(3A^2-6)\cos A + (A^3-6A)\sin A + 6\}]}{A^5} \qquad (17)$$

e,

$$\alpha = \frac{(1+2\eta)^2}{(1-\eta)^4}, \qquad \beta = \frac{-6\eta(1+\eta/2)^2}{(1-\eta)^4}, \qquad \gamma = \frac{\eta\alpha}{2} \tag{18}$$

Esta metodologia pode ser ampliada de modo a introduzir outras formas de interação. Se sistemas esféricos são assumidos, pode-se utilizar interações como "esfera rígida colante" (*sticky hard spheres*) (Baxter, 1968) ou esferas com interação de Coulomb (*Rescaled Mean Spherical Approximation - RMSA*) (Hansen & Hayter, 1982). Além disso, em todos estes casos pode-se ainda incluir fatores de polidispersidade.

Aglomerados podem ser modelados de várias formas. Por exemplo, quando são formados grandes aglomerados pode-se ter informação tanto do tamanho destes agregados quanto da forma com que as subunidades se empacotam no mesmo. Nestes casos o sistema pode ser modelado como formando um sistema fractal, com fator de estrutura descrito por (Teixeira, 1988, Oliveira, Santos*, et al.*, 2014)

$$\begin{aligned} S_{Frac}(q) &= 1 + \frac{D}{R^D}\int_0^\infty r^{D-1}\exp(-r/\xi)\frac{\sin(qr)}{qr}dr \\ &= 1 + \frac{1}{(qR)^D}\frac{D\Gamma(D-1)}{\left[1+1/(q^2\xi^2)\right]^{(D-1)/2}}\sin\left[(D-1)\tan^{-1}(q\xi)\right] \end{aligned} \tag{19}$$

onde D é a dimensão fractal, R a dimensão típica das subunidades e ξ o tamanho do agregado fractal.

Se os agregados formados são flexíveis, é possível descrever o fator de estrutura através de uma expressão obtida assumindo-se para N pontos aleatórios com passo constante D (Giehm *et al.*, 2010):

$$S_N(q) = \left[\frac{2}{1+\sin(qD)/(qD)} - 1 - \frac{2\left[1-(\sin(qD)/(qD))^N\right]}{N(1-\sin(qD)/(qD))^2}\frac{\sin(qD)}{qD}\right] \tag{20}$$

Para composições de dímeros e trímeros uma expressão muito simples para o fator de estrutura pode ser obtida (Oliveira *et al.*, 2010),

$$S_{tot}(q) = f_{\text{mon}} + f_{\text{dim}} \cdot S_{\text{dim}}(q) + f_{\text{trim}} \cdot S_{trim}(q) \tag{21}$$

onde, $\sum_k f_k = 1$, e f_i são as frações de número de cada espécie, monômero, dímero e trímero. Os fatores de estrutura parciais são dados por,

$$S_{\dim}(q) = 2 + 2\frac{\sin(qd)}{qd} \qquad (22)$$

e (trímeros lineares)

$$S_{trim}(q) = 3 + 4\frac{\sin(qd)}{qd} + 2\frac{\sin(2qd)}{2qd} \qquad (23)$$

Para agregados globulares sem forma específica uma alternativa é de se utilizar uma curva Gaussiana de modo a obter o raio de Guinier (R_G) do agregado e uma indicação da contribuição do agregado na intensidade espalhada (S_C^{agg}) (Landa *et al.*, 2013, Oliveira, Monteiro*, et al.*, 2014).

$$S_{Gui}(q) = 1 + S_C^{agg}\exp\left(-q^2 R_G^2/3\right) \qquad (24)$$

Todas estas metodologias de modelagem estão implementadas no programa WGIFT (Oliveira *et al.*, 2009, Oliveira, Santos*, et al.*, 2014, Oliveira, Monteiro*, et al.*, 2014), permitindo sua aplicação para o estudo de diversos sistemas. O ponto principal desta metodologia é a possibilidade de poder-se desacoplar informações de fator de forma e fator de estrutura. Como mostrarei a seguir, tal desacoplamento permite o estudo de peculiaridades dos sistemas, mesmo quando as subunidades de interesse encontram-se agregadas. O programa está em constante desenvolvimento incorporando outros fatores de estrutura e opções.

4.3 Modelagem dependente da forma – Assumindo um fator de forma conhecido

Para formas simples pode-se integrar a equação (2) e obter o fator de forma de amplitude $f(\vec{q})$. Com esta expressão para a amplitude pode-se fazer a média angular e de modo a obter a intensidade e de espalhamento *I(q)*. Alguns exemplos são mostrados na tabela 1. Uma lista mais completa de fatores de forma pode ser encontrada na literatura (Pedersen, 1997), bem como diversas implementações mais avançadas (Szekely *et al.*, 2010, Giehm *et al.*, 2010).

Tabela 1 – Alguns exemplos de expressões semi-analíticas para intensidades de espalhamento calculadas para partículas com formas simples

Forma	*Fator de Forma Normalizado*
Esfera Homogênea com raio R	$I_1(q) = f_1(q)^2 = \left(\frac{3[\sin(qR) - qR\cos(qR)]}{(qR)^3} \right)^2$
Casca esférica com raio externo R_1 e raio interno R_2	$I_1(q) = \left[\frac{V(R_1) f_1(q, R_1) - V(R_2) f_2(q, R_2)}{V(R_1) - V(R_2)} \right]^2$ $V(R) = 4\pi R^3 / 3$
Cilindro Homogêneo com raio R e comprimento L	$I_1(q) = \int_0^{\pi/2} \left[\frac{2J_1(qR\sin\alpha)}{qR\sin\alpha} \frac{\sin(qL\cos\alpha/2)}{qL\cos\alpha/2} \right]^2 \sin\alpha d\alpha$
Elipsóide de revolução com semi-eixos R, R e εR	$I_1(q) = \int_0^{\pi/2} f_1(q, r(R, \varepsilon, \alpha)) \sin\alpha d\alpha$ $r(R, \varepsilon, \alpha) = R(\sin^2\alpha + \varepsilon\cos^2\alpha)^{1/2}$

A principal vantagem de se utilizar uma expressão analítica ou semi-analítica é o fato de que, em geral, utiliza-se um número relativamente pequeno de parâmetros para descrever o modelo. Além disso, expressões para modelos simples podem ser combinadas formando estruturas mais complexas (Yan *et al.*, 2009, Giehm *et al.*, 2010). Em diversas aplicações a forma da partícula é conhecida, mas o cálculo analítico é impraticável. Nestes casos é possível utilizar o método de elementos finitos para construir a partícula utilizando subunidades esféricas, e utilizar a equação de Debye para o cálculo da intensidade (Debye, 1915, Glatter, 1980):

$$P_{Model}(q) = \frac{f_1(q, r_{bead})^2}{N^2} \sum_{i,j=1}^{N} \frac{\sin(qr_{ij})}{qr_{ij}} \qquad (25)$$

Este procedimento permite o cálculo e otimização de modelos bastante complexos (Oliveira *et al.*, 2010, Pedersen *et al.*, 2012, Oliveira *et al.*, 2009, Oliveira, 2005, 2001). Em todos estes casos pode-se incluir possíveis interações entre as partículas utilizando a aproximação de desacoplamento (equação 14). Um exemplo de aplicação é mostrado na Figura 9 onde é mostrado um estudo *in situ* da fibrilação da molécula glucagon. Neste estudo foi possível modelar as fibras no estágio final como sendo compostas por três fibras mais finas entrelaçadas (Oliveira *et al.*, 2009).

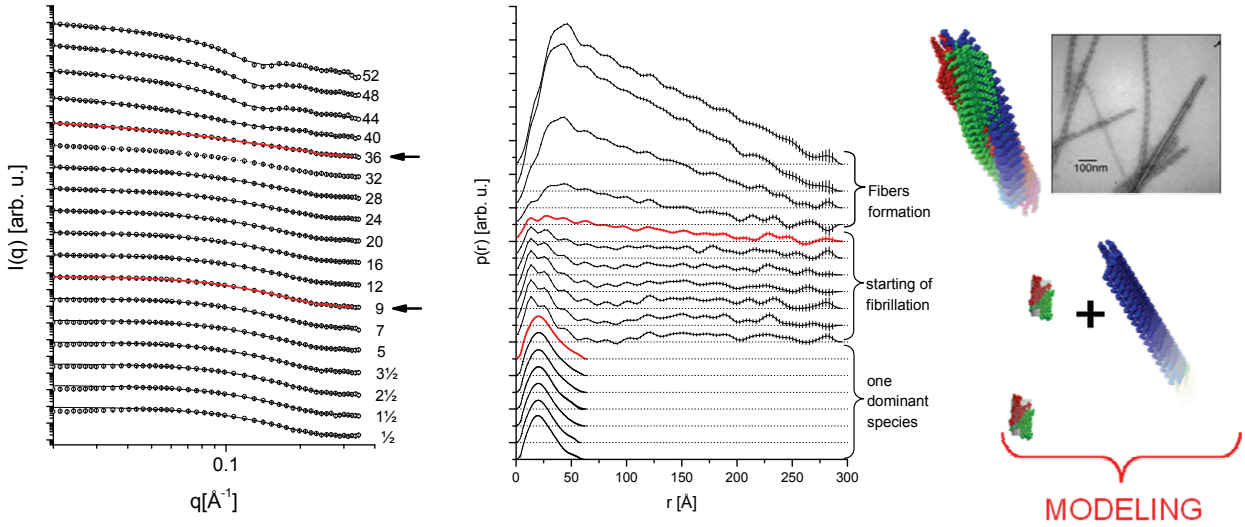

Figura 9 – Estudos de SAXS para agregação de glucagon em fibras amilóides. Da esquerda para a direita: Serie de dados de SAXS coletados em função da temperatura, curvas de distribuição de pares de distâncias p(r) para cada curva de espalhamento, modelos obtidos através da construção por elementos finitos e uma imagem de TEM obtida para o sistema de fibras amilóides maduras. Figura baseada em (Oliveira *et al.*, 2009).

Em muitos casos a construção do modelo utilizando subunidades esféricas também pode não ser trivial. Nestes casos deve-se desenvolver procedimentos específicos para a construção dos modelos antes do cálculo da intensidade. Este procedimento foi desenvolvido em um artigo recente (Alves *et al.*, 2014) onde demonstramos em detalhe a construção de modelos de alta simetria utilizando a técnica de elementos finitos. Para estes desenvolvimentos, toma-se como ponto de partida um conjunto de pontos na superfície de uma esfera, que pode definir uma dada geometria. Um exemplo é a biblioteca ***netlib*** (Hume) que fornece uma grande quantidade de coordenadas dos vértices e conectividades para mais de 150 corpos geométricos. Tendo-se estes vértices, diversos procedimentos de construção do modelo podem ser executados, como indicado na Figura 10. Corpos sólidos e estruturas tipo casca também podem ser construídos através da definição da região externa/interna do modelo. Este procedimento é explicado em detalhe em (Alves *et al.*, 2014, Alves, 2015), mas uma descrição simplificada é mostrada na Figura 11.

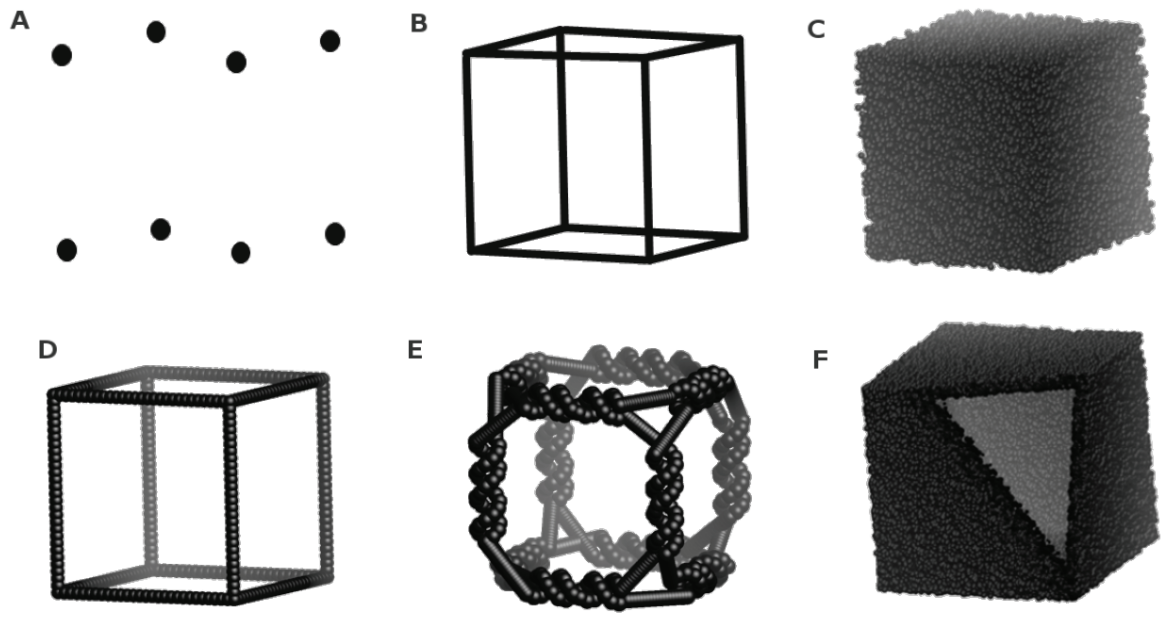

Figura 10 – Construção do modelo. A) Posição dos vértices de um cubo. B) União dos vértices com segmentos de retas. C) Modelo do tipo sólido. D) União dos vértices com subunidades esféricas. E) União dos vértices com DNA. F) Modelo do tipo casca. Figura adaptada de (Alves *et al.*, 2014).

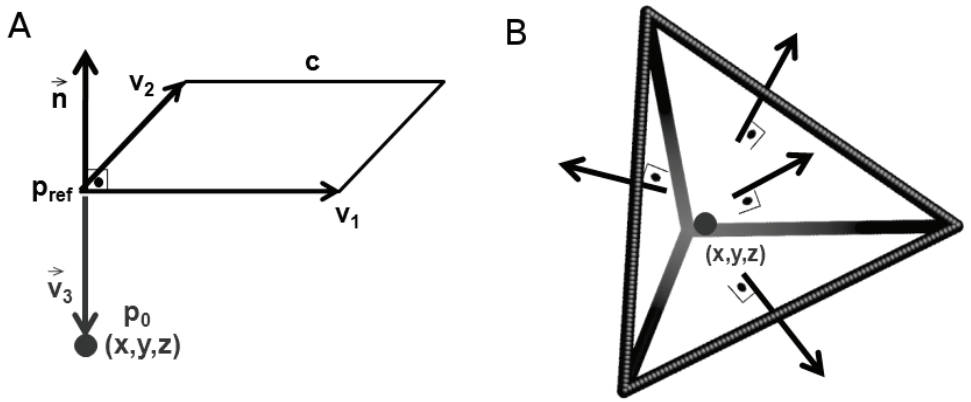

Figura 11 – Considerações sobre posições e planos. O vetor *n* é a normal ao plano definido pelos vetores v_1 e v_2. O vetor v_3 conecta o ponto de referência p_{ref} ao ponto de interesse p_0. (a) Se $v_3 \bullet n = 0$ p0 está no plano, se $v_3 \bullet n < 0$ p_0 está no semi espaço negativo e se $v_3 \bullet n > 0$ p_0 está no semi espaço positivo do plano. (b) p_0 está dentro do tetraedro quando $v_3 \bullet n < 0$ para todos os vetores normais às faces do tetraedro.

Utilizando estes procedimentos de modelagem é possível fazer o cálculo teórico de variados modelos com geometrias variadas. Estes modelos são descritos por um número pequeno de parâmetros que podem ser otimizados no ajuste de dados experimentais (Alves *et al.*, 2014, Oliveira *et al.*, 2010). Exemplos de cálculo são mostrados na Figura 12.

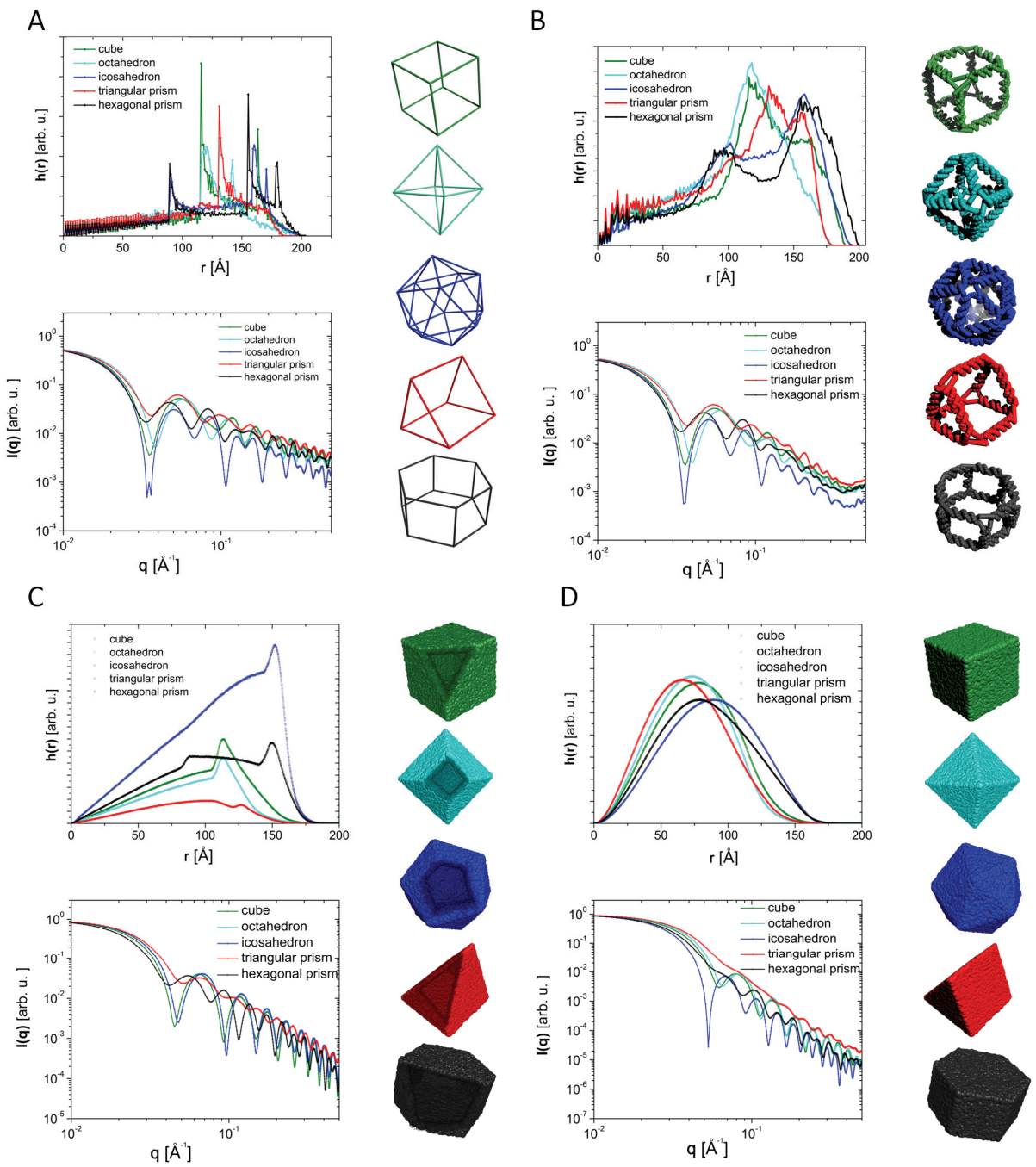

Figura 12 – Calculo de intensidades teóricas para diversos corpos geométricos. Corpos construídos unindo-se os vértices com segmentos de reta (a) corpos construídos com segmentos tipo DNA nas arestas (b), corpos tipo casca (c) e corpos sólidos (d). Figura tirada de (Alves *et al.*, 2014).

4.4 Métodos de Modelagem ab initio

Existem na literatura diversos métodos de modelagem que fornecem um modelo tridimensional a partir de curvas de espalhamento unidimensionais. Estes métodos, também chamados *ab initio*, podem ser implementados de várias formas, dependendo de peculiaridades do sistema e também da quantidade de informação disponível (programa ASSA / SASHA (Svergun *et al.*, 1997); programa DALAI (Chacon *et al.*, 1998); programa DAMMIN (Svergun, 1999); programa SAXS3D (Walther

et al., 2000); programa GASBOR (Svergun *et al.*, 2001)). Um exemplo de aplicação é mostrado na Figura 13 onde um modelo de baixa resolução para a lisozima é obtido diretamente dos dados experimentais (Oliveira, 2011).

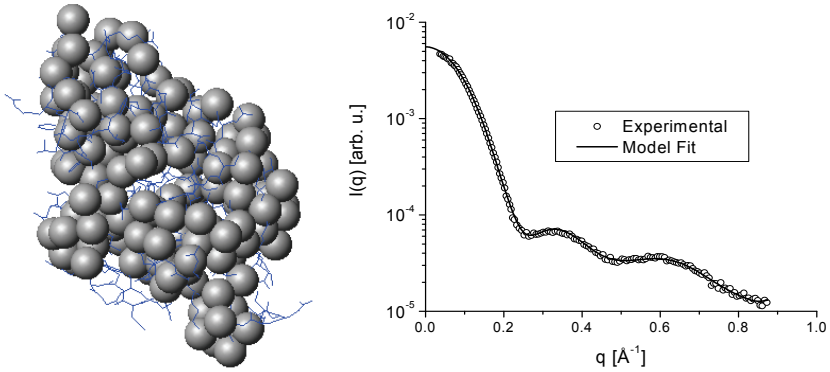

Figura 13 – Exemplo de modelagem *ab initio* para dados de SAXS utilizando o programa GASBOR. Esquerda: Estrutura otimizada (esferas sólidas) superposta pela estrutura real conhecida por cristalografia de proteínas (arquivo pdb 6lyz.pdb). Direita: Ajuste dos dados experimentais. Círculos abertos – dados experimentais. Linha sólida – ajuste do modelo. Figura tirada de (Oliveira, 2011).

Especificamente para sistemas compostos por proteínas, complexos protéicos, RNA e DNA, métodos *ab initio* podem ser combinados com estruturas a nível atômico, obtidas por cristalografia de proteínas, ressonância nuclear magnética, modelos teóricos ou obtidos por outras técnicas (programa CRYSOL, (Svergun *et al.*, 1995) programas BUNCH, SASREF e CORAL, (Petoukhov & Svergun, 2005). Nestes casos os dados de SAXS podem fornecer informações importantes sobre a forma dos complexos formados bem como o arranjo de domínios. A principal limitação desta metodologia reside no fato de que curvas de SAXS possuem uma quantidade de informação muito pequena o que faz com que não se possa obter um resultado único para as modelagens, isto é, diversos ajustes independentes fornecerão resultados parecidos, mas não idênticos. Devido a essa limitação, resultados de SAXS sempre devem ser correlacionados com dados obtidos por outras técnicas (Oliveira, 2011).

Venho trabalhado há vários anos com a utilização destes métodos para o estudo de diversos tipos de sistemas biológicos (da Silva *et al.*, 2014, Demasi, Hand*, et al.*, 2014, Demasi, Netto*, et al.*, 2014, Oliveira & Pedersen, 2013, Andersen *et al.*, 2012, Behrens *et al.*, 2012, Calcutta *et al.*, 2012, Silva *et al.*, 2012, Oliveira, 2011, Rasmussen, Pinto Oliveira*, et al.*, 2011, Rasmussen, Oliveira*, et al.*, 2011), entre diversos outros artigos. Em muitos casos é necessário desenvolver metodologias complementares para o ajuste dos dados experimentais de modo a incluir elementos adicionais na modelagem. Em um estudo recente, foi possível obter a estrutura do complexo hemoglobina-haptoglobina. A Hemoglobina é o transportador fundamental da molécula de oxigênio no sangue, mas também um componente potencialmente nocivo a tecidos devido a seus grupos heme serem altamente reativos. Durante a hemólise intravascular, comum quando o individuo possui malária ou

outras hemoglobinopatias, hemoglobina é liberada no sangue sendo então capturada pela proteína haptoglobina, a qual possui ação de proteção para esta fase aguda. Este artigo foi publicado na revista *NATURE* (Andersen *et al.*, 2012) e apresentou, pela primeira vez, a estrutura cristalográfica do complexo hemoglobina-haptoglobina em nível atômico (resolução de 2.9Å). A estrutura revelou que o complexo é formado um homodímero de haptoglobinas nas quais dois dímeros de hemoglobina se ligam covalentemente. Também foi possível obter como este complexo se liga ao receptor necrófago CD163, o qual possui a função de limpeza e defesa do organismo. Com os resultados deste trabalho, processos fundamentais relacionados à forma de interação entre a hemoglobina e haptoglobina, bem como sua forma de ligação ao receptor CD163 puderam finalmente ser compreendidos.

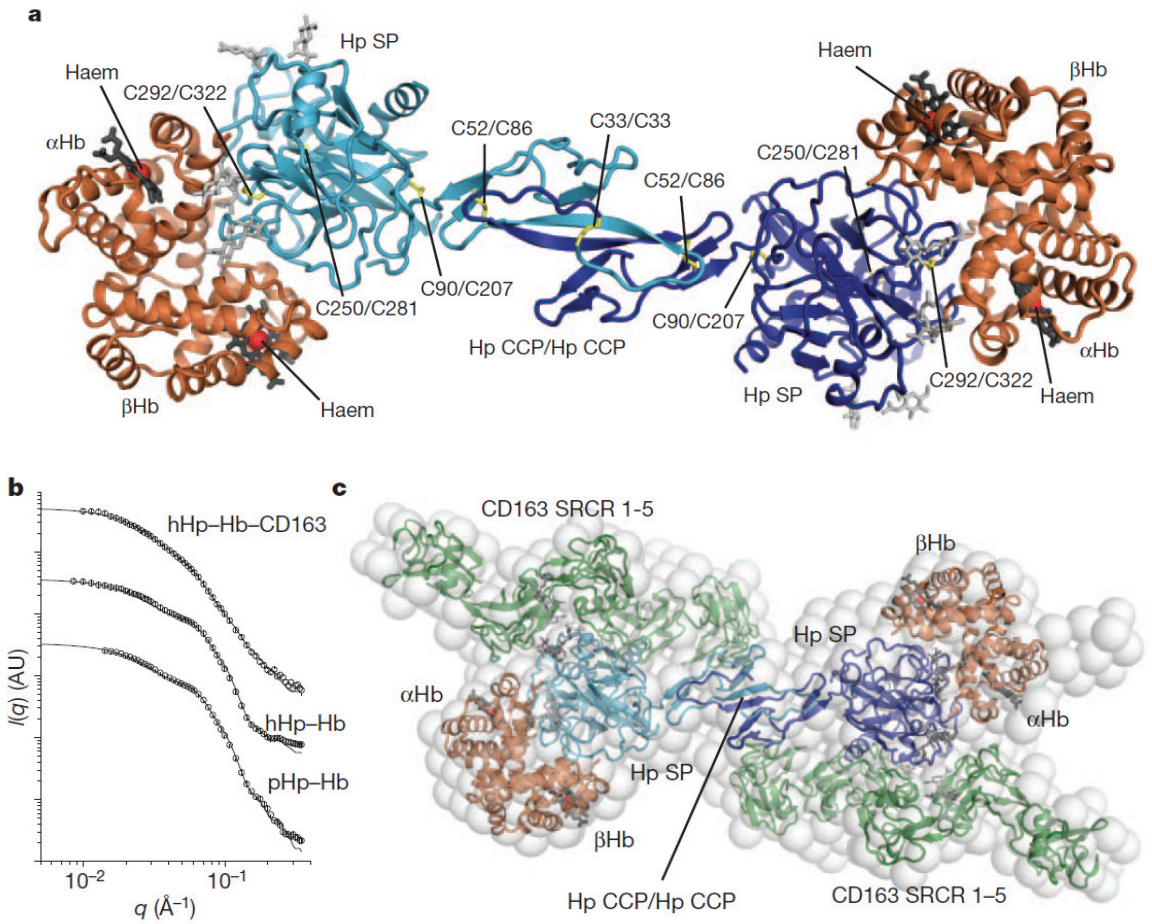

Figura 14 – Complexo hemoglobina-haptoglobina-CD163. (a) estrutura cristalográfica do complexo hemoglobina-haptoglobina (Hp-Hb). (b) cálculo da intensidade teórica de espalhamento para as cristalográficas do complexo em humanos (hHp-Hb) e em suínos (pHp-Hb). O ajuste dos dados do complexo Hp-Hb com o receptor CD163 (hHp-Hb-CD163) e o correspondente modelo foi obtido utilizando o programa CORAL. Figura tirada de (Andersen *et al.*, 2012).

4.5 Deconvolução Quadrática – obtenção do perfil de densidade eletrônica

Em diversas aplicações a forma da partícula é conhecida, mas o perfil de densidade de comprimento de espalhamento e as dimensões do sistema devem ser determinados. Moléculas anfifílicas como surfactantes e diversos tipos de polímeros dibloco se auto organizam em estruturas que podem ser modeladas desta forma (Jones, 2002). Diversas proposições para a deconvolução de perfis de densidade eletrônica a partir de dados experimentais podem ser encontradas na literatura (Pape & Kreutz, 1978, Zhang *et al.*, 1994). Nestas proposições o passo inicial era tirar a raiz quadrada da intensidade de espalhamento de modo a se obter o valor absoluto da amplitude *f(q)*. Ao final, por uma transformada de Fourier pode-se obter o perfil de densidade eletrônica *ρ(r)*. No entanto, este procedimento possui sérios problemas uma vez que os sinais corretos da amplitude *f(q)* não são conhecidos e devem ser propostos. Além disso, a região muito limitada do espaço recíproco impede um cálculo preciso da transformada de Fourier inversa. Um método mais estável foi proposto por Glatter (Glatter, 1981, Glatter & Hainisch, 1984, Bergmann *et al.*, 2000, Pedersen, 1992) onde a convolução é feita a partir pelo uso da função *p(r)*. Este método permite a correta determinação do perfil de densidade eletrônica como demonstrado em diversos exemplos na literatura (Rathgeber *et al.*, 2002). Um exemplo de aplicação é mostrado na Figura 15.

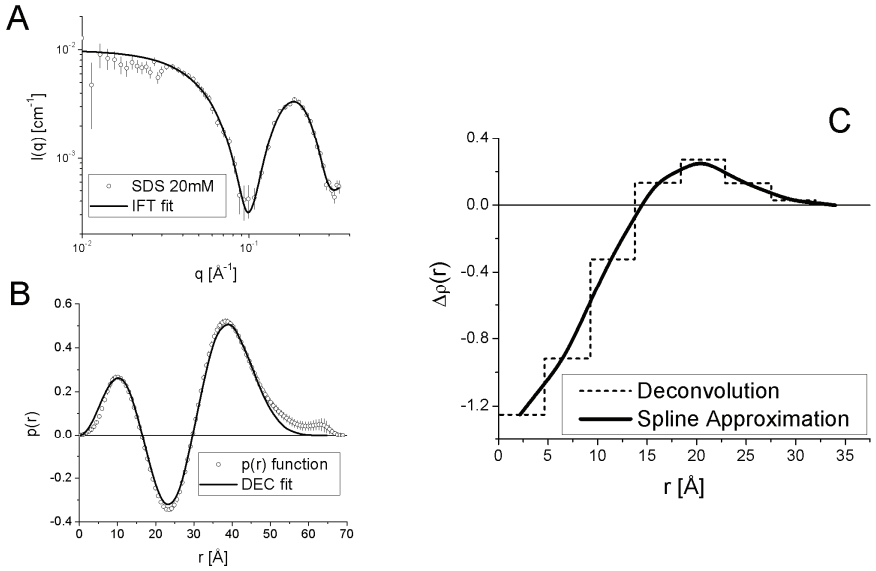

Figura 15 – Exemplo de aplicação do método de deconvolução quadrática. A) Dados experimentais de SDS (círculos abertos) e o ajuste obtido pelo método de IFT (linha sólida). B) Função p(r) calculada pelo método de IFT (círculos abertos) e a p(r) teórica obtida pelo método de deconvolução usando o método de Glatter (linha sólida). C) Perfil de densidade eletrônica obtido representado por funções degrau (linhas tracejadas) e por uma representação suave (linha sólida). Figura retirada de (Oliveira, 2011).

Neste método de deconvolução é necessário o cálculo da função *p(r)* do sistema uma vez que o ajuste é feito nesta função. Este requerimento limita a aplicabilidade do método, particularmente para

a deconvolução de sistemas com fatores de estrutura (Oliveira *et al.*, 2012). Uma abordagem inovadora pode ser utilizada, como apresento nos próximos tópicos.

4.6 Efeitos de tamanho do feixe e resolução do detetor

Nas descrições anteriores foram assumidas condições ideais: o feixe incidente era um ponto, isto é, com, dimensões desprezáveis; o detetor é assumido como tendo resolução infinita, ou seja, não distorce os dados experimentais; o feixe incidente é assumido como sendo perfeitamente monocromático, com um comprimento de onda único.

Em alguns casos estas aproximações são válidas e podem ser utilizadas nas descrições dos dados. No entanto para a correta interpretação dos dados, particularmente para casos onde se tem efeitos de aberração ou borramento experimentais (*smearing*) afetam bastante os dados experimentais, é necessário incluir estes efeitos na modelagem dos dados.

A inclusão de efeitos de borramento na descrição dos dados experimentais é objeto de estudo por vários autores (Guinier *et al.*, 1955, Glatter & Kratky, 1982, Lindner & Zemb, 2002, Feigin & Svergun, 1987, Pedersen *et al.*, 1990, Oliveira, 2005). Uma forma bastante interessante de incluir estes efeitos foi proposta por Pedersen (Pedersen *et al.*, 1990, Pedersen & Riekel, 1991),

$$I^{smeared}\left(\langle\vec{q}\rangle\right)=\int R\left(\vec{q},\langle\vec{q}\rangle\right)I^{point}\left(\langle\vec{q}\rangle\right)d\vec{q} \qquad (26)$$

Onde $\vec{q}$ é o vetor transferência de momento do espaço recíproco e $\langle\vec{q}\rangle$ é o vetor médio em torno do qual a função de resolução é relevante. $I^{smeared}\left(\langle\vec{q}\rangle\right)$ é a intensidade com os efeitos de resolução, $I^{point}\left(\langle\vec{q}\rangle\right)$ é a intensidade (teórica) para um foco ponto ideal e $R\left(q,\langle\vec{q}\rangle\right)$ é a função de resolução do sistema. Para sistemas onde a intensidade espalhada é circularmente simétrica a integração angular pode ser realizada e somente o modulo de $\vec{q}$ é importante,

$$I^{smeared}\left(\langle q\rangle\right)=\int_0^\infty R_{AV}\left(q,\langle q\rangle\right)I^{point}\left(\langle q\rangle\right)d\vec{q} \qquad (27)$$

Nesta descrição todos os efeitos de borramento são inseridos em uma única função de resolução $R_{AV}\left(q,\langle\vec{q}\rangle\right)$. Neste desenvolvimento a contribuição para a função de resolução total de cada uma das fontes de borramento e assumida tendo uma forma Gaussiana com uma dada largura σ_i. Na função de resolução final, as variâncias de cada uma das fontes de borramento são compostas na forma $\sigma^2=\sum\sigma_i^2$. A função de resolução $R_{AV}\left(q,\langle\vec{q}\rangle\right)$ é dada por,

$$R_{AV}(q,\langle q\rangle)=(q/\sigma^2)\exp\left[-\frac{1}{2}\left(q^2+\langle q\rangle^2/\sigma^2\right)\right]I_0\left(q\langle q\rangle/\sigma^2\right) \quad (28)$$

onde I_0 é a função de Bessel modificada de primeiro tipo e ordem zero. Quando se faz necessário incluir os ajustes com função de resolução tem-se um custo computacional grande uma vez que cada ponto da curva teórica é o resultado de uma integração adicional, como dada na equação (27).

A inclusão ou não de efeitos de borramento depende das características do experimento. Para raios X, em geral, com colimação utilizando fendas ou *pinholes*, estes efeitos são pequenos e somente são incluídos em casos onde a intensidade de espalhamento possui mínimos ou máximos bastante acentuados como, por exemplo, picos de difração. Se a intensidade de espalhamento varia suavemente os efeitos de borramento acabam sendo mínimos e não precisam ser inseridos. Quando se utilizam nêutrons, por outro lado, o tamanho de feixe e polidispersidade de comprimentos de onda são aumentados de modo a se ter um maior fluxo. Neste caso os efeitos de borramento são maiores e correções são necessárias.

4.7 Modelagem simultânea de fatores de forma e de estrutura

Nos casos citados até o momento, a inclusão de fatores de estrutura restringiu-se a situações em que estes efeitos afetassem principalmente a parte inicial de curvas de espalhamento. Seja para a formação de agregados ou interações interpartículas, as expressões mostradas causam alterações principalmente a baixos valores de q sendo que para ângulos maiores ter-se-á apenas o fator de forma das partículas espalhadoras (Glatter & Kratky, 1982). No entanto, existem outros casos onde pode ocorrer ordenação a longo alcance, o que acaba por gerar picos de correlação em curvas de espalhamento. Nestas situações a inclusão de fatores de estrutura é muito mais complicada, pois eles afetarão a curva toda. Ao final, a curva de intensidade será o resultado da combinação dos fatores de forma das subunidades e do fator de estrutura do sistema. Os picos de difração obtidos são semelhantes aos obtidos por sistemas cristalinos, mas com a diferença de dizerem respeito a distâncias de correlação cerca de duas ordens de grandeza maiores.

a) Sistemas hexagonais

Vários tipos de sistemas possuem estas características. Por exemplo, na Figura 16 é mostrado um exemplo de aplicação na qual estudamos a formação *in situ* de uma rede hexagonal de micelas cilíndricas de P123, induzida pela incorporação de sílica no meio (Sundblom *et al.*, 2009).

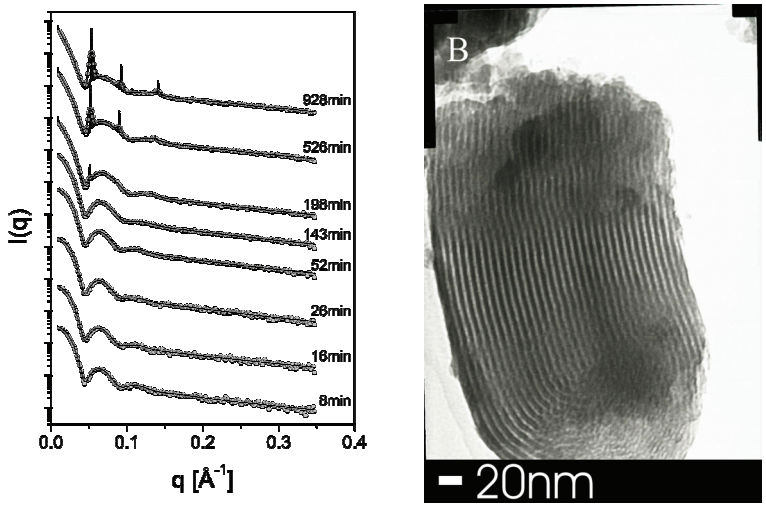

Figura 16 – Estudo de sílica mesoporosa ordenada em sistemas hexagonais. Esquerda: curvas de SAXS obtidas para diferentes instantes do estudo *in situ*. Direita: Figura de TEM para o sistema final calcinado. Figura tirada de (Sundblom *et al.*, 2009).

Esta metodologia foi proposta por Föster (Forster *et al.*, 2005), Freiberger (Freiberger & Glatter, 2006) e Sunblom (Sundblom *et al.*, 2009) e permite a modelagem simultânea tanto do fator de forma quanto de estrutura. Para o caso da rede hexagonal de micelas cilíndricas utilizou-se a seguinte expressão para a intensidade:

$$I(q) = Sc_1 P_{rod}(q)\left\langle F_{CS}(q)^2 \right\rangle \left(1 + \beta(q)\left[\langle Z(q)\rangle - 1\right] G(q)\right) \qquad (29)$$

sendo $F_{CS}(q)$ o fator de forma da sessão transversal de um cilindro *core shell*,

$$F_{CS}(q) = \frac{\Delta\rho_{out}}{\Delta\rho_{in}} R_{out}^2 \frac{2J_1(qR_{out})}{qR_{out}} \exp\left[-\frac{1}{2}q^2\sigma_{\text{int}}\right] - \left(\frac{\Delta\rho_{out}}{\Delta\rho_{in}} - 1\right) R_{in}^2 \frac{2J_1(qR_{in})}{qR_{in}} \qquad (30)$$

Sendo R_{out} o raio externo e R_{in} o raio interno do cilindro. Os termos $\Delta\rho_{out}$ e $\Delta\rho_{in}$ são os contrastes de densidade eletrônica externa e interna respectivamente. Como mencionado, o fator de forma é descrito como uma estrutura *core shell*. Composições mais complexas podem ser feitas, como demonstrarei posteriormente. O termo $P_{rod}(q)$ já foi mostrado anteriormente na equação (7).

A média indicada na equação (29) $\langle F_{CS}(q)\rangle$ decorre do fato de ser introduzida polidispersidade no diâmetro, dado pela fórmula,

$$\left\langle F_{CS}(q)^2 \right\rangle = \frac{\int_0^\infty D(r) F_{CS}{}^2(q,r)\,dr}{\int_0^\infty D(r)\,dr} \qquad (31)$$

onde se utilizou uma distribuição de Schulz-Zimm,

$$D(x) = \left(\frac{z+1}{x_0}\right)^{z+1} \frac{x^z}{\Gamma(z+1)} \exp\left(-(z+1)\frac{x}{x_0}\right) \qquad (32)$$

sendo x_0 o centro da distribuição e z está relacionado com a polidispersidade relativa σ_R/R dos raios pelo termo $z = 1/(\sigma_R/R)^2 - 1$. O fator de estrutura é introduzido pelo termo $Z_0(q)$

$$Z_0(q) = c\frac{2}{\sqrt{3}a^2 q}\sum_{\{hk\}} m_{hk} L_{hk}(q) \qquad (33)$$

Sendo c uma constante de proporcionalidade, a o parâmetro de rede e m_{hk} a multiplicidade do pico. Os picos são descritos pela função $L_{hk}(q)$,

$$L_{hk}(q) = \frac{2}{\pi\delta}\left|\frac{\Gamma[\nu/2 + i\gamma_\nu 2(q-q_{hk})/(\pi\delta)]}{\Gamma[\nu/2]}\right|^2, q_{hk} = \left(4\pi/a\sqrt{3}\right)\sqrt{h^2+hk+k^2} \qquad (34)$$

sendo h,k os índices de Miller do pico e ν o parâmetro que define a forma do pico ($\nu \to \infty$, Gaussiana, $\nu \to 0$, Lorentziana). Estas condições impostas para os índices de Miller dizem respeito a sistemas hexagonais. Expressões para outros tipos de simetrias podem ser obtidas na literatura (Forster *et al.*, 2005, Cullity & Stock, 2001). O termo $G(q)$ introduz o efeito de desordem dos cilindros na rede cristalina:

$$G(q) = \exp\left(-\sigma_a^2 a^2 q^2\right) \qquad (35)$$

sendo σ_a parâmetro de desordem. O acoplamento entre o fator de forma e de estrutura é feito pelo parâmetro $\beta(q)$,

$$\beta(q) = \frac{\langle F_{CS}(q)\rangle^2}{\langle F_{CS}(q)^2\rangle} \qquad (36)$$

Apesar de o cálculo ser bastante elaborado, é possível incorporar todas estas expressões em um único procedimento de minimização, permitindo o ajuste simultâneo do fator de forma de estrutura. Como apresentado por Förster (Forster *et al.*, 2005), fatores de estrutura para outras simetrias (cubicas, planares, etc) podem ser incorporadas permitindo a expandindo deste método. O procedimento apresentado aqui foi desenvolvido por mim em colaboração com o Prof. Jan Skov Pedersen e foi utilizado com sucesso em diversas aplicações (Sundblom *et al.*, 2009, Sundblom *et al.*, 2010, 2011). Em um trabalho recente, realizado em colaboração com a Profa. Dra. Marcia Carvalho de Abreu Fantini (Mariano-Neto *et al.*, 2014) foi demonstrada a incorporação de moléculas biológicas dentro dos poros da sílica mesoporosa. Neste trabalho, que foi parte da tese de doutoramento do Dr. Francisco Mariano Neto (Mariano Neto, 2013), do qual fui co-orientador, a sílica foi utilizada como adjuvante imunológico podendo facilitar a aplicação de medicamento no organismo. Ainda como resultado da tese de doutoramento do Dr. Mariano Neto, artigos estão sendo

preparados demonstrando a aplicação de diversos adjuvantes, inclusive em sistemas modelo como ratos e cavalos (Mariano-Neto *et al.*, 2014).

b) Sistemas Planares – Deconvolução Gaussiana

Moléculas anfifílicas são compostas por duas regiões, com diferentes afinidades para com moléculas de água. Uma região, dita cauda hidrofóbica, não faz pontes de hidrogênio e desta forma quando inserida em sistemas aquosos obriga uma estruturação das moléculas de agua ao redor da mesma. Um exemplo de moléculas puramente hidrofóbicas são óleos em geral: quando dispersados em água, dependendo da concentração do óleo na água pode-se ter até a separação das fases àgua-óleo (Jones, 2002). No entanto, as moléculas anfifílicas possuem outra região, dita cabeça hidrofílica, que faz pontes de hidrogênio e sendo assim possui afinidade com a água. Esta molécula anfifílica, com caráter heterogêneo, quando colocada em água apresenta uma auto-organização, de modo a expor a região hidrofílica ao solvente e esconder a região hidrofóbica diminuindo assim a energia livre total do sistema. Dependendo de suas características geométricas as estruturas formadas podem ser micelas (esféricas ou cilíndricas) ou estruturas planares, bicamadas, podendo estas serem unilamelares ou multilamelares (Jones, 2002, Hamley, 2000). Dados de espalhamento a baixos ângulos são bastante pertinentes para o estudo destes sistemas devido aos diferentes contrastes de comprimento de espalhamento. Quando o estudo é feito utilizando raios X em sistemas aquosos, a "cabeça" pode ter contraste positivo com relação ao solvente enquanto que a cauda pode ter contraste negativo. Este contraste positivo/negativo fornece uma característica bastante peculiar à intensidade de espalhamento para este tipo de sistema, como pode ser visto na Figura 15 para micelas de SDS.

Dados de espalhamento para estruturas planares multilamelares contém informações sobre o fator de forma (da bicamada lipídica) e também fator de estrutura (do sistema lamelar). Diversas proposições para a modelagem deste tipo de sistema podem ser encontradas na literatura. No final dos anos 60 Worthington propôs uma metodologia simplificada (Worthington, 1969), onde o perfil de densidade de espalhamento da bicamada (descrito como funções degrau) era replicado para mimetizar o efeito do fator de estrutura. Com a introdução do fator de estrutura para sistemas lamelares feita por Caillè (Caillé, 1972), Nagle e colaboradores propuseram uma metodologia para a obtenção do fator de forma e de estrutura em sistemas de multicamadas lipídicas (Nagle *et al.*, 1996). No entanto, este procedimento era extremamente trabalhoso e não permitia o ajuste direto do fator de forma. Nallet e colaboradores (Nallet *et al.*, 1993) propuseram uma metodologia para modelagem simultânea de fatores de forma (duas funções degrau) e do fator de estrutura. Este trabalho foi o primeiro na literatura a propor tal ajuste simultâneo. Pabst e colaboradores (Pabst *et al.*, 2000) propuseram uma metodologia semelhante descrevendo a bicamada pela soma de duas funções Gaussianas. Em ambos os casos a descrição da bicamada é bastante rudimentar e não é capaz de descrever com precisão o

perfil de densidade eletrônica. Em uma tentativa de melhorar a descrição do perfil de densidade eletrônica Glatter e Fritz (Fritz & Glatter, 2006) propuseram uma metodologia combinando o método de deconvolução quadrática mencionado anteriormente com a modelagem do fator de estrutura lamelar. Tal abordagem consegue descrever o perfil de densidade eletrônica, mas requer o calculo da função *p(r)* correspondente à bicamada lipídica, o que acaba por introduzir instabilidades na modelagem.

Desenvolvi recentemente uma metodologia capaz de obter simultaneamente o fator de forma e de estrutura para este caso (Oliveira *et al.*, 2012), mas que permite uma descrição otimizada do fator de forma do sistema. O perfil de densidade eletrônica para este caso é descrito por uma combinação de funções Gaussianas,

$$\rho(z) = \sum_{n=1}^{n_{\max}} a_n \left[G_s(z, z_n, \sigma_n) + G_s(z, -z_n, \sigma_n) \right] / \left(1 + \delta_{i1}\right)$$
$$\delta_{i1} = 1, i = 1 \qquad (37)$$
$$\delta_{i1} = 0, i = 2,3, n_{\max}$$

onde

$$G_s\left(z, z_n, \sigma\right) = \frac{1}{\sigma\sqrt{2\pi}} \exp\left[-(z - z_n)^2 / 2\sigma^2 \right] \qquad (38)$$

O termo δ_{i1} é introduzido para impedir uma contagem dupla da função Gaussiana central. n é a ordem da função Gaussiana e o perfil é definido pelos fatores de amplitude a_n. Os centros das funções Gaussianas são definidos em termos da meia largura da bicamada, Z, e da largura das Gaussianas utilizadas, σ.

$$z_n = (n-1)2\sigma, \qquad \sigma = \frac{Z}{2n_{\max}\sqrt{2\ln 2}} \qquad (39)$$

Esta escolha de centros e larguras gera uma superposição entre as Gaussianas o que permite a construção de perfiz suaves. Para o caso unidimensional de uma bicamada centrossimétrica, a transformada de Fourier de um perfil Gaussiano é dado por (Pabst *et al.*, 2000, Abramowitz & Stegun, 1972):

$$F(q, n) = \sqrt{2\pi}\sigma \exp\left(-\frac{\sigma^2 q^2}{2} \right) \cos\left(q z_n\right) \qquad (40)$$

A expressão final para a amplitude de espalhamento da bicamada é dada por:

$$F(q) = \sum_{n=1}^{n_{\max}} a_n F(q,n) \qquad (41)$$

O fator de estrutura pode ser introduzido pela teoria de Cailè modificada MCT (*Modified Cailé Theory*), sendo dado por (Zhang *et al.*, 1994):

$$S_{MCT}(q) = 1 + 2\sum_{n=1}^{N-1}\left(1 - \frac{n}{N}\right)\cos(nqd)e^{-(d/2\pi)^2 q^2 \eta\gamma}(\pi q)^{-(d/2\pi)^2 q^2 \eta} \qquad (42)$$

sendo d a distancia interplanar, N o número de camadas correlatas e γ a constante de Euler. A intensidade de espalhamento final incorporando o fator de forma e de estrutura é dada por,

$$I(q) = P(q)_{plane}\left(|F(q)|^2 S_{MCT}(q)\right) \qquad (43)$$

sendo $P(q)_{plane}$ dado pela equação (9). Para o caso de sistemas lamelares a aproximação $P(q)_{plane} \approx 1/q^2$ é válida pois o tratam-se de planos cujas dimensões são muito maiores do que a espessura da bicamada. No entanto, este procedimento pode ser utilizado em casos onde temos planos finitos e deste modo o fator de forma $P(q)_{plane}$ pode fornecer o tamanho dos planos.

No processo de minimização as amplitudes que descrevem as funções Gaussianas devem ser otimizadas juntamente como com os outros parâmetros. No entanto, o fato de curva de espalhamento possuir uma quantidade de informação pequena faz com que esta otimização não seja estável (*ill poised problem*). É por este motivo que autores citados anteriormente, ao tentarem otimizar simultaneamente o fator de forma e estrutura se restringiam a descrições simplificadas da bicamada lipídica, de modo a diminuir estas instabilidades. Este problema pode ser contornado pela introdução de um termo de estabilização no processo de minimização. Um procedimento similar é utilizado no método de IFT mencionado anteriormente.

Como mencionado anteriormente, no procedo de ajuste de dados experimentais, busca-se um conjunto de coeficientes do modelo proposto que fornece o mínimo da função $\chi^2 = \sum_{i-1}^{M}\left[I(q)^{\exp} - I^{\mathrm{mod}}(q)\right]^2 / \sigma_i^2$.

Em um caso geral, a intensidade teórica não é expressa como uma combinação linear dos coeficientes do modelo e assim a minimização da função χ^2 requer o uso de procedimentos de

minimização por mínimos quadrados não lineares. Existem diversos métodos de minimização disponíveis na literatura, mas neste trabalho utilizamos o algoritmo de Marquardt-Levenberg (Pedersen, 1992, 1997, Glatter & Hainisch, 1984). O conjunto de equações normais que deve ser resolvido iterativamente é:

$$\sum_{\nu=1}^{J} \alpha_{\mu\nu} \Delta a_{\nu} = -\beta_{\mu}, \qquad \mu = 1,2,...,J \qquad (44)$$

Sendo J o numero de parâmetros do modelo e Δa_{ν} as mudanças no parâmetro a_{ν} em cada iteração. Este processo iterativo é feito até que as mudanças ficam abaixo de um dado limite. A matriz $\alpha_{\mu\nu}$ e o vetor β_{μ} são dados por (Pedersen, 1997, Press, 1992):

$$\begin{aligned} \alpha_{\mu\nu} &= \sum_{i=1}^{M} \frac{\partial I^{\mathrm{mod}}(q_i)}{\partial a_{\mu}} \frac{\partial I^{\mathrm{mod}}(q_i)}{\partial a_{\nu}} / \sigma_i^2 \\ \beta_{\mu} &= \sum_{i=1}^{M} \left[I(q)^{\exp} - I^{\mathrm{mod}}(q) \right] \frac{\partial I^{\mathrm{mod}}(q_i)}{\partial a_{\mu}} / \sigma_i^2 \end{aligned} \qquad (45)$$

Como requerido para qualquer procedimento de minimização não linear, um conjunto de valores iniciais deve ser utilizado. Para o caso onde somente o perfil de densidade de espalhamento é modelado, uma função "quadrada" onde todos os parâmetros possuem o mesmo valor é suficiente para que se obtenha a convergência no processo de minimização. Para casos mais complicados onde tanto o fator de forma quanto o fator de estrutura são otimizados, algum conhecimento prévio ou alguns ajustes iniciais manuais são necessários. Como mencionado anteriormente, a solução do problema inverso de espalhamento leva a instabilidades na modelagem e sendo assim é necessário a adição de vínculos de estabilização que levam a minimização a soluções com significado físico. Um procedimento consiste na adição da função de estabilização (N_c) ao termo χ^2 :

$$\begin{aligned} N_c &= \sum_{n=1}^{P-1} \left(a_{n+1} - a_n \right)^2 \\ \chi^2 + \lambda N_c &= \min \end{aligned} \qquad (46)$$

Sendo P os numero de parâmetros que se deseja impor vínculos ($P \leq J$). As equações normais modificadas são (Pedersen, 1992, Pedersen & Hamley, 1994a, b, Oliveira *et al.*, 2012):

$$\sum_{\nu=1}^{P}\left(\alpha_{\mu\nu}+\lambda K_{\mu\nu}\right)\Delta a_{\nu}=-\left(\beta_{\mu}+\lambda L_{\mu}\right), \qquad \mu=1,2,...,P \qquad (47)$$

A matriz $K_{\mu\nu}$ é definida como,

$$K=\begin{pmatrix} 1 & -1 & & & & & \\ -1 & 2 & -1 & & & 0 & \\ & -1 & 2 & -1 & & & \\ & & ..... & ..... & ..... & & \\ & & & ..... & ..... & & \\ & 0 & & & -1 & 2 & -1 \\ & & & & & -1 & 1 \end{pmatrix} \qquad (48)$$

No lado direito da equação (47) L_{μ} é dado por,

$$L_{\mu}=\begin{cases} a_i-a_{i+1} & \text{para } i=1 \\ 2a_i-a_{i+1}-a_{i-1} & \text{para } 2\le i\le P-1 \\ a_i-a_{i-1} & \text{para } i=P \end{cases} \qquad (49)$$

Em um caso geral, somente alguns parâmetros devem conter vínculos. Assim, $P<J$ e a soma na equação (47) é feita somente nos parâmetros que devem ser vinculados. Por exemplo, quando ajustamos o fator de forma e fator de estrutura, somente as amplitudes relativas ao fator de forma (perfil de densidade de espalhamento) devem ser vinculadas, enquanto que os parâmetros do fator de estrutura, entre outros, não devem conter restrições.

Deste modo deve-se obter o fator de estabilização λ que forneça os melhores resultados. Este parâmetro λ pode ser compreendido como um multiplicador de Lagrange que altera o peso de N_C na função de ajuste (equação (47)). Pode-se imaginar este multiplicador como o valor da "constante de mola" que liga os coeficientes. Valores grandes de λ forçarão os coeficientes a serem bastante próximos, de modo que N_C deve ser pequeno para fornecer um mínimo em (46). Por outro lado, valores pequenos de λ permitirão grandes variações nos coeficientes. No processo de otimização varia-se λ e para cada valor deste multiplicador obtém-se o conjunto de parâmetros que melhor ajusta os dados experimentais. Tipicamente varia-se λ entre 5 a 10 ordens de grandeza. O valor ótimo de λ (λ_{opt}) é obtido pelo método de ponto de inflexão (Glatter, 1977). Neste método busca-se uma região onde N_C atinge um platô em várias ordens de grandeza de λ, enquanto o ajuste ainda é bom (χ^2 pequeno). Na região de platô, busca-se um ponto de inflexão, com $(N_C)'$ mínimo e preferivelmente

$(N_C)''$ positivo. Todas estas considerações são inseridas em um único funcional de onde se obtém o valor de λ_{opt} automaticamente por um ajuste com uma parábola (Oliveira *et al.*, 2012):

$$\lambda_{opt} = Min\left\{\zeta_1\chi^2 + \zeta_2\left|\left(N_C\right)'\right| + \zeta_3\left|\left(N_C\right)''\right|\right\} \qquad (50)$$

Um exemplo de aplicação é mostrado na Figura 17.

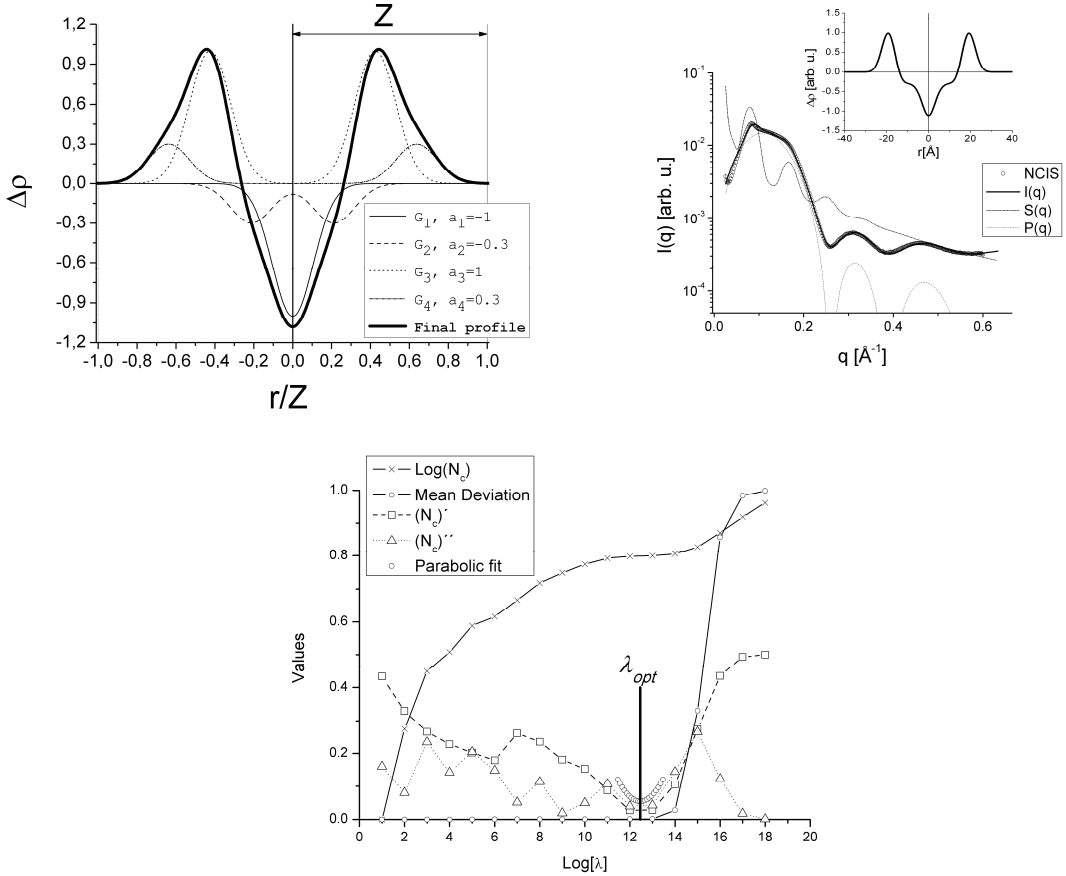

Figura 17 – Esquerda: Construção do perfil de densidade eletrônica utilizando quatro Gaussianas (G1, G2, G3 and G4) com quatro diferentes amplitudes (-1, -0.3, 1, 0.3). São mostrados com quatro linhas diferentes. O perfil resultante é motrado em linha continua e grossa. Direita: Ajuste de dados experimentais utilizando o modelo de 4 gaussianas. Circulos Abertos: dados experimentais para sistema de lipossomas de fosfatidilcolina de ovo. Linha continua: Intensidade teórica. Linha pontilhada: fator de estrutura. Linha Tracejada: fator de forma $|F(q)|^2$. O perfil de densidade eletronica obtido é mostrado como um inset. Abaixo: Método de ponto de inflexão, executado automaticamente pelo programa de ajuste para determinar o valor de λ_{opt}. Figura tirada de (Oliveira *et al.*, 2012)

Este método mostrou-se extremamente poderoso na descrição de sistemas lipídicos auto organizados uma vez que permite a modelagem simultânea do fator de forma e do fator de estrutura do sistema, e vem sendo aplicado em variadas aplicações e teses de mestrado e doutorado (Balbino *et al.*, 2013, Balbino *et al.*, 2012, Bougis *et al.*, 2014, Gerbelli, 2012, Rubim, 2014). Além disso, este método pode ser expandido para outras geometrias, como será apresentado a seguir.

c) Método de Deconvolução Generalizado

Como descrevi anteriormente, modelagem de dados através do ajuste direto da curva de espalhamento apresentam diversas vantagens. Modelagem no espaço reciproco permite a fácil inclusão de termos adicionais como *backgrounds*, anisotropias, polidispersidades e contribuições diversas.

Diversos sistemas podem ser satisfatoriamente descritos como possuindo fatores de forma compostos por lamelas (planos), cilindros ou esferas (esferóides), com uma densidade de espalhamento variável ao longo da partícula. Nestes sistemas pode-se ainda ter a presença de fatores de estrutura, seja indicando ordenamento ou simplesmente algum tipo de interação. Sendo assim, o método de modelagem deve permitir a descrição tanto do fator de forma, com forma definida para a partícula, mas permitindo a modelagem da variação da densidade de espalhamento ao longo da partícula, e também a descrição do fator de estrutura, descrito por uma função analítica, semi-analitica ou simulada.

Este procedimento generalizado foi proposto por Glatter (Freiberger & Glatter, 2006, Fritz & Glatter, 2006, Bergmann *et al.*, 2000, Fritz *et al.*, 2000), requerendo, no entanto, o cálculo da função *p(r)* para a descrição do fator de forma. A necessidade do calculo da função *p(r)* gera dificuldades intrínsecas devido à inclusão de vínculos na modelagem, além de impossibilitar a inclusão características como anisotropias, polidispersidades e componentes adicionais para a intensidade. Como demonstrado para o Método de Deconvolução Gaussiana, ajustes no espaço reciproco inferem uma maior flexibilidade à modelagem.

Funções Gaussianas mostraram-se bastante versáteis para o caso unidimensional (lamelas) (Oliveira *et al.*, 2012), pois a equação (2), que fornece a amplitude de espalhamento a partir da densidade de espalhamento, é integrável, fornecendo assim uma expressão analítica. Para o caso bidimensional (cilindros) e tridimensional (esferas) não se tem funções integráveis e a utilização de um perfil Gaussiano para a descrição da densidade de espalhamento necessitaria de um cálculo numérico da função. Por outro lado, funções degrau são integráveis nas três geometrias e deste modo podem ser utilizadas para a descrição do perfil de densidade de espalhamento (Glatter & Hainisch, 1984, Glatter, 1981).

O ponto inicial do procedimento consiste em descrever o fator de forma. Se expressões analíticas ou semi-analíticas são disponíveis, as expressões gerais para a intensidade e amplitude de espalhamento são dadas por:

$$P_{MOD}(q) = \frac{\int_0^\infty D(r)m(r)^2 P_{Mon}(q,r)dr}{\int_0^\infty D(r)m(r)^2 dr} \quad (51)$$

$$A_{MOD}(q) = \frac{\int_0^\infty D(r)m(r)^2 A_{Mon}(q,r)dr}{\int_0^\infty D(r)m(r)^2 dr} \quad (52)$$

onde é utilizado uma polidispersidade em tamanho. Diversas distribuições podem ser utilizadas, como por exemplo, distribuições Gaussianas, Lorentzianas ou distribuições de Shulz-Zimm. A função *m(r)* depende da geometria assumida. Para partículas esferoidais, *m(r)=V*, onde *V* é o volume das partículas. Para partículas cilíndricas, *m(r)=A*, sendo *A* a área da sessão transversal do cilindro. Para partículas lamelares, *m(r)=L* onde *L* é a espessura da lamela. Os fatores de forma de intensidade P_{Mon}(q) e de amplitude A_{Mon}(q) são dados por:

- Esfera / Partículas elipsoidais

$$P_{Mon}(q) = \int_0^{\pi/2} \left(F_M\left[q, r(R,\varepsilon,\alpha)\right] \exp\left[-\frac{1}{2}q^2\sigma_{\text{int}}\right]\right)^2 \sin\alpha \, d\alpha \quad (53)$$

$$A_{Mon}(q) = \int_0^{\pi/2} F_M\left[q, r(R,\varepsilon,\alpha)\right] \exp\left[-\frac{1}{2}q^2\sigma_{\text{int}}\right] \sin\alpha \, d\alpha \quad (54)$$

onde $r(R,\varepsilon,\alpha) = R\left(\sin^2\alpha + \varepsilon\cos^2\alpha\right)^{1/2}$ é o elemento radial de integração, R é o raio da seção transversal e εR é o semi-eixo vertical do elipsoide de revolução. A multiplicação por uma função Gaussiana faz a convolução da função F_M(q) e da função Gaussiana promovendo um *smearing* da função degrau.

- Cilindros longos

$$P_{Mon}(q) = \left(F_M[q,r] \exp\left[-\frac{1}{2} q^2 \sigma_{\text{int}} \right] \right)^2 P_{ROD}(q,L) \qquad (55)$$

$$A_{Mon}(q) = F_M[q,r] \exp\left[-\frac{1}{2} q^2 \sigma_{\text{int}} \right] \qquad (56)$$

Onde R é o raio do cilindro e L seu comprimento. $P_{ROD}(q,L)$ é o fator de forma de um bastão infinitamente fino, já mostrado na equação (7).

- Lamelas / Sistemas planares

$$P_{Mon}(q) = \left(F_M[q,r] \exp\left[-\frac{1}{2} q^2 \sigma_{\text{int}} \right] \right)^2 / q^2 \qquad (57)$$

$$A_{Mon}(q) = F_M[q,r] \exp\left[-\frac{1}{2} q^2 \sigma_{\text{int}} \right] \qquad (58)$$

A função $F_M(q,R)$ é dada por :

$$F_M(q) = \frac{1}{M_M} \left[\rho_1 m(R_1) F_S(q,R_1) + \sum_{i=2}^{N} (\rho_i - \rho_{i-1}) m(R_i) F_S(q,R_i) \right] \qquad (59)$$

$$M_M = \rho_1 m(R_1) + \sum_{i=2}^{N} m(R_i)(\rho_i - \rho_{i-1}) \qquad (60)$$

onde ρ_i é a densidade de comprimento de espalhamento da *i*-ésima camada, N é o número de camadas descrevendo o modelo e a função $F_S(q,R)$ depende da geometria assumida, sendo dada por:

- Esfera com raio R

$$F_S(q,R) = \frac{3[\sin(qR) - qR\cos(qR)]}{(qR)^3} \qquad (61)$$

- Seções circulares (2D) com raio R

$$F_S(q,R) = \frac{J_1(qR)}{qR} \tag{62}$$

Sendo $J_1(x)$ uma função de Bessel de primeiro tipo.

- Lamelas (1D) com espessura R

$$F_S(q,R) = \frac{\sin(qR)}{qR} \tag{63}$$

Apesar de não termos explicitado, tanto os cilindros quanto as lamelas também podem conter polidispersidades, como indicado pelas equações 51 e 52.

5. Exemplos de Aplicação

Ao longo do texto, apresentei diversos exemplos de aplicação de métodos de análise para dados de espalhamento e difração a baixos ângulos, que resultaram em artigos científicos de minha autoria. A seguir mostro em maior detalhe algumas aplicações.

5.1 Estudos de Sistemas lamelares

Como descrito anteriormente, surfactantes quando colocados em sistemas aquosos se auto organizam de variadas formas para minimizar a energia livre do sistema. Lipídeos são surfactantes que possuem, em geral, duas cadeias hidrofóbicas e acabam por se auto organizar em sistemas planares, formando bicamadas lipídicas. Dependendo da forma de preparação da amostra e da concentração do sistema, pode-se formar sistemas vesiculares tanto unilamelares quanto multilamelares bem como sistemas contendo grandes aglomerados lipídicos compostos por domínios multilamelares (Jones, 2002, Hamley, 2000, Israelachvili, 2007). Em conjunto com a apresentação do método de Deconvolução Gaussiana (Oliveira *et al.*, 2012), aplicou-se o método à caracterização de sistemas compostos por multicamadas lipídicas de lecitina de soja. As amostras foram adquiridas junto à Avanti-Polar e utilizadas sem preparação posterior, sendo diluídas em água Milli-Q. Os dados foram coletados no equipamento NANOSTAR-Bruker, localizado no Instituto de Física da Universidade de São Paulo.

Os dados experimentais são mostrados na Figura 18, juntamente com o ajuste utilizando o método de deconvolução Gaussiana. Como pode ser visto nos ajustes, os dados experimentais são corretamente descritos pelo modelo para toda a serie de concentrações, sendo que em cada caso o respectivo fator de forma e de estrutura são obtidos pela modelagem. Um caso bastante interessante é visto para φ_{lip}=0.871. Note que nos dados experimentais aparentemente não temos o pico de segunda

ordem, na posição q = 0.26Å^{-1}. O ajuste utilizando o modelo teórico demostra que, na realidade, tem-se uma superposição entre o máximo do fator de estrutura (pico de difração) e o mínimo do fator de forma, ocasionando o aparente desaparecimento do pico de difração. Além disso, para cada caso também é calculado o perfil de densidade de comprimento de espalhamento, que neste caso representa o perfil de densidade eletrônica perpendicular à bicamada lipídica.

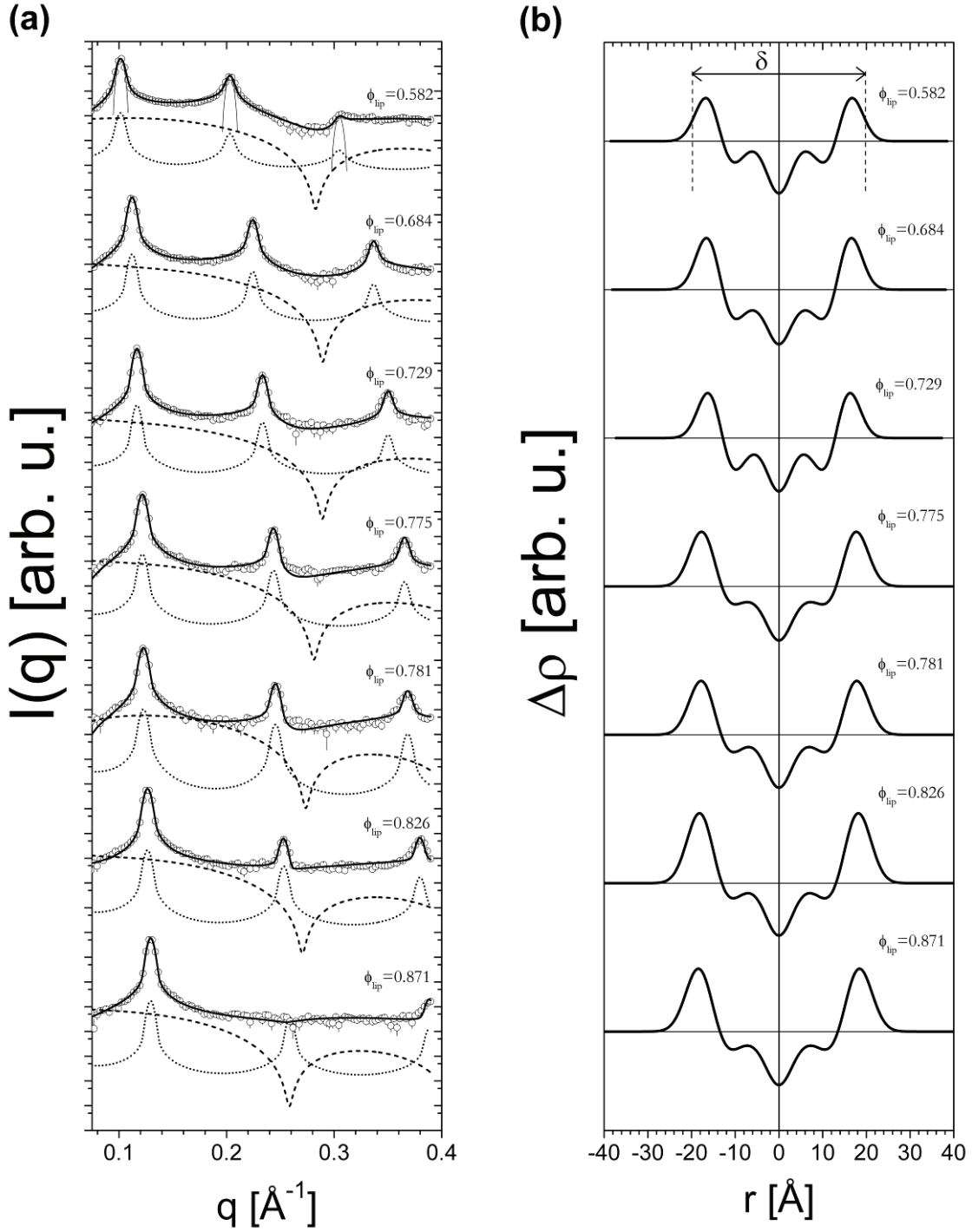

Figura 18 – (a) Curvas experimentais de SAXS para a fase lamelar com variadas frações de volume do lipídio (φ). As linhas finas para φ=0.582 representam as funções de resolução para as três posições de picos. As linhas tracejadas são os fatores de forma e as linhas pontilhadas os fatores de estrutura obtidos utilizando o procedimento de minimização descrito no texto. (b) Perfis de densidade eletrônica e definição da espessura da membrana δ. Em todos os casos as curvas foram deslocadas para melhor clareza. Figuras tiradas de (Oliveira *et al.*, 2012).

Em outra aplicação, foi estudado e efeito da incorporação de um surfactante artificial em membranas lipídicas. A molécula *Simulsol*™ feito pela empresa *Seppic*, é composto por uma cauda hidrofóbica e uma cadeia de polietileno glicol (PEG). Quando colocado em conjunto com lipídeos, esta molécula se incorpora na membrana compondo um sistema misto. Por ser uma molécula sintética, é possível variar o comprimento da cadeia polimérica e estudar o efeito deste e outros parâmetros na estabilidade e características físicas da membrana (Bougis *et al.*, 2014, Rubim, 2014, Gerbelli *et al.*, 2013, Gerbelli, 2012). Na Figura 19 são mostrados resultados para um estudo onde se tinha cadeias de *Simulsol* com 10 monômeros na média, mas com comprimento máximo indo até 20 monômeros (Gerbelli *et al.*, 2013). Neste estudo demonstrou-se que as moléculas de *Simulsol* se incorporam na membrana lipídica e alteram suas dimensões e propriedades estruturais.

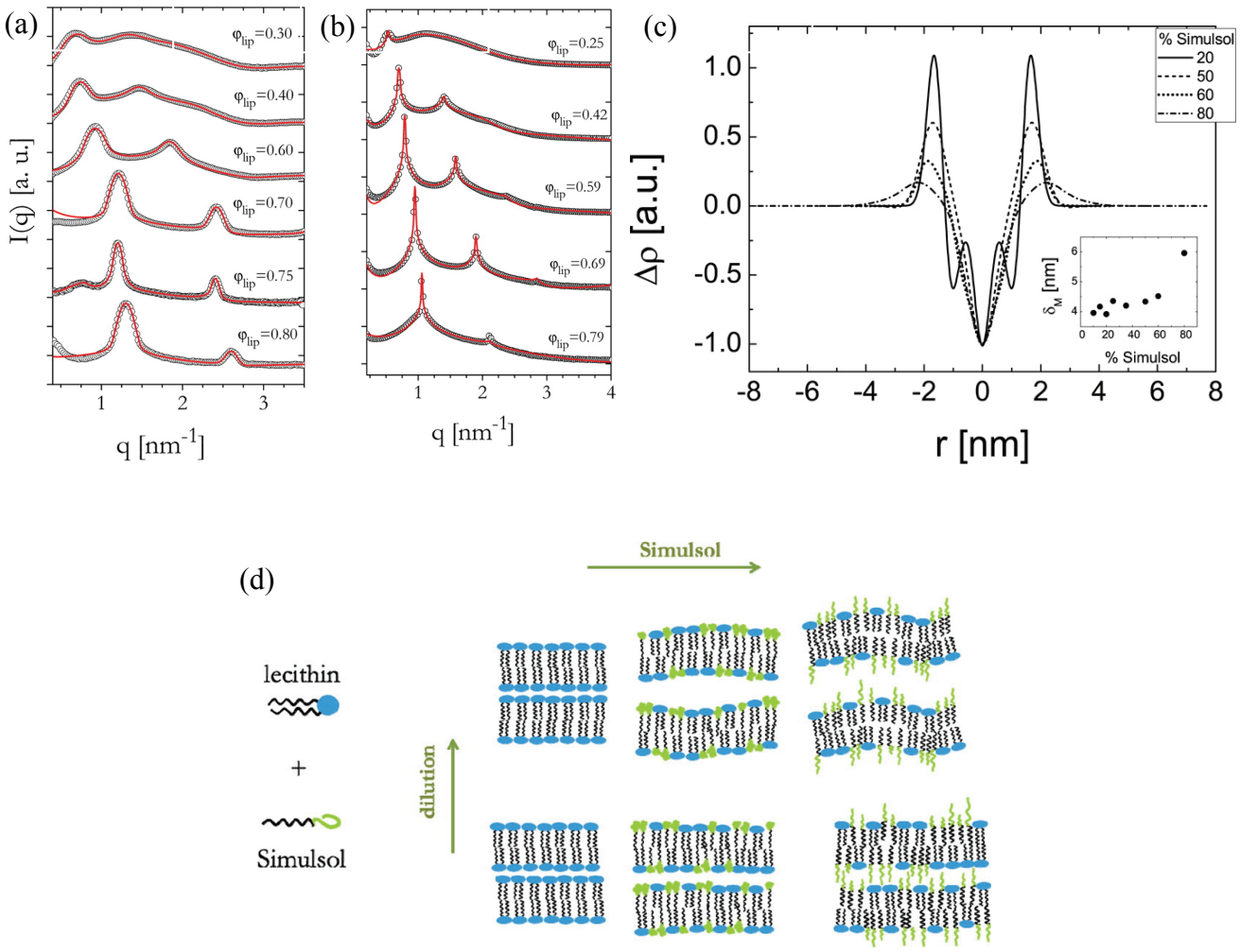

Figura 19 – Resultados de SAXS para o sistema Lecitina + Simulsol. Dados experimentais (símbolos) e o respectivo ajuste por modelo teórico (linhas solidas) para composições de membrana (fração em massa do Simulsol): 30% (a) e 90% (b). Em (a) as curvas foram obtidas em um equipamento de laboratório (NANOSTAR / IFUSP) e em (b) os dados foram obtidos na linha SWING do Síncrotron Soleil. (c) Perfil de densidade eletrônica obtida pelo procedimento de ajuste, com quantidade variável de Simulsol. Na figura, r = 0 representa o centro da bicamada e a definição de valores negativos e positivos é dado tendo-se a água como referencia. Inserção: Efeito do cosurfactante na espessura da bicamada. (d) Representação esquemática do efeito do simulsol na flutuação da espessura da bicamada. Figura baseada em (Gerbelli *et al.*, 2013).

Outros exemplos de aplicação deste método foram utilizados no estudo de lipídeos catiônicos e a influencia da incorporação de DNA no sistema (Balbino *et al.*, 2012, Balbino *et al.*, 2013), sistemas de lipídeos não iônicos e a influencia da incorporação de moléculas de betacaroteno no sistema (Carvalho *et al.*, 2015), entre diversas outras aplicações em andamento.

5.2 Estudos em Lipoproteínas

Lipoproteínas são estruturas supramoleculares essenciais no corpo humano. Entre diversas funções no organismo, são as responsáveis pelo transporte de colesterol no sistema circulatório. Lipoproteínas são geralmente classificadas de acordo com seu tamanho e densidade. Lipoproteínas de alta densidade (*High density lipoproteins* - HDL) e Lipoproteínas de baixa densidade (*Low density lipoproteins* - LDL) são as principais componentes desta classe. Em exames de sangue é corriqueiro serem fornecidos os níveis de LDL e HDL no sangue uma vez que estes níveis podem indicar risco de doenças coronarianas, formação de placas arterioscleróticas entre diversas outras potenciais patologias.

Estudos recentes demonstram que não somente os níveis destas lipoproteínas são importantes para a saúde do individuo, mas principalmente informações estruturais das mesmas no sistema. O estudo aprofundado das peculiaridades destas lipoproteínas requer o trabalho conjunto de diversas áreas de conhecimento, de modo a permitir uma abordagem multidisciplinar sobre estes sistemas. Tal estratégia vem sendo aplicada com sucesso por pesquisadores do Instituto de Física da USP, particularmente em uma colaboração já de vários anos entre o Grupo de Fluidos Complexos com pesquisadores da Faculdade de Medicina, Instituto de Ciências Biomédicas da USP e da UNIFESP no estudo de lipoproteínas.

A investigação da estrutura interna de lipoproteínas utilizando métodos de espalhamento de raios X já aparece na década de 1970 em artigos seminais de Deckelbaum, Laggner e Atkinson (Deckelbaum *et al.*, 1975, Atkinson *et al.*, 1977, Deckelbaum *et al.*, 1977, Laggner *et al.*, 1977, Laggner & Muller, 1978), e mais recentemente por Perkins, Laggner e colaboradores (Prassl *et al.*, 2008, Meyer *et al.*, 1996). Nestes trabalhos a estrutura de lipoproteínas foi estudada na forma nativa, quando submetida à variação de temperatura bem como nível de oxidação do meio.

Para a modelagem de dados de espalhamento a baixos ângulos por lipoproteínas diversas metodologias foram aplicadas. Em uma abordagem bastante limitada, Laggner e Muller propuseram a obtenção da amplitude de espalhamento através raiz quadrada da intensidade de espalhamento. Como neste processo não se tem a informação sobre os sinais (positivo / negativo) da amplitude deve-se escolher arbitrariamente estes sinais. Esta abordagem permite a obtenção de um perfil tentativo para a densidade eletrônica da macromolécula, assumindo-se uma simetria esférica perfeita

(Laggner & Muller, 1978). De toda maneira esta forma de analise simplificada demonstrou a possibilidade de ser obter informações estruturais de lipoproteínas através da técnica de SAS. Posteriormente Glatter propôs o método de deconvolução quadrática onde, a partir do cálculo da função *p(r)*, era possível se obter o perfil de densidade de comprimento de espalhamento assumindo-se uma simetria bem definida (Glatter, 1981, Glatter & Hainisch, 1984). As limitações descritas para este método já foram abordadas em capítulos anteriores, sendo a principal limitação o fato de se necessitar da função *p(r)*.

Tais limitações não existem no método proposto por mim, tanto na Deconvolução Gaussiana como no Método de Deconvolução Generalizada. Como descrito anteriormente, estas abordagens permitem a modelagem direta da curva experimental de espalhamento. Tal metodologia foi utilizada no estudo de lipoproteínas, especificamente a LDL e HDL (Oliveira, Santos*, et al.*, 2014, Oliveira, Monteiro*, et al.*, 2014), bem como fez parte da tese de doutoramento da Dra. Priscila Santos (Santos, 2013).

Na Figura 20 e na Figura 21 são mostrados os ajustes obtidos pelo método de deconvolução generalizado (Seção 3.7c) no ajuste dos fatores de forma de espalhamento para a LDL e HDL. As amostras eram sujeitas a oxidação por Cobre, seguindo protocolos previamente definidos (Alves & Figueiredo Neto, 2014, Gomez *et al.*, 2008) e os dados de espalhamento foram obtidos a diferentes tempos de oxidação. Os dados para a LDL foram obtidos na linha de SAXS-1 do Laboratório nacional de Luz Síncrotron (LNLS) enquanto que os dados para a HDL foram obtidos no equipamento de laboratório Bruker-NANOSTAR do IFUSP. Detalhes sobre a preparação das amostras e procedimentos de oxidação podem ser obtidos no artigo publicado (Oliveira, Santos*, et al.*, 2014). Aplicações da técnica de SAXS ao estudo dos efeitos de oxidação em lipoproteínas foram publicados previamente por Perkins e colaboradores (Meyer *et al.*, 1996), mas naquele trabalho efeitos de polidispersidade da amostra bem como limitações inerentes ao método utilizado para a analise dos dados (deconvolução quadrática – Glatter) limitaram bastante as conclusões obtidas.

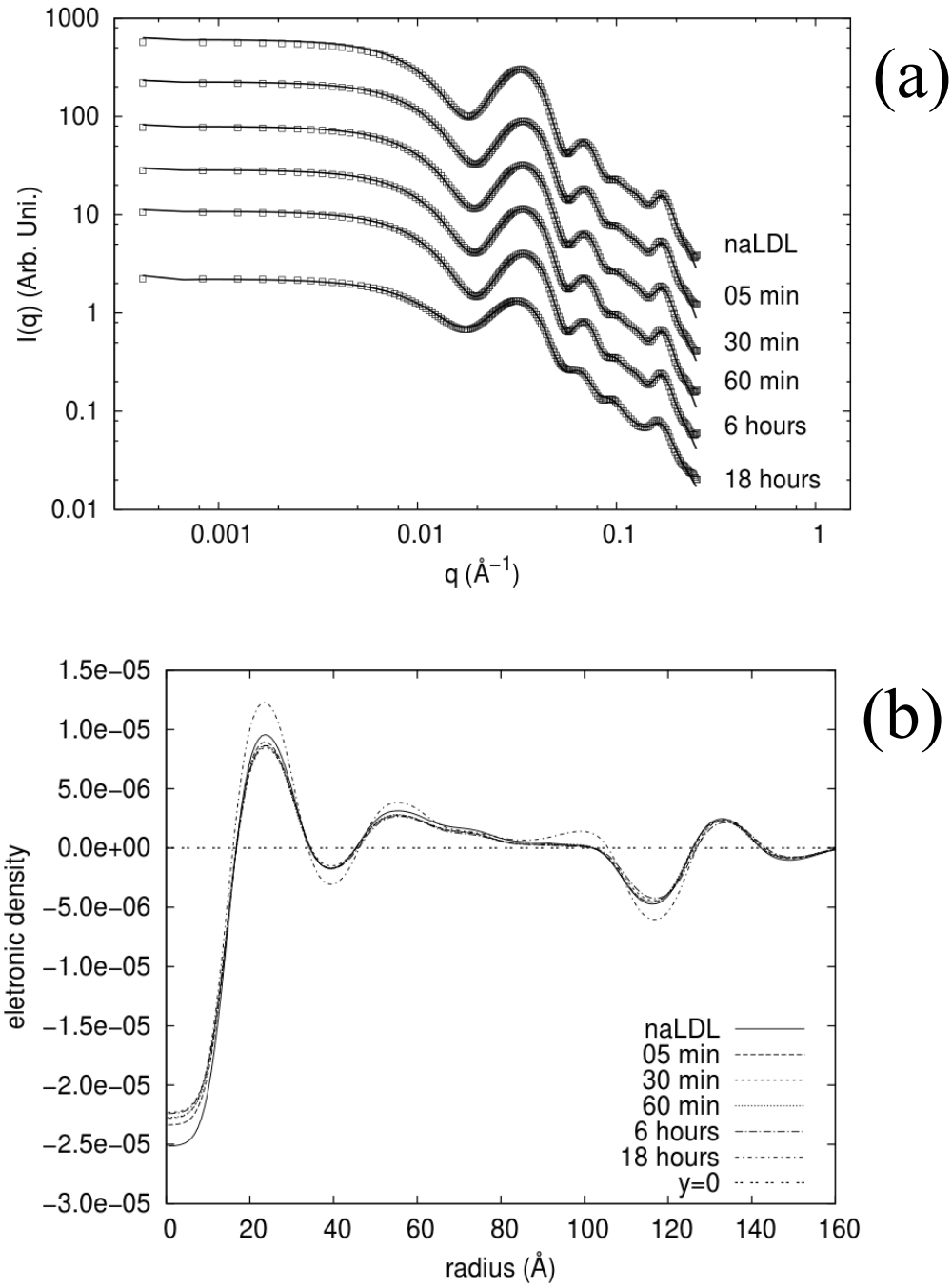

Figura 20 – Método de deconvolução aplicado à modelagem de SAXS para LDL para diferentes tempos de oxidação por Cobre. a) Fator de Forma ajustado com o método de deconvolução. Dados experimentais (símbolos abertos) e ajuste do modelo (linha solida). b) Perfis de densidade eletrônica obtidos com o método de deconvolução. Figura tirada de (Oliveira, Santos, *et al.*, 2014).

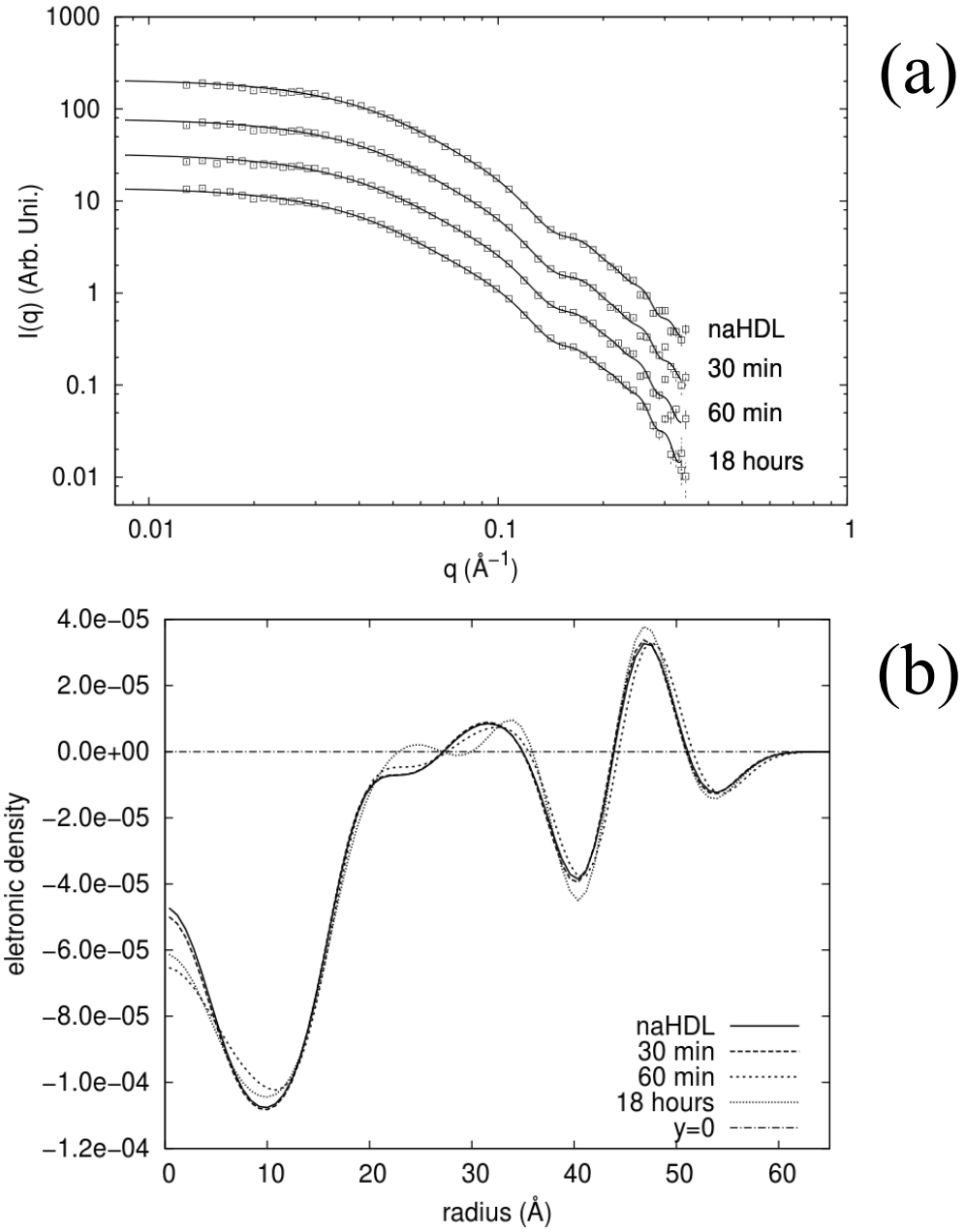

Figura 21 – Método de deconvolução aplicado à modelagem de SAXS para HDL para diferentes tempos de oxidação por Cobre. a) Fator de Forma ajustado com o método de deconvolução. Dados experimentais (símbolos abertos) e ajuste do modelo (linha solida). b) Perfis de densidade eletrônica obtidos com o método de deconvolução. Figura tirada de (Oliveira, Santos, *et al.*, 2014).

Para os dados apresentados aqui, como procedimento prévio à deconvolução realizou-se o desacoplamento entre o fator de forma e fator de estrutura utilizando o método descrito na seção 4.2. A descrição precisa do fator de forma e correspondente perfil de densidade eletrônica obtido pelo método de deconvolução somente foi possível graças ao desacoplamento entre os fatores de forma e estrutura. O fator de estrutura utilizado neste caso foi o de um sistema fractal, dado pela equação (19). Este procedimento de desacoplamento aplicado aos dados de LDL é mostrado na Figura 22. Para as amostras HDL não foi necessário realizar o desacoplamento uma vez que não foi detectado a presença de fatores de estrutura no sistema.

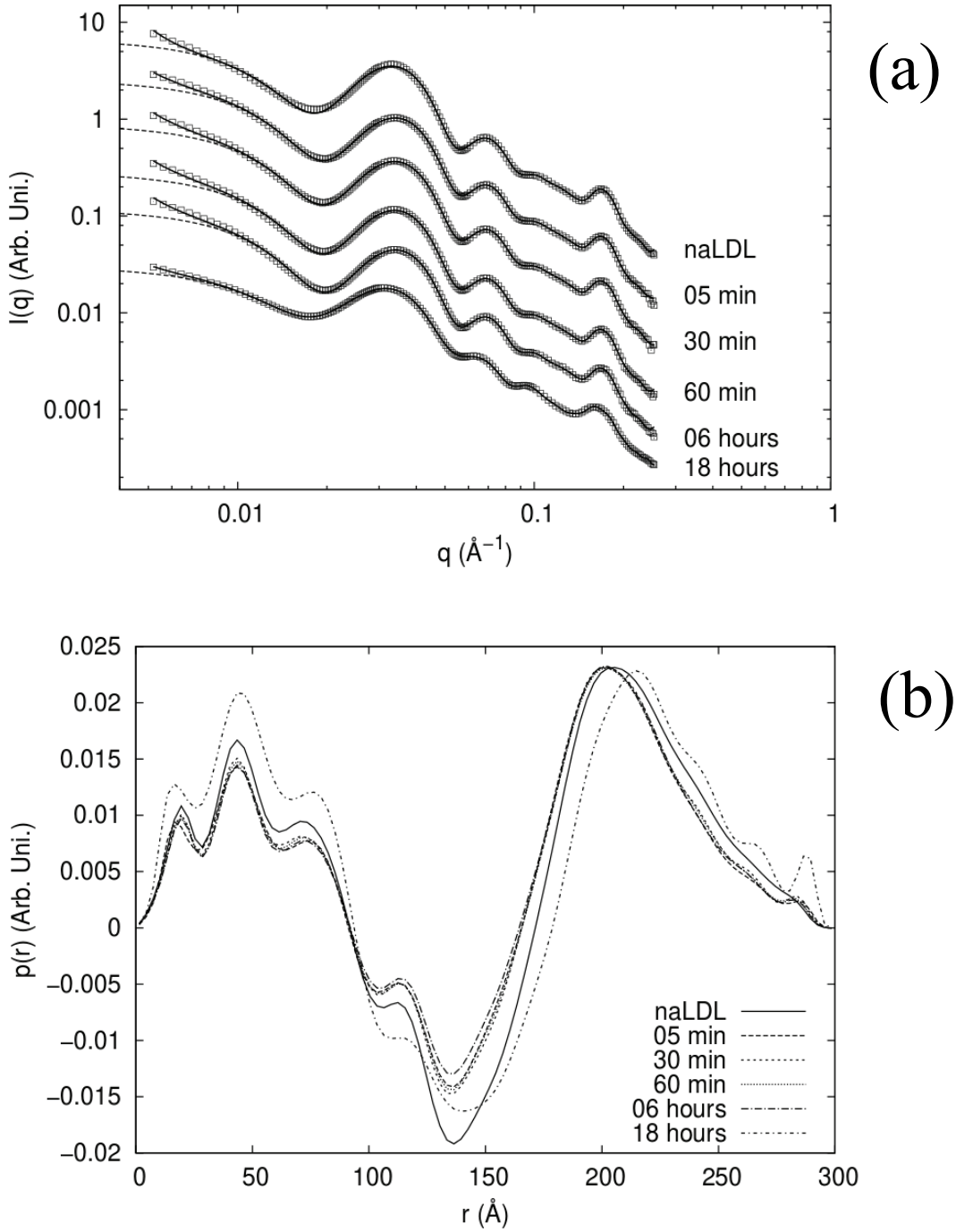

Figura 22 – Método de Transformada de Fourier Generalizado (GIFT) aplicado ao desacoplamento entre fatores de forma e estrutura nos dados de SAXS para LDL. a) Ajuste (linha continua) dos dados experimentais de LDL (círculos abertos) utilizando o método GIFT. O fator de forma obtido neste procedimento linha tracejada foi utilizado no método de deconvolução. b) Curvas de distribuição de pares de distâncias *p(r)* obtidas pelo ajuste do método GIFT. Figura tirada de (Oliveira, Santos*, et al.*, 2014).

Combinando resultados de SAXS com análises de escaneamento Z (*Z-Scan*) e espalhamento de luz dinâmico (*DLS – Dynamic Light Scatering*), foi possível demonstrar que lipoproteínas de alta densidade (HDL) são bastante resistentes à oxidação enquanto que lipoproteínas de baixa densidade

(LDL) apresentam importantes alterações estruturais quando sofrem oxidação, o que e isso pode ser diretamente relacionado com mudanças em seu funcionamento no sistema vivo.

Em um estudo subsequente, efeitos da variação abrupta da temperatura em amostras de LDL foram investigados. As partículas de LDL são ricas em ésteres de colesterol e pobres em triglicérides e colesterol livre. Além disso, cada partícula de LDL contém somente uma apolipoproteína B100 (apoB-100), que é responsável pela integridade da partícula e metabolismo. A estrutura da LDL é muito sensível a mudanças no meio o que pode alterar sua função. Os mecanismos pelos quais a LDL *in vivo* é modificada ainda não são completamente compreendidos. Sabe-se que a estrutura da apoB-100 é sensível a modificações químicas como oxidação por radicais livres e mudanças de temperatura (Prassl *et al.*, 2008).

Como mencionado anteriormente, métodos de espalhamento foram aplicados ao estudo de modificações estruturais da LDL devido a alterações de temperatura (Deckelbaum *et al.*, 1975, Atkinson *et al.*, 1977, Deckelbaum *et al.*, 1977, Laggner & Muller, 1978, Prassl *et al.*, 2008). No entanto, em todos os casos a analise dos dados é limitada devido à presença de agregados (induzidos pela variação de temperatura) e também por problemas em se obter um perfil de densidade de comprimento de espalhamento confiável. Em um estudo recente, Jayaraman e colaboradores investigaram a estabilidade térmica da LDL utilizando várias técnicas indicando calorimetria, dicroísmo circular, fluorescência, turbidez e microscopia eletrônica (Jayaraman, 2005). Estes dados demonstram que o rompimento da estrutura da LDL induzido pela temperatura envolve mudanças irreversíveis como a liberação de lipídios neutros do núcleo da LDL.

Utilizando os métodos de analise apresentados anteriormente, foi realizado um estudo sistemático de mudanças estruturais na estrutura nativa da LDL induzida por mudanças na temperatura. Os dados que serão apresentados foram obtidos na linha SAXS-1 do Laboratório Nacional de Luz Síncrotron (LNLS). Detalhes da preparação da amostra bem como do aparato experimental utilizado podem ser obtidos no artigo original (Oliveira, Monteiro*, et al.*, 2014). Em resumo, amostras nativas de LDL eram submetidas a mudanças abruptas de temperatura e a evolução do sistema era acompanhada em tempo real através de exposições curtas (1 min) de SAXS. Dados foram coletados à temperatura de 22ºC (temperatura ambiente), 42ºC, 60ºC e 80ºC. Para medidas à temperatura ambiente apenas cinco exposições foram realizadas uma vez que a amostra era estável ao longo do tempo. Para medidas a temperaturas maiores 5 exposições de 1 min foram realizadas nos instantes 0 min, 5 min, 10 min, 20 min, 40 min, 60 min e 80 min após a injeção da amostra no porta amostras. Os vários dados obtidos para cada instante eram comparados e promediados. Na Figura 23 são mostrados todos os dados de SAXS coletados nestes experimentos. Como pode ser observado pela evolução das curvas experimentais, a temperatura induz a formação de agregados no sistema. A presença destes agregados torna a análise dos dados mais elaborada.

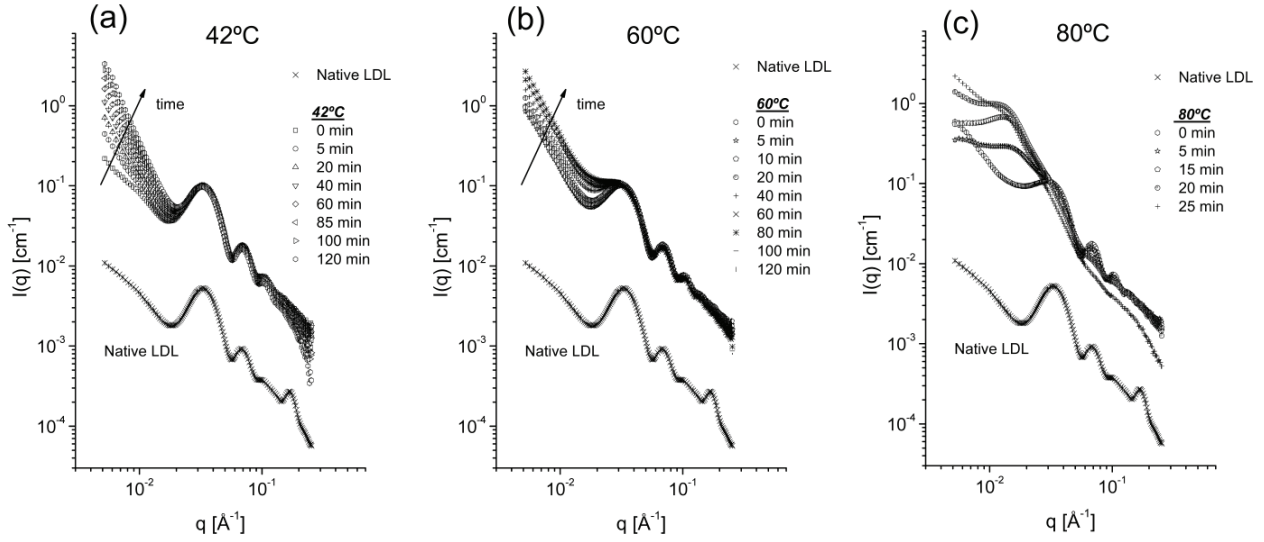

Figura 23 – Serie de dados de SAXS para os experimentos realizados. (a) Dados à 42ºC. (b) Dados à 60ºC. (c) Dados à 80ºC. Em todos os casos a curva da LDL nativa medida à 22ºC é mostrada para comparação. Esta curva foi deslocada para melhor visualização. Figura tirada de (Oliveira, Monteiro, *et al.*, 2014).

Para os dados a 42º e 60º pode-se observar que as mudanças principais na curva ocorrem na parte inicial, sendo os máximos e mínimos subsequentes são bastante similares aos presentes na curva da LDL nativa. Isto indica que a estrutura interna das partículas de LDL se mantém e que estas provavelmente estão formando agregados. Sendo assim, as curvas de intensidade espalhada podem ser compreendidas como correspondendo à composição de fatores de forma e de estrutura, sendo o fator de forma correspondente às moléculas de LDL, que podem se aglomerar formando agregados. Tais agregados podem ser descritos por um fator de estrutura. Para os dados a 80º vê-se uma clara mudança na forma da curva e perda da similaridade com a curva de LDL nativa. Isto indica a ruptura da estrutura das partículas de LDL e a formação de agregados não específicos.

Similarmente ao caso anterior, foi necessária a utilização do método GIFT (Seção 4.2) para desacoplamento entre o fator de forma e de estrutura. A aplicação deste método permitiu a obtenção de informações independentes sobre alterações na estrutura interna da LDL devido à temperatura bem como peculiaridades sobre os agregados formados em cada caso.

Como demonstrado no artigo original, o fator de estrutura que melhor descreveu os dados experimentais correspondeu a um fator de estrutura de aglomerado globular, indicando que os agregados formados possuem este tipo de conformação. Assim, como mostrado anteriormente, a intensidade pode ser descrita por,

$$I(q) = P_{MOD}(q) S_{Gui}(q) \tag{64}$$

Sendo $P_{MOD}(q)$ dado pela equação (51) e $S_{Gui}(q)$ dado pela equação (23). Assumindo-se que no sistema pode-se ter uma fração de LDL livres e outra de LDL formando o agregado, é possível estimar, a partir das curvas de intensidade, a fração correspondente aos agregados bem como à fração correspondente às partículas de LDL livres no sistema. Os detalhes deste cálculo podem ser obtidos no artigo correspondente (Oliveira, Monteiro*, et al.*, 2014), mas como resultado final temos,

$$f_{LDL}^{i} = \frac{1}{1 + S_C^{agg}\left(\frac{R_G^{LDL}}{R_G^{agg}}\right)^{3\alpha}} \tag{65}$$

$$f_{agg}^{i} = \frac{1}{1 + \frac{1}{S_C^{agg}}\left(\frac{R_G^{agg}}{R_G^{LDL}}\right)^{3\alpha}} \tag{66}$$

Para fração de numero de partículas temos i="num" e α=2, para fração de volumes, i="vol" e α=1 e para fração de intensidade, i="int" e α=0. O significado destas frações está relacionado ao peso que é utilizado para o cálculo em cada caso. A fração numérica não possui nenhum peso, a fração de volume é pesada pelo volume das partículas enquanto que a fração de intensidades é pesada pelo volume quadrado (Oliveira, Monteiro*, et al.*, 2014).

Os detalhes da analise dos dados não serão reproduzidos aqui e podem ser obtidos no artigo original. No entanto, foi possível obter uma interessante descrição das alterações estruturais das partículas de LDL bem como a evolução dos agregados obtidos. Na Figura 24 e Figura 25 são apresentados resultados para 42ºC e na Figura 26 e Figura 27 os resultados para 60ºC. Em ambos os casos é possível ver um aumento da contribuição dos agregados na intensidade espalhada, como indicado pelos valores das frações em cada caso. Além disso, os perfis de densidade eletrônica obtidos pelo método de deconvolução apresentam importantes diferenças quando comparados ao perfil da lipoproteína nativa (Figura 20b).

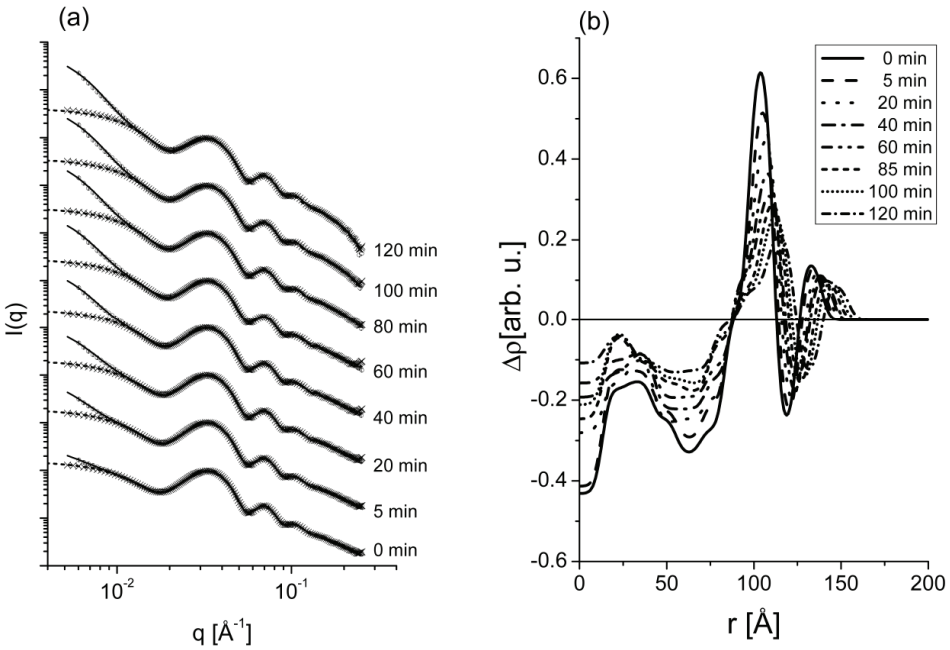

Figura 24 – Método GIFT e resultados de deconvolução para a LDL a 42ºC. (a) Dados experimentais de SAXS para diferentes instantes (círculos abertos), ajuste teórico obtido pelo método GIFT (linha sólida), fator de forma desacoplado (símbolos em "X") e o ajuste do fator de forma utilizando o método de deconvolução (linha tracejada). (b) Perfil de densidade eletrônica obtido para cada instante. Figura tirada de (Oliveira, Monteiro, *et al.*, 2014).

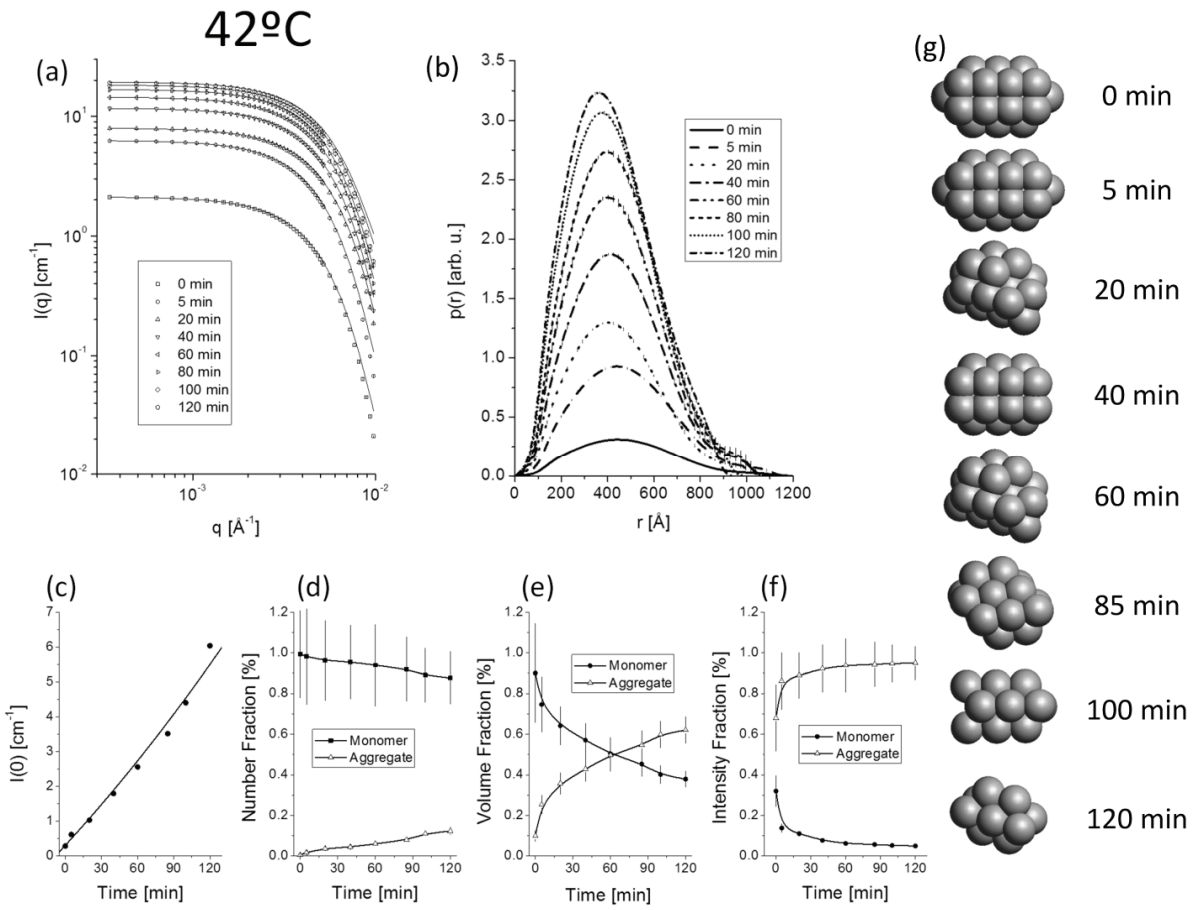

Figura 25 – Agregação da LDL à 42ºC. Análise por IFT: (a) Intensidade de espalhamento para os agregados (círculos) obtida pelo método GIFT. A curva *p(r)* correspondente é mostrada em (b). Cálculo das frações: (c) intensidade na origem para dados coletados à 42ºC (círculos) indicando um aumento monótono da intensidade. Isto indica um aumento sistemático da contribuição dos agregados. A linha neste gráfico é apenas para guia visual. (d) fração de número dos monômeros de LDL (círculos) e agregados (triângulos abertos). (e) fração de volume monômeros de LDL (círculos) e agregados (triângulos abertos). (f) fração de intensidade dos monômeros de LDL (círculos) e agregados (triângulos abertos). Todas as frações foram calculadas utilizando as equações 62 e 63 com os correspondentes valores de α. As linhas indicadas no gráfico são para guia visual. Modelagem dos agregados: utilizando modelagem *ab initio* tipo *dummy atom* (Seção 4.4) é possível ajustar os dados (linhas sólidas em (a)) e obter os modelos 3D para os agregados, mostrados em (g) para cada instante. Note que as esferas em (g) possuem o diâmetro de 350Å. Figura tirada de (Oliveira, Monteiro, *et al.*, 2014).

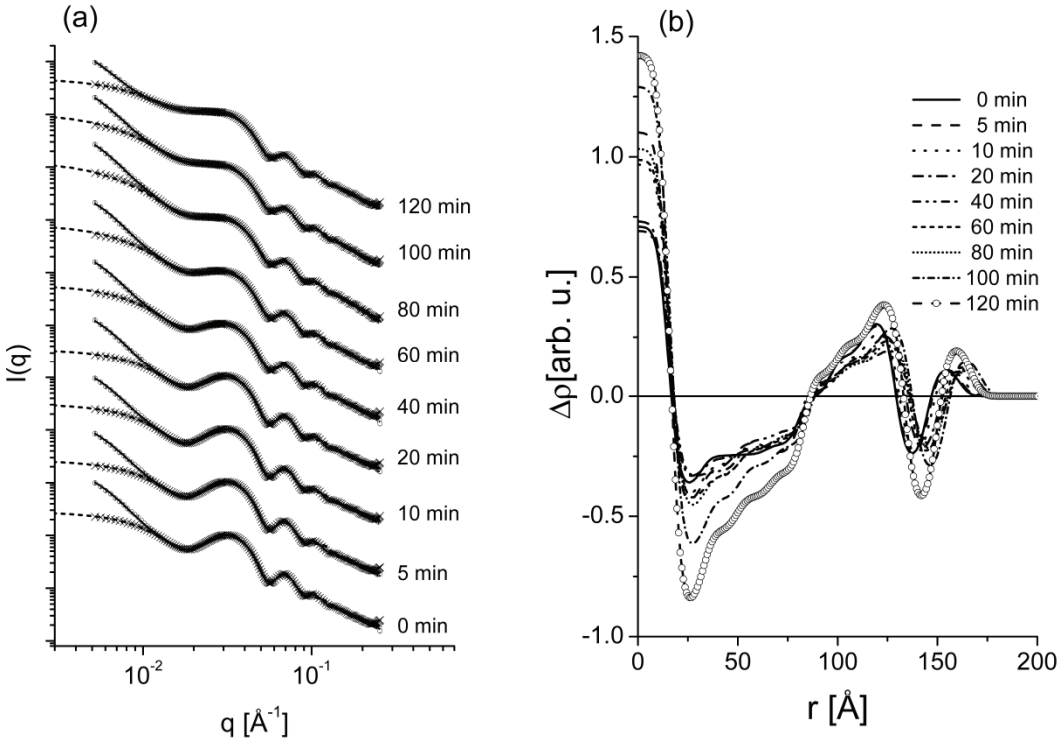

Figura 26 – Método GIFT e resultados de deconvolução para a LDL a 60ºC. (a) Dados experimentais de SAXS para diferentes instantes (círculos abertos), ajuste teórico obtido pelo método GIFT (linha sólida), fator de forma desacoplado (símbolos em "X") e o ajuste do fator de forma utilizando o método de deconvolução (linha tracejada). (b) Perfil de densidade eletrônica obtido para cada instante. Figura tirada de (Oliveira, Monteiro, *et al.*, 2014).

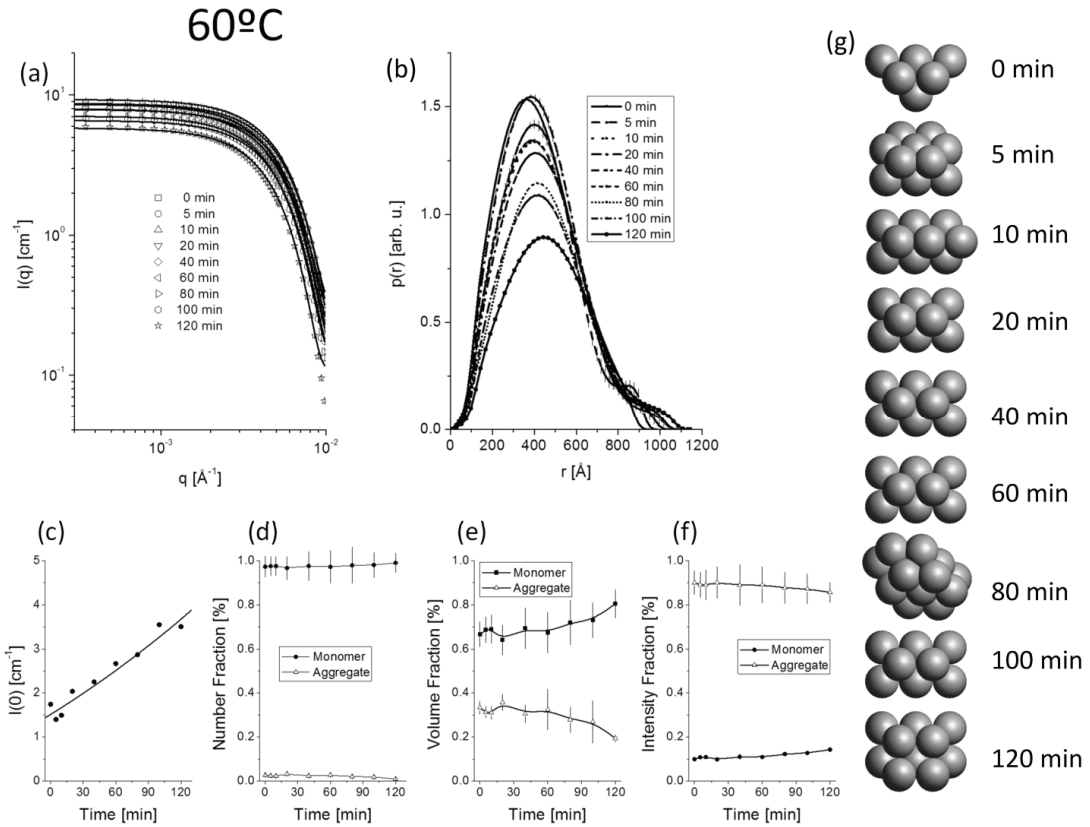

Figura 27 – Agregação da LDL à 60ºC. Análise por IFT: (a) Intensidade de espalhamento para os agregados (círculos) obtida pelo método GIFT. A curva p(r) correspondente é mostrada em (b). Cálculo das frações: (c) intensidade na origem para dados coletados à 42ºC (círculos) indicando um aumento monótono da intensidade. Isto indica um aumento sistemático da contribuição dos agregados. A linha neste gráfico é apenas para guia visual. (d) fração de número dos monômeros de LDL (círculos) e agregados (triângulos abertos). (e) fração de volume monômeros de LDL (círculos) e agregados (triângulos abertos). (f) fração de intensidade dos monômeros de LDL (círculos) e agregados (triângulos abertos). Todas as frações foram calculadas utilizando as equações 62 e 63 com os correspondentes valores de α. As linhas indicadas no gráfico são para guia visual. Modelagem dos agregados: utilizando modelagem *ab initio* tipo *dummy atom* (Seção 4.4) é possível ajustar os dados (linhas sólidas em (a)) e obter os modelos 3D para os agregados, mostrados em (g) para cada instante. Note que as esferas em (g) possuem o diâmetro de 350Å. Figura tirada de (Oliveira, Monteiro, *et al.*, 2014).

Todos os resultados obtidos pelas analises dos dados de espalhamento lipoproteínas foram inéditos na literatura devido à qualidade dos ajustes e nível de detalhamento dos perfis de densidade eletrônica obtidos e definem um novo padrão para análise de dados de espalhamento para lipoproteínas, permitindo a obtenção de informações estruturais internas às lipoproteínas bem como formas de interação e agregação.

6. Considerações Finais e Perspectivas

Neste trabalho foram apresentados diversos métodos para modelagem de dados de espalhamento e difração a baixos ângulos. Metodologias inovadoras foram desenvolvidas e puderam ser aplicadas ao estudo de variados tipos de sistemas. A maioria dos métodos apresentados foi desenvolvida ou otimizada após meu inicio como docente no Instituto de Física da Universidade de São Paulo em Janeiro de 2010.

Quando se coletam dados de espalhamento a baixos ângulos por um sistema, a curva de intensidade pode conter informações tanto da forma e estrutura interna da partícula (fator de forma) quanto organização espacial e interação entre as partículas (fator de estrutura) com os métodos apresentados aqui é possível satisfatoriamente desacoplar a contribuição dos fatores de forma e de estrutura do sistema, permitindo a modelagem precisa de todas as contribuições. Detalhes dos procedimentos matemáticos e numéricos implementados nos programas foram descritos bem como as formas de otimização.

Este variado leque de métodos de modelagem e analise de dados vem sendo utilizado para a descrição de um elevado numero de sistemas, permitindo o desenvolvimento de pesquisas de alto nível no IFUSP. Em conjunto com o desenvolvimento e melhoria de infra-estrutura experimental, estes resultados têm tornado o IFUSP referencia internacional em métodos de espalhamento a baixos ângulos, favorecendo a obtenção de recursos bem como a formação de recursos humanos (alunos de mestrado, doutorado e pós-doutores).

A publicação dos resultados obtidos, em revistas indexadas de alto impacto, atesta a qualidade dos trabalhos realizados. No entanto, muitos outros avanços podem ser feitos. Pretendo prosseguir no desenvolvimento de métodos de modelagem, expandindo o número de modelos bem como metodologias de otimização. Ate agora o enfoque foi em sistemas randomicamente orientados, de modo que a intensidade de espalhamento bidimensional é isotrópica e pode ser integrada em todo o circulo, fornecendo uma curva 1D. No entanto, para sistemas orientados tem-se imagens de espalhamento anisotrópicas e metodologias diferentes devem ser utilizadas. Ferramentas computacionais para lidar com este tipo de problemas serão desenvolvidas. Além disso, venho trabalhando em colaboração com grupos que realizam dinâmica molecular de sistemas biológicos, já tendo participado em diversas publicações (Iacovelli *et al.*, 2014, Oteri *et al.*, 2011, Oliveira *et al.*, 2010, Falconi *et al.*, 2009). A combinação de simulações de Dinâmica Molecular com dados de SAS para otimização conjunta já vem sendo tentada por diversos grupos (Oroguchi & Ikeguchi, 2012) e permite a obtenção de resultados mais confiáveis para modelagens. Tal implementação também será realizada no IFUSP. Por fim, estudos da interação entre complexos entre proteínas e surfactantes também vem sendo realizadas em meu grupo. Para este caso dados de calorimetria de titulação

isotérmica, fluorescência, dicroísmo circular e espalhamento de raios X a baixos ângulos vêm sendo realizados de modo a prover informações termodinâmicas e estruturais dos complexos formados (Sun *et al.*, *submitted*).

7. Bibliografia

Abramowitz, M. & Stegun, I. A. (1972). *Handbook of mathematical functions : with formulas, graphs and mathematical tables*. New York: Wiley.

Almeida, N. L., Oliveira, C. L. P., Torriani, I. L. & Loh, W. (2004). *Colloids and Surfaces B-Biointerfaces* **38**, 67-76.

Alves, C. (2015). thesis, Universidade de São Paulo.

Alves, C., Pedersen, J. S. & Pinto Oliveira, C. L. (2014). *Journal of Applied Crystallography* **47**, 84-94.

Alves, S. & Figueiredo Neto, A. M. (2014). *Liquid Crystals* **41**, 465-470.

Andersen, C. B. F., Torvund-Jensen, M., Nielsen, M. J., Pinto de Oliveira, C. L., Hersleth, H.-P., Andersen, N. H., Pedersen, J. S., Andersen, G. R. & Moestrup, S. K. (2012). *Nature* **489**, 456-U150.

Atkinson, D., Deckelbaum, R. J., Small, D. M. & Shipley, G. G. (1977). *Proceedings of the National Academy of Sciences of the United States of America* **74**, 1042-1046.

Balbino, T. A., Aoki, N. T., Gasperini, A. A. M., Oliveira, C. L. P., Azzoni, A. R., Cavalcanti, L. P. & de la Torre, L. G. (2013). *Chemical Engineering Journal* **226**, 423-433.

Balbino, T. A., Gasperini, A. A. M., Oliveira, C. L. P., Azzoni, A. R., Cavalcanti, L. P. & de La Torre, L. G. (2012). *Langmuir* **28**, 11535-11545.

Baxter, R. J. (1968). *Journal of Chemical Physics* **49**, 2770-&.

Behrens, M. A., He, Y., Oliveira, C. L. P., Andersen, G. R., Pedersen, J. S., Nielsen, K. H. & Jankowsky, E. (2012). *Rna Helicases* **511**, 191-212.

Bergmann, A., Fritz, G. & Glatter, O. (2000). *Journal of Applied Crystallography* **33**, 1212-1216.

Bougis, K., Rubim, R. L., Ziane, N., Peyencet, J., Bentaleb, A., Février, A., Oliveira, C. L. P., Oliveira, E. A., Navailles, L. & Nallet, F. (2014). *submitted*.

Caillé, A. (1972). *Comptes Rendus Hebdomadaires Des Séances De L Académie Des Sciences Série B* **274**, 891-&.

Calcutta, A., Jessen, C. M., Behrens, M. A., Oliveira, C. L. P., Renart, M. L., Gonzalez-Ros, J. M., Otzen, D. E., Pedersen, J. S., Malmendal, A. & Nielsen, N. C. (2012). *Biochimica Et Biophysica Acta-Biomembranes* **1818**, 2290-2301.

Carvalho, J., Toniazzo, T., Cavalcanti, L., Moraes, I., Oliveira, C. & Pinho, S. (2015). *submitted*.

Chacon, P., Moran, F., Diaz, J. F., Pantos, E. & Andreu, J. M. (1998). *Biophysical Journal* **74**, 2760-2775.

Cullity, B. D. & Stock, S. R. (2001). *Elements of X-ray diffraction*, 3. ed. Upper Saddle River, N.J.: Prentice Hall.

da Silva, V. M., Colussi, F., Neto, M. D., Braz, A. S. K., Squina, F. M., Oliveira, C. L. P. & Garcia, W. (2014). *Plos One* **9**.

Debye, P. (1915). *Annalen Der Physik* **46**, 809-823.

Deckelbaum, R. J., Shipley, G. G. & Small, D. M. (1977). *Journal of Biological Chemistry* **252**, 744-754.

Deckelbaum, R. J., Shipley, G. G., Small, D. M., Lees, R. S. & George, P. K. (1975). *Science* **190**, 392-394.

Demasi, M., Hand, A., Oliveira, C. L. P., Bicev, R. N., Bertoncini, C. A. & Netto, L. E. S. N. (2014). *Archives of Biochemistry and Biophysics* ***in press***, -.

Demasi, M., Netto, L. E. S., Silva, G. M., Hand, A., Oliveira, C. L. P., Bicev, R. N., Gozzo, F., Barros, M. H., Leme, J. M. M. & Ohara, E. (2014). *Redox Biology* **2**, 44 - 51.
Falconi, M., Oteri, F., Chillemi, G., Andersen, F., Tordrup, D., Oliveira, C., Pedersen, J., Knudsen, B. & Desideri, A. (2009). *ACS NANO* **3**, 1813-1822.
Feigin, L. & Svergun, D. (1987). *Structure Analysis by Small-Angle X-Ray and Neutron Scattering*. Plenum Publishing Corporation – Plenum Press, New York.
Forster, S., Timmann, A., Konrad, M., Schellbach, C., Meyer, A., Funari, S. S., Mulvaney, P. & Knott, R. (2005). *Journal of Physical Chemistry B* **109**, 1347-1360.
Freiberger, N. & Glatter, O. (2006). *Journal of Physical Chemistry B* **110**, 14719-14727.
Fritz, G., Bergmann, A. & Glatter, O. (2000). *Journal of Chemical Physics* **113**, 9733-9740.
Fritz, G. & Glatter, O. (2006). *Journal of Physics-Condensed Matter* **18**, S2403-S2419.
Gerbelli, B. B. (2012). thesis*,* University of São Paulo.
Gerbelli, B. B., Rubim, R. L., Silva, E. R., Nallet, F., Navailles, L., Oliveira, C. L. P. & de Oliveira, E. A. (2013). *Langmuir* **29**, 13717-13722.
Giehm, L., Oliveira, C., Christiansen, G., Pedersen, J. & Otzen, D. (2010). *Journal of Molecular Biology* **401**, 115-133.
Glatter, O. (1977). *Journal of Applied Crystallography* **10**, 415-421.
Glatter, O. (1980). *Acta Physica Austriaca* **52**, 243-256.
Glatter, O. (1981). *Journal of Applied Crystallography* **14**, 101-108.
Glatter, O. & Hainisch, B. (1984). *Journal of Applied Crystallography* **17**, 435-441.
Glatter, O. & Kratky, O. (1982). *Small Angle X-ray Scattering*. Academic Press, London.
Gomez, S. L., Turchiello, R. F., Jurado, M. C., Boschcov, P., Gidlund, M. & Figueiredo Neto, A. M. (2008). *Atherosclerosis Supplements* **9**, 154-154.
Guinier, A. a. F., Fournet, G. r., Walker, C. B. & Yudowitch, K. L. (1955). *Small-Angle Scattering of X-Rays ... Translation by Christopher B. Walker ... Followed by a bibliography by Kenneth L. Yudowitch*. pp. xi. 268. John Wiley & Sons: New York; Chapman & Hall: London.
Hamley, I. W. (2000). *Introduction to soft matter polymers, colloids, amphiphiles and liquid crystals*. Chichester: Wiley.
Hansen, J. P. & Hayter, J. B. (1982). *Molecular Physics* **46**, 651-656.
Hume, A. *Polyhedron Database,* http://www.netlib.org/polyhedra/.
Iacovelli, F., Alves, C., Falconi, M., Oteri, F., de Oliveira, C. L. P. & Desideri, A. (2014). *Biopolymers* **101**, 992-999.
Israelachvili, J. N. (2007). *Intermolecular and surface forces*, 2. ed. Amsterdam: Academic Press.
Jayaraman, S. a. G. D. a. G. O. (2005). *Biochemistry* **44**, 3965-3971.
Jones, R. A. L. (2002). *Soft condensed matter*. Oxford: Oxford University Press.
Kinning, D. J. & Thomas, E. L. (1984). *Macromolecules* **17**, 1712-1718.
Knoll, G. F. (2010). *Radiation detection and measurement*, 4th ed. ed. Hoboken, N.J.: Wiley.
Kotlarchyk, M. & Chen, S. H. (1983). *Journal of Chemical Physics* **79**, 2461-2469.
Kratky, O. & Porod, G. (1949). *Journal of Colloid Science* **4**, 35-70.
Laggner, P., Degovics, G., Muller, K. W., Glatter, O., Kratky, O., Kostner, G. & Holasek, A. (1977). *Hoppe-Seylers Zeitschrift Fur Physiologische Chemie* **358**, 771-778.
Laggner, P. & Muller, K. W. (1978). *Quarterly Reviews of Biophysics* **11**.
Landa, R. A., Soledad Antonel, P., Ruiz, M. M., Perez, O. E., Butera, A., Jorge, G., Oliveira, C. L. P. & Martin Negri, R. (2013). *Journal of Applied Physics* **114**.
Lindner, P. & Zemb, T. (2002). *Neutrons, X-rays and light : scattering methods applied to soft condensed matter*. Amsterdam ; Oxford: Elsevier.
Mariano Neto, F. (2013). thesis*,* Universidade de São Paulo, Brazil.
Mariano-Neto, F., Matos, J. R., Cides da Silva, L. C., Carvalho, L. V., Scaramuzzi, K., Sant'Anna, O. A., Oliveira, C. P. & Fantini, M. C. A. (2014). *Journal of Physics D-Applied Physics* **47**.
Meyer, D. F., Nealis, A. S., MacPhee, C. H., Groot, P. H. E., Suckling, K. E., Bruckdorfer, K. R. & Perkins, S. J. (1996). *Biochemical Journal* **319**, 217-227.

Nagle, J. F., Zhang, R. T., TristramNagle, S., Sun, W. J., Petrache, H. I. & Suter, R. M. (1996). *Biophysical Journal* **70**, 1419-1431.
Nallet, F., Laversanne, R. & Roux, D. (1993). *Journal De Physique Ii* **3**, 487-502.
Neugebauer, T. (1942). *Annalen Der Physik* **42**, 509-533.
Oliveira, C. (2001). thesis, Universidade Estadual de Campinas, Brazil.
Oliveira, C. (2005). thesis, Universidade Estadual de Campinas, Brazil.
Oliveira, C. L. P. (2011). *Current Trends in X-Ray Crystallography,* edited by D. A. Chandrasekaran, pp. 367-392: InTech.
Oliveira, C. L. P., Behrens, M. A., Pedersen, J. S. & al., e. (2009). *Journal of Molecular Biology* **387**, 147-161.
Oliveira, C. L. P., Gerbelli, B. B., Silva, E. R. T., Nallet, F., Navailles, L., Oliveira, E. A. & Pedersen, J. S. (2012). *Journal of Applied Crystallography* **45**, 1278-1286.
Oliveira, C. L. P., Juul, S., Jorgensen, H. L., Knudsen, B., Tordrup, D., Oteri, F., Falconi, M., Koch, J., Desideri, A., Pedersen, J. S., Andersen, F. F. & Knudsen, B. R. (2010). *Acs Nano* **4**, 1367-1376.
Oliveira, C. L. P., Monteiro, A. M. & Figueiredo Neto, A. M. (2014). *Brazilian Journal of Physics* **44**, 753-764.
Oliveira, C. L. P. & Pedersen, J. S. (2013). *Amyloid Fibrils and Prefibrillar Aggregates,* edited by D. E. Otzen. Weinheim: Wiley-VCH.
Oliveira, C. L. P., Santos, P., Monteiro, A. & Figueiredo Neto, A. M. (2014). *Biophysical Journal* **106**, 2595–2605.
Oroguchi, T. & Ikeguchi, M. (2012). *Chemical Physics Letters* **541**, 117-121.
Oteri, F., Falconi, M., Chillemi, G., Andersen, F. F., Oliveira, C. L. P., Pedersen, J. S., Knudsen, B. R. & Desideri, A. (2011). *Journal of Physical Chemistry C* **115**, 16819-16827.
Pabst, G., Rappolt, M., Amenitsch, H. & Laggner, P. (2000). *Physical Review E* **62**, 4000-4009.
Pape, E. H. & Kreutz, W. (1978). *Journal of Applied Crystallography* **11**, 421-429.
Pedersen, J. S. (1992). *Journal of Applied Crystallography* **25**, 129-145.
Pedersen, J. S. (1997). *Advances in Colloid and Interface Science* **70**, 171-210.
Pedersen, J. S. & Hamley, I. W. (1994a). *Journal of Applied Crystallography* **27**, 36-49.
Pedersen, J. S. & Hamley, I. W. (1994b). *Physica B* **198**, 16-23.
Pedersen, J. S., Oliveira, C. L. P., Hubschmann, H. B., Arleth, L., Manniche, S., Kirkby, N. & Nielsen, H. M. (2012). *Biophysical Journal* **102**, 2372-2380.
Pedersen, J. S., Posselt, D. & Mortensen, K. (1990). *Journal of Applied Crystallography* **23**, 321-333.
Pedersen, J. S. & Riekel, C. (1991). *Journal of Applied Crystallography* **24**, 893-909.
Petoukhov, M. V. & Svergun, D. I. (2005). *Biophysical Journal* **89**, 1237-1250.
Prassl, R., Pregetter, M., Amenitsch, H., Kriechbaum, M., Schwarzenbacher, R., Chapman, J. M. & Laggner, P. (2008). *Plos One* **3**.
Press, W. H. (1992). *Numerical recipes in FORTRAN : the art of scientific computing*, 2nd ed. ed. Cambridge: Cambridge University Press.
Rasmussen, L. C. V., Oliveira, C. L. P., Byron, O., Jensen, J. M., Pedersen, J. S., Sperling-Petersen, H. U. & Mortensen, K. K. (2011). *Biochemical and Biophysical Research Communications* **416**, 140-145.
Rasmussen, L. C. V., Pinto Oliveira, C. L., Pedersen, J. S., Sperling-Petersen, H. U. & Mortensen, K. K. (2011). *Biochemistry* **50**, 9779-9787.
Rathgeber, S., Monkenbusch, M., Kreitschmann, M., Urban, V. & Brulet, A. (2002). *Journal of Chemical Physics* **117**, 4047-4062.
Rubim, R. L. (2014). thesis, University of São Paulo.
Sales, E. (2015). thesis, Universidade de São Paulo.
Santos, P. (2013). thesis, Universidade de São Paulo, Brazil.
Semenyuk, A. V. & Svergun, D. I. (1991). *Journal of Applied Crystallography* **24**, 537-540.

Silva, G. M., Netto, L. E. S., Simoes, V., Santos, L. F. A., Gozzo, F. C., Demasi, M. A. A., Oliveira, C. L. P., Bicev, R. N., Klitzke, C. F., Sogayar, M. C. & Demasi, M. (2012). *Antioxidants & Redox Signaling* **16**, 1183-1194.

Sun, Y., Oseliero Filho, P. L., Junior, J., Carvalho, J., Schreier, S. & Oliveira, C. L. P. (*submitted*).

Sundblom, A., Oliveira, C., Palmqvist, A. & Pedersen, J. (2009). *Journal of Physical Chemistry C* **113**, 7706-7713.

Sundblom, A., Oliveira, C., Pedersen, J. & Palmqvist, A. (2010). *Journal of Physical Chemistry C* **114**, 3483-3492.

Sundblom, A., Oliveira, C., Pedersen, J. & Palmqvist, A. (2011). *Microporous and Mesoporous Materials* **145**, 59-64.

Svergun, D., Barberato, C. & Koch, M. H. J. (1995). *Journal of Applied Crystallography* **28**, 768-773.

Svergun, D. I. (1999). *Biophysical Journal* **77**, 2896-2896.

Svergun, D. I., Petoukhov, M. V. & Koch, M. H. J. (2001). *Biophysical Journal* **80**, 2946-2953.

Svergun, D. I., Volkov, V. V., Kozin, M. B., Stuhrmann, H. B., Barberato, C. & Koch, M. H. J. (1997). *Journal of Applied Crystallography* **30**, 798-802.

Szekely, P., Ginsburg, A., Ben-Nun, T. & Raviv, U. (2010). *Langmuir* **26**, 13110-13129.

Teixeira, J. (1988). *Journal of Applied Crystallography* **21**, 781-785.

Walther, D., Cohen, F. E. & Doniach, S. (2000). *Journal of Applied Crystallography* **33**, 350-363.

Worthington, C. (1969). *Biophysical Journal* **9**, 222-234.

Yan, Y., de Keizer, A., Martens, A., Oliveira, C., Pedersen, J., de Wolf, F., Drechsler, M., Stuart, M. & Besseling, N. (2009). *LANGMUIR* **25**, 12899-12908.

Zhang, R. T., Suter, R. M. & Nagle, J. F. (1994). *Physical Review E* **50**, 5047-5060.

8. Apêndice

a. Publicações selecionadas

research papers

Journal of
Applied
Crystallography
ISSN 0021-8898

Received 25 June 2012
Accepted 6 October 2012

Gaussian deconvolution: a useful method for a form-free modeling of scattering data from mono- and multilayered planar systems

Cristiano L. P. Oliveira,* Barbara B. Gerbelli, Emerson R. T. Silva, Frédéric Nallet, Laurence Navailles, Elisabeth A. Oliveira and Jan Skov Pedersen

Department of Experimental Physics, University of Sao Paulo, 66318, Sao Paulo, 05314-970, Brazil. Correspondence e-mail: crislpo@if.usp.br

A new method for analysis of scattering data from lamellar bilayer systems is presented. The method employs a form-free description of the cross-section structure of the bilayer and the fit is performed directly to the scattering data, introducing also a structure factor when required. The cross-section structure (electron density profile in the case of X-ray scattering) is described by a set of Gaussian functions and the technique is termed Gaussian deconvolution. The coefficients of the Gaussians are optimized using a constrained least-squares routine that induces smoothness of the electron density profile. The optimization is coupled with the point-of-inflection method for determining the optimal weight of the smoothness. With the new approach, it is possible to optimize simultaneously the form factor, structure factor and several other parameters in the model. The applicability of this method is demonstrated by using it in a study of a multilamellar system composed of lecithin bilayers, where the form factor and structure factor are obtained simultaneously, and the obtained results provided new insight into this very well known system.

© 2012 International Union of Crystallography
Printed in Singapore – all rights reserved

1. Introduction

Lamellar systems of lipid bilayers have been widely used as model systems for biological membranes. They allow the study of, for example, phase transitions and interactions between membranes and with biological macromolecules. The organization of the lipid molecules on the microscopic level is closely related to the macroscopic properties of the membrane and determines key properties such as elasticity, permeability to small molecules, and interactions with proteins or peptides. X-ray scattering techniques are particularly suitable for obtaining information on the microscopic organization of the molecules. Since the pioneering work of Luzzati & Tardieu (1974), many researchers have developed new methods to analyze experimental data, allowing determination of relevant parameters characterizing the lamellar structure.

Several methods for analyzing X-ray scattering profiles for lamellar systems have been proposed. Seminal work using Gaussian functions to describe the electron density profile was described by Pape & Kreutz (1978) and by Nagle & Wiener (1989); however, these methods are very sensitive to the first estimate of the parameters describing the profile, *i.e.* they require good *a priori* information about the signs and the positions of the Gaussians. The situation is even more complicated when multilayered lamellar systems have to be described, and several strategies for modeling the form factor and structure factor effects have been proposed (Nallet *et al.*, 1993; Nagle *et al.*, 1996; Petrache *et al.*, 1998). More recently, an approach was presented by Pabst *et al.* (2000*b*), where Gaussian functions were again used to describe the lamellar cross-section profile, and as the coupling between the form factor and structure factor was taken into account, the full scattering intensity profile could be described by this method. However, the approach was restricted to the use of only two Gaussian functions to avoid model instabilities, as previously mentioned by other authors (Pape & Kreutz, 1978).

An approach to overcome instabilities in the modeling of electron density profiles was introduced in the so-called square-root deconvolution method, originally proposed by Glatter (1981). It enables the retrieval of the electron density profile for a given geometry (planar, cylindrical or spherical) by describing the electron density profile by a set of basis functions (step functions) and using these for modeling the pair distance distribution function. The method was originally applied to scattering data from uncorrelated objects (*i.e.* without structure factor effects) but later was also adapted for including possible high-order arrangements (Fritz & Glatter, 2006). However, one of the limitations of this approach is the need to make the intermediate step of first determining the pair distance distribution function, which might preclude the optimization of other structural features that might also be present, such as, for example, free bilayers (Pabst *et al.*, 2000*a*). On the other hand, the main advantage of this procedure is the possibility of retrieving the electron density profile in a free form without any previous assumptions. The number of

electronic reprint

degrees of freedom in the expression for the electron density profiles is usually large and this means that the solution has to be 'stabilized'. This stabilization can be done by the addition of a smoothness constraint to the usual χ^2 as a penalty function with a certain weight relative to χ^2. The weight of the penalty function is determined by the use of the point-of-inflection method during the minimization procedure (Glatter, 1977). A similar two-step analysis method for analysis of specular reflectivity data was introduced by Pedersen (1992). A new and more sophisticated approach is to model the lipid membrane based on scattering density profile methods (Heberle *et al.*, 2012). This approach permits the inclusion of molecular information and the use of molecular dynamics simulations as inputs for the fitting of scattering data. Although this method can provide more advanced results, it requires several pieces of *a priori* information about the system and its composition and fine details about the lipid molecules. As will be described below, the Gaussian deconvolution approach, on the other hand, does not require any *a priori* information for the fitting procedure and the obtained profile can be used as input for other more sophisticated analyses.

In the present work a new method is presented for modeling small-angle X-ray scattering (SAXS) experimental data for systems containing both unilamellar and multilamellar planar membranes. As will be discussed in the next section, a model approach similar to that used by Glatter (1981) in his deconvolution method can be used to stabilize the modeling of the electron density profile by a set of Gaussian functions. However, the main advantage of this approach is the fact that the scattering intensity is adjusted and not the pair distance distribution function. This is similar to the method introduced by Pedersen & Hamley (1994*a*,*b*) for analysis of specular reflectivity data. By the new method it is possible to retrieve a smooth electron density profile for which the calculated intensity gives the best fit of the experimental data. The approach allows, by the use of a least-squares procedure, the simultaneous determination of the amplitudes of the Gaussian functions that describe the electron density profile and several other parameters, such as, for example, those describing structure factor effects, background *etc.*

The new method is applied for determining the swelling properties of a lamellar phase composed of lecithin bilayers, providing a good fit quality for the full set of experimental scattering curves for a series of increasing degree of membrane hydration. New insight emerges from the analysis of the experimental data on the structure of the bilayer as extracted from the electron contrast profile. It is shown that the Caillé parameter, which characterizes the flexibility of lipid membranes together with intermembrane interactions, passes through two regimes. This provides information on the role of hydration and fluctuation forces for stabilizing the lamellar structure.

2. Theoretical model description

The scattering from a system of scattering objects can be described by the following expression:

$$I(q) = c\{P_{3D}(q)S(q)\}, \tag{1}$$

where c is related to the concentration of particles in the system, $P_{3D}(q) = |F(q)|^2$ is the form factor of the three-dimensional objects and carries information about particle shapes and contrasts, and $S(q)$ is the system structure factor, which carries information about possible interparticle interactions and ordering. The parameter q is the modulus of the scattering vector and it is given by $q = 4\pi\sin(\theta)/\lambda$, where 2θ is the scattering angle and λ is the wavelength of the radiation. The brackets '$\langle\ \rangle$' indicate that in the general case these two contributions have to be averaged together in the calculation. For locally highly anisotropic systems, like planar systems or large vesicles for example, where the transverse dimensions are much larger than the perpendicular dimension, the form factor can be described by a product of a form factor, for the perpendicular direction (one-dimensional function), and a factor $1/q^2$ related to the transverse dimensions. In this case, equation (1) can be rewritten as (Glatter & Kratky, 1982)

$$I(q) = (c/q^2)\{P(q)S(q)\}. \tag{2}$$

An often used approach is to employ the decoupling approximation and treat the form factor and structure factor separately (Kotlarchyk & Chen, 1983). For a multilayered lamellar system, with periodicity d, the structure factor is well described by the modified Caillé theory (MCT) (Zhang *et al.*, 1994):

$$S_{\rm MCT}(q) = 1 + 2\sum_{n=1}^{N-1}\Big\{(1 - n/N)\cos(nqd) \times \exp\big[-(d/2\pi)^2 q^2 \eta\gamma\big](\pi n)^{-(d/2\pi)^2 q^2 \eta}\Big\}. \tag{3}$$

The mean number of coherent scattering bilayers in the stack is denoted as N, and γ is Euler's constant. The Caillé parameter η is related to both the bending modulus K of lipid bilayers and the bulk modulus B for compression (Zhang *et al.*, 1994; Caillé, 1972):

$$\eta = \frac{\pi kT}{2d^2(BK)^{1/2}}. \tag{4}$$

In this expression k is Boltzmann's constant and T is the absolute temperature. The description of the form factor can be done at several levels of detail. The form factor has to describe the differences in electron density for the molecules constituting the bilayer. In addition, for several applications it is a good approximation to assume that the bilayer is symmetric with respect to its center. One of the simplest approximations is to consider the two-step model given by Worthington (1969), Nallet *et al.* (1993) and Brotons *et al.* (2005):

$$P(q) = (4/q^2)\{\Delta\rho_{\rm H}\sin[q(\delta_{\rm H} + \delta_{\rm T})] - \Delta\rho_{\rm H}\sin(q\delta_{\rm T}) + \Delta\rho_{\rm T}\sin(q\delta_{\rm T})\}^2, \tag{5}$$

where $\Delta\rho_{\rm H}$ and $\Delta\rho_{\rm T}$ are, respectively, the head group and tail group electron density contrasts and $\delta_{\rm H}$ and $\delta_{\rm T}$ are the respective sizes of the head group and tail group regions. Since

electronic reprint

this expression is very simple, it usually gives too crude a description of the electron density profile and in several cases a better description is needed. With a similar step-model strategy, Glatter and co-workers developed the deconvolution square-root method (Glatter, 1981; Fritz & Glatter, 2006), where the electron density is described by a series of step functions. The height of the steps is determined using a constrained least-squares fitting procedure. However, in this approach the fit is done to the pair distance distribution and not directly to the experimental intensity. The intermediate step of determining the pair distance distribution function by a Fourier transform can cause several limitations for the method.

Another strategy was proposed by Pabst *et al.* (2000*b*), who suggested to model the bilayer using two Gaussian functions: a central Gaussian placed at the origin, which models the central part of the bilayer where hydrocarbon tails from the opposite sides meet, and a second Gaussian placed at a certain distance for modeling the head group region. The central part is known to have negative contrast with respect to a water buffer for X-rays, whereas the head groups are electron rich and have a positive contrast. This model is also a crude approximation of the electron density profile since it assumes that the tail groups have almost the same electron density as the water and that it is only the most central part of the bilayers, where the hydrocarbon chains meet, that have a negative contrast. However, surprisingly, the model is sufficient to obtain a reasonable description of the scattering data for several examples in the literature (Pabst *et al.*, 2000*a*). The smoothness introduced by the Gaussian profiles seems to improve the fit quality as compared to the simple two-step model. However, this model also fails for high-quality data, in particular for high q values where high-resolution information on the structure is probed. In the present work we combine the advantages of the Gaussian description of the electron density profiles with the stability introduced by Glatter in the free-form method. This enables a more flexible and stable modeling procedure.

In the new approach, the profile is described by a set of equally spaced Gaussian functions. During the optimization, it is necessary to constrain only the amplitudes of the Gaussian functions and not the other model parameters. As will be shown in the next section, this can be done by an appropriate change of the design matrix of the least-squares problem, introducing the Lagrange multiplier λ only at the necessary positions in the matrix. During the fitting procedure, the Lagrange multiplier is varied and the other parameters are optimized for each λ value. By using the point-of-inflection method, it is possible to obtain the λ value by an automatic procedure that gives both a good fit to the scattering data and the optimum constraint of the Gaussian amplitudes.

With this approach is possible to obtain a smooth profile that can describe more accurately the electron density of the lipid bilayer simultaneously with the optimization of the structure factor and other model parameters. In the following we present the procedure for symmetric and asymmetric bilayers.

3. Symmetric bilayer

For the description of a symmetric planar bilayer, a given number, $n_{\max}$, of Gaussian functions are used for describing the profile. This basis of functions is constructed in such a way that there is a central Gaussian at $z = 0$ and that the rest of the Gaussians are at equidistant positions mirrored so that a symmetric profile is obtained. The central Gaussian can represent the ends of the bilayer tail groups and the other centrosymmetric Gaussians build the remaining parts corresponding to the tail groups and the head groups. The electron density is thus described by

$$\begin{aligned} \rho(z) &= \sum_{n=1}^{n_{\max}} a_n\big[G_s(z, z_n, \sigma) + G_s(z, -z_n, \sigma)\big]/(1+\delta_{n1}), \\ \delta_{n1} &= 1, \quad n = 1, \\ \delta_{n1} &= 0, \quad n = 2, 3, n_{\max}, \end{aligned} \tag{6}$$

where

$$G_s(z, z_n, \sigma) = [1/\sigma(2\pi)^{1/2}]\exp[-(z - z_n)^2/2\sigma^2] \tag{7}$$

and the Kronecker delta function δ_{n1} is used to avoid double counting of the central Gaussian ($z_1 = 0$). n is the order of Gaussian used. The profile is defined by the values of the amplitudes a_n.

The half-bilayer width Z is defined as the distance between the center of the bilayer and the position where the last Gaussian reaches a width of two standard deviations (σ). With this definition, the positions of the Gaussians and the standard deviation (σ value) are calculated as follows:

$$z_n = (n-1)2\sigma, \quad \sigma = Z/[2n_{\max}(2\ln 2)^{1/2}]. \tag{8}$$

This choice of the centers and standard deviation gives a reasonable overlap between the Gaussian functions, enabling the construction of smooth profiles. The choice of the number of Gaussian functions ($n_{\max}$) will depend on the level of detail that is needed to build the profile. Since the scattering profile contains a low information content (Moore, 1980) a general rule that can be adopted is to use the minimum required number of terms for the modeling, which can be obtained from a few simple tests. If the number of terms used is larger than the ideal value, the obtained profile will have the same shape but some artificial oscillations. A typical profile built using equation (7) is shown in Fig. 1(*a*). One of the advantages of using a Gaussian set of functions for the representation of the profile is that, for the one-dimensional case of centrosymmetric bilayers, the Fourier transform of the electron density has an analytical solution, providing the scattering amplitudes (Abramowitz & Stegun, 1972; Pabst *et al.*, 2000*a*)

$$F(q, n) = (2\pi)^{1/2}\sigma\exp\big(-\sigma^2 q^2/2\big)\cos(qz_n). \tag{9}$$

The final profile scattering amplitude of the lamellar cross section is just the sum of all the $F(q, n)$ terms,

$$F(q) = \sum_{n=1}^{n_{\max}} a_n F(q, n), \tag{10}$$

and the form factor of the infinite lamellar system is

electronic reprint

$$P(q) = |F(q)|^2. \tag{11}$$

A theoretical simulation is shown in Fig. 1(*b*), where a profile with four Gaussian functions was used and combined with the structure factor of the modified Caillé theory to provide the combined $I(q)$ intensity.

4. Asymmetric bilayer

An expression for the form factor from the asymmetric bilayer was proposed by Brzustowicz & Brunger (2005):

$$P(q) = \langle F(q)^2 \rangle = \sum_{k,k'} \{a_k a_{k'} \sigma_k \sigma_{k'} \exp[-q^2(\sigma_k^2 + \sigma_{k'}^2)/2] \times \cos[q(z_k - z_{k'})]\}, \tag{12}$$

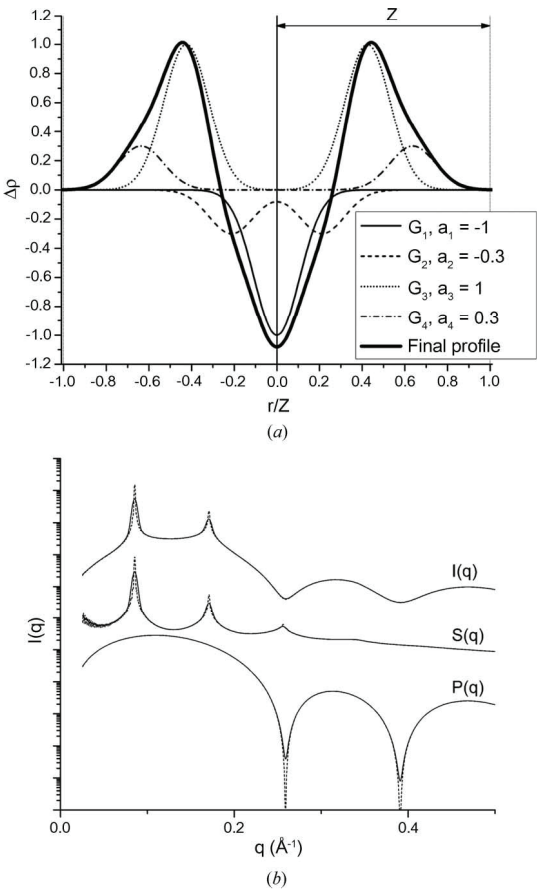

Figure 1
(*a*) Construction of the electron density profile using four Gaussians (G1, G2, G3 and G4) with four different amplitudes (−1, −0.3, 1, 0.3). They are shown by four different line styles. The final resultant electron density profile from the Gaussian model is shown as a solid thick line. (*b*) Final intensity and the corresponding form factor and structure factor. In each case the instrumentally smeared (solid line) and ideal nonsmeared (dotted line) curves are presented. In this simulation the number of layers used was $N = 50$, the interplanar distance $d = 73.5$ Å, the half-bilayer size $Z = 30$ Å and the Caillé parameter $\eta = 0.12$.

where σ_i are the Gaussian widths, a_i are the Gaussian amplitudes and z_i are the Gaussian centers, with respect to a common origin. For this case the construction of the profile is slightly different. Since the symmetry is lost, the electron density profile is given by

$$\rho(z) = \sum_{n=1}^{n_{\max}} a_n G_s(z, z_n, \sigma). \tag{13}$$

In this case, Z, which is a measure of the full bilayer thickness, the centers of the Gaussians and the standard deviation are defined and related as follows:

$$z_n = (n-1)\sigma, \quad \sigma = Z/[n_{\max}(2\ln 2)^{1/2}]. \tag{14}$$

This choice of the centers and standard deviation gives again a reasonable overlap between the Gaussian functions, enabling the construction of smooth profiles. A typical profile obtained using equation (13) and the corresponding scattering intensity calculated by equation (12) are shown in Fig. 2.

5. Final intensity expression

The expressions given in the previous sections permit the calculation of the scattering intensity for the proposed electron density profiles. In the case of multilamelar planar membranes (or large vesicles), this electron density profile will be a repeating unit and a structure factor has to be included for describing the ordered stacks. In the present context it is the structure factor from the modified Caillé theory [equation (3)] that is used, and the final scattering intensity of the cross-section structure of the system is then (Pabst *et al.*, 2000*a*)

$$I_{\rm MLV}(q) = [|F(q)|^2 S_{\rm MCT}(q) + N_{\rm diff}|F(q)|^2], \tag{15}$$

where the second term is included for describing the diffuse scattering that might appear from the presence of single bilayers in the system. Instrumental smearing effects, which are a consequence of the collimation of the camera pinholes, wavelength bandwidth, detector resolution *etc.*, can be taken into account by smearing the intensity expression by the resolution function $R(\langle q \rangle, q)$ as described by Pedersen *et al.* (1990). The final expression used to describe the data from multilamellar planar bilayers is

$$I_{\rm FIT}(q) = {\rm Sc}_1 I_{\rm MLV}(\langle q \rangle)/q^2 + {\rm Back}, \tag{16}$$

where Sc_1 is an overall scale factor and Back is a background expression. All parameters are optimized during the data fitting. One of the main advantages of this approach is the fact that the scattering intensity is adjusted and not the pair distance distribution function. In this way, it is very simple to add an additional contribution for the scattering, like particle flexibility (which would lead to a polymer-like contribution at high angles) or a given low scattering angle contribution, and optimize all parameters in the same least-squares fit. Using the above-mentioned procedure it is possible to perform a full curve fitting, retrieving simultaneously information about the form factor and structure factor.

electronic reprint

6. Optimization method

In the previous section, expressions for the theoretical intensity for planar bilayers with and without structure factor effects have been given; we distinguish the theoretical intensity here as $I^{\rm mod}(q)$. As mentioned above, the next step is to optimize the model parameters, which is done by a least-squares procedure. The coefficients are obtained by the minimization of the weighted χ^2 (or mean deviation):

$$\chi^2 = \sum_{i=1}^{M} \left[I^{\rm exp}(q_i) - I^{\rm mod}(q_i) \right]^2 / \sigma_i^2, \tag{17}$$

where M is the number of experimental points; $I^{\rm exp}(q_i)$ and σ_i are the experimental data and the standard errors, respectively. Since the theoretical intensity is not expressed as a linear combination of the model coefficients, the minimization of equation (17) requires the application of a nonlinear least-squares procedure. There are several minimization methods available in the literature, and in the present work we applied the Marquardt–Levenberg algorithm (Pedersen, 1992, 1997; Glatter & Hainisch, 1984). The set of normal equations that need to be solved iteratively are

$$\sum_{\nu=1}^{J} \alpha_{\mu\nu} \Delta a_\nu = -\beta_\mu, \quad \mu = 1, 2, \ldots, J, \tag{18}$$

where J is the number of fitting parameters and Δa_ν are the changes in the parameters a_ν at each interaction. The iteration procedure is continued until the changes are zero within some specified limit. The matrix $\alpha_{\mu\nu}$ and the vector β_μ are given as follows:

$$\begin{aligned} \alpha_{\mu\nu} &= \sum_{i=1}^{M} \frac{\partial I^{\rm mod}(q_i)}{\partial a_\mu} \frac{\partial I^{\rm mod}(q_i)}{\partial a_\nu} \Big/ \sigma_i^2, \\ \beta_\mu &= \sum_{i=1}^{M} \left[I^{\rm exp}(q_i) - I^{\rm mod}(q_i) \right] \frac{\partial I^{\rm mod}(q_i)}{\partial a_\mu} \Big/ \sigma_i^2. \end{aligned} \tag{19}$$

As required for any nonlinear procedure, a set of starting values has to be used. For the case where only the electron density profile is modeled, an initial square function where all parameters have the same value, chosen in such a way that the forward scattering value is reproduced, is good enough to ensure the convergence of the minimization procedure. For more complicated cases where both form factor and structure factor are optimized, some prior knowledge or manual adjustments are required. In all cases, because of the low information content in the scattering profiles and the fact that they describe a very small fraction of the reciprocal space, the solution of the inverse scattering problem (obtain real-space information from the reciprocal-space data) usually leads to ill posed problems, generating solutions with large oscillations that have no physical meaning. In order to overcome this problem, it is necessary to add model constraints, which lead to solutions that are more physically reasonable. One procedure is to add a stabilizing function ($N_{\rm c}$) to χ^2:

$$N_{\rm c} = \sum_{n=1}^{P-1} \left(a_{n+1} - a_n \right)^2, \quad \chi^2 + \lambda N_{\rm c} = \min, \tag{20}$$

where P is the number of parameters that are to be constrained ($P \leq J$). The modified normal equations are (Pedersen, 1992; Pedersen & Hamley, 1994*a*,*b*)

$$\sum_{\nu=1}^{P} \left(\alpha_{\mu\nu} + \lambda K_{\mu\nu} \right) \Delta a_\nu = -\left(\beta_\mu + \lambda L_\mu \right), \quad \mu = 1, 2, \ldots, P. \tag{21}$$

The matrix of components $K_{\mu\nu}$ is defined as

$$K = \begin{pmatrix} 1 & -1 & & & & & \\ -1 & 2 & -1 & & & 0 & \\ & -1 & 2 & -1 & & & \\ & & \cdots & \cdots & \cdots & & \\ & & & \cdots & \cdots & & \\ & 0 & & & -1 & 2 & -1 \\ & & & & & -1 & 1 \end{pmatrix}. \tag{22}$$

On the right hand of equation (21) L_μ is given by

$$L_\mu = \begin{cases} a_i - a_{i+1} & \text{for } i = 1, \\ 2a_i - a_{i+1} - a_{i-1} & \text{for } 2 \leq i \leq P-1, \\ a_i - a_{i-1} & \text{for } i = P. \end{cases} \tag{23}$$

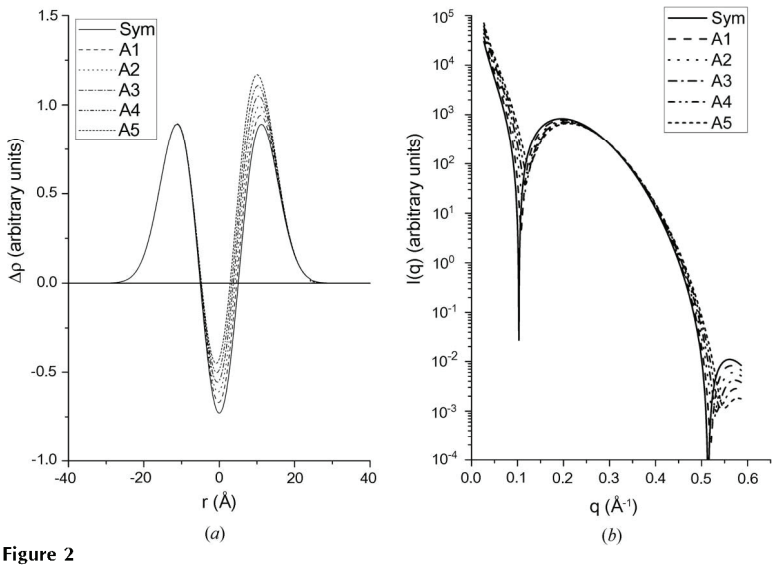

Figure 2
(*a*) An electron density profile constructed using five Gaussians. The profile is symmetric (Sym, solid curve) and becomes increasingly more asymmetric (A1 *etc.*). This asymmetry is obtained by an appropriate choice of Gaussian amplitudes. (*b*) Calculated intensity for the different profiles. Interestingly, the breaking of the symmetry induces significant changes in the form factor profile.

electronic reprint

In general only a subset of the fit parameters are used to describe the profile, and therefore just this subset have to be constrained. Therefore $P < J$ and the sum in equation (20) will run only over the parameters that are to be constrained. For example, when fitting the form factor and structure factor, only the amplitudes related to the form factor (electron density profile) have to be constrained, whereas the parameters in the structure factor or background factors should not.

The weight of the constraint relative to χ^2 is given by the parameter λ (also called Lagrange multiplier), which can be determined by the point-of-inflection method, as described by Glatter (1977). In this method, the optimum λ value ($\lambda_{\rm opt}$) is obtained using graphs of the dependency of $N_{\rm c}$, the first derivative of $N_{\rm c}$, the second derivative of $N_{\rm c}$ and the mean deviation as a function of λ. The parameter λ is generally varied over ten or more orders of magnitude with equidistant steps on a logarithm scale. In this so-called stability plot, the value given by a position where $N_{\rm c}$ is on a plateau, the first derivative is at a minimum and the second derivative is positive, while the mean deviation is still low, is the optimum Lagrange multiplier. By an appropriate scaling of all these quantities, it is possible to build a functional that can be minimized in order to give the most suitable $\lambda_{\rm opt}$:

$$\lambda_{\rm opt} = \min\left[\zeta_1\chi^2 + \zeta_2|(N_{\rm c})'| + \zeta_3|(N_{\rm c})''|\right], \qquad (24)$$

where ζ_1, ζ_1 and ζ_3 are normalization parameters and the prime and double prime denote the first and second derivatives of $N_{\rm c}$ against λ. The normalization is performed in such a way that the variables are restricted to the interval from 0 to 1. This minimization can be easily performed by fitting a parabolic function to the functional, and the minimum of the parabola provides the optimal value $\lambda_{\rm opt}$. This procedure can be implemented to give an automatic determination of $\lambda_{\rm opt}$. It has previously been successfully applied for indirect Fourier transformation of small-angle scattering from particulate systems (Oliveira *et al.*, 2009), providing a reliable determination of $\lambda_{\rm opt}$. Automatic determinations of the Lagrange multiplier in indirect Fourier transformation procedures had already been proposed by other authors (Semenyuk & Svergun, 1991; Hansen, 2000).

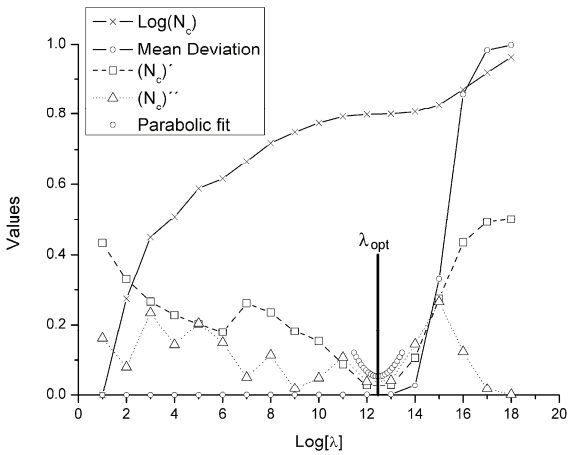

Figure 3
Automatic determination of the optimum Lagrange multiplier value. The information about the mean deviation value, the smoothness parameter $N_{\rm c}$ and its derivatives against λ are combined and adjusted by a parabolic fitting in order to provide the optimum value.

The constrained optimization method and the automated point-of-inflection procedure for determining the optimum Lagrange multiplier λ were implemented for the Gaussian deconvolution method, permitting the determination of the cross-section electron density profile through the simultaneous fitting of form factor and structure factor in systems of planar multilayers. An example of the automatic determination of the Lagrange multiplier is shown in Fig. 3. The applicability of this method will be demonstrated in the examples in the following.

7. Application

7.1. Hydration effects on lamellar multilayers

Lamellar phases were prepared by hydrating soya lecithin (Avanti Polar), used without any further purification, using Milli-Q water in desired proportions. The density of lecithin was considered as 1070 kg m^{-3} and samples of various volume fractions were prepared along the dilution line. The homogeneity of the samples was achieved by shaking and centrifugation processes. X-ray scattering was performed on 'powder' (randomly oriented lamellar) samples, placed in glass capillaries using the laboratory SAXS equipment (Bruker Nanostar) at the Institute of Physics of the University of São Paulo. The experiments were performed at room temperature (~295 K). X-ray experiments in wide-angle X-ray scattering geometry have shown that for this temperature all the samples are in the fluid lamellar phase, as confirmed by a broad band at $q = 1.5$ Å (not shown here). The beam diameter is about 1 mm at the sample position, which leads to smearing effects that have to be taken into account in the modeling procedure (peak broadening) (Pedersen *et al.*, 1990). In the standard SAXS setup ($0.01 < q < 0.38$ Å^{-1}), up to three Bragg reflections could be observed in the experimental scattering curves, as illustrated in Fig. 4 for varying lipid volume fractions (φ). In the figure, it can also be observed that the intensity of the second-order peak decreases with increasing lipid content, and it is completely absent for the more concentrated sample: $\varphi = 0.87$. This effect, however, cannot be ascribed to a decrease of smectic ordering, since the distance between the membranes is decreasing.

Using the analysis method presented above (with $n_{\rm max}$ fixed and chosen to be equal to 4) it was possible to obtain the form and structure factors that give the best fit to the scattering intensity, shown in Fig. 4 as dashed and dotted lines, respectively. It was observed that the local minimum of the form factor moved in q space with decreasing amounts of water,

electronic reprint

which reflects structural changes in the bilayer. Therefore it is not possible to fit the set of experimental curves by the same form factor. The changes become more evident for samples with high concentrations, where the minimum of the form factor approaches the second-order peak of the structure factor.

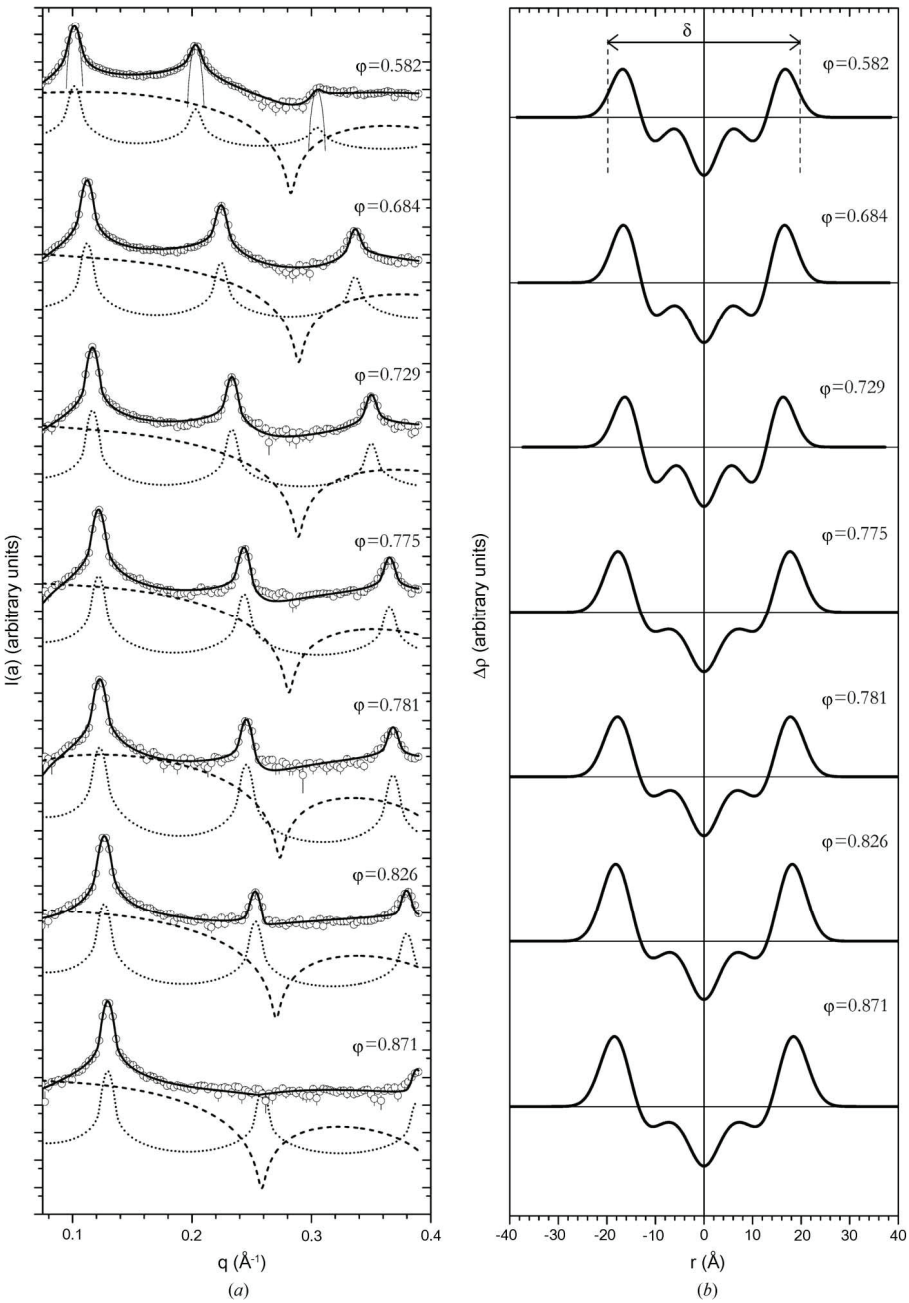

Figure 4
(*a*) Experimental scattering curves of the lamellar phase for varying lipid volume fraction (φ). The solid thin lines shown for $\varphi = 0.582$ represent the resolution functions at the three peak positions. The dashed lines are the form factor and the dotted lines are the structure factors obtained from the minimization procedure described in the text. The solid lines represent the final fitted scattering intensity. (*b*) Electron density profiles and definition of effective membrane thickness δ. In all cases the curves were shifted for clarity.

electronic reprint

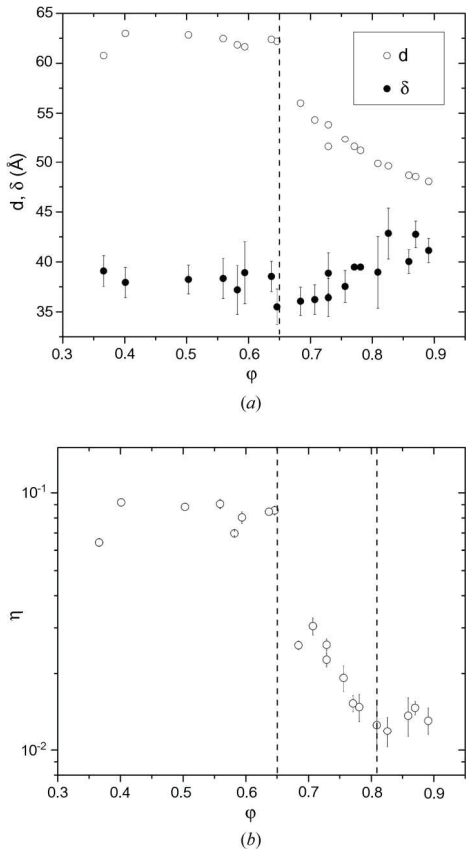

Figure 5
(*a*) Variation of lamellar period, *d*, and membrane effective thickness, δ, for varying lipid volume fractions. The dashed line indicates the separation of the two dilution regimes (see discussion in text). (*b*) Behavior of the Caillé parameter. The second dashed line was added to identify the confined regime.

In the diluted regime, for lipid volume fractions lower than 0.65, the lamellar phase has attained the hydration limit, with an interplanar distance of approximately 62 Å, and coexists with water in excess. In this regime, the lamellar period and membrane thickness do not change significantly (Fig. 5*a*) compared to the variations taking place for lipid volume fractions above 0.65. In this second regime the lamellar period decreases with dehydration, and the membrane effective thickness δ increases by approximately 6 Å. In the literature a smaller variation of bilayer thickness has been reported, about 2 Å (McIntosh *et al.*, 1987). However, the determination of this parameter was based either (i) on previous assumptions about the conformation of carbon chains and polar groups, which were made to obtain the electron contrast, or (ii) on pair correlation function calculations, which, in contrast to the present study, were not optimized during the fitting procedure (Nagle *et al.*, 1996; Zhang *et al.*, 1994; McIntosh *et al.*, 1987).

The behavior of the Caillé parameter, η, also indicates significant changes in membrane elasticity upon dehydration, as shown in Fig. 5(*b*). Three regimes can be identified: the first one, corresponding to the maximum hydrated lamellar phase, has a constant and high value of the Caillé parameter; the second regime has an exponential decrease of the Caillé parameter with increasing lipid volume fraction; finally, a third regime can be identified, corresponding to a strong confinement of bilayers and typical separation distances ($d - \delta$) smaller than ~8 Å. For such small separation distances, the hydration force (McIntosh *et al.*, 1987; Parsegian *et al.*, 1979) is dominant and responsible for a strong repulsion between bilayers, resulting in a constant value of the Caillé parameter of $\sim 10^{-2}$.

8. Conclusions

Although many studies of lecithin lamellar systems have been published in the literature, the application of the Gaussian deconvolution method to fit the experimental small-angle X-ray scattering data of lecithin lamellar phases has revealed new aspects of the structure and elastic properties of such systems. The determination of the membrane thickness and the Caillé parameter are of crucial importance for obtaining information on the interactions between the membranes. The results presented here showed that dehydration does not consist only of removing water from the space between the bilayers, but also affects the membrane structure with consequences on its elastic properties. The change of behavior of the Caillé parameter in the confined regime occurs when the water space between bilayers is reduced to a few layers of water molecules, which seems to play a major role for the elastic properties of the bilayers. The exponential dependence of the Caillé parameter on the lipid volume fraction shows that, because of membrane fluctuations, the interactions between the membranes in the dilution range are not dominated by steric interactions and that dipolar electrostatic interactions arising from water organization are probably also relevant.

These new aspects of the lecithin lamellar system could only be obtained by the full curve fitting and simultaneous optimization of the form factor and structure factor that is possible with the Gaussian deconvolution method. The obtained electron density profile can be subject to further analysis; for example, specific assumptions about the membrane components (Heberle *et al.*, 2012) would permit the determination of the individual contributions. The new results obtained for the simple lecithin system demonstrate the robustness and potential of this modeling approach, which can be applied to any mono- or multilayered systems.

CLPO and EAO were supported by FAPESP and INCT(FCx). ERTS was supported by CAPES and the EIFFEL Foundation. BBG was supported by CAPES.

References

Abramowitz, M. & Stegun, I. A. (1972). *Handbook of Mathematical Functions: With Formulas, Graphs and Mathematical Tables.* New York: Wiley.

electronic reprint

Brotons, G., Dubois, M., Belloni, L., Grillo, I., Narayanan, T. & Zemb, T. (2005). *J. Chem. Phys.* **123**, 024704.
Brzustowicz, M. R. & Brunger, A. T. (2005). *J. Appl. Cryst.* **38**, 126–131.
Caillé, A. (1972). *C. R. Acad. Sci. Ser. B*, **274**, 891–893.
Fritz, G. & Glatter, O. (2006). *J. Phys. Condens. Matter*, **18**, S2403–S2419.
Glatter, O. (1977). *J. Appl. Cryst.* **10**, 415–421.
Glatter, O. (1981). *J. Appl. Cryst.* **14**, 101–108.
Glatter, O. & Hainisch, B. (1984). *J. Appl. Cryst.* **17**, 435–441.
Glatter, O. & Kratky, O. (1982). *Small Angle X-ray Scattering.* London: Academic Press.
Hansen, S. (2000). *J. Appl. Cryst.* **33**, 1415–1421.
Heberle, F. A., Pan, J., Standaert, R. F., Drazba, P., Kucerka, N. & Katsaras, J. (2012). *Eur. Biophys. J.* **41**, 875–890.
Kotlarchyk, M. & Chen, S. H. (1983). *J. Chem. Phys.* **79**, 2461–2469.
Luzzati, V. & Tardieu, A. (1974). *Annu. Rev. Phys. Chem.* **25**, 79–94.
McIntosh, T. J., Magid, A. D. & Simon, S. A. (1987). *Biochemistry*, **26**, 7325–7332.
Moore, P. B. (1980). *J. Appl. Cryst.* **13**, 168–175.
Nagle, J. F. & Wiener, M. C. (1989). *Biophys. J.* **55**, 309–313.
Nagle, J. F., Zhang, R. T., Tristram-Nagle, S., Sun, W., Petrache, H. I. & Suter, R. M. (1996). *Biophys. J.* **70**, 1419–1431.
Nallet, F., Laversanne, R. & Roux, D. (1993). *J. Phys. II*, **3**, 487–502.
Oliveira, C. L., Behrens, M. A., Pedersen, J. S., Erlacher, K., Otzen, D. & Pedersen, J. S. (2009). *J. Mol. Biol.* **387**, 147–161.
Pabst, G., Rappolt, M., Amenitsch, H. & Laggner, P. (2000*a*). *Phys. Rev. E*, **62**, 4000–4009.
Pabst, G., Rappolt, M. P., Amenitsch, H. & Laggner, P. (2000*b*). *Biophys. J.* **78**, 21A21A.
Pape, E. H. & Kreutz, W. (1978). *J. Appl. Cryst.* **11**, 421–429.
Parsegian, V. A., Fuller, N. & Rand, R. P. (1979). *Proc. Natl Acad. Sci. USA*, **76**, 2750–2754.
Pedersen, J. S. (1992). *J. Appl. Cryst.* **25**, 129–145.
Pedersen, J. S. (1997). *Adv. Colloid Interface Sci.* **70**, 171–210.
Pedersen, J. S. & Hamley, I. W. (1994*a*). *J. Appl. Cryst.* **27**, 36–49.
Pedersen, J. S. & Hamley, I. W. (1994*b*). *Physica B*, **198**, 16–23.
Pedersen, J. S., Posselt, D. & Mortensen, K. (1990). *J. Appl. Cryst.* **23**, 321–333.
Petrache, H. I., Gouliaev, N., Tristram-Nagle, S., Zhang, R. T., Suter, R. M. & Nagle, J. F. (1998). *Phys. Rev. E*, **57**, 7014–7024.
Semenyuk, A. V. & Svergun, D. I. (1991). *J. Appl. Cryst.* **24**, 537–540.
Worthington, C. R. (1969). *Biophys. J.* **9**, 222–234.
Zhang, R. T., Suter, R. M. & Nagle, J. F. (1994). *Phys. Rev. E*, **50**, 5047–5060.

electronic reprint

Langmuir

Article

pubs.acs.org/Langmuir

Steric-Induced Effects on Stabilizing a Lamellar Structure

Barbara B. Gerbelli,[†] Rafael L. Rubim,[†] Emerson R. Silva,[†,§] Frédéric Nallet,[‡] Laurence Navailles,[‡] Cristiano L. P. Oliveira,[†] and Elisabeth A. de Oliveira*[,†]

[†]Instituto de Física, Universidade de São Paulo, Caixa Postal 66318, 05314-970 São Paulo, Brazil

[‡]Université de Bordeaux, Centre de Recherche Paul-Pascal − CNRS, 115 avenue du Docteur-Schweitzer, F-33600 Pessac, France

ABSTRACT: We investigate the behavior of multilamellar phases composed of lecithin and a commercial cosurfactant (Simusol), which is a mixture of ethoxylated fatty acids. Using X-ray scattering and a new procedure to fit the data, relevant parameters characterizing the lamellar structure were determined as a function of membrane composition, varying from 100% of lecithin to 100% of Simulsol. Scattering data illustrating the swelling of the lamellae for different amounts of cosurfactant are presented with the respective behavior of the Caillé parameter. With this experimental approach, we show that the incorporation of ethoxy brushes onto the lipid surface enhances repulsive interactions arising from membrane fluctuations and changes the interactions at the interface between bilayers.

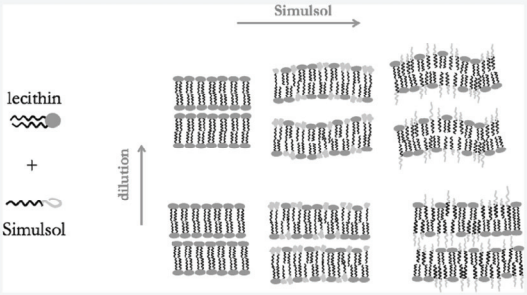

■ INTRODUCTION

Lamellar systems composed of regularly stacked bilayers have been used to investigate several biological processes,[1−4] providing important knowledge on fundamental aspects such as interactions between membranes,[5−8] and also on many biotechnological applications.[9−12] The structure is periodic only across the direction perpendicular to the membrane surface whereas in the other two dimensions the bilayers behave as a fluid. The fluidity of the membranes comes either from the orientational and translational disordering of surfactant molecules or from the flexibility of hydrocarbon chains.[13−15] Thermal fluctuations in membranes give rise to repulsive interactions as a result of the mutual steric hindrance when they are in close proximity. Such interaction plays a fundamental role for stabilizing the lamellar structure since its range and strength competes with van der Waals attraction for flexible enough bilayers.[16−19]

X-ray and neutron scattering techniques have proved to be powerful tools to obtain a detailed picture of the lamellar structure.[20−28] Thermal fluctuations deeply affect the (quasi) long-range positional order, resulting in an enhanced diffuse scattering. The appropriate analysis of the scattering data brings information not only about the structure of the lamellar phase but also on its elastic properties. In this context, a major variable is the so-called Caillé parameter, which carries coupled information on both the bending constant of membranes and the compression modulus of the stack.[29]

In previous reports, some of us demonstrated the ability of mixed lecithin/Simulsol phase to host DNA fragments and form lipoplexes from neutral lipids.[30−34] Our findings have shown that steric forces in lamellar system play a major role for complexation with DNA and hydration of the system (and consequently, its smectic periodicity) is able to drive confinement of nucleotides in-between bilayers. The confinement induces a rich polymorphism of supramolecular ordering of DNA-double-chains embedded in lamellar stacks. In the current work, we further investigate on steric interplay in these lecithin/Simulsol phases by using a recently developed model to analyze X-ray scattering data.[23]

We investigate the stability of lamellar structures, when the range and strength of steric repulsive interactions are modulated by varying the amount of (short) amphiphilic polymers playing the role of a cosurfactant grafted at the membrane surface. The experimental approach consists in a systematic variation of the membrane composition, by adding the cosurfactant to the bilayers composed, initially, of lecithin, a common lipid. The cosurfactant, commercially known as Simusol, is a mixture of ethoxylated fatty acids with, typically, about 10 ethoxy groups. Because of its nonionic nature, the overall charge of the membrane remains neutral since lecithin is a zwitterionic molecule. The incorporation of single chain molecules to the bilayer is expected to increase its flexibility; however a second effect related to the hydrophilic part of the cosurfactant molecules is found: an extra repulsion of steric origin between membranes with an extended range depending on both grafting density and chain length, arises because water at room temperature is a good solvent for the ethoxylated part of the cosurfactant. Different domains of interactions between membranes can be experimentally accessed, by varying two experimental parameters. The first one is the hydration of the

Received: August 6, 2013
Revised: October 11, 2013
Published: October 15, 2013

ACS Publications © 2013 American Chemical Society

lamellar phase, which affects the distance between bilayers. The second is the membrane composition with consequences on both the flexibility and the range and strength of the extra steric repulsions.[28,35]

We determine relevant parameters of the lamellar structure by varying the membrane composition from 100% of lecithin to 100% of Simulsol and scanning a dilution line for each composition. In the analysis of X-ray scattering data, the electron density profile is modeled by a set of symmetrical Gaussian functions.[23] The fitting is performed directly to the scattered intensity, using a partial constrained least-squares routine, which allows the simultaneous determination of the form and structure factors and several other parameters that describe the model, such as bilayer thickness and Caillé parameter. The systematic variation of composition combined with the analysis method reveals a new regime of intermembrane interactions that is not accessible for membranes composed of pure lecithin.

■ THEORETICAL BACKGROUND

The stability of lamellar phases is usually described as the interplay between attractive van der Waals interactions and repulsive forces that can be of different natures.[16−19,36−38] Experimentally, for highly dehydrated compositions where bilayers are almost in contact a strong short-range repulsive interaction has been observed, which is known as hydration force.[39,40] A second repulsive mechanism, conceptually a subtle consequence of the previous one, was proposed by Helfrich,[16] considering the fluid aspects of the membranes, which can present undulations. It gives rise to a repulsive force that for flexible enough bilayers is comparable in order of magnitude and range to the (attractive) van der Waals forces. One of the simplest possible approaches is to assume that the various interaction potentials can be added. In this case, the free energy density of a multilayered structure composed of noncharged flexible bilayers could be tentatively written as[36,41]

$$V = V_{\mathrm{hyd}} + V_{\mathrm{vdW}} + V_{\mathrm{und}} \tag{1}$$

with V_{hyd}, V_{vdW}, and V_{und} referring to hydration, van der Waals, and undulation forces, respectively.

When bilayers are brought closer together, there is a loss of configurational entropy associated to bilayer undulations. This is accompanied by an increase in free energy and, according to Helfrich, this contribution is expressed as[16]

$$V_{\mathrm{und}} = \frac{3\pi^2}{128}\left(\frac{k_{\mathrm{B}}T}{\kappa a^2}\right) \tag{2}$$

where κ is the bending rigidity of the bilayer, a is the membrane separation, and T is the temperature. The free energy density can then be written as

$$V = -\frac{H}{12\pi}\left[\frac{1}{a^2} - \frac{2}{(a+\delta_{\mathrm{M}})^2} + \frac{1}{(a+2\delta_{\mathrm{M}})^2}\right] + V_{\mathrm{hyd}}e^{-a/\lambda_{\mathrm{H}}} + \frac{3\pi^2}{128}\left(\frac{k_{\mathrm{B}}T}{\kappa a^2}\right) \tag{3}$$

with H equal to the Hamaker constant of the bilayer—solvent system; δ_{M} the membrane thickness, and λ_{H} is the decaying length of the hydration force. Other attempts to describe theoretically the potential between membranes have been done, introducing modifications in the above expressions. Such trials have resulted in predictions about the stability of the lamellar phase and the nature of the transition from bounded to nonbounded states, depending on the strength of interactions.[17−19,42]

The membrane fluidity has been recognized as an important parameter driving long-range repulsive forces and displacing the minimum energy to larger values of membrane separation distance.[17,43−45] This problem has been theoretically[17−19,43,46] and experimentally[28,43,44,47,48] addressed using different approaches. In literature, there are experimental works investigating on the dependence of bending rigidity upon membrane composition and salt content in aqueous solutions.[35,47−51] More recently, computational simulations have been conducted to investigate the molecular origin of bending rigidity.[52−55]

From the experimental point of view, information about elastic properties of lamellar phases can be obtained using X-ray scattering techniques. Since thermal fluctuations destroy long-range positional order, Bragg peaks become broader and the intensity of high order peaks decays very fast. As above-mentioned, the analysis of full-range scattered intensities provides detailed information, not only about the global structure but also on thermal fluctuations.[20−28] The Caillé parameter describes the decaying of elastic correlations and is given by:[29]

$$\eta = \frac{q_0^2 k_{\mathrm{B}}T}{8\pi\sqrt{BK}} \tag{4}$$

where K and B are the curvature and compression modulus of the lamellar phase, respectively, and q_0 is the wave vector of the first-order Bragg peak.

Global analysis of X-ray scattering data has been used for investigating several lamellar systems dominated by undulation forces.[26,44] It has been shown that the experimental values of Caillé parameter then follow a universal expression given by

$$\eta = \frac{4}{3}\left(1 - \frac{\delta_{\mathrm{M}}}{D}\right)^2 \tag{5}$$

providing experimental evidence of the expression derived by Helfrich for the undulation force. In this expression, D is the smectic period, equal to $2\pi/q_0$, related to the previously defined geometric parameters by $D = \delta_{\mathrm{M}} + a$.

■ MATERIALS AND METHODS

The mixture of lipids was prepared by cosolubilizing in cyclohexane soya lecithin (Avanti Polar) and Simusol 2599 PHA (Seppic) in suitable proportions. These products (initially chosen[30−32,34] despite their complex analytical compositions because they are pharmaceutical excipients complying with the European Pharmacopoeia) were used without further purification and the solvent was evaporated in a desiccator. The major constituent of soya lecithin is dilinoleoylphosphatidylcholine and its specific mass is 1.01 g/cm^3. The major constituent of the hydrophobic part of Simulsol is oleic acid (∼72%) with also palmitic (∼11%) and stearic (3%) acid chains in noticeable amounts. The ethoxylated chain consists of polyethylene glycol (PEG) with 10 monomers on average but the longest chains may contain up to 20 monomers.[56] The average length estimated for the polymer chain is 3−4 nm fully extended but longer chains up to 7 nm can also be present. The specific mass is 1.02 g/cm^3.

The membrane composition is expressed in terms of the percentage in mass of Simulsol incorporated to lecithin membranes. The lamellar phase was prepared by adding the lipid mixture and distilled water (Milli-Q) in proper quantities. The samples were submitted to shake and centrifugation processes until homogeneity was achieved. The composition of the lamellar phase is expressed in terms of the total lipid volume fraction (φ_{lip}), that is, lecithin plus Simulsol. The

membrane composition was varied from 100% of lecithin to 100% of Simulsol and for each composition the lipid volume fraction was varied, scanning the dilution line.

X-ray scattering experiments were performed in samples placed in glass capillaries using a laboratory equipment (Nanostar-Bruker) with resolution $\Delta q = 0.334\ \mathrm{nm}^{-1}$, is related to the beam size and detector resolution that defines the minimum distance that can be resolved in the reciprocal space by the experimental setup. This resolution also creates a peak broadening which was taken into account in the modeling procedures. The experimental data were expressed as a function of the scattering vector **q**, which is the reciprocal space momentum transfer modulus. This vector is given by $\mathbf{q} = (4\pi \sin \theta)/\lambda$, where λ is the radiation wavelength (0.154 nm) and 2θ is the scattering angle. In the standard configuration where $0.1\ \mathrm{nm}^{-1} < \mathbf{q} < 3.5\ \mathrm{nm}^{-1}$, up to three Bragg reflections could be observed in the concentrated regime. Experiments at higher angles with **q** values in the range 0.5−30 nm^{-1} were also performed aiming to check the nature of the lamellar phase. For some samples, experiments were performed at the Soleil Synchrotron facility, SWING beamline, with beam energy of 12 keV (λ = 0.103 nm), $\Delta\mathbf{q} = 0.038\ \mathrm{nm}^{-1}$, and accessible **q** vectors in the range from 0.3 to 17.45 nm^{-1}. The lower the value of the $\Delta\mathbf{q}$ (higher resolution in **q** space), the sharper the Bragg peaks will appear on the scattering data. All scattering experiments were performed at room temperature (∼22 °C).

As a complementary technique, polarizing microscopy observations were carried out to verify whether the samples presented the typical texture of lamellar phases.

■ EXPERIMENTAL RESULTS

The experimental scattering data were analyzed with a recently published modeling procedure,[23] where the electron density profile is described by a set of Gaussian functions and the fitting is performed directly on the scattered intensity. With this modeling method, the parameters describing the form and structure factors of the system are optimized simultaneously. The quality of the fitting is quite good (except for very low angle region) as it is shown in Figure 1 for scattering data obtained from both a laboratory equipment and synchrotron source. It is important to note that since resolution effects are included in the fitting procedure the full **q** range of the experimental data can be described for data obtained in equipments with different resolution values. The analysis method was therefore applied to the whole set of experimental data.

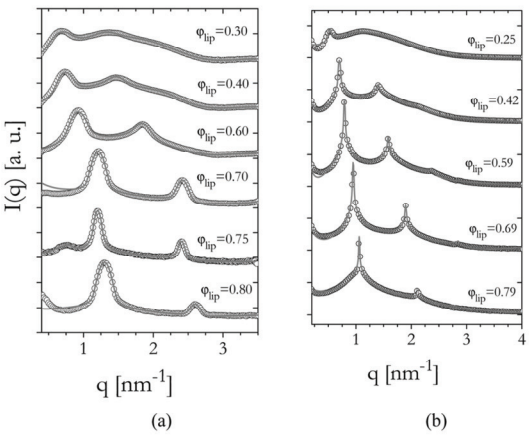

Figure 1. Scattering experimental data (symbols) and the respective theoretical fits (solid lines) for two membrane compositions (Simulsol mass fraction): 30% (a) and 90% (b). In (b), the scattering curves were obtained in a Synchrotron line.

In Figure 1, it is possible to note that as the phase is hydrated the peaks become broader and the second order Bragg reflection disappears. The scattering curves are indexed to a single smectic phase except in a narrow band where we assume that two lamellar phases coexist. The biphasic domain occurs for lipid volume fraction around 0.7 with width $\Delta\varphi_{\mathrm{lip}} \approx 0.05$ and Simulsol content between 10 and 80% in mass. An example of coexisting phases is shown in Figure 1a for $\varphi_{\mathrm{lip}} = 0.75$ with the respective fitting curve. The assumption of two coexisting lamellar structures is supported by optical observations in polarizing microscopy (data not shown). One phase is clearly similar to the one present at similar lipid volume fractions and the coexisting phase could be described as a phase with larger periodicities. It might be related to a phase of pure Simulsol. Since the scattered intensity from one of the lamellar phases is much lower than the other, one can conclude that this phase corresponds to a small fraction of the system as well as presenting a low number of correlated planes. In the following, the analysis of scattering curves concerning the data obtained for the single lamellar phase domain will be presented only.

A broad peak at $\mathbf{q} \sim 14\ \mathrm{nm}^{-1}$, characteristic of a fluid lamellar phase, was observed for wide-angle experiments (WAXS data not shown), in the whole dilution range and membrane compositions explored in this work.

The effect of the cosurfactant amount on the swelling behavior of the phase is presented in Figure 2a, where data is obtained from the

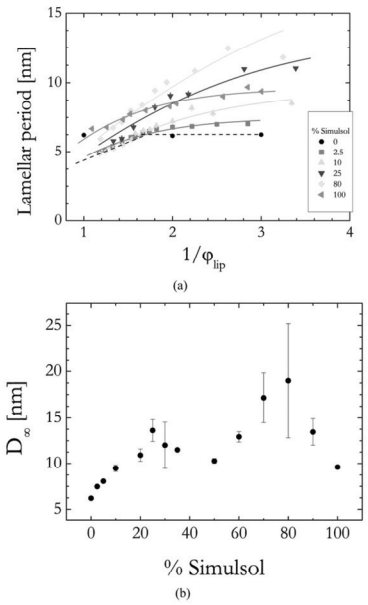

Figure 2. (a) Swelling behavior of the lamellar phase for different amounts of cosurfactant incorporated to the lamellar phase. The solid lines are fits of eq 6 to experimental data. The dashed line is a guide to the eyes and illustrates the swelling regime and the dilution limit of the pure lecithin lamellar phase. (b) Asymptotic lamellar period D_∞ obtained by extrapolating $1/\varphi_{\mathrm{lip}} \rightarrow \infty$.

structure factor parameter $\mathbf{q}_0$. It can be noted that lamellar stacks composed of pure lecithin attain a maximum dilution limit with smectic periodicity equal to 6.3 nm. On the other hand, lamellae containing cosurfactant are able to incorporate larger amounts of water, attaining higher periodicities around 12 nm for 80% Simulsol (Figure 2a). The evolution of the smectic step as a function of the inverse lipid volume fraction cannot be described with the simple dilution law, namely $D = \delta_M/\varphi_{\mathrm{lip}}$, which is encountered in many lamellar systems. This simple law is derived from geometric

membrane composition was varied from 100% of lecithin to 100% of Simulsol and for each composition the lipid volume fraction was varied, scanning the dilution line.

X-ray scattering experiments were performed in samples placed in glass capillaries using a laboratory equipment (Nanostar-Bruker) with resolution $\Delta q = 0.334\ \mathrm{nm}^{-1}$, is related to the beam size and detector resolution that defines the minimum distance that can be resolved in the reciprocal space by the experimental setup. This resolution also creates a peak broadening which was taken into account in the modeling procedures. The experimental data were expressed as a function of the scattering vector $\mathbf{q}$, which is the reciprocal space momentum transfer modulus. This vector is given by $\mathbf{q} = (4\pi \sin \theta)/\lambda$, where λ is the radiation wavelength (0.154 nm) and 2θ is the scattering angle. In the standard configuration where $0.1\ \mathrm{nm}^{-1} < \mathbf{q} < 3.5\ \mathrm{nm}^{-1}$, up to three Bragg reflections could be observed in the concentrated regime. Experiments at higher angles with $\mathbf{q}$ values in the range 0.5−30 nm^{-1} were also performed aiming to check the nature of the lamellar phase. For some samples, experiments were performed at the Soleil Synchrotron facility, SWING beamline, with beam energy of 12 keV ($\lambda = 0.103$ nm), $\Delta\mathbf{q} = 0.038\ \mathrm{nm}^{-1}$, and accessible $\mathbf{q}$ vectors in the range from 0.3 to 17.45 nm^{-1}. The lower the value of the $\Delta\mathbf{q}$ (higher resolution in $\mathbf{q}$ space), the sharper the Bragg peaks will appear on the scattering data. All scattering experiments were performed at room temperature (∼22 °C).

As a complementary technique, polarizing microscopy observations were carried out to verify whether the samples presented the typical texture of lamellar phases.

■ EXPERIMENTAL RESULTS

The experimental scattering data were analyzed with a recently published modeling procedure,[23] where the electron density profile is described by a set of Gaussian functions and the fitting is performed directly on the scattered intensity. With this modeling method, the parameters describing the form and structure factors of the system are optimized simultaneously. The quality of the fitting is quite good (except for very low angle region) as it is shown in Figure 1 for scattering data obtained from both a laboratory equipment and synchrotron source. It is important to note that since resolution effects are included in the fitting procedure the full $\mathbf{q}$ range of the experimental data can be described for data obtained in equipments with different resolution values. The analysis method was therefore applied to the whole set of experimental data.

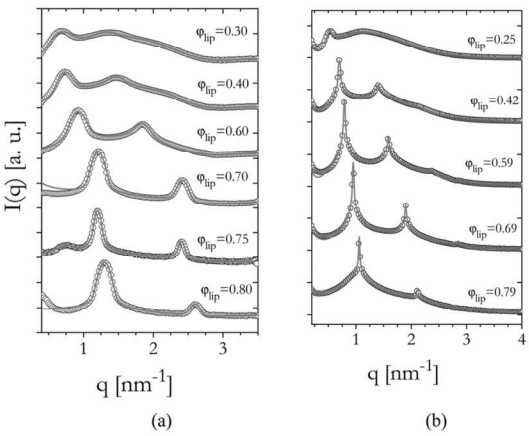

Figure 1. Scattering experimental data (symbols) and the respective theoretical fits (solid lines) for two membrane compositions (Simulsol mass fraction): 30% (a) and 90% (b). In (b), the scattering curves were obtained in a Synchrotron line.

In Figure 1, it is possible to note that as the phase is hydrated the peaks become broader and the second order Bragg reflection disappears. The scattering curves are indexed to a single smectic phase except in a narrow band where we assume that two lamellar phases coexist. The biphasic domain occurs for lipid volume fraction around 0.7 with width $\Delta\varphi_{\mathrm{lip}} \approx 0.05$ and Simulsol content between 10 and 80% in mass. An example of coexisting phases is shown in Figure 1a for $\varphi_{\mathrm{lip}} = 0.75$ with the respective fitting curve. The assumption of two coexisting lamellar structures is supported by optical observations in polarizing microscopy (data not shown). One phase is clearly similar to the one present at similar lipid volume fractions and the coexisting phase could be described as a phase with larger periodicities. It might be related to a phase of pure Simulsol. Since the scattered intensity from one of the lamellar phases is much lower than the other, one can conclude that this phase corresponds to a small fraction of the system as well as presenting a low number of correlated planes. In the following, the analysis of scattering curves concerning the data obtained for the single lamellar phase domain will be presented only.

A broad peak at $\mathbf{q} \sim 14\ \mathrm{nm}^{-1}$, characteristic of a fluid lamellar phase, was observed for wide-angle experiments (WAXS data not shown), in the whole dilution range and membrane compositions explored in this work.

The effect of the cosurfactant amount on the swelling behavior of the phase is presented in Figure 2a, where data is obtained from the

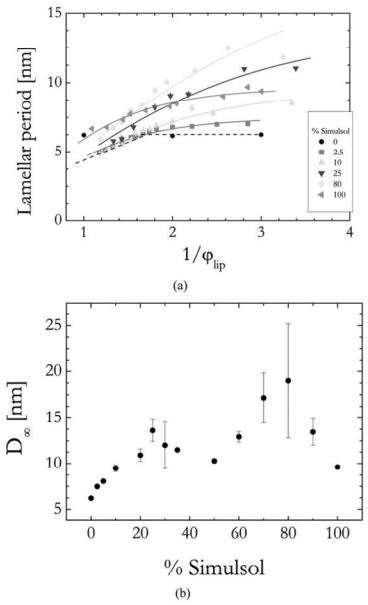

Figure 2. (a) Swelling behavior of the lamellar phase for different amounts of cosurfactant incorporated to the lamellar phase. The solid lines are fits of eq 6 to experimental data. The dashed line is a guide to the eyes and illustrates the swelling regime and the dilution limit of the pure lecithin lamellar phase. (b) Asymptotic lamellar period D_∞ obtained by extrapolating $1/\varphi_{\mathrm{lip}} \rightarrow \infty$.

structure factor parameter $\mathbf{q}_0$. It can be noted that lamellar stacks composed of pure lecithin attain a maximum dilution limit with smectic periodicity equal to 6.3 nm. On the other hand, lamellae containing cosurfactant are able to incorporate larger amounts of water, attaining higher periodicities around 12 nm for 80% Simulsol (Figure 2a). The evolution of the smectic step as a function of the inverse lipid volume fraction cannot be described with the simple dilution law, namely $D = \delta_M/\varphi_{\mathrm{lip}}$, which is encountered in many lamellar systems. This simple law is derived from geometric

considerations where the area per lipid molecule at the bilayer−solvent interface is constant, and the bilayers are rigid enough to remain flat. The observed departure from the geometric swelling law being from below, it cannot be ascribed here to bilayer undulations, by the way, a rather small effect.[49,57−60] It is thus the consequence of a significant increase of the (effective) area per lipid/cosurfactant molecule as dilution proceeds, itself presumably resulting from conformational changes (or perhaps even transitions, when the lamellar−lamellar phase separation is encountered at low hydration for most membrane compositions for instance) of the Simulsol ethoxy heads, as argued below from a different perspective. As the lamellar phase is hydrated, the period tends to a limiting value and an attempt of describing the behavior of D as a function of $1/\varphi_{lip}$ can be done with the help of the parametric function

$$D = D_\infty \tanh\left[\frac{\delta_M}{D_\infty \varphi_{lip}}\right] \quad (6)$$

where D_∞ is the maximum lamellar period extrapolated for $1/\varphi_{lip} \rightarrow \infty$, that is, pure water, and δ_M is a parameter that can be interpreted as the membrane thickness in the highly dehydrated limit. As shown in Figure 2a, this phenomenological expression provides a reasonable fit to the swelling data, even though the parameter D_∞ is obviously not precisely defined when the departure from the simple swelling law is small—80% Simulsol being the most questionable sample in this respect.

Larger limiting lamellar periods can be obtained with the incorporation of cosurfactant to the lecithin lamellar phase with D_∞ values around 15−18 nm for certain compositions (Figure 2b). Nevertheless, the dependence of D_∞ on the amount of Simulsol does not follow a simple monotonic function, and 50% visually marks a kind of boundary between two otherwise qualitatively similar domains, one rich in lecithin and the other rich in Simulsol.

The evolution along dilution lines of the structure factor-related Caillé parameter reveals a conspicuous behavior (Figure 3). The presence of cosurfactant in the membrane introduces significant changes in elastic fluctuations and two distinct hydration regimes can be observed, apparently universal and independent of the amount of cosurfactant incorporated to the bilayer. Two roughly exponential dependences on hydration are observed with a change taking place for a lamellar period of approximately 6.5 nm. Taking δ_M = 4 nm as the typical value that results from fits of eq 6 to our data, such a distance corresponds to a separation between membranes equal to 2.5 nm, a value comparable to the extended length of the polymer chains of Simulsol molecules, consisting on average of 10 ethylene glycol monomers.

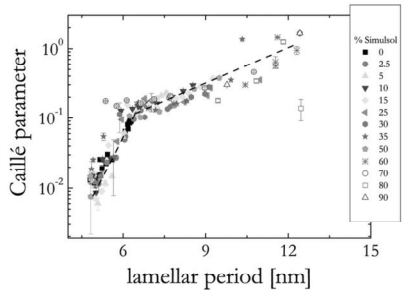

Figure 3. Caillé parameters obtained from fits to the scattering curves, varying the amount of cosurfactant incorporated to the lipid membranes and the hydration. The two dashed lines are only guides to the eyes.

In the more hydrated regime, the Caillé parameter attains values close to 1, usually characterizing very flexible membranes. Considering the lamellar period in the range of 10−12 nm, the distance between bilayers is typically 2.5−3 times larger than the membrane thickness and the membranes should be weakly interacting. The behavior of the Caillé parameter shows that in fact the incorporation of single chain molecules into the lecithin bilayers contributes for increasing membrane flexibility, opening a new regime of interactions that was not present in the lamellar phase composed of lecithin only.

Another remarkable effect, related to cosurfactant polymer chains at the interfaces of bilayers, has emerged from our investigations. It is revealed by our form factor model description of the scattering intensity and can be noticed by comparing the electronic contrast of the bilayers, as shown in Figure 4a, for increasing amounts of cosurfactant at constant lamellar period, $D \approx 8$ nm. The contrast of the polar region becomes less pronounced and broader as the amount of Simulsol in the membrane increases. The membrane thickness, not to be confused with parameter δ_M in eq 6, being obtained from the electronic profiles considering the distance between the points where the contrast falls to the half of the maximum value,[23] its values are plotted in the inset of Figure 4a. The increase in membrane thickness with Simulsol content also appears as a two-step effect.

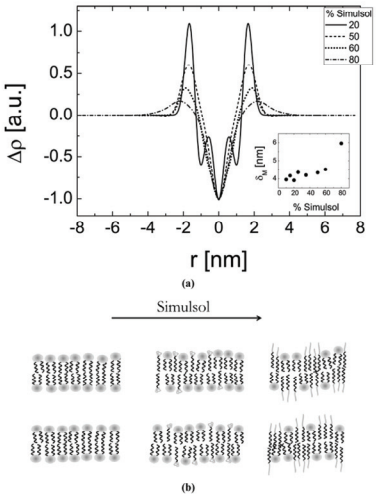

Figure 4. (a) Electronic contrast obtained from the fitting procedure for a lamellar period approximately equal to 8 nm and varying amount of Simulsol. In the figure, r = 0 represents the center of one bilayer, and the definition of negative and positive contrasts is taken by using the electron density of water as reference. Inset: Effect of the cosurfactant on the membrane thickness, as it results from the electron density profile. (b) Schematic representation at maximum swelling of lipid bilayers initially composed of lecithin with incorporation of Simulsol molecules.

We tentatively propose that a kind of transition from mushroom to brush conformation of the ethoxy chains takes place for increasing density of Simulsol grafted on the bilayer surface,[57] as shown schematically in Figure 4b. The experimental data indeed suggest that such a transition occurs when the Simulsol amount in the membrane grows from 40 to 60%; as it appears in Figure 4a, the contrast of the polar region becomes diffuse in this range of grafting density with a significant and rather sharp increase of about 2 nm in the effective membrane thickness (inset in Figure 4a) mainly due to the hydrophilic part of the chains.

■ DISCUSSION AND CONCLUSIONS

The results presented in this paper show that the systematic variation of the membrane composition and hydration changes both structural and elastic properties of the lamellar phase. The

incorporation of cosurfactant modifies the swelling properties, as well as the dilution limit, of the lamellar phase, an effect already reported in the literature[35,44] It also opens a new regime of interactions between bilayers that was not present in the lamellar phase composed of lecithin only and that may explain the stability of complexes where DNA is incorporated into the lamellar structure.[30−32,34]

We have explored a wide range of membrane compositions and hydrations and we observed that the behavior of the Caillé parameter is apparently well described by a master curve, independent of the amount of cosurfactant, as a function of hydration. At low water amounts, a first regime can be identified, characterized by a strong longitudinal (i.e., along the stacking axis) confinement with the typical separation distances comparable to the length of the polymer chains. Although the bilayers are expected to become more flexible with the incorporation of ethoxylated fatty acids, the longitudinal confinement of the hydrophilic end of the cosurfactant severely restricts undulation fluctuations and elastic properties are therefore still dominated by the contribution of short-range interactions: In this limit, lateral confinement effects of the hydrophilic part of Simulsol (mushroom-to-brush transition for instance) appear irrelevant. In the second regime, the Caillé parameter increases slower than in the first one and the values may become as large as 1, indicating very flexible and rather weakly interacting bilayers. Since hydration is now significant, lateral confinement effects presumably come into play. It may then seem paradoxical that they do not affect the Caillé parameter, but the universality of the Helfrich mechanism should be remembered. Indeed, membrane flexibility does not enter eq 5. The cancellation between an increased bending modulus K and a decreased compression modulus B in the product KB that enters eq 4 apparently still operates, even though the Helfrich mechanism does obviously not dominate interbilayer interactions for our dilute lecithin-Simulsol systems.

Lateral confinement effects are rather directly observed in electron density profiles for Simulsol-rich bilayers and water content large enough. We believe that they are also indirectly suggested by the surprising shape of Figure 2b, because a Simulsol-rich behavior can be distinguished from a lecithin-rich one when the cosurfactant content reaches the value where electron density profiles start to spread. The nonmonotonous evolution of the dilution limit in each region could then be associated to the mushroom-to-brush transition through the delicate interplay between steric (repulsive) and van der Waals (attractive) interactions driving the unbinding transition[19,42,43] but the actual relevance of this qualitative argument remains to be firmly established. Work is currently in progress in this respect.

In summary, the incorporation of ethoxylated cosurfacant provides a tool for controlling the intensity of repulsive interactions between bilayers. Whereas the hydrophobic part of the molecules modifies the membrane flexibility, the density and the length of polymer chains allows a fine control for modulating the interactions between membranes and the regime of fluctuations. We believe that such mechanism could open an interesting experimental window to explore interfacial phenomena in flexible membranes found in biological structures.

■ AUTHOR INFORMATION

Present Address

[§](E.R.S.) Universidade Federal do ABC, Centro de Ciências Naturais e Humanas, Av. Dos Estados 5001,09210−580, Santo André, Brazil.

Author Contributions

The manuscript was written through contributions of all authors. All authors have given approval to the final version of the manuscript.

Funding

FAPESP-2011/22394, FAPESP 2011/16149−8, INCT of Complex Fluids

Notes

The authors declare no competing financial interest.

■ ACKNOWLEDGMENTS

To CNPQ, FAPESP, CAPES, INCT/CNPQ, Egide. Soleil synchrotron kindly allocated beam time on the SWING station, proposal number 20101084.

■ REFERENCES

(1) Siddhanta, A.; Shields, D. Secretory Vesicle Budding from the Trans Golgi Network is Mediated by Phosphatidic Acid Levels. *J. Biol. Chem.* **1998**, *273*, 17995−17998.

(2) Sackmann, E.; Bruinsma, R. F. Cell adhesion as wetting transition. *ChemPhysChem* **2002**, *3*, 262−269.

(3) Sackmann, E. Thermo-elasticity and adhesion as regulators of cell membrane architecture and function. *J. Phys.: Condens. Matter* **2006**, *18*, R785−R825.

(4) Anderson, R. W. The caveolae membrane system. *Annu. Rev. Biochem.* **1998**, *67*, 199−225.

(5) Israelachvili, J.; Wennerström, H. Role of hydration and water structure in biological and colloidal interactions. *Nature* **1996**, *379*, 219−225.

(6) Tayebi, L.; Ma, Y.; Vashaee, D.; Chen, S.; Sinha, S. K.; Parikh, A. N. Long-range interlayer alignment of intralayer domains in stacked lipid bilayers. *Nat. Mater.* **2012**, *11*, 1074−1080.

(7) Winter, R.; Jeworrek, C. Effect of pressure on membranes. *Soft Matter* **2009**, *5*, 3157−3173.

(8) Szekely, P.; Asor, R.; Dvir, T.; Szekely, O.; Raviv, U. Effect of Temperature on the Interactions between Dipolar Membranes. *J. Phys. Chem. B* **2012**, *116*, 3519−3524.

(9) Malmsten, M. Soft drug delivery systems. *Soft Matter* **2006**, *2*, 760−769.

(10) Koynova, R.; Tenchov, B. Cationic phospholipids: structure-transfection activity relationships. *Soft Matter* **2009**, *5*, 3187−3200.

(11) Puri, A.; Blumenthal, R. Polymeric Lipid Assemblies as Novel Theranostic Tools. *Acc. Chem. Res.* **2011**, *44*, 1071−1079.

(12) Chang, D. P.; Jankunec, M.; Barauskas, J.; Tiberg, F.; Nylander, T. Adsorption of Lipid Liquid Crystalline Nanoparticles: Effects of Particle Composition, Internal Structure, and Phase Behavior. *Langmuir* **2012**, *28*, 10688−10696.

(13) Fernandez-Puente, L.; Bivas, I.; Mitov, M. D.; Méléard, P. Temperature and chain-length effects on bending elasticity of phosphatidylcholine bilayers. *Europhys. Lett.* **1994**, *28*, 181−186.

(14) Arriaga, L. R.; López-Montero, I.; Monroy, F.; Orts-Gil, G.; Farago, B.; Hellweg, T. Stiffening Effect of Cholesterol on Disordered Lipid Phases: A Combined Neutron Spin Echo plus Dynamic Light Scattering Analysis of the Bending Elasticity of Large Unilamellar Vesicles. *Biophys. J.* **2009**, *96*, 3629−3637.

(15) Khelashvili, G.; Rappolt, M.; Chiu, S. W.; Pabst, G.; Harries, D. Impact of sterol tilt on membrane bending rigidity in cholesterol and 7DHC-containing DMPC membranes. *Soft Matter* **2011**, *7*, 10299−10312.

(16) Helfrich, W. Steric interaction of fluid membranes in multilayer systems. *Z. Naturforsch.* **1978**, *33a*, 305−315.

(17) Sornette, D.; Ostrowsky, N. Importance of membrane fluidity on bilayer interactions. *J. Chem. Phys.* **1986**, *84*, 4062−4067.
(18) Goldstein, R. E.; Leibler, S. Structural phase-transitions of interacting membranes. *Phys. Rev. A: At., Mol., Opt. Phys.* **1989**, *40*, 1025−1035.
(19) Podgornik, R.; Parsegian, V. A. Thermal Mechanical Fluctuations of Fluid Membranes in Confined Geometries − The Case of Soft Confinement. *Langmuir* **1992**, *8*, 557−562.
(20) Zhang, R.; Suter, R. M.; Nagle, J. F. Theory of the structure factor of lipid bilayers. *Phys. Rev. E.* **1994**, *50*, 5047−5060.
(21) Nallet, F.; Laversanne, R.; Roux, D. Modeling X-ray or neutron-scattering spectra of lyotropic lamellar phases − interplay between form and structure factors. *J. Phys. II France* **1993**, *3*, 487−502.
(22) Pabst, G. Global properties of biomimetic membranes: Perspectives on molecular features. *Biophys. Rev. Lett.* **2006**, *1*, 57−84.
(23) Oliveira, C. L. P.; Gerbelli, B. B.; Silva, E. R. T.; Nallet, F.; Navailles, L.; Oliveira, E. A.; Pedersen, J. S. Gaussian deconvolution: a useful method for a form-free modeling of scattering data from mono- and multilayered planar systems. *J. Appl. Crystallogr.* **2012**, *45*, 1278−1286.
(24) Kucerka, N.; Nieh, M.; Pencer, J.; Harroun, H.; Katsaras, J. The study of liposomes, lamellae and membranes using neutrons and X-rays. *Curr. Opin. Colloid Interface Sci.* **2007**, *12*, 17−22.
(25) Kucerka, N.; Nagle, J. F.; Sachs, J. N.; Feller, S. E.; Pencer, J.; Jackson, A.; Katsaras, J. Lipid bilayer structure determined by the simultaneous analysis of neutron and x-ray scattering data. *Biophys. J.* **2008**, *95*, 2356−2367.
(26) Safinya, C. R.; Roux, D.; Smith, G. S.; Sinha, S. K.; Dimon, P.; Clark, N. A.; Bellocq, A. M. Steric interactions in a model multimembrane system − a synchrotron X-ray study. *Phys. Rev. Lett.* **1986**, *57*, 2718−2721.
(27) Frühwirth, T.; Fritz, G.; Freiberger, N.; Glatter, O. Structure and order in lamellar phases determined by small-angle scattering. *J. Appl. Crystallogr.* **2004**, *37*, 703−710.
(28) Katsaras, J.; Stinson, R. H. High-resolution electron-density profiles reveal influence of fatty-acids on bilayer structure. *Biophys. J.* **1990**, *57*, 649−655.
(29) Caillé, A. X-ray scattering by smectic A crystals. C. R. *Acad. Sc. Paris* **1972**, *274*, 891.
(30) Oliveira, E. A. de; Teixeira da Silva, E. R.; Fevrier, A.; Grelet, E.; Nallet, F.; Navailles, L. Confinement-induced phase transition in a DNA-lipid hydrated complex. *Europhys. Lett.* **2010**, *91*, 28001−28006.
(31) Dobrindt, J.; Teixeira da Silva, E. R.; Alves, C.; Oliveira, E. A.; Nallet, F.; Navailles, L. Anisotropic Brownian motion in ordered phases of DNA fragments. *Eur. Phys. J. E* **2012**, *35*, 3−15.
(32) Teixeira da Silva, E. R.; Oliveira, E. A.; de Fevrier, A.; Nallet, F.; Navailles, L. Supramolecular polymorphism of DNA in non-cationic L-alpha lipid phases. *Eur. Phys. J. E* **2011**, *34*, 83−94.
(33) Colin, A.; Roux, D. Incorporating DNA in a lamellar phase: A Flory model. *Eur. Phys. J. E* **2002**, *8*, 499−506.
(34) Pott, T.; Colin, A.; Navailles, L.; Roux, D. DNA intercalation in neutral multilamellar membranes: Experiments and theory. *Interface Sci.* **2003**, *11*, 249−257.
(35) Ligoure, C. Hairy self-assemblies of surfactants. *J. Phys.: Condens. Matter* **2005**, *17*, S2911−S2922.
(36) Petrache, H. I.; Gouliaev, N.; Tristram-Nagle, S.; Zhang, R.; Suter, R. M.; Nagle, J. F. Interbilayer interactions from high-resolution x-ray scattering. *Phys. Rev. E: Stat., Nonlinear, Soft Matter Phys.* **1998**, *57*, 7014−7024.
(37) MacIntosh, T. J. Short-range interactions between lipid bilayers measured by X-ray diffraction. *Curr. Opin. Struct. Biol.* **2000**, *10*, 481−485.
(38) Nagle, J. F.; Tristram-Nagle, S. Lipid bilayer structure. *Curr. Opin. Struct. Biol.* **2000**, *10*, 474−480.
(39) LeNeveu, D. M.; Rand, R. P.; Gingell, D.; Parsegian, V. A. Measurement and Modification of forces between lecithin bilayers. *Biophys. J.* **1977**, *18*, 209−230.
(40) McIntosh, T. J.; Simon, S. A. Area per molecule and distribution of water on fully hydrated dilauriylphosphatidylethanolamine bilayers. *Biochemistry* **1986**, *25*, 4058−4066.
(41) Roux, D.; Safinya, C. R.; Nallet, F. In *Micelles, Membranes, Microemulsions and Monolayers*; Gelbart, W. M., Shaul, A. B., Roux, D., Eds.; Springer: New York, 1994.
(42) Lipowsky, R.; Leibler, S. Unbinding transitions of interacting membranes. *Phys. Rev. Lett.* **1986**, *56*, 2541−2544.
(43) Milner, S. T.; Roux, D. Flory theory of the unbinding transition. *J. Phys. (Paris)* **1992**, *2*, 1741−1754.
(44) Safinya, C. R.; Sirota, E.; Roux, D.; Smith, G. S. Universality in interacting membranes − the effect of cosurfactants on the interfacial rigidity. *Phys. Rev. Lett.* **1989**, *62*, 1134−1137.
(45) Bagger-Jörgensen, H.; Olsson, U. Experimental Study of Undulation Forces in a Nonionic Lamellar Phase. *Langmuir* **1996**, *12*, 4057−4063.
(46) Golubovic, L.; Lubensky, T. C. Smectic elastic-constants of lamellar fluid membrane phases − crumpling effects. *Phys. Rev. B: Condens. Matter Mater. Phys.* **1989**, *39*, 12110−12133.
(47) Pan, J.; Tristram-Nagle, S.; Nagle, J. F. Effect of cholesterol on structural and mechanical properties of membranes depends on lipid chain saturation. *Phys. Rev. E: Stat., Nonlinear, Soft Matter Phys.* **2009**, *80*, 021931−021959.
(48) Pabst, G.; Danner, S.; Podgornik, R.; Katsaras, J. Entropy-Driven Softening of Fluid Lipid Bilayers by Alamethicin. *Langmuir* **2007**, *23*, 11705−11711.
(49) Freyssingeas, E.; Roux, D.; Nallet, F. The effect of water thickness on the bending rigidity of inverted bilayers. *J. Phys.: Condens. Matter* **1996**, *8*, 2801−2806.
(50) Sottmann, T.; Strey, R.; Chen, S. A small-angle neutron scattering study of nonionic surfactant molecules at the water-oil interface: Area per molecule, microemulsion domain size, and rigidity. *J. Chem. Phys.* **1997**, *106*, 6483−6501.
(51) Kurtisovski, E.; Taulier, N.; Ober, R.; Waks, M.; Urbach, W. Molecular origin of model membrane bending rigidity. *Phys. Rev. Lett.* **2007**, *98*, 258103−258107.
(52) Hamm, M.; Kozlov, M. M. Elastic energy of tilt and bending of fluid membranes. *Eur. Phys. J. E* **2000**, *3*, 323−335.
(53) Wurger, A. Bending elasticity of surfactant films: The role of the hydrophobic tails. *Phys. Rev. Lett.* **2000**, *85*, 337−340.
(54) Shiba, H.; Noguchi, H. Estimation of the bending rigidity and spontaneous curvature of fluid membranes in simulations. *Phys. Rev. E: Stat., Nonlinear, Soft Matter Phys.* **2011**, *84*, 031926−031940.
(55) Thakkar, F. M.; Maiti, P. K.; Kumaran, V.; Ayappa, K. G. Verifying scalings for bending rigidity of bilayer membranes using mesoscale models. *Soft Matter* **2011**, *7*, 3963−3966.
(56) Product Information n. 38387a. Technical report, Seppic
(57) Strey, R.; Schomäcker, R.; Roux, D.; Nallet, F.; Olsson, U. Dilute lamellar and L_3 phases in the binary water—$C_{12}E_5$ system. *J. Chem. Soc., Faraday Trans.* **1990**, *86*, 2253−2261.
(58) Freyssingeas, E.; Nallet, F.; Roux, D. Measurement of the Membrane Flexibility in Lamellar and "Sponge" Phases of the $C_{12}E_5$/Hexanol/Water System. *Langmuir* **1996**, *12*, 6028−6035.
(59) Von Berlepsch, H.; de Vries, R. Weakly charged lamellar bilayer system: Interplay between thermal undulations and electrostatic repulsion. *Eur. Phys. J. E* **2000**, *1*, 141−152.
(60) Milner, S. T. Polymer brushes. *Science* **1991**, *251*, 905−914.

Journal of
Applied
Crystallography
ISSN 1600-5767

Received 17 May 2013
Accepted 17 October 2013

Modelling of high-symmetry nanoscale particles by small-angle scattering[1]

Cassio Alves,[a] Jan Skov Pedersen[b] and Cristiano Luis Pinto Oliveira[a]*

[a]Institute of Physics, University of São Paulo, Rua do Matão 187, São Paulo, São Paulo, 05314-970, Brazil, and [b]Department of Chemistry, University of Aarhus, Gustav Wieds Vej 14, Aarhus, DK-8000 C, Denmark. Correspondence e-mail: crislpo@if.usp.br

A versatile procedure to build high-symmetry objects and to calculate their corresponding small-angle scattering intensity is presented. Starting from a set of vertex positions, available from a large and extensible database, it is possible to build several types of bodies using spherical subunits. A fast implementation, based on the Debye formula using a histogram of distance, is then used to compute the theoretical scattering intensity. Since the model is built from the definition of a small set of parameters, it is possible to perform an optimization of structural parameters against experimental data. Finally, affine size polydispersities can be easily included by the rescaling of the histogram of the positions used in the calculations. Several examples of the calculations are presented, demonstrating the method and its applicability.

© 2014 International Union of Crystallography

1. Introduction

Particles with nanoscale dimensions have an enormous range of applications in almost all areas. From colloidal suspensions to magnetic materials, nanoparticles play a very important role since they might control the chemical and physical properties of such systems (Jones, 2002; Uchida *et al.*, 2007). Therefore, there is a large group of techniques that are aimed at the characterization of such systems, providing important and, in several cases, complementary information. Some of the key techniques for such studies are the scattering methods. In this class, small-angle scattering (SAS) can give important information about the particle dimensions, shapes, polydispersity, orientation *etc.*, among several other structural parameters. Since it is a simple and non-invasive technique, it can be applied in a broad range of applications, particularly to investigate colloidal systems directly in solution. A reasonably large region of the sample is illuminated by the X-ray or neutron beam and therefore the scattering data are a result of an ensemble average over a very large number of particles. Because of these properties the SAS technique is a unique way to investigate nanoscaled particles.

An interesting example of nanoparticles is the particles obtained by programmed assembly of DNA structures. With recent important developments in bioengineering and bioinformatics, it is possible to design sequences of DNA that can assemble in programmed pre-defined shapes. There are several examples of such constructs in the literature. The first proposition of DNA self-assembled structures in the literature was made by Seeman for an assembly with a cubic shape (Chen & Seeman, 1991), and later for a truncated octahedron (Zhang & Seeman, 1994). However, those propositions were only theoretical models. The approach was then successfully implemented experimentally, providing the self-assembly of DNA in the form of an octahedron (Shih *et al.*, 2004; Andersen *et al.*, 2008; Falconi *et al.*, 2009; He *et al.*, 2010), a tetrahedron (Goodman *et al.*, 2005; He *et al.*, 2008; Kato *et al.*, 2009; Li *et al.*, 2009), trigonal bipyramids (Erben *et al.*, 2007), a dodecahedron (He *et al.*, 2008), an icosahedron (Zhang *et al.*, 2008; Bhatia *et al.*, 2009) and a truncated icosahedron (He *et al.*, 2008). It was also possible to build hybrid structures with synthetic connections at the vertices (Aldaye & Sleiman, 2007; Zimmermann *et al.*, 2008; Yang *et al.*, 2009), and large structures, based on the development of a DNA origami technique (Rothemund, 2006; Dietz *et al.*, 2009; Douglas *et al.*, 2009; Endo *et al.*, 2009; Ke *et al.*, 2009). In other applications, it was shown that it was possible to encapsulate proteins (Erben *et al.*, 2006) and nanoparticles (Erben *et al.*, 2007; Yang *et al.*, 2009) inside of a DNA polyhedron. There are several examples of the assembly of DNA nanostructures with high symmetry (*e.g.* Seeman, 2010), and Han *et al.* (2011) have used the DNA origami approach to build structures with high curvature. In all cases, after the experimental assembly, it is necessary to be able to confirm the formed shape and the assembly efficiency. One common procedure to check the assembly formation is gel chromatography (Douglas *et al.*, 2009), where by the indication of the molecular weight, the assembly can be inferred. Although this procedure gives a good indication of the correct assembly, it is not a measure of it. Electron microscopy techniques permit a direct visualization of such structures and can, in several cases, provide a three-dimensional reconstruction (Kato *et al.*, 2009). Nevertheless, such techniques can have limitations since they might require quite invasive sample treatment for the experiments, which can influence the results. Also the information obtained

[1] This article will form part of a virtual special issue of the journal, presenting some highlights of the 15th International Small-Angle Scattering Conference (SAS2012). This special issue will be available in early 2014.

electronic reprint

about the assembly efficiency on the system is limited because such methods usually cover a very small volume of the system (Andersen *et al.*, 2008). Scattering methods, on the other hand, are non-invasive methods, which can be applied directly in solution and provide ensemble-averaged results on a very large number of particles. The main drawback of the scattering techniques is that they provide information in reciprocal (Fourier) space. It has been shown that an ideal situation is the combination of electron microscopy techniques and scattering methods, since it might enable a better investigation of the system (Andersen *et al.*, 2009; Oliveira *et al.*, 2010) with direct visualization of the structure as well as information on the ensemble-average structure of the particles.

Although scattering experiments are relatively simple, the data analysis and interpretation can be quite complicated. The scattering intensity of a sample is given as the absolute square of the Fourier transformation of the scattering length density contrast with additional ensemble-average and orientation-average operations. Because of this, analytical expressions are restricted to simple shapes and geometries (Pedersen, 1997). More complicated shapes cannot be described analytically and, for such cases, alternative methods are required.

In this work a useful procedure is presented, where models with a large number of possible geometries can be easily built and the corresponding scattering intensity calculated. Since the number of parameters describing the models is very low, they can be quickly optimized against experimental data. A special scheme is presented to efficiently model the assembled DNA structures.

2. Theoretical aspects, methods and results

2.1. Small-angle scattering (SAS) and model calculation

In a typical SAS experiment, the incoming beam passes through the sample, probing a large number of randomly oriented particles, which then leads to an ensemble averaging of the total scattering intensity that also includes averaging over the orientation of the particles. A general expression for the measured scattering intensity is given by

$$I(q) = N\Delta\rho^2 V^2 P(q) S_{\rm m}(q). \qquad (1)$$

In this expression, q is the modulus of the scattering vector [defined as $q = (4\pi/\lambda)\sin\theta$, where 2θ is the scattering angle and λ is the wavelength of the monochromatic beam], N is the average number of particles illuminated by the beam, $\Delta\rho$ is the scattering length density contrast between the particles and the medium in which they are immersed, and V is the particle volume. $P(q)$ is the normalized particle form factor [$P(0) = 1$], which is the squared Fourier transformation of the particle scattering length density contrast, averaged over all possible particle orientations:

$$P(q) = \left\langle \frac{A(q)^2}{A(0)^2} \right\rangle_\Omega = \left\langle \left[\frac{\int_V \Delta\rho(\mathbf{r}) \exp(i\mathbf{q}\cdot\mathbf{r}) {\rm d}\mathbf{r}}{\int_V \Delta\rho(\mathbf{r}) {\rm d}\mathbf{r}} \right]^2 \right\rangle_\Omega . \qquad (2)$$

Here $\mathbf{q}$ is the three-dimensional scattering vector, $\Delta\rho(\mathbf{r})$ is the particle scattering length density contrast distribution at position $\mathbf{r}$ and the angle brackets $\langle\rangle$ indicate an average over the solid angle Ω. This equation reflects that the form factor $P(q)$ is directly related to the particle shape. It is interesting to note that, for X-rays, the scattering length density contrast is proportional to the difference in electron density between the particles and the medium. The term $S_{\rm m}(q)$ is the (effective) structure factor, which describes possible particle interactions. For very dilute systems, the structure factor always approaches a constant value of unity and, therefore, the expression for this case reduces to

$$I(q) = N\Delta\rho^2 V^2 P(q) = N I_1(q), \qquad (3)$$

where the last equal sign is valid for identical particles without any internal degrees of freedom like flexibility, so that $I_1(q)$ is the scattering intensity of a single particle. Therefore the measured intensity, which corresponds to the sum of a large number of scatterers, is a direct representation of the scattering from a single particle and can provide information about its structure. There are several methods in the literature for data analysis and modelling of SAS data (Glatter, 1977; Glatter & Kratky, 1982; Feigin & Svergun, 1987; Semenyuk & Svergun, 1991; Pedersen, 1997). However, the application of traditional methods for programmed self-assembly structures has some intrinsic peculiarities. Even with the loss of information related to the ensemble average of the randomly oriented particles, the so called *ab initio* methods can provide reasonable three-dimensional models directly from the one-dimensional experimental data (Svergun & Stuhrmann, 1991; Chacón *et al.*, 1998; Svergun, 1999; Walther *et al.*, 2000). These methods can also be combined with knowledge of the atomic resolution structure of proteins, DNA and RNA in order to obtain the overall organization of the complex that fits the scattering data (Petoukhov & Svergun, 2005). However, the restored models are not unique and there might be several possible models that fit the experimental data (Svergun *et al.*, 1996; Volkov & Svergun, 2003; Petoukhov & Svergun, 2013). In order to increase the reliability of such procedures, the modelling of the scattering data has been combined with external information, for example, the inclusion of model constraints, symmetry conditions and contrast variation data (mostly available for neutron scattering), and also, in very recent applications, the inclusion of simultaneous modelling of scattering and NMR data (Evrard *et al.*, 2011; Wasserman *et al.*, 2012). Such procedures and methods constitute a very useful tool box for modelling structures for biological complexes in a growing number of applications (Petoukhov & Svergun, 2013). However, there are some cases where such methods can fit the scattering data but the resulting models are not in agreement with the known shape. Such a limitation occurs either from the lack of external information that can be used or from the lack of the proper symmetry constraint available in the programs. One example is the case of the programmed self-assembly of DNA cages, which can adopt highly symmetrical shapes (Douglas *et al.*, 2009) on which it might be difficult to apply *ab initio* methods in the modelling of the corresponding scattering data (Andersen *et al.*, 2008; Oliveira *et al.*, 2010). On the other hand, since the expected shape for

electronic reprint

these cases is known, one could *a priori* build the scattering length density profile $\rho(\mathbf{r})$ and calculate the theoretical intensity. However, this approach depends on the calculation of a Fourier integral and the orientation averaging, which can be solved analytically or semi-analytically only for simple shapes, like spheres, cylinders and ellipsoids (Pedersen, 1997). For more complex shapes, equation (2) is not directly applicable and alternative methods have to be used. One very powerful method is the finite element technique, where the model is built using small subunits like spheres or points (Glatter, 1972). In the case of spherical subunits, the normalized scattering intensity can be calculated using of the Debye formula (Debye, 1915):

$$I(q) = (1/M_{\rm Tot}^2)\sum_{i,j}^{P} M(i)M(j)A_i(q)A_j(q)\sin(qr_{ij})/(qr_{ij}), \quad (4)$$

where $A_i(q)$ and $M(i)$ are, respectively, the normalized scattering amplitude and the scattering mass [$M(i) = V(i)\Delta\rho$, the product of the subunit volume and the scattering length density contrast] of the ith homogeneous sphere, P is the total number of subunits in the model, r_{ij} is the distance between the ith and jth sphere, and

$$M_{\rm Tot}(i) = \sum_{i,j}^{P} M(i). \quad (5)$$

The computation requires prior construction of a model composed by the known subunits. It should be noted that the term subunits refers only to the small beads that are used to build the model. Having the model, the calculation can be very time consuming for models composed of a large number of subunits since equation (4) involves a double summation and the computation time grows with the square of the number of subunits [$O(P^2)$].

In order to speed up the calculation, it is possible to replace the double sum by a single sum on the histogram of pair distances $h(r)$. This histogram is calculated using all the subunits on the model and it is weighted by the local electron density of each point (Glatter, 1972; Pantos & Bordas, 1994):

$$I(q) = (1/M_{\rm Tot}^2)\left[\sum_{i=1}^{P} I(q) + 2A^2(q)\sum_{k=1}^{n_{\rm bins}} h(r_k)\sin(qr_k)/(qr_k)\right], \quad (6)$$

where $n_{\rm bins}$ is the total number of channels (bins) in the histogram, $A(q)$ is the normalized form factor amplitude of the subunit and $h(r)$ is the histogram of pairs of distances. In this calculation, the approximation is made by the discretization of the distances over the histogram channels. This implementation permits the fast computation of the theoretical scattering intensity since the sum is now made over the histogram channels and, therefore, the computation cost is of the order of the number of channels $O(n_{\rm bins})$. The construction of the histogram, however, still goes as P^2 but it is performed only once for all q values.

If the number of points that composes the model is sufficiently large (typically more than 5000 subunits), it is also possible to speed up the histogram calculation. This is performed by the division of the points into several blocks. The definition of the block size can be coupled to the maximum value of the scattering vector, $q_{\rm max}$. As a rule of thumb, the subunit radius has to be smaller than $\pi/q_{\rm max}$ to eliminate any influence of the subunit size on the calculation of the scattering intensity (Glatter, 1972). This information can also be used for an automatic determination of the block size. For each block the histogram is calculated individually, and at the end, all the contributions are summed. As also shown by other authors (Hansen, 1990; Pedersen *et al.*, 2012), this procedure speeds up the computation of the histogram since it now runs with $\sim(P^2/n_{\rm blocks})$, where $n_{\rm blocks}$ is the number of blocks the system is split into. Finally, having the histogram, one can easily introduce affine polydispersities by the rescaling of the histogram itself (Pedersen *et al.*, 2012). In this way the 'affine polydispersity' indicates that all dimensions of the model are scaled by the same relative value. Another very effective procedure for fast computation of scattering intensities is the use of spherical harmonics as proposed by Stuhrmann and Svergun (Stuhrmann, 1970; Svergun & Stuhrmann, 1991; Svergun, 1999), but this approach is not used in the present work.

2.2. Short program description

The procedures presented in this work enable the modelling, simulation and optimization of bodies with different geometries and shapes. A database with more than 100 different shapes (see the complete list in Table 1) containing information of vertex position and edge connectivity for the structures is used. There is also an implementation that allows the automatic connectivity of any set of points in a three-dimensional arrangement. Such large feasibility is to our knowledge not available in any of the procedures present in the literature (Zhou *et al.*, 2005). With this information different types of models can be built: solid, shell-like and edge-like structures. The models are represented by the use of spherical subunits, which allows the precise computation of the theoretical intensity. The main advantage of this approach is that the model construction only requires a very low number of parameters for its description, even for very complicated geometrical bodies. This enables an easy optimization of the model against experimental data. The optimization is performed by the use of standard least-squares methods (Press, 1992; Pedersen, 1997). The routines were written in Fortran90. Images of the models were built using the programs *MolMol* (Koradi *et al.*, 1996), the UCSF *Chimera* package (Pettersen *et al.*, 2004) and the *PyMOL* Molecular Graphics System (Schrödinger LLC, Version 1.3, 2010; http://www.pymol.org).

2.3. Procedures to create models composed of subunits

In the present work, two general strategies were used to build the models composed of subunits. In one case, the subunits with a given radius form a compact set with well defined positions to build up the model. This approach, which will be called the finite element (FE) method, is used for the

electronic reprint

Table 1
Structures with high symmetry.

0	Tetrahedron	57	Pentagonal dipyramid (J13)	100	Metabiaugmented hexagonal prism (J56)
1	Cube	58	Elongated triangular dipyramid (J14)	101	Triaugmented hexagonal prism (J57)
2	Octahedron	59	Elongated square dipyramid (J15)	102	Augmented dodecahedron (J58)
3	Dodecahedron	60	Elongated pentagonal dipyramid (J16)	103	Parabiaugmented dodecahedron (J59)
4	Icosahedron	61	Gyroelongated square dipyramid (J17)	104	Metabiaugmented dodecahedron (J60)
5	Small stellated dodecahedron	62	Elongated triangular cupola (J18)	105	Triaugmented dodecahedron (J61)
6	Great dodecahedron	63	Elongated square cupola (J19)	106	Metabidiminished icosahedron (J62)
7	Great stellated dodecahedron	64	Elongated pentagonal cupola (J20)	107	Tridiminished icosahedron (J63)
8	Great icosahedron	65	Elongated pentagonal rotunda (J21)	108	Augmented tridiminished icosahedron (J64)
22	Triangular prism	66	Gyroelongated triangular cupola (J22)	109	Augmented truncated tetrahedron (J65)
23	Pentagonal prism	67	Gyroelongated square cupola (J23)	110	Augmented truncated cube (J66)
24	Hexagonal prism	68	Gyroelongated pentagonalcupola (J24)	111	Biaugmented truncated cube (J67)
25	Octagonal prism	69	Gyroelongated pentagonal rotunda (J25)	112	Augmented truncated dodecahedron (J68)
26	Decagonal prism	70	Gyrobifastigium (J26)	113	Parabiaugmented truncated dodecahedron (J69)
27	Square antiprism	71	Triangular orthobicupola (J27)	114	Metabiaugmented truncated dodecahedron (J70)
28	Pentagonal antiprism	72	Square orthobicupola (J28)	115	Triaugmented truncated dodecahedron (J71)
29	Hexagonal antiprism	73	Square gyrobicupola (J29)	116	Gyraterhombicosidodecahedron (J72)
30	Octagonal antiprism	74	Pentagonal orthobicupola (J30)	117	Parabigyraterhombicosidodecahedron (J73)
31	Decagonal antiprism	75	Pentagonal gyrobicupola (J31)	118	Metabigyraterhombicosidodecahedron (J74)
33	Rhombic dodecahedron	76	Pentagonal orthocupolarontunda (J32)	119	Trigyraterhombicosidodecahedron (J75)
34	Triakis octahedron	77	Pentagonal gyrocupolarotunda (J33)	120	Diminished rhombicosidodecahedron (J76)
35	Tetrakis hexahedron	78	Pentagonal orthobirotunda (J34)	121	Paragyrate diminished rhombicosidodecahedron (J77)
36	Trapezoidal icositetrahedron	79	Elongated triangular orthobicupola (J35)	122	Metagyrate diminished rhombicosidodecahedron (J78)
37	Hexakis octahedron	80	Elongated triangular gyrobicupola (J36)	123	Bigyrate diminished rhombicosidodecahedron (J79)
38	Pentagonal icositetrahedron (dextro)	81	Elongated square gyrobicupola (J37)	124	Parabidiminishedrhombicosidodecahedron (J80)
39	Rhombic triacontahedron	82	Elongated pentagonal orthobicupola (J38)	125	Metabidiminishedrhombicosidodecahedron (J81)
40	Triakis icosahedron	83	Elongated pentagonal gyrobicupola (J39)	126	Gyrate bidiminished rhombicosidodecahedron (J82)
41	Pentakis dodecahedron	84	Elongated pentagonal orthocupolarotunda (J40)	127	Tridiminished rhombicosidodecahedron (J83)
42	Trapezoidal hexecontahedron	85	Elongated pentagonal gyrocupolarotunda (J41)	128	Snub disphenoid (J84)
43	Hexakis icosahedron	86	Elongated pentagonal orthobirotunda (J42)	129	Snub square antiprism (J85)
44	Pentagonal hexecontahedron (dextro)	87	Elongated pentagonal gyrobirotunda (J43)	130	Sphenocorona (J86)
45	Square pyramid (J1)	88	Gyroelongated triangular bicupola (J44)	131	Augmented sphenocorona (J87)
46	Pentagonal pyramid (J2)	89	Gyroelongated square bicupola (J45)	132	Sphenomegacorona (J88)
47	Triangular cupola (J3)	90	Gyroelongated pentagonal bicupola (J46)	133	Hebesphenomegacorona (J89)
48	Square cupola (J4)	91	Gyroelongated pentagonal cupolarotunda (J47)	134	Disphenocingulum (J90)
49	Pentagonal cupola (J5)	92	Gyroelongated pentagonalbirotunda (J48)	135	Bilunabirotunda (J91)
50	Pentagonal rotunda (J6)	93	Augmented triangular prism (J49)	136	Triangular hebesphenorotunda (J92)
51	Elongated triangular pyramid (J7)	94	Biaugmented triangularprism (J50)	137	Tetrahemihexahedron
52	Elongated square pyramid (J8)	95	Triaugmented triangular prism (J51)	138	Octahemioctahedron
53	Elongated pentagonal pyramid (J9)	96	Augmented pentagonal prism (J52)	139	Small ditrigonal icosidodecahedron
54	Gyroelongated square pyramid (J10)	97	Biaugmented pentagonal prism (J53)	140	Dodecadodecahedron
55	Gyroelongated pentagonal pyramid (J11)	98	Augmented hexagonal prism (J54)	141	Echidnahedron
56	Triangular dipyramid (J12)	99	Parabiaugmented hexagonal prism (J55)		

construction of models with a relatively small number of subunits. In the other case, the model is built by the use of a large number of points, which are randomly distributed within the structure. This approach, which will be called the Monte Carlo (MC) method, usually uses a larger number of subunits. Depending on the application, one method might be more suitable than the other, as will be demonstrated by the examples below. In general, the MC method can be used to build complex models, either solid or shell-like, since the large number of subunits can be combined to describe the interfaces. On the other hand, the FE method uses a small number of subunits and is suitable for cases where the subunit itself can be seen as an important model element. For example, for the cases of DNA-like structures or protein-like structures, the subunits can describe the backbone of such structures. Also, the two approaches can be combined, permitting a more flexible procedure. One example of such an application is shown in Fig. 1, where a cube is built. The corners constitute the vertices and a model can be generated by placing an array of small subunits along the edges of the cubes. The construction of other polyhedron types is very easy if information

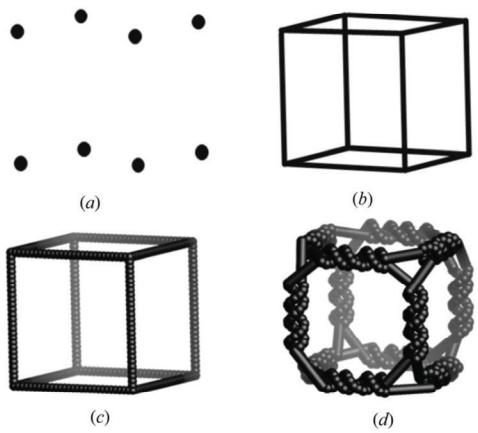

Figure 1
Construction of the model. Starting from the set of vertex positions (*a*), the skeleton of the model can be built by just connecting the vertices (*b*). In order to enable an easy computation of the intensity the vertices can be represented using spherical subunits (*c*). The vertices can be connected using more elaborate edges like ones with DNA-like double helices (*d*).

electronic reprint

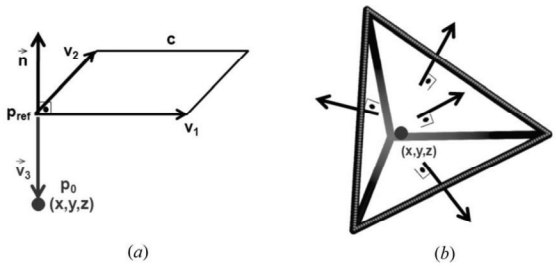

Figure 2
Considerations about positions and planes. The vector $\mathbf{n}$ is the normal to the plane defined by the vectors $\mathbf{v}_1$ and $\mathbf{v}_2$. Also, the vector $\mathbf{v}_3$ connects the reference point $\mathbf{p}_{\rm ref}$ on the plane to a given point $\mathbf{p}_0$. (*a*) If $\mathbf{v}_3 \cdot \mathbf{n} = 0$, $\mathbf{p}_0$ is in the plane. If $\mathbf{v}_3 \cdot \mathbf{n} < 0$, $\mathbf{p}_0$ is on the negative semi-space of the plane, and if $\mathbf{v}_3 \cdot \mathbf{n} > 0$, $\mathbf{p}_0$ is on the positive semi-space of the plane. (*b*) $\mathbf{p}_0$ is inside of the tetrahedron when $\mathbf{v}_3 \cdot \mathbf{n} < 0$ for all vectors $\mathbf{n} = \mathbf{v}_1 \times \mathbf{v}_2$ built with the vectors $\mathbf{v}_1$, $\mathbf{v}_2$ oriented in a counterclockwise direction on the faces.

about the positions of the vertices and faces is available. Such information on Cartesian coordinates of the vertices as well as the connectivity between them is indeed available in the literature (Coxeter, 1973) and on the web (Andrew Hume's Polyhedron Database; http://www.netlib.org/polyhedra/). An automatic procedure was developed in the present work for reading this information and building several types of models from the vertices. It is possible to construct the skeleton of the polyhedron, placing spheres at the edge positions (Fig. 1*c*). It is also possible to place DNA-like structures at the edges and connect the double strands at a given corner in an appropriate way (Fig. 1*d*). The latter approach uses the FE method and it has already been successfully applied for the study of truncated octahedron systems (Oliveira *et al.*, 2010).

If the information about the connectivity between the edges is not known, a prior procedure for generating this is required. Given a set of coordinates representing the polyhedron vertices, is possible to use an adaptation of the Chand & Kapur (1970) algorithm and the Jarvis (1973) algorithm for generating the skeleton of the polyhedron. The data structure used in this case assumes that the polyhedron is convex, *i.e.* each edge divides no more than two faces and each face divides the semi-space into semi-regions, and that each semi-region starts at the corresponding side of this face. In summary, the program searches for the first three vertices in a certain direction and makes a triangular face. Starting from this first triangular face, the other triangular faces are constructed by the proper selection of vertices, in such a way that the new triangles have a common edge with a previous one. The correct face is chosen in order to have the minimum angle between the current and the new face. The process is repeated until all the most peripheral points are considered. By the use of the Euler relation [equation (7)], the polyhedrons can be built automatically using the three-dimensional Gift Wrap (GW) (Preparata & Shamos, 1985) algorithm. A relation exists between the number of vertices, v, the number of faces, f, and the number of edges, e,

$$v + f = e + 2. \qquad (7)$$

Information about the position of a given point (inside or outside the object) can easily be obtained by simple scalar products. For a given face plane, the vector normal to this face can be found with three points at the plane face, $\mathbf{n} = \mathbf{v}_1 \times \mathbf{v}_2$ (Fig. 2*a*), where $\mathbf{v}_1$ and $\mathbf{v}_2$ connect the points pairwise. With the normal vector $\mathbf{n}$ it is possible to determine at which side of the plane a given point $\mathbf{p}_0(x, y, z)$ is located. Let $\mathbf{v}_3$ be a vector starting on the plane face and ending at the position $\mathbf{p}_0$. If the scalar product between the normal vector $\mathbf{n}$ and vector $\mathbf{v}_3$ is $\mathbf{v}_3 \cdot \mathbf{n} < 0$, $\mathbf{p}_0$ is placed at the internal side (negative semi-space) of the plane. If $\mathbf{v}_3 \cdot \mathbf{n} > 0$, $\mathbf{p}_0$ is placed on the external side (positive semi-space). Finally, if $\mathbf{v}_3 \cdot \mathbf{n} = 0$, $\mathbf{p}_0$ lies on the plane of the face. If we extrapolate this procedure to all polyhedral faces, it is possible to determine if $\mathbf{p}_0$ is inside or outside the body (Fig. 2*b*).

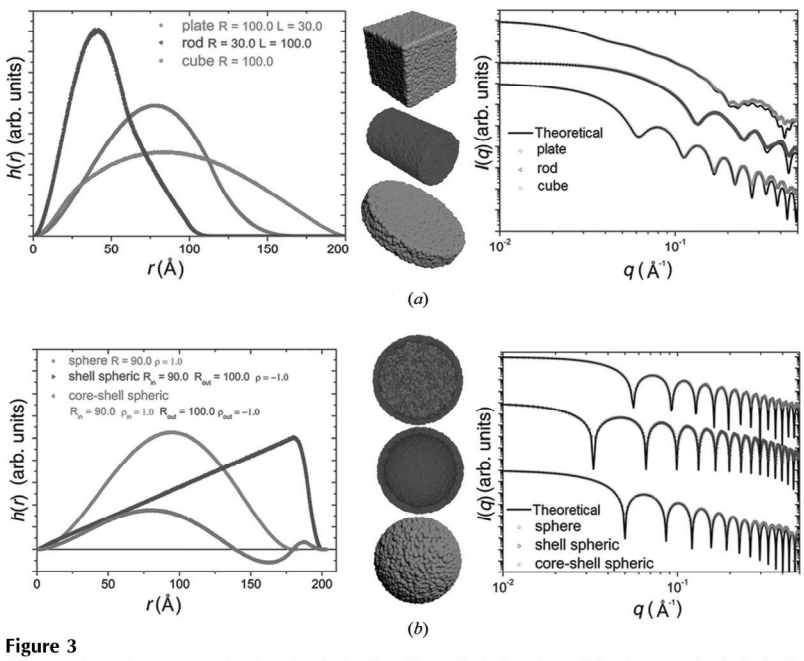

Figure 3
Computation of test examples for simple bodies. The calculation for solid spheres, spherical shells, spherical core–shell structures (*a*) and cubes, short rods and plates (*b*), compared with theoretical intensities. The very good agreement between the curves demonstrates an accurate calculation of the scattering intensity by the use of the Debye formula.

electronic reprint

This definition of internal and external regions of a given object can be applied in several model strategies. If one considers only the edges, a skeleton-like model can easily be constructed. By the use of the above method, solid or shell-like models are easily built. This approach is the basis for the construction of more sophisticated models, as shown in the next section.

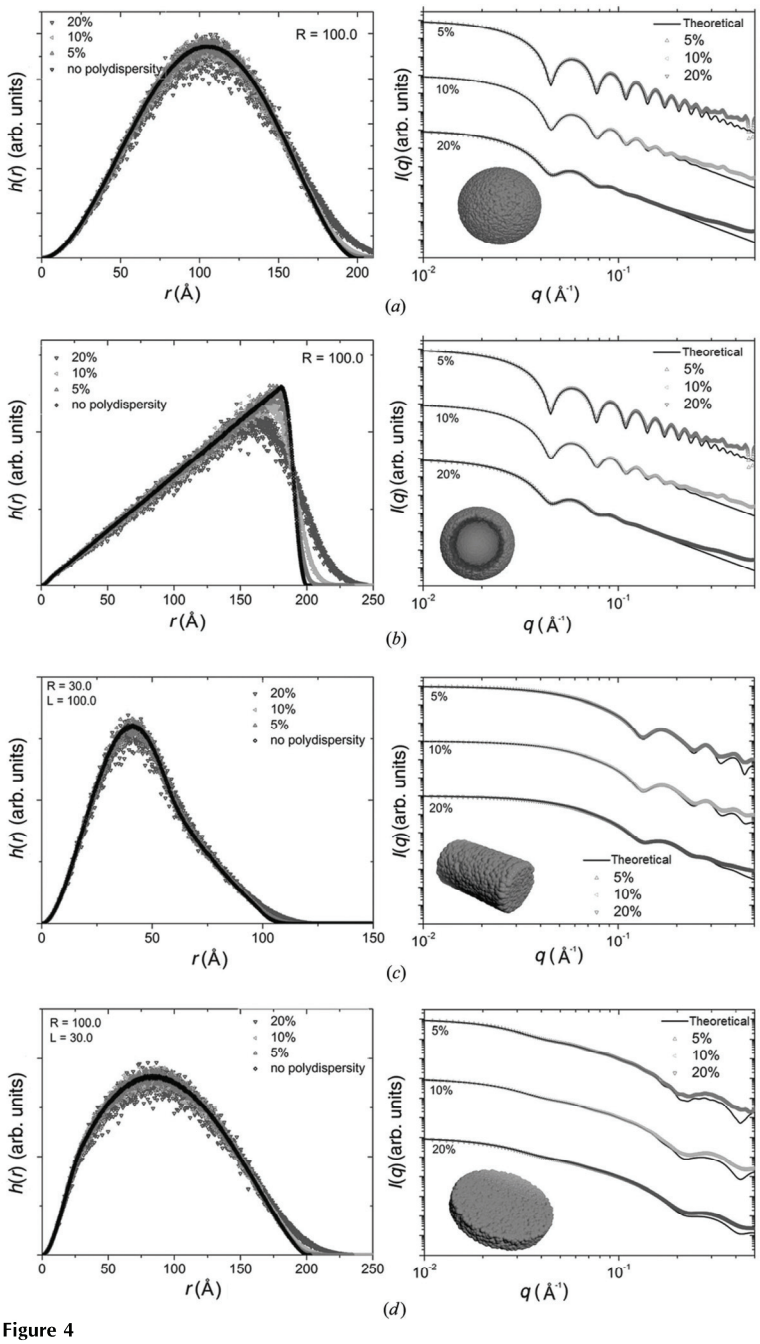

Figure 4
Computation of affine polydispersity by rescaling the histogram of distances. The simulated intensities are compared with the theoretical curves obtained from equation (8).

2.4. Test examples

In order to test the whole procedure, bodies with simple geometries were built to enable a comparison with the known analytic expressions (Pedersen, 1997). These results provide the necessary validation before the computation of the scattering for more sophisticated models. Fig. 3 shows the computation for spheres, spherical shells and core–shell models with negative/positive contrasts, as well as for cubes, rods and plates.

Affine polydispersities can be introduced in the models by the rescaling of the histogram as described by Pedersen *et al.* (2012). Briefly summarized, the bin size of the histogram is kept fixed and the original histogram is expanded or shrunk according to a given distribution. The rescaled histograms are weighted by the distribution function and the square of the scattering mass, and then projected onto the bins. As mentioned above, with this procedure all dimensions of the model are scaled by the same relative value. As a result, the final histogram can be used in the calculation of the intensity. The precision of such an approach can be confirmed by the calculation of simple geometrical bodies for which the theoretical intensity can be computed. A general expression for polydisperse systems is given by

$$I(q) = \frac{\int_0^\infty D_{\rm N}(R)M^2(R)P(q,R)\,{\rm d}R}{\int_0^\infty D_{\rm N}(R)M^2(R)\,{\rm d}R}, \qquad (8)$$

where $D_{\rm N}(R)$ is the number distribution, $M(R) = V(R)\Delta\rho$ is the scattering mass given by the product of the particle volume and the scattering length density contrast, and $P(q, R)$ is the normalized form factor. It is possible to have different types of distributions by a combination of the number weight and the volume factor. For the volume weighted distribution $[D_{\rm V}(R) = D_{\rm N}(R)M(R)]$, the scattering mass term is combined with the number distribution and for the intensity weighted distribution $[D_{\rm I}(R) - D_{\rm N}(R)M^2(R)]$ the square

electronic reprint

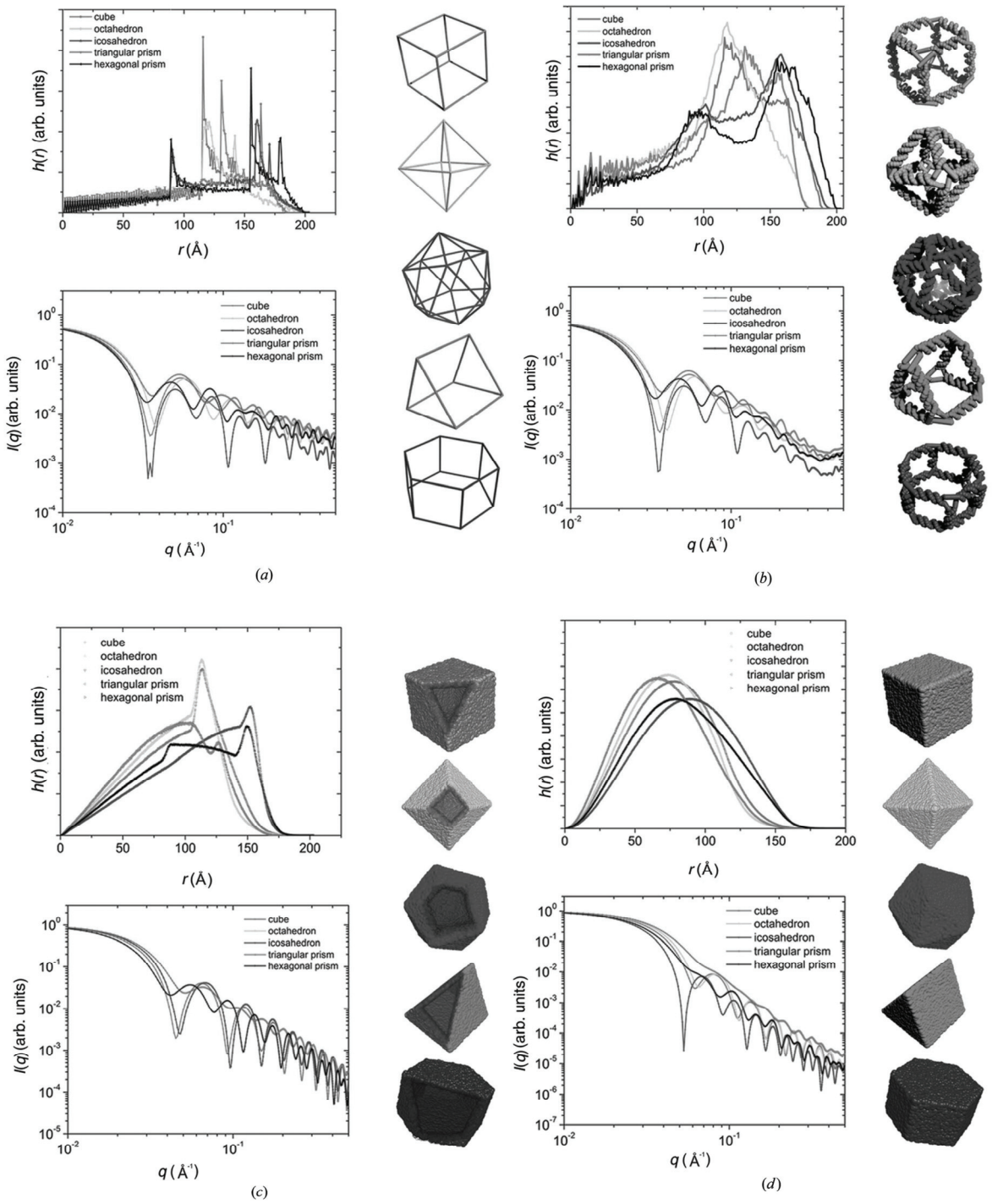

Figure 5
Calculation of theoretical intensities for several geometrical bodies. Edge-like bodies (*a*), DNA-like bodies (*b*), shell-like bodies (*c*) and solid bodies (*d*) were built and their respective histograms and theoretical intensities were computed. In all cases, the bodies were confined within a sphere of radius 100 Å.

electronic reprint

of the scattering mass is combined with the number distribution. These variations are very useful when comparing the model with real experimental data.

Fig. 4 shows the intensity with the polydispersity calculated by the use of the histogram rescaling and the theoretical computation using the full analytical calculation [equation (8)]. In all cases, the polydispersity was assumed to have Gaussian form. One can clearly see that the affine polydispersity calculations applied on the histogram are in very good agreement with the theoretical curves. Altogether, these simulated tests give the necessary support for the application of the method to the computation of intensities of any proposed shape.

2.5. SAXS simulation of polyhedron shapes

The applicability of the method is demonstrated on the computation of scattering intensities from geometrical bodies. Starting from a set of vertices, solid, shell-like and skeleton-like bodies were built and the intensities were calculated using the above-mentioned methods.

Several examples are shown in Fig. 5. Using the same geometries (cube, octahedron, icosahedron, triangular prism and hexagonal prism), a set of constructions is shown with the respective histograms and theoretical scattering intensity. It is interesting to note that the obtained histograms and intensities are remarkably different between those bodies, indicating that the small-angle scattering technique is capable of distinguishing between them. There are also large differences between solid and shell-like structures.

As mentioned above, by the use of specially designed oligo sequences, it is possible to assemble DNA structures into specific predefined shapes. In the majority of the examples available in the literature, the structure resembles the skeleton-like structure that is shown in Fig. 5(*a*). However, the edges in this case are built by DNA strands and therefore the use of a simple array of spheres to represent the DNA helix can be a too crude approximation, as already demonstrated in the literature (Oliveira *et al.*, 2010), and which is also clearly evident from the above simulations. For modelling such structures the edges can be built using DNA-like double helices as building blocks. Those parts can be obtained from known atomic resolution structures available for DNA molecules and, in order to speed up the calculations, one can use coarse grain models by only considering the positions of the C* atoms (or any other that is selected by the user) and placing spherical subunits at these positions. In this way, the edges can be built by the double helix and the termini connected by single strands. Starting from the information on the vertices and connections (Polyhedron Database; Preparata & Shamos, 1985) an automatic procedure has been implemented, which builds the whole structure with DNA double helices and the connections with single linkers (Fig. 5*b*).

The affine polydispersities can also be included for the DNA-like structures by the use of the rescaling of the histogram. An example of such an application is shown in Fig. 6 where a polydispersity of 20% in number is included. As a result, intensity with less pronounced oscillations averaged over the distribution of sizes is obtained. This approach is not entirely correct for DNA-like structures since the number of nucleotides is fixed. As mentioned above, the affine polydispersity assumes that the model keeps its original shape but varies its size, according to some distribution function. For DNA-like structures it is known that, owing to some degree of flexibility in its structure, the particle shape can fluctuate and a more correct approach would be to create an ensemble of shapes and take averages over it. Since the correct creation of such an ensemble may demand molecular dynamics simulations, this procedure can be a very complicated and cumbersome task (Falconi *et al.*, 2009; Oteri *et al.*, 2011). Nevertheless, because of the low resolution of the SAS data, affine polydispersity might provide similar results to the ensemble average over different shapes, principally for not too large variations in shape.

There are several routes to design nanomaterials to work as nanocapsules or nanocages. Beyond the design of nanocages using DNA and blending of DNA with organic and inorganic molecules (Sleiman *et al.*, 2011), other materials can be used such as metal–organic polyhedrons (Seidel & Stang, 2002; Hamilton & MacGillivray, 2004; Perry *et al.*, 2009), viral capsids and other protein cages (Uchida *et al.*, 2007) which have also presented the possibility of use as nanocontainers or nanocapsules. In this approach, it was demonstrated that it is possible to transport different kinds of molecules inside or

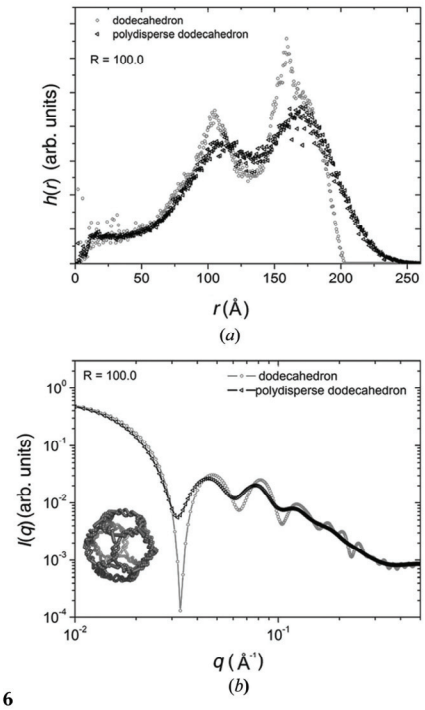

Figure 6
The influence of affine polydispersity for DNA cages. (*a*) Histogram of pair of distances. (*b*) Calculated scattering intensity. The polydispersity smears out the oscillations in the scattering intensity.

electronic reprint

attached to the nanocapsules (Uchida *et al.*, 2007; Bhatia *et al.*, 2009; Walsh *et al.*, 2011). Inspired by these experiments, an example of the combination of shapes is presented in Fig. 7, where an icosahedral shell-like structure with a DNA cage in its interior is simulated. In this simulation the initial model of the DNA cage, built by the use of the FE approach, provided the arrangement of spheres in a well defined way. This arrangement is later replaced by random points in an MC box in such a way that the DNA cage has the same density of points as the icosahedral shell. This step is necessary to ensure the correct relative electron density values. The procedure enables an easy construction and calculation of the scattering intensity for the composed model.

As a final example, the construction of a model for a given set of points is shown in Fig. 8. In this case a set of points is selected and the GW algorithm creates the connectivity of such points by the definition of triangular faces. The points may correspond to regular polyhedra or to any random arrangement of points (Chand & Kapur, 1970; Jarvis, 1973; Preparata & Shamos, 1985). Having this information about faces and edges, all of the modelling approaches mentioned before can be applied. In the example shown in Fig. 8, two random sets of vertices are created, one with five vertices and other with nine vertices. The GW algorithm defines the outer faces of the polyhedra as triangles and, as an example of application, builds them with DNA double helices (Fig. 8*b*). The corresponding histogram and scattering intensity are shown for the case of thin edges and DNA-like edges (Figs. 8*a* and 8*c*). This procedure can be used as a general framework for modelling scattering data. The selection of random points can be combined with an heuristic procedure in order to enable the optimization of the shape against experimental data. This procedure has not yet been implemented but it might be a potential *ab initio* modelling method for SAS data.

3. Conclusions

A useful method for the fast construction of high-symmetry objects and the computation of scattering intensity is

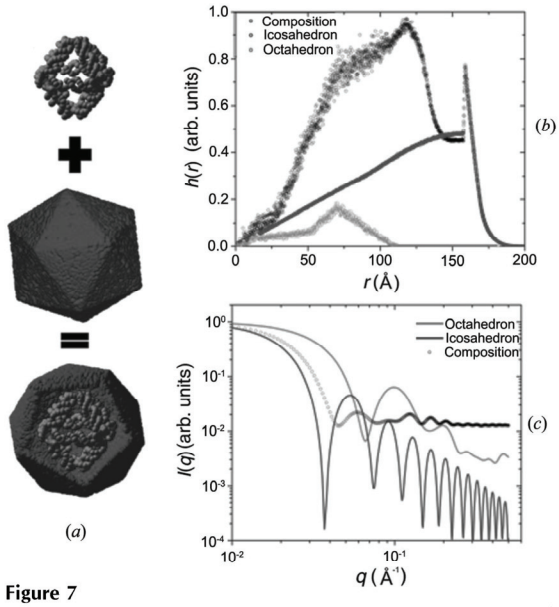

Figure 7
Composition of a shell-like structure with a DNA cage in its interior. (*a*) Models assumed. (*b*) Histograms of pairs of distances for each model. (*c*) Calculated scattering intensities. The assumed sizes and relative electron densities for each object are given on the figure. The procedure enables an easy construction and calculation of the scattering intensity for the composed model.

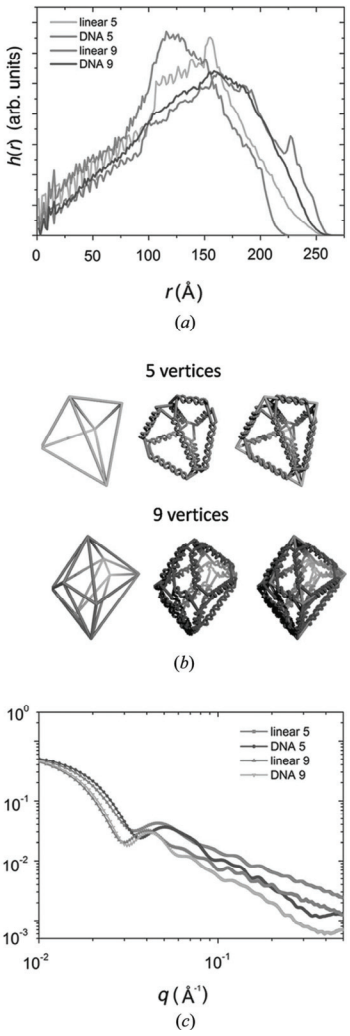

Figure 8
Example of the model construction based on a set of random points. (*a*) Histograms of pairs of distances for each model. (*b*) The obtained model for five and nine random points composed of linear arrays of spheres and DNA-like strands, respectively. The superposition of such models is just for comparison. The points were randomly generated on a surface of a sphere and the GW algorithm was used to build the object, as described in §2.3. (*c*) Calculated scattering intensities.

electronic reprint

presented. Starting from a set of vertex positions, different types of models, such as solids, shell-like, edge-like and DNA-like models, can be built. Also, as presented in the results, the methods can be combined, permitting a versatile toolbox for the calculation of the small-angle scattering from complicated models.

By the use of a large and expandable database of shapes, it is possible to have access to a large number of shapes of regular polyhedra. Also, by the use of the GW method, it is possible to build polyhedrons from any collection of points defining a convex solid.

A specific procedure was developed permitting the construction of DNA-like structures for any geometry. This procedure fills an existing gap in the literature where several DNA cage-like structures have already been assembled but the major experimental technique used to investigate the structure has been that of microscopy. As demonstrated in several works (Andersen *et al.*, 2008, 2009; Oliveira *et al.*, 2010), the use of scattering methods permits a direct access to the ensemble-average structure and, therefore, also gives information on the assembly efficiency.

The possibility of combining several types of models, including also models with different electron densities for each component with a low number of parameters describing the system, provides a powerful tool for modelling and analysing scattering data.

The procedure is implemented in a program called *POLYGEN*, which is available upon request to the corresponding author.

CLPO was supported by FAPESP, CNPq and INCT(Fcx). CA was supported by CAPES, CNPq and INCT(Fcx).

References

Aldaye, F. A. & Sleiman, H. F. (2007). *J. Am. Chem. Soc.* **129**, 10070–10071.

Andersen, E. S., Dong. M, Nielsen, M. M., Jahn, K., Subramani, R., Mamdouh, W., Golas, M. M., Sander, B., Stark, H., Oliveira, C. L., Pedersen, J. S., Birkedal, V., Besenbacher. F., Gothelf, K. V. & Kjems, J. (2009). *Nature*, **459**, 73–76.

Andersen, F. F. *et al.* (2008). *Nucleic Acids Res.* **36**, 1113–1119.

Bhatia, D., Mehtab, S., Krishnan, R., Indi, S., Basu, A. & Krishnan, Y. (2009). *Angew. Chem.* **48**, 4134–4137.

Bou Sleiman, H., Ritacco, L. E., Aponte-Tinao, L., Muscolo, D. L., Nolte, L. P. & Reyes, M. (2011). *Ann. Biomed. Eng.* **39**, 1720–1727.

Coxeter, H. S. M. (1973). *Regular Polytopes*, 3rd ed. New York: Dover Publications.

Chacón, P., Morán, F., Díaz, J. F., Pantos, E. & Andreu, J. M. (1998). *Biophys. J.* **74**, 2760–2775.

Chand, D. R. & Kapur, S. S. (1970). *J. Assoc. Comput. Mach.* **17**, 78–86.

Chen, J. H. & Seeman, N. C. (1991). *Nature*, **350**, 631–633.

Debye, P. (1915). *Ann. Phys.* **46**, 809–823.

Dietz, H., Douglas, S. M. & Shih, W. M. (2009). *Science*, **325**, 725–730.

Douglas, S. M., Dietz, H., Liedl, T., Hoegberg, B., Graf, F. & Shih, W. M. (2009). *Nature*, **459**, 414–418.

Endo, M., Hidaka, K., Kato, T., Namba, K. & Sugiyama, H. (2009). *J. Am. Chem. Soc.* **131**, 15570–15571.

Erben, C. M., Goodman, R. P. & Turberfield, A. J. (2006). *Angew. Chem.* **45**, 7414–7417.

Erben, C. M., Goodman, R. P. & Turberfield, A. J. (2007). *J. Am. Chem. Soc.* **129**, 6992–6993.

Evrard, G., Mareuil, F., Bontems, F., Sizun, C. & Perez, J. (2011). *J. Appl. Cryst.* **44**, 1264–1271.

Falconi, M., Oteri, F., Chillemi, G., Andersen, F., Tordrup, D., Oliveira, C., Pedersen, J., Knudsen, B. & Desideri, A. (2009). *ACS Nano*, **3**, 1813–1822.

Feigin, L. & Svergun, D. (1987). *Structure Analysis by Small-Angle X-ray and Neutron Scattering.* New York: Plenum Press.

Glatter, O. (1972). *Acta Phys. Aust.* **36**, 307–315.

Glatter, O. (1977). *J. Appl. Cryst.* **10**, 415–421.

Glatter, O. & Kratky, O. (1982). *Small Angle X-ray Scattering.* London: Academic Press.

Goodman, R. P., Schaap, I. A. T., Tardin, C. F., Erben, C. M., Berry, R. M., Schmidt, C. F. & Turberfield, A. J. (2005). *Science*, **310**, 1661–1665.

Hamilton, T. D. & MacGillivray, L. R. (2004). *Cryst. Growth Des.* **4**, 419–430.

Han, D., Pal, S., Nangreave, J., Deng, Z., Liu, Y. & Yan, H. (2011). *Science*, **332**, 342–346.

Hansen, S. (1990). *J. Appl. Cryst.* **23**, 344–346.

He, Y., Su, M., Fang, P.-A., Zhang, C., Ribbe, A. E., Jiang, W. & Mao, C. (2010). *Angew. Chem. Int. Ed. Engl.* **49**, 748–751.

He, Y., Ye, T., Su, M., Zhang, C., Ribbe, A. E., Jiang, W. & Mao, C. (2008). *Nature*, **452**, 198–201.

Jarvis, R. A. (1973). *Inf. Process. Lett.* **2**, 18–21.

Jones, R. A. L. (2002). *Soft Condensed Matter.* Oxford University Press.

Kato, T., Goodman, R. P., Erben, C. M., Turberfield, A. J. & Namba, K. (2009). *Nano Lett.* **9**, 2747–2750.

Ke, Y., Sharma, J., Liu, M., Jahn, K., Liu, Y. & Yan, H. (2009). *Nano Lett.* **9**, 2445–2447.

Koradi, R., Billeter, M. & Wüthrich, K. (1996). *J. Mol. Graph.* **14**, 51–55.

Li, Z., Wei, B., Nangreave, J., Lin, C., Liu, Y., Mi, Y. & Yan, H. (2009). *J. Am. Chem. Soc.* **131**, 13093–13098.

Oliveira, C., Juul, S., Jorgensen, H., Knudsen, B., Tordrup, D., Oteri, F., Falconi, M., Koch, J., Desideri, A., Pedersen, J., Andersen, F. & Knudsen, B. (2010). *ACS Nano*, **4**, 1367–1376.

Oteri, F., Falconi, M., Chillemi, G., Andersen, F. F., Oliveira, C. L. P., Pedersen, J. S., Knudsen, B. R. & Desideri, A. (2011). *J. Phys. Chem. C*, **115**, 16819–16827.

Pantos, E. & Bordas, J. (1994). *Pure Appl. Chem.* **66**, 77–82.

Pedersen, J. S. (1997). *Adv. Colloid Interface Sci.* **70**, 171–210.

Pedersen, J. S., Oliveira, C. L., Hübschmann, H. B., Arleth, L., Manniche, S., Kirkby, N. & Nielsen, H. M. (2012). *Biophys. J.* **102**, 2372–2380.

Perry, J. J., Perman, J. A. & Zaworotko, M. J. (2009). *Chem. Soc. Rev.* **38**, 1400–1417.

Petoukhov, M. V. & Svergun, D. I. (2005). *Biophys. J.* **89**, 1237–1250.

Petoukhov, M. V. & Svergun, D. I. (2013). *Int. J. Biochem. Cell Biol.* **45**, 429–437.

Pettersen, E. F., Goddard, T. D., Huang, C. C., Couch, G. S., Greenblatt, D. M., Meng, E. C. & Ferrin, T. E. (2004). *J. Comput. Chem.* **25**, 1605–1612.

Preparata, F. P. & Shamos, M. I. (1985). *Computational Geometry: an Introduction.* New York: Springer-Verlag.

Press, W. H. (1992). *Numerical Recipes in FORTRAN: the Art of Scientific Computing.* Cambridge University Press.

Rothemund, P. W. K. (2006). *Nature*, **440**, 297–302.

Seeman, N. C. (2010). *Ann. Rev. Biochem.* **79**, 65–87.

Seidel, S. R. & Stang, P. J. (2002). *Acc. Chem. Res.* **35**, 972–983.

Semenyuk, A. V. & Svergun, D. I. (1991). *J. Appl. Cryst.* **24**, 537–540.

Shih, W. M., Quispe, J. D. & Joyce, G. F. (2004). *Nature*, **427**, 618–621.

Stuhrmann, H. B. (1970). *Acta Cryst.* A**26**, 297–306.

Svergun, D. I. (1999). *Biophys. J.* **76**, 2879–2886.

Svergun, D. I. & Stuhrmann, H. B. (1991). *Acta Cryst.* A**47**, 736–744.

electronic reprint

Svergun, D. I., Volkov, V. V., Kozin, M. B. & Stuhrmann, H. B. (1996). *Acta Cryst.* A**52**, 419–426.
Uchida, M., Klem, M., Allen, M., Suci, P., Flenniken, M., Gillitzer, E., Varpness, Z., Liepold, L., Young, M. & Douglas, T. (2007). *Adv. Mater.* **19**, 1025–1042.
Volkov, V. V. & Svergun, D. I. (2003). *J. Appl. Cryst.* **36**, 860–864.
Walsh, A. S., Yin, H., Erben, C. M., Wood, M. J. A. & Turberfield, A. J. (2011). *ACS Nano*, **5**, 5427–5432.
Walther, D., Cohen, F. E. & Doniach, S. (2000). *J. Appl. Cryst.* **33**, 350–363.
Wassenaar, T. A. *et al.* (2012). *J. Grid Comput.* **10**, 743–767.
Yang, H., McLaughlin, C. K., Aldaye, F. A., Hamblin, G. D., Rys, A. Z., Rouiller, I. & Sleiman, H. F. (2009). *Nat. Chem.* **1**, 390–396.
Zhang, C., Su, M., He, Y., Zhao, X., Fang, P. A., Ribbe, A. E., Jiang, W. & Mao, C. (2008). *Proc. Natl Acad. Sci. USA*, **105**, 10665–10669.
Zhang, Y. W. & Seeman, N. C. (1994). *J. Am. Chem. Soc.* **116**, 1661–1669.
Zhou, J., Deyhim, A., Krueger, S. & Gregurick, S. (2005). *Comput. Phys. Commun.* **170**, 186–204.
Zimmermann, J., Cebulla, M. R. J., Moenninghoff, S. & Kiedrowski, G. von (2008). *Angew. Chem. Int. Ed. Engl.* **47**, 3626–3630.

electronic reprint

Biophysical Journal Volume 106 June 2014 2595–2605

Effect of Oxidation on the Structure of Human Low- and High-Density Lipoproteins

Cristiano L. P. Oliveira,* Priscila R. Santos, Andrea M. Monteiro, and Antonio M. Figueiredo Neto
Instituto de Física, Universidade de São Paulo, São Paulo, Brazil

ABSTRACT This work presents a controlled study of low-density lipoprotein (LDL) and high-density lipoprotein (HDL) structural changes due to in vitro oxidation with copper ions. The changes were studied by small-angle x-ray scattering (SAXS) and dynamic light scattering (DLS) techniques in the case of LDL and by SAXS, DLS, and Z-scan (ZS) techniques in the case of HDL. SAXS data were analyzed with a to our knowledge new deconvolution method. This method provides the electron density profile of the samples directly from the intensity scattering of the monomers. Results show that LDL particles oxidized for 18 h show significant structural changes when compared to nonoxidized particles. Changes were observed in the electrical density profile, in size polydispersity, and in the degree of flexibility of the APO-B protein on the particle. HDL optical results obtained with the ZS technique showed a decrease of the amplitude of the nonlinear optical signal as a function of oxidation time. In contrast to LDL results reported in the literature, the HDL ZS signal does not lead to a complete loss of nonlinear optical signal after 18 h of copper oxidation. Also, the SAXS results did not indicate significant structural changes due to oxidation of HDL particles, and DLS results showed that a small number of oligomers formed in the sample oxidized for 18 h. All experimental results for the HDL samples indicate that this lipoprotein is more resistant to the oxidation process than are LDL particles.

INTRODUCTION

Cholesterol is a hydrophobic molecule that is essential for the structure of the cell membrane and is a precursor of bile acids, vitamin D, and other steroids. Plasma lipoproteins are responsible for the transport of cholesterol between cells. These quasispherical particles of different size and composition are composed of a lipid core of triglycerides and cholesterol esters surrounded by a monolayer of phospholipids, free cholesterol, and apolipoproteins (Apo). Apolipoproteins are essential for the structural integrity of the particle in addition to controlling lipoprotein metabolism through binding to specific cell-membrane receptors (1,2). The low-density lipoprotein (LDL), responsible for the delivery of cholesterol to peripheral tissues, has only one apolipoprotein (ApoB, predominantly B-100) (3), whereas high-density lipoproteins (HDLs), which mediate the inverse process of cholesterol transport (4), contain several apolipoproteins (e.g., ApoA, C, and E) (5,6).

It is well established that lipoproteins play a key role in atherosclerosis. This illness is the leading cause of death in the western world. It is characterized as a dynamic and progressive inflammatory disease that promotes lipid deposition in the arteries that may result in the formation of atherosclerotic plaques in the intima of the vessel. Elevated (reduced) plasma levels of LDL (HDL) are associated with an increase of coronary artery disease (CAD) (7,8).

LDL particles can undergo a modification process due to the action of reactive oxygen species (ROS) and reactive nitrogen species (RNS). The oxidation of LDL is a complex process that begins with the peroxidation of some polyunsatured fatty acids (PUFAs), mainly phospholipids and cholesteryl esters. Moreover, the oxidation products cause changes in the ApoB conformation and affect the functional properties of LDL (9). Structural and/or chemical changes generate different types of modified LDL particles (mLDL), of which one of the most common is oxidized LDL (oxLDL). OxLDL is removed by intima macrophages via scavenger receptors that are not downregulated, causing an excessive intracellular accumulation of LDL and foam-cell formation (10). This process characterizes the first phase of atheroma plaque formation. Studies show that in contrast, HDL may play an antiatherogenic and antithrombotic role (11) by protecting LDL against lipid peroxidation and reducing the deleterious effect of the oxLDL (12–14).

There are few methods to quantify the oxLDL in the plasma. Gomez et al. (15) developed a new method to determine the concentration of oxLDL by measuring the nonlinear optical response of LDL solutions. The Z-Scan (ZS) technique was used to investigate the nonlinear optical properties of native LDL and oxLDL. The higher the degree of oxidation of LDL particles, the smaller was the nonlinear optical signal. Applying the ZS technique, Monteiro et al. (16) showed that periodontitis patients have higher concentrations of modified LDL compared to individuals without periodontal disease. Moreover, periodontal treatment reduced the concentration of oxLDL in the plasma (17).

The use of small angle x-ray scattering (SAXS) to study the structure of HDL and LDL particles dates back to the 1970s. Laggner and co-workers suggested that HDL particles were spherical objects with an average diameter of 9.6 nm (18). That work and others of the same period presented the first electron density profiles of HDL and LDL particles obtained by SAXS measurements made using

Submitted February 24, 2014, and accepted for publication April 30, 2014.
*Correspondence: crislpo@if.usp.br
Editor: Lukas Tamm
© 2014 by the Biophysical Society
0006-3495/14/06/2595/11 $2.00

http://dx.doi.org/10.1016/j.bpj.2014.04.049

simplified procedures, which were only capable of providing an overview of the internal structure of these lipoprotein particles. Scattering results also suggested that the LDL particles are spherical in shape, with an average diameter of 24 nm and a possible lamellar organization of the lipid core (19,20). Since these seminal works, methods for analyzing results obtained using the SAXS technique have evolved significantly. The deconvolution square-root procedure proposed by Glatter (21,22) has been applied in several studies of lipoproteins (23). Such studies represented important advances in understanding the structure of lipoproteins. For example, SAXS results for measurements of in vitro oxLDL particles showed no major structural changes in samples oxidized with copper for <25 h (23). Over the past 40 years, knowledge about lipoprotein structure has expanded considerably, but several questions about cholesterol packing in the inner region of LDL particles and the conformational orientation of apolipoproteins remain (24–26). Recent studies with cryomicroscopy point to a lamellar organization of cholesterol in the inner region of LDL particles and to the influence of triglycerides on the temperature at which the transition from this lamellar phase to a disorganized one occurs (27).

In this work, we investigate the structure of LDL and HDL particles using the SAXS technique and present to our knowledge a new approach for analysis of these data. This approach was originally developed by Oliveira and co-workers to model experimental curves of scattering intensity and obtain electron density profiles of lamellar systems (28). The model was adapted to systems with spherical symmetry so that it could be used for LDL and HDL SAXS data. The obtained fits of the experimental scattering curves are significantly better than those reported in the literature (19,20,23), producing more accurate and reliable curves for the electron density profile. The discussion of the results and analysis of the structural properties of the particles is complemented by dynamic light scattering (DLS) measurements and the nonlinear optical response of the particles. As this response has already been discussed in the literature for LDL particles, ZS experiments were performed with HDL solutions to get a complete set of data for both lipoproteins.

MATERIALS AND METHODS

Isolation and oxidation of LDL and HDL

Blood was drawn from healthy normolipidemic donors, and the plasma was obtained after centrifugation at 1000 × *g* at 4°C for 15 min. Benzamidine (2 mM), chloramphenicol (0.25%), phenylmethylsulfonyl fluoride (0.5 mM), gentamicin (0.5%), and aprotinin (0.1 U/mL) were added to the plasma. LDL (1.006 < d < 1.063 mg/dL) and HDL (1.063 < d < 1.21 mg/dL) were isolated by density difference in a sequential ultracentrifugation (29) process at $10^5 \times g$ at 4°C, using the rotor of an ultracentrifuge (Hitachi Ultracentrifuge, Tokyo, Japan). The obtained samples with LDL and HDL were dialyzed for 24 h at 4°C against phosphate-buffered saline (PBS), pH 7.4. The LDL and HDL were put through a filter with micrometer-sized pores (Millipore, Schwalbach, Germany), and the protein concentration was determined using a bicinchoninic acid protein assay kit (Pierce, Stowe, VT), with bovine serum albumin as standard.

In vitro oxLDL and oxHDL were obtained by incubation of native LDL (naLDL) and HDL (naHDL), respectively, with 20 μM $CuSO_4$/mg protein at 37°C (30). The samples were oxidized for 5, 30, and 60 min, 6 h, and 18 h (Table 1). At each predefined time, the oxidation reaction was inhibited with the addition of 1 mM of EDTA to the sample solution. After this procedure, HDL and LDL samples are ready to be used.

Z-scan

The ZS setup was composed of a continuous-wave Nd:YVO_4 ($\lambda = 532$ nm) Verdi V10 laser from Coherent (Santa Clara, CA), with a Gaussian profile beam. In this setup, the laser beam was chopped at 17 Hz and focused by a 25.4 mm lens with focal distance $f = 150$ mm, which gave a Rayleigh length of $z_0 = 3.84 \pm 0.20$ mm (31). In these conditions, the beam (consecutively) illuminates the sample during the time interval $\Delta t = 30$ ms. A silicon photodetector (PDA36A, THORLABS, Newton, NJ), positioned at the far field, collected the transmitted light. All HDL samples were investigated using glass sample holders 200 μm thick and 180 mW of incident power of the laser on the samples. In the ZS experiment, the sample is moved along the z axis, around the laser-beam focus position. The detector collects the transmitted light as a function of the z-position and time $I(z,t)$. At a given z-position the transmittance is recorded during the time $0 < t < \Delta t$. The z-dependence of the normalized transmittance, $\Gamma_N(z)$, is written as (31):

$$\Gamma_N(z) = \frac{I(z,t=0) - I(z,t=\Delta t)}{I(z,t=\Delta t)} = \theta\left(\frac{2(z/z_0)}{1+(z/z_0)^2}\right) + \theta^2\left(\frac{1}{1+(z/z_0)^2}\right), \quad (1)$$

where θ is a dimensionless parameter that measures the strength of the thermal lens formed in the sample. The typical ZS-position-dependent curve has a peak and a valley. The peak to valley amplitude is proportional to the parameter θ. Thus, the bigger θ is, the larger is the peak-to-valley amplitude and, consequently, the thermal lens strength. Each measurement was repeated 10 times in 80 different z-positions around the beam waist. The data were analyzed using the Thermal Lens model (31). More details about the setup, data acquisition, and data treatment can be found in a previous work (32).

SAXS

LDL SAXS measurements were performed at the Brazilian Synchrotron Light Laboratory (LNLS) at the SAXS1 beamline (33). The sample holder, a cell with dimensions $1 \times 4 \times 8$ mm^3 and mica windows, was connected to a thermal bath, enabling LDL sample measurements with the temperature controlled at 22°C. The wavelength of the incoming monochromatic

TABLE 1 Descriptions of all lipoprotein samples

Sample	Description
naLDL	Native LDL
oxLDL-05min	LDL oxidized with Cu for 5 min
oxLDL-30min	LDL oxidized with Cu for 30 min
oxLDL-60min	LDL oxidized with Cu for 60 min
oxLDL-6h	LDL oxidized with Cu for 6 h
oxLDL-18h	LDL oxidized with Cu for 18 hours
naHDL	Native HDL
oxHDL-30min	HDL oxidized with Cu for 30 min
oxHDL-60min	HDL oxidized with Cu for 60 min
oxHDL-18h	HDL oxidized with Cu for 18 h

x-ray beam was $\lambda = 1.48$ Å, and the distance between the sample and the detector was set to 3200 mm, providing a q (scattering vector modulus) interval from 0.006 to 0.25 $Å^{-1}$, where $q = 4\pi(\sin\xi)/\lambda$ and 2ξ is the scattering angle. The 2D scattering data were collected on a Pilatus 300k detector (Dectris, Baden, Switzerland), and integration of the SAXS patterns and data treatment were performed using FIT2D software (34). Error estimation and normalization to absolute scale were performed with the SUPERSAXS package (C. L. P. Oliveira and J. S. Pedersen, unpublished). A beam size of 300×100 μm was used. This beam size is further convoluted with a detector resolution of 172 μm. The experimental setup provided a spacing in q values of $\Delta q = 0.00042 Å^{-1}$.

HDL SAXS measurements were performed on the laboratory SAXS instrument Nanostar (Bruker, Billerica, MA) at the Institute of Physics, University of São Paulo. This equipment is improved by the use of microfocus source Genix3D coupled with Fox3D multilayer optics and two sets of scatterless slits for beam definition, all provided by Xenocs (Sassenage, France). The samples were kept on a quartz capillary glued to a stainless-steel case, which facilitated proper rinse and reuse of the sample holder, permitting an accurate background subtraction. The scattering of water measured on the same sample holders was used to normalize the data to absolute scale. The sample temperature was controlled by a circulating bath and was kept constant at 25°C. Several 900 s frames were recorded for each sample to monitor radiation damage and beam stability. The wavelength of the incoming monochromatic x-ray beam was $\lambda = 1.54$ Å ($Cu_{k\alpha}$) and the sample-to-detector distance was 0.67 m, providing a q interval from 0.009 to 0.35 $Å^{-1}$. The 2D scattering data were collected on a Vantec2000 detector (Bruker), and integration of the SAXS patterns was performed using Bruker SAXS software. The data treatment, normalization to absolute scale, and averaging procedures were performed using the SUPERSAXS package (C. L. P. Oliveira and J. S. Pedersen, unpublished). A beam size of 1 mm in diameter was used. This beam size is further convoluted with a detector resolution of 160 μm. The experimental setup provided a q-value spacing of $\Delta q = 0.00142 Å^{-1}$.

The treated and normalized SAXS data for the sample series of LDL and HDL is shown in Fig. S1 in the Supporting Material.

SAXS data analysis and modeling

The analysis of the SAXS data was performed in several steps. First, the data were analyzed by the indirect Fourier transformation (IFT) method (35) in a slightly different implementation (36,37). The IFT fits for several data sets and the corresponding $p(r)$ functions are shown in Fig. S2, *a* and *b*. From these analyses, initial information about size, shape, and possible aggregation were obtained. For the LDL samples, it was observed that the presence of oligomers or larger aggregates depends on the level of oxidation. Interestingly, for the HDL samples, no aggregation was detected. To be able to analyze the contribution only from the LDL particles, not from the aggregates, it is necessary to decouple the form and structure factors of the scattering data. We were able to do so using the generalized IFT method (GIFT) (36). In this case, a theoretical function is used for the structure-factor contribution and it is possible, by simultaneous optimization of the $p(r)$ function (form-factor) and structure-factor parameters, to obtain the theoretical form factor without the structure-factor contribution. For the case of HDL, this decoupling procedure was not necessary.

Having the form factors for each case, a new analysis method was used. This procedure is based on the square-root deconvolution method originally proposed by Glatter (21,22), but with a different implementation, similar to that proposed by Oliveira (28). In the original method proposed by Glatter, modeling was performed by fitting the $p(r)$ curve. This approach limits the generality of the model, since only spherical (cylindrical and lamellar) systems could be studied, without the inclusion of any kind of anisotropy. In the proposed new method, since the scattering data are adjusted, it is possible to introduce several types of anisotropy, e.g., as polydispersity, as well as to perform a simultaneous fitting of additional backgrounds to the scattering data and several other types of contribution (28).

The description of the normalized intensity form factor ($P(q)$) and amplitude form factor ($A(q)$) is performed using an analytical or semianalytical expression that can be written as

$$P_{MOD}(q) = \frac{\int_0^\infty D(r)m(r)^2 P_{Mon}(q,r)dr}{\int_0^\infty D(r)m(r)^2 dr} \tag{2}$$

$$A_{MOD}(q) = \frac{\int_0^\infty D(r)m(r)^2 A_{Mon}(q,r)dr}{\int_0^\infty D(r)m(r)^2 dr}, \tag{3}$$

where a number distribution polydispersity in size was assumed. Several types of distribution, for example, Shulz-Zimm distributions, can be assumed. The function $m(r)$ depends on the assumed geometry. For spheroidal particles, $m(r) = V$, where V is the particle volume. Different geometries may have different weighting functions. The intensity and amplitude form factors, $P_{Mon}(q)$ and $A_{Mon}(q)$ for ellipsoidal particles are given by

$$P_{Mon}(q) = \int_0^{\pi/2} \left(F_M[q, r(R,\varepsilon,\alpha)] \exp\left[-\frac{1}{2} q^2 \sigma_{\text{int}} \right] \right)^2 \sin\alpha \, d\alpha \tag{4}$$

$$A_{Mon}(q) = \int_0^{\pi/2} F_M[q, r(R,\varepsilon,\alpha)] \exp\left[-\frac{1}{2} q^2 \sigma_{\text{int}} \right] \sin\alpha \, d\alpha, \tag{5}$$

where $r(R, \varepsilon, \alpha) = R(\sin^2\alpha + \varepsilon \cos^2\alpha)^{1/2}$ is the radial element for the integration, R is the transversal radius, and εR is the vertical radius of the ellipsoid of revolution. The Gaussian term on the formula provides a smearing of the interface.

The function $F_M(q,R)$ describes an ellipsoidal particle with several shells of different electron density (Fig. 1) and is given by

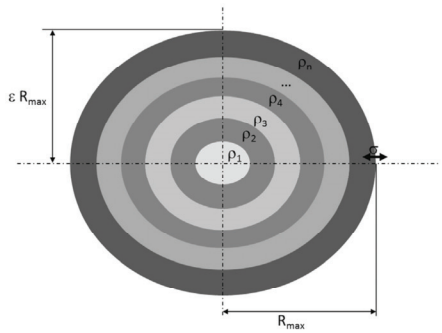

FIGURE 1 Schematic drawing of the model used to obtain the electron density profile of lipoproteins. R_{max} is the maximum radius of the particle and ε is its anisotropy. Thus, if $\varepsilon = 1$, the particle is spherical, if $\varepsilon < 1$, it is an oblate spheroid, and if $\varepsilon > 1$, the particle has the shape of a prolate spheroid.

$$F_M(q) = \frac{1}{M_M}\left[\rho_1 m(R_1)F_S(q,R_1) + \sum_{i=2}^{N}(\rho_i - \rho_{i-1})m(R_i)F_S(q,R_i)\right] \quad (6)$$

$$M_M = \rho_1 m(R_1) + \sum_{i=2}^{N} m(R_i)(\rho_i - \rho_{i-1}), \quad (7)$$

where ρ_i is the electron density for the ith layer, N is the number of shells/layers describing the model, and $F_S(q,R)$ is the amplitude form factor for a sphere of radius R:

$$F_S(q,R) = \frac{3[\sin(qR) - qR\cos(qR)]}{(qR)^3}. \quad (8)$$

The final expression used for fitting the theoretical data is

$$I(q) = S_{C_1}P_{MOD}(q) + S_{C_2}P_{Deb}(q) + Back. \quad (9)$$

In this expression, the form factor $P_{MOD}(q)$ is defined in Eq. 1, S_{C1} and S_{C2} are scale factors, *Back* is a constant background, and $P_{Deb}(q)$ is the intensity factor for the scattering from a Gaussian chain, given by

$$P_{Deb}(q) = 2[\exp(-u) + u - 1]/u^2, \quad (10)$$

where $u = Rg^2q^2$, where Rg is the average radius of gyration of the Gaussian chain. This expression was used to describe two general features of the lipoprotein systems that may directly affect the scattering data. The first is the presence of proteins on the surface of the lipoprotein (ApoB for LDL and several proteins for HDL), which introduce a break in symmetry in the system that naturally makes the form-factor minima shallower. Also, those proteins can have floppy or flexible regions that can also be described by Eq. 10.

In the results shown in this work, a total of $N = 10$ shells was considered in Eq. 6. The modeling parameters are the electron densities, ρ_i, of each shell; the maximum radius of the particle; the polydispersity in radius, assuming a Shulz-Zimm distribution; the particle anisotropy, ε (>1 for prolate and <1 for oblate); two scale factors, S_{C1} and S_{C2}, the radius of gyration of the Gaussian chain, and a constant background. All these parameters were optimized in the same fitting procedure. We used a nonlinear partially constrained least-squares fitting (28,38) in which the ρ_i values are stabilized by the use of a Lagrange multiplier that is varied during the fitting procedure. The best value of this Lagrange multiplier is automatically determined by the modeling procedure.

Dynamic light scattering (DLS)

The DLS technique was used to evaluate the particle-size distribution on the samples. LDL measurements were performed using a Zetasizer Nano ZS (Malvern, Worcestershire, United Kingdom) at the Institute of Chemistry, University of São Paulo. The experimental setup was composed of a 633 nm wavelength laser beam and a photon detector positioned at 7° (with respect to the detector). HDL measurements were performed using a 90Plus Particle Size Analyzer (Brookhaven, Holtsville, NY) located at the Institute of Physics, University of São Paulo. The setup was composed of a laser beam with wavelength 657 nm and a detector positioned at 90°. Temporal autocorrelation curves were obtained using standard routines of the acquisition programs. Through standard DLS models and the Contin method (39), we calculated the average diameter of monomers and clusters comprising the samples. The DLS experiment was performed in homodyne mode on both instruments.

RESULTS

SAXS results

Low-density lipoproteins

The analysis of LDL samples started with the use of the IFT method. The obtained pair distance distribution functions, ($p(r)$), for all samples showed a well-defined monomeric region and a second region that could be related to the presence of small oligomers in the samples (data shown only in Fig. S2, *a* and *b*). Decoupling of the monomer contribution (form factor) and the small-oligomer contribution (structure factor) was performed using the GIFT method (36). One example of fitting and its contributions is shown in Fig. 2. In this case, we used a structure factor of a fractal system (40). One can clearly see that this model is able to describe the full SAXS curve. It is easy to see that the form factor detaches from the experimental data for small q values, suggesting that this region of the scattering data is dominated by larger objects, the LDL oligomers, which are then described by the structure factor. The presence of such oligomers is supported both by IFT analysis of LDLs (Fig. S2 *b*) and by previous TEM studies (41). In all LDL samples, the clusters were best fitted as fractals, with fractal dimension compatible with 3.0, indicating that they were volume (3D) fractals. Since just a few points are related to the structure factor on the SAXS profile, the average size/correlation of such fractals (the so-called cutoff length on the model used (40)) was not well defined and varied between ~2000 and ~4000 Å. In any case, the modeling of such oligomers is an approximation and has to be viewed as a procedure to decouple the best form factor for this system.

The maximum appearing at $q = 0.17$ Å^{-1} in the experimental scattering data (Fig. 3 *a*), is related to the repetition distance of ~37 Å associated with a lamellar packing of the lipid content in the LDL core (27). The lamellae are composed of two bound molecules of cholesterol esters.

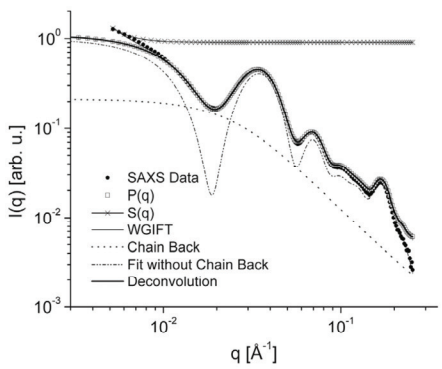

FIGURE 2 Example of data fitted with the GIFT and deconvolution methods, showing the contribution of each component in the fit. For details, see text.

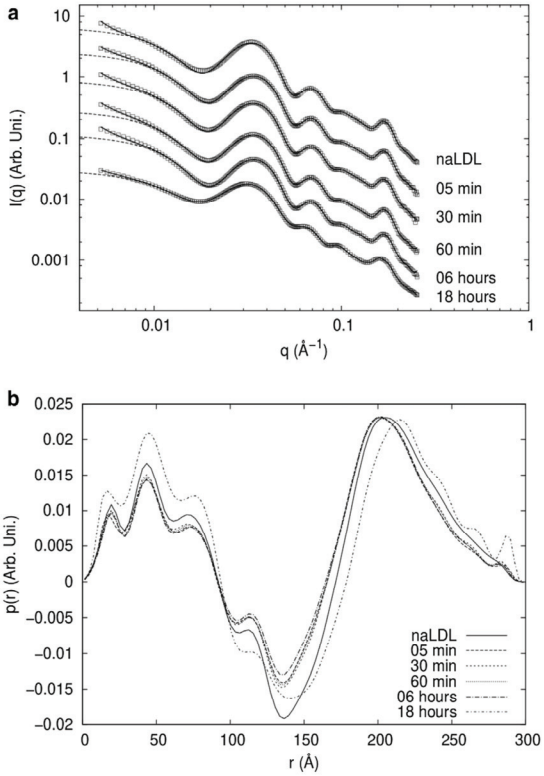

FIGURE 3 GIFT applied to LDL SAXS data. (*a*) Fitting (*solid curve*) of scattering data of LDL samples by the GIFT method. Also shown are the form factors (*dashed curves*) obtained from the decoupling procedure. (*b*) Pair distance distribution functions, $p(r)$, obtained with the GIFT method for LDL samples.

This maximum appears in the scattering data of all samples, but oxLDL-18 h has a broader maximum. These results show that the internal lamellar packing is preserved, at least partially, during the oxidation process.

The $p(r)$ curves obtained for the LDL particles show very similar features in the region between 0 and 300 Å for native LDL (naLDL) and oxLDL samples (Fig. 3 *b*). The maximum at ~200 Å is shifted to higher values in the oxLDL-18h sample, which might indicate changes in the electron density profile of LDL in this sample. The $p(r)$ curves obtained for the other oxLDL samples did not show clear differences when compared to the $p(r)$ from the naLDL sample.

Using the GIFT method, it is possible to obtain a good extrapolation for the form factor at angles lower than that given in the original experimental data. This is very important when using the deconvolution procedure to improve modeling stability. By using this to our knowledge new modeling method, it is possible to obtain a very good fit of the experimental data and calculate the electron density profile of the lipoproteins. To fit the form factor, we used a fixed anisotropy of 0.9, because LDL particles are known to be slightly oblate (42). The fixation of this parameter was necessary to improve the modeling stability, since anisotropy and size polydispersity can be correlated. The fitting parameters were the average radius, the size polydispersity, the constant background, and the scale factors. The radius of gyration of the Gaussian chain was determined for native LDL (naLDL) as 54 ± 5 Å, and this value was kept fixed for the other oxLDL samples. The fitting results can be seen in Fig. 4 *a* and the electron density profiles are shown in Fig. 4 *b*.

It is possible to observe several oscillations in the LDL electron density profile, which can be understood as variations on the electron density profile of the LDL particle. Interestingly, the positive-negative variation observed between ~100 and 140 Å, corresponds approximately to the length of phosphatidylcholine, the primary phospholipid in the LDL outer layer. This outer particle surface also has the presence of ApoB, which may slightly alter the height of these oscillations and probably is

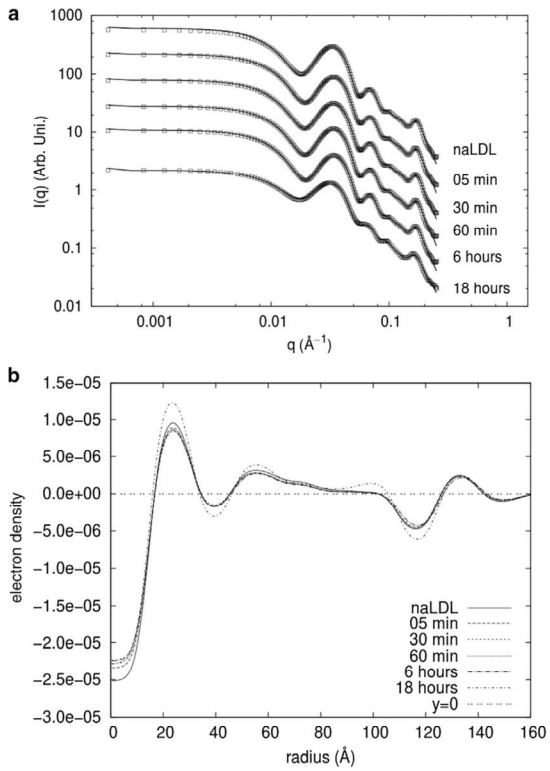

FIGURE 4 Deconvolution procedure applied to modeling of LDL SAXS data. (*a*) Form factor fitted with the deconvolution modeling procedure. Experimental data (*open squares*) and model fit (*solid lines*) are shown. (*b*) Electron density profiles of LDL samples obtained with the deconvolution modeling procedure.

responsible for the negative density that occurs for radius values >140 Å. For radius values <100 Å, it is possible to observe other systematic variations in the electron density profile that are related to the well-defined region (oriented) in the center of the particle. This large variation in electron density profile may be due to the existing lamellar organization within LDL particles, which is associated with the maximum correlation curves scattering at $q = 0.17$ Å^{-1}. It is noteworthy that the sample oxLDL-18h has a significantly different electron density profile when compared with less oxidized and native LDL profiles. This difference indicates changes in both the core region and the phospholipid layer on the 18-h-oxidized particles.

The parameters obtained by deconvolution are shown in Table 2. As can be seen, there was no evolution of the mean radius of particles as a function of sample oxidation time. Moreover, size polydispersity of LDL particles increased significantly for the oxLDL-18h sample. Taking into account that polydispersity is ~15 Å for all samples, the obtained particle sizes are consistent with those presented in the literature (27,41).

Interestingly, there is a significant change in the Debye scale factor (S_{C2} in Eq. 9) for the sample oxidized for 18 h (Table 2). This can be interpreted as an increase in the amount of flexible chains of ApoB exposed on the surface of LDL particles. This result is consistent with the idea that LDL oxidation occurs initially on the lipids and also at ApoB hydrophobic sites (43,44). These sites, initially immersed in the region of phospholipid carbon chains, become exposed when oxidized.

High-density lipoproteins

HDL samples did not show evidence of oligomerization, and therefore, it was not necessary to apply the GIFT method to retrieve the form factor. Fig. 5, *a* and *b*, shows the experimental scattering data fitted with the IFT method and the obtained $p(r)$ curves. As can be seen from the scattering intensity and corresponding $p(r)$ curves, the results with HDL are very different from those obtained with the LDL samples. This indicates that there are important structural differences between the two types of lipoprotein. From the results, one can see that the oxidation process in HDL induces small changes in the scattering intensities and $p(r)$ curves, indicating that no significant structural changes are induced by oxidation.

TABLE 2 Parameters obtained by the deconvolution modeling procedure for LDL samples

Sample	Radius (Å)	Polydispersity (Å)	S_{C2}
naLDL	155.7 ± 2.8	14.3 ± 0.4	0.19 ± 0.05
05 min	155.6 ± 1.0	14.34 ± 0.24	0.203 ± 0.008
30 min	156.1 ± 0.8	14.07 ± 0.22	0.206 ± 0.007
60 min	155.4 ± 1.0	14.11 ± 0.25	0.204 ± 0.008
06 hours	156.7 ± 1.1	14.42 ± 0.20	0.206 ± 0.008
18 hours	156.0 ± 2.8	15.8 ± 0.6	0.292 ± 0.018

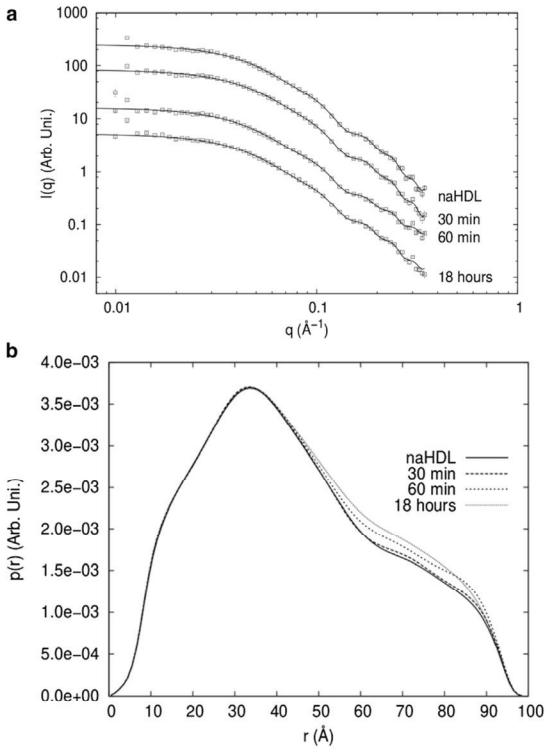

FIGURE 5 Indirect Fourier transform applied to HDL SAXS data. (*a*) HDL scattering intensity data fitted with the IFT method. Experimental data (*open squares*) and model fit (*solid lines*) are shown. (*b*) HDL pair distance distribution function curves, $p(r)$, obtained by the IFT method.

Fig. 6 *a* shows the experimental scattering data for HDL fitted with the deconvolution method. The results obtained with this method are shown in Table 3. Fitting results were obtained by fixing particle anisotropy at 1.0. This assumption was based on data from several studies in the literature that indicate that HDL particles are practically spherical. Also, similar to the LDL case, the fitting procedure is not stable if both anisotropy and polydispersity are optimized, since they make similar contributions to the scattering intensity. Another important aspect is that the contribution from a Gaussian chain was not important and always gave scale factors close to zero, with large uncertainty. Because of this, this parameter was not considered in the analysis procedure, and was fixed at zero. This is an interesting result and suggests that for HDL, the proteins should be located around the entire surface and not only in a particular region, as in the case of the LDL. Also, oxidation does not induce the appearance of floppy or flexible regions in the HDL structure.

HDL electron density profiles (Fig. 6 *b*) present a positive-negative variation between ~40 and 60 Å, which may correspond to the phospholipid monolayer region with the

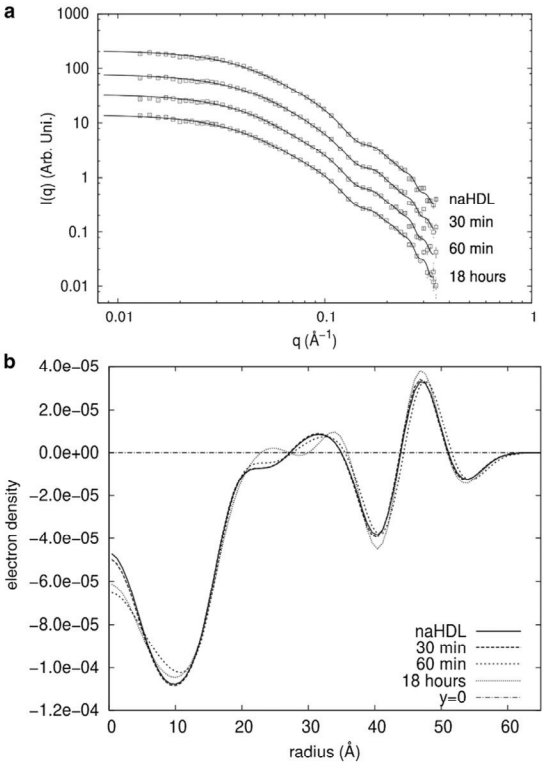

FIGURE 6 Deconvolution procedure applied to the modeling of LDL SAXS data. (*a*) HDL scattering intensity data fitted with the deconvolution modeling procedure. Experimental data (*open squares*) and model fit (*solid lines*) are shown. (*b*) Electron density profiles for HDL samples obtained with the deconvolution modeling procedure.

proteins immersed. This region does not vary between the different samples, suggesting that it is not affected by the oxidation of the samples. Likewise, all the curves converge to zero in the same radius value, indicating that the particle diameter does not change due to oxidation. Some small changes in the electron density profile are observed mainly below 30 Å and may be induced by oxidation effects.

The HDL electron density profiles have far fewer oscillations than those obtained for LDL samples, in agreement with the fact that these two lipoproteins have important structural and size differences. HDL particles have a less organized core than LDL particles and higher relative size polydispersity. In addition, the proteins that compose the two lipoprotein structures are very different. Although LDL particles have only ApoB, HDLs may contain serveral apolipoproteins, the amount varying from particle to particle (45). This variable number of proteins in HDL particles makes them intrinsically less monodisperse and with a less well defined structure compared to LDL particles. These peculiarities of HDL particles are reflected on the obtained electron density profiles and on the model results.

In any case, since it was not possible to observe any significant structural difference in HDL electron density profiles induced by copper oxidation, the SAXS results and modeling indicate that HDL particles are more resistant to copper oxidation than are LDL particles.

TABLE 3 Parameters obtained by the deconvolution modeling procedure for HDL samples

Sample	Radius (Å)	Polydispersity (Å)
naHDL	55 ± 6	8.5 ± 1.0
30 min	55 ± 3	8.3 ± 0.8
60 min	56 ± 7	8.7 ± 1.1
18 hours	55 ± 6	8.9 ± 1.0

DLS results

A comparison of the temporal autocorrelation curves of all LDL samples (Fig. S3 *a*) indicates that only the sample oxidized for 18 h shows a significant change. This difference is probably related to the increase in size polydispersity of the sample, which was also observed on the SAXS analyses. Fig. S3 *a* shows a slight variation in the temporal autocorrelation curve of oxLDL-6h as well. The experimental data and the fitting curve are slightly more visible from 300 μs and further.

It is possible to estimate the average diameter of the particles in each sample through the diameter distribution. The average diameter is taken as the maximum of the distribution and the uncertainty of each diameter as the width at two-thirds of the maximal high.

Experimental autocorrelation data from HDL samples can be seen in Fig. S3 *b*. The main information present in these curves is the appearance of clusters in the oxHDL-18h data, which is characterized by a slower decay compared to other autocorrelation curves. Although for naHDL and other oxidation curves the autocorrelation data reach (near) zero when $\tau = 100$ μs, the oxHDL-18h data reach (near) zero when $\tau = 400$ μs. These clusters have diameters estimated at 50 ± 17 nm, which may explain why they have not been observed in SAXS measurements, as the resolution of the experimental setup was ~70 nm. The obtained mean radius of each sample is presented in Table 4.

TABLE 4 Radius values obtained through DLS measurements

Sample	Mean diameter (nm)
naLDL	20 ± 6
oxLDL-05min	20 ± 6
oxLDL-30min	20 ± 6
oxLDL-60min	19 ± 6
oxLDL-6h	20 ± 6
oxLDL-18h	21 ± 7
naHDL	5.7 ± 2.3
oxHDL-30min	7.3 ± 2.5
oxHDL-60min	7.5 ± 2.9
oxHDL-18h	8 ± 4

ZS results

Typical results for normalized transmittance as a function of z-position of the sample are presented in Fig. 7 *a*. It can be observed that the peak-to-valley distance decreases with an increase in sample oxidation time. Through the fit to the experimental data using the thermal lens model (Eq. 1), we obtained the parameter θ of each sample, which is proportional to the peak-to-valley distance. Results show a decrease of θ as a function of sample oxidation time (Fig. 7 *b*). A similar behavior was observed with LDL particles (32,41). LDL samples stop presenting a nonlinear optical response ($\theta = 0$) at ~90 min of in vitro oxidation with copper, whereas HDL samples presented a nonlinear optical response (under the same experimental conditions) even after 18 h of in vitro oxidation time. This indicates that there are important differences between the two lipoprotein types in the oxidation process and also supports SAXS results indicating that HDL particles are more resistant to oxidation than LDL particles.

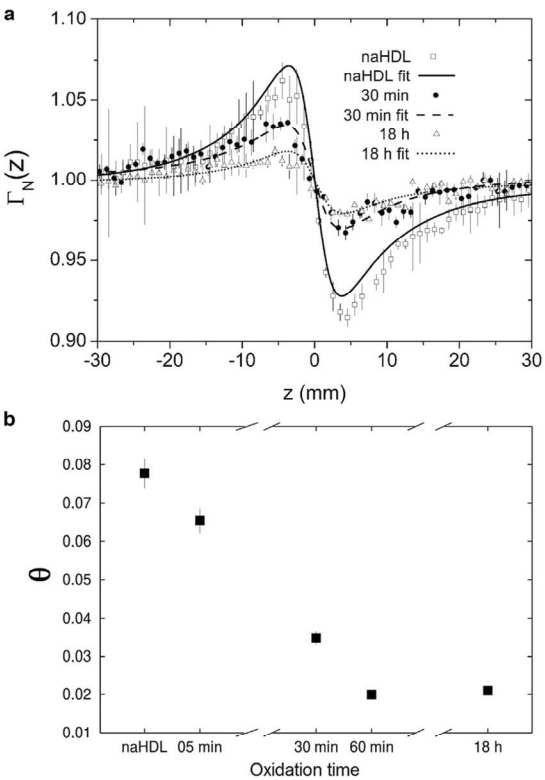

FIGURE 7 Results from ZS analysis. (*a*) Average nonlinear transmittance curves of naHDL, oxHDL-30min and oxHDL-18h. The solid and dashed lines are fits obtained with the thermal lens model. (*b*) θ parameter as a function of oxidation time for HDL samples, obtained with the thermal lens model.

DISCUSSION

The values of the average particle diameters for LDL and HDL samples obtained using the DLS and SAXS techniques show that oxidation process does not alter particle size. On the other hand, the SAXS data of LDL samples indicate that the size polydispersity of particles increases when the samples are subjected to long oxidation times (e.g., 18 h). Interestingly, in the case of HDL particles, there appeared to be no evidence of increased size polydispersity of particles as a function of sample oxidation time.

SAXS results also showed that LDL particles have a lamellar packing of cholesterol in their core. This organization remains, at least partially, even after 18 h of in vitro oxidation with copper ions. In contrast, SAXS curves of HDL showed no characteristic peak associated with repetition distance, which indicates that HDL particles have a disorganized lipid core.

LDL samples in the different stages of oxidation presented the formation of small aggregates, which could be modeled as volume fractal clusters by using the GIFT method of analysis. However, due to the limited experimental resolution, it was not possible to obtain a precise size for such clusters. Moreover, from the analysis of the HDL SAXS results (at least on the angular range covered in the experiments), no formation of aggregates or oligomers was observed. On the other hand, the DLS technique indicated that the oxHDL-18h sample showed formation of larger aggregates. However, since the fraction of such aggregates was very small, and since their size is near that of SAXS setup resolution, it was not possible to detect their influence on the SAXS data.

None of the LDL samples oxidized for up to 6 h showed any change in the intensity scattering data and electron density profile compared to the naLDL results. However the oxLDL-18h sample presented important differences: an increase of polydispersity, differences across the electron density profile, and an increase in the Gaussian chain scale factor. The increase of size polydispersity of particles on the sample oxidized for 18 h was also confirmed by the DLS data. Interestingly, for the oxLDL-18h, the electron density profile differs from that of the naLDL not only in the inner core, but also in the outer shell region of the particles (Fig. 4 *b*), which might indicate an important change over the complete structure of the lipoprotein. Finally, the observed increase in the Gaussian chain scale factor can be understood as an increase in the number of flexible or floppy regions on the protein sequence, which may indicate that somehow the oxidation is changing the protein structure, either by making it less structured or by causing some regions of the protein that were attached to the surface detach and become loose. All these results provide indications regarding the structural changes induced in the LDL particles due to the oxidation process. It is well known that oxidative modification of LDLs leads to loss of

recognition by the LDL receptor and a shift to recognition by scavenger receptors present in macrophages (10). Scavenger receptors are not downregulated in response to increased intracellular cholesterol and the accumulation of cholesterol leading to the development of foam cells, the hallmark of the artery lesion known as fatty streak. The failure in particle recognition by the system is related to the alteration of the protein structure. Therefore, oxidation induces changes in the ApoB constituent, making the particle unable to bind the LDL receptor (46). Such a change in protein structure was detected in the SAXS results, mainly by changes on the electron density profile and the Gaussian chain contribution. On the other hand, HDL samples showed no significant differences between native and oxidized samples, indicating that this kind of lipoprotein is more resistant to oxidation. This resistance to oxidation is due to the presence of several antioxidant enzymes associated with HDL particles, such as paraoxonase (47) and apolipoproteins (48).

The modeling strategy applied to the analysis of SAXS data, as well as use of the to our knowledge new deconvolution procedure, provided a unique way to study lipoproteins, permitting calculation of the electron density profile directly from the experimental SAXS data. In all the cases presented, we were able to obtain a very good fit to the experimental data.

It is interesting to compare the ZS results obtained with HDL and LDL particles. Since all lipoproteins present similarities in their overall structure, it is possible that the mechanism of thermal lens formation is also similar. The ZS experiments with HDL samples showed that the decrease of the θ parameter as a function of oxidation time occurs at a lower rate than observed for the LDL samples (32).Although LDL loses the nonlinear optical response signal altogether after <2 h of in vitro oxidation, HDL presents this signal for over 18 h. It has been shown previously in the case of LDL experiments that the behavior of the parameter θ is inversely proportional to the sample's thermal diffusivity (32). The thermal lens is formed because the sample absorbs heat from the Gaussian laser beam, which diffuses radially across it, imposing a temperature gradient. If the heat propagates slowly, it creates a variation of the refractive index through the radial direction, which gives rise to the lens formation. However, the more oxidized the LDL sample, the greater is the thermal diffusivity, and for samples oxidized for >90 min, the thermal lens does not form in the timescale of the experiment (milliseconds) (32). Recent studies have shown that the increase of thermal diffusivity is partially associated with the production of hydroperoxides during the oxidation process (32). From this picture, one can conclude that the changes in the ZS signal are related to a global modification in the sample as a function of the oxidation process, namely, to structural modifications and chemical reactions occurring in the solution, which form hydroperoxides. The SAXS results showed that when subjected to oxidation, HDL particles presented significantly fewer structural changes than did LDL particles. This information on the nanoscale can be directly correlated to ZS results, which provide information on a much larger length scale.

CONCLUSIONS

We have presented a controlled and systematic study of LDL and HDL structural changes due to in vitro oxidation of the samples with copper ions. SAXS, DLS, and ZS techniques were used to investigate and characterize the structure of the particles directly in solution. The SAXS data were analyzed using a to our knowledge new methodology capable of fitting the experimental scattering data and providing the corresponding electron density profile and other structural parameters. We conclude that compared to previous works using different modeling approaches, this to our knowledge new modeling approach provides much more reliable results and therefore seems to be more appropriate for the study of lipoproteins in solution. Also, the SAXS strategy for data analysis and modeling presented in this work can certainly be used as a guide for analyzing this kind of nanoparticle in solution. Results showed differences in the electron density profile both in the cholesterol core and in the phospholipid monolayer for samples oxidized for 18 h, compared to native particles. Furthermore, size polydispersity of oxLDL-18h increased, as did the scale factor of the Gaussian chain contribution. This term may be associated with changes (loss) in the overall symmetry of the particle, an increase in the flexible parts of the lipoprotein, which may indicate structural changes on the protein that embraces the lipoprotein, or some breakage of ApoB.

Our SAXS results with LDL samples show that the lamellar organization of cholesterol in the particle core remains at least partially structured even after 18 h of oxidation. All these results show that, despite the fact that LDL particles lose their biological function after an oxidation process as extensive as that generated by 18 h of incubation with copper, the overall structure of the lipoprotein is still similar to that of the native particle. This indicates that severe changes might occur in ApoB due to oxidation.

With respect to HDL, both optical and structural characterization results reveal that this particle presents a higher resistance to oxidation than do LDL particles. With the ZS technique, even after oxidation for 18 h, HDL samples continue to show a nonlinear optical signal distinguishable from the background. As in the case of LDL, oxidation of HDL particles shows a decrease of the amplitude of this signal as a function of oxidation time, but unlike the case for LDL, oxidation of HDL particles does not lead to a complete loss of signal. SAXS results did not show any drastic structural changes due to oxidation of HDL particles. The DLS technique showed a tendency in the oxHDL-18h

sample to form a small fraction of aggregates. All the structural investigations for the nanoparticles presented in this work indicated that LDL particles are more susceptible to oxidation than HDL particles.

SUPPORTING MATERIAL

Three figures are available at http://www.biophysj.org/biophysj/supplemental/S0006-3495(14)00469-X.

The authors thank Dennys Reis and Renata N. Bicev for their support on the DLS measurements. The authors acknowledge the Brazilian Synchrotron Light Laboratory (LNLS) for SAXS data acquisition (project num. SAXS1 - 10713).

This study was supported by The National Counsel for Scientific and Technological Development (CNPq), São Paulo Research Foundation (FAPESP), and the National Institute of Science and Technology of Complex Fluids (INCT-FCx).

REFERENCES

1. Dominiczak, M. H., and M. J. Caslake. 2011. Apolipoproteins: metabolic role and clinical biochemistry applications. *Ann. Clin. Biochem.* 48:498–515.
2. Harris, J. R., S. Lund-Katz, and M. Phillips. 2010. High density lipoprotein structure–function and role in reverse cholesterol transport. *In* Cholesterol Binding and Cholesterol Transport Proteins Springer, Dordrecht, The Netherlands, pp. 183–227.
3. Esterbauer, H., J. Gebicki, …, G. Jürgens. 1992. The role of lipid peroxidation and antioxidants in oxidative modification of LDL. *Free Radic. Biol. Med.* 13:341–390.
4. Zhang, Y., I. Zanotti, …, D. J. Rader. 2003. Overexpression of apolipoprotein A-I promotes reverse transport of cholesterol from macrophages to feces in vivo. *Circulation.* 108:661–663.
5. Movva, R., and D. J. Rader. 2008. Laboratory assessment of HDL heterogeneity and function. *Clin. Chem.* 54:788–800.
6. Superko, H. R. 2009. Advanced lipoprotein testing and subfractionation are clinically useful. *Circulation.* 119:2383–2395.
7. Badimon, L., R. F. Storey, and G. Vilahur. 2011. Update on lipids, inflammation and atherothrombosis. *Thromb. Haemost.* 105 (*Suppl 1*):S34–S42.
8. Mahdy Ali, K., A. Wonnerth, …, J. Wojta. 2012. Cardiovascular disease risk reduction by raising HDL cholesterol—current therapies and future opportunities. *Br. J. Pharmacol.* 167:1177–1194.
9. Yoshida, H., and R. Kisugi. 2010. Mechanisms of LDL oxidation. *Clin. Chim. Acta.* 411:1875–1882.
10. Yu, X.-H., Y.-C. Fu, …, C.-K. Tang. 2013. Foam cells in atherosclerosis. *Clin. Chim. Acta.* 424:245–252.
11. Viswambharan, H., X. F. Ming, …, Z. Yang. 2004. Reconstituted high-density lipoprotein inhibits thrombin-induced endothelial tissue factor expression through inhibition of RhoA and stimulation of phosphatidylinositol 3-kinase but not Akt/endothelial nitric oxide synthase. *Circ. Res.* 94:918–925.
12. Navab, M., S. Y. Hama, …, A. M. Fogelman. 2000. Normal high density lipoprotein inhibits three steps in the formation of mildly oxidized low density lipoprotein: step 1. *J. Lipid Res.* 41:1481–1494.
13. Navab, M., J. A. Berliner, …, A. M. Fogelman. 2001. HDL and the inflammatory response induced by LDL-derived oxidized phospholipids. *Arterioscler. Thromb. Vasc. Biol.* 21:481–488.
14. Navab, M., G. M. Ananthramaiah, …, A. M. Fogelman. 2004. The oxidation hypothesis of atherogenesis: the role of oxidized phospholipids and HDL. *J. Lipid Res.* 45:993–1007.
15. Gómez, S. L., R. F. Turchiello, …, A. M. F. Neto. 2004. Characterization of native and oxidized human low-density lipoproteins by the Z-scan technique. *Chem. Phys. Lipids.* 132:185–195.
16. Monteiro, A. M., M. A. N. Jardini, …, M. Gidlund. 2009. Cardiovascular disease parameters in periodontitis. *J. Periodontol.* 80:378–388.
17. Monteiro, A. M., M. A. N. Jardini, …, M. Gidlund. 2012. Measurement of the nonlinear optical response of low-density lipoprotein solutions from patients with periodontitis before and after periodontal treatment: evaluation of cardiovascular risk markers. *J. Biomed. Opt.* 17:115004.
18. Laggner, P., K. Müller, …, A. Holasek. 1973. Studies on the structure of lipoprotein A of human high density lipoprotein HDL3: the spherically averaged electron density distribution. *FEBS Lett.* 33:77–80.
19. Atkinson, D. D., R. J. Deckelbaum, …, G. G. Shipley. 1977. Structure of human plasma low-density lipoproteins: molecular organization of the central core. *Proc. Natl. Acad. Sci.* 74:1042–1046.
20. Laggner, P., K. Müller, and O. Kratky. 1976. X-ray small angle scattering on human plasma lipoproteins. *J. Colloid Interface Sci.* 55:102–108.
21. Glatter, O. 1981. Convolution square root of band-limited symmetrical functions and its application to small-angle scattering data. *J. Appl. Crystallogr.* 14:101–108.
22. Glatter, O., and B. Hainisch. 1984. Improvements in real-space deconvolution of small-angle scattering data. *J. Appl. Crystallogr.* 17:435–441.
23. Meyer, D. F., A. S. Nealis, …, S. J. Perkins. 1996. Time-course studies by synchrotron x-ray solution scattering of the structure of human low-density lipoprotein during Cu^{2+}-induced oxidation in relation to changes in lipid composition. *Biochem. J.* 319:217–227.
24. Liu, Y., D. Luo, and D. Atkinson. 2011. Human LDL core cholesterol ester packing: three-dimensional image reconstruction and SAXS simulation studies. *J. Lipid Res.* 52:256–262.
25. Prassl, R. 2011. Human low density lipoprotein: the mystery of core lipid packing. *J. Lipid Res.* 52:187–188.
26. Prassl, R., and P. Laggner. 2009. Molecular structure of low density lipoprotein: current status and future challenges. *Eur. Biophys. J.* 38:145–158.
27. Ren, G., G. Rudenko, …, H. J. Pownall. 2010. Model of human low-density lipoprotein and bound receptor based on cryoEM. *Proc. Natl. Acad. Sci. USA.* 107:1059–1064.
28. Oliveira, C. L. P., B. B. Gerbelli, …, J. S. Pedersen. 2012. Gaussian deconvolution: a useful method for a form-free modeling of scattering data from mono- and multilayered planar systems. *J. Appl. Crystallogr.* 45:1278–1286.
29. Havel, R. J., H. A. Eder, and J. H. Bragdon. 1955. The distribution and chemical composition of ultracentrifugally separated lipoproteins in human serum. *J. Clin. Invest.* 34:1345–1353.
30. Fernvik, E. C., D. F. Ketelhuth, …, M. Gidlund. 2004. The autoantibody repertoire against copper- or macrophage-modified LDL differs in normolipidemics and hypercholesterolemic patients. *J. Clin. Immunol.* 24:170–176.
31. Carter, C. A., and J. M. Harris. 1984. Comparison of models describing the thermal lens effect. *Appl. Opt.* 23:476–481.
32. Santos, P. R., T. C. Genaro-Mattos, …, A. M. Figueiredo Neto. 2012. Behavior of the thermal diffusivity of native and oxidized human low-density lipoprotein solutions studied by the Z-scan technique. *J. Biomed. Opt.* 17:105003.
33. Kellermann, G., F. Vicentin, …, I. Torriani. 1997. The small-angle x-ray scattering beamline of the Brazilian Synchrotron Light Laboratory. *J. Appl. Crystallogr.* 30:880–883.
34. Hammersley, A. P., S. O. Svensson, …, D. Hausermann. 1996. Two-dimensional detector software: from real detector to idealised image or two-theta scan. *High Press. Res.* 14:235–248.
35. Glatter, O. 1977. A new method for the evaluation of small-angle scattering data. *J. Appl. Crystallogr.* 10:415–421.
36. Oliveira, C. L. P., M. A. Behrens, …, J. S. Pedersen. 2009. A SAXS study of glucagon fibrillation. *J. Mol. Biol.* 387:147–161.

37. Pedersen, J. S., S. Hansen, and R. Bauer. 1994. The aggregation behavior of zinc-free insulin studied by small-angle neutron scattering. *Eur. Biophys. J.* 22:379–389.

38. Pedersen, J. S., and I. W. Hamley. 1994. Analysis of neutron and x-ray reflectivity data. 2. Constrained least-squares methods. *J. Appl. Crystallogr.* 27:36–49.

39. Provencher, S. W. 1982. CONTIN: a general-purpose constrained regularization program for inverting noisy linear algebraic and integral equations. *Comput. Phys. Commun.* 27:229–242.

40. Teixeira, J. 1988. Small-angle scattering by fractal systems. *J. Appl. Crystallogr.* 21:781–785.

41. Gómez, S. L., A. M. Monteiro, …, A. M. F. Neto. 2010. Cu and Fe metallic ions-mediated oxidation of low-density lipoproteins studied by NMR, TEM and Z-scan technique. *Chem. Phys. Lipids.* 163:545–551.

42. Orlova, E. V., M. B. Sherman, …, A. M. Gotto, Jr. 1999. Three-dimensional structure of low density lipoproteins by electron cryomicroscopy. *Proc. Natl. Acad. Sci. USA.* 96:8420–8425.

43. Singh, S., R. Suri, and C. G. Agrawal. 1995. Fluorescence properties of oxidised human plasma low-density lipoproteins. *Biochim. Biophys. Acta.* 1254:135–139.

44. Prassl, R., B. Schuster, …, M. J. Chapman. 1998. Thermal stability of apolipoprotein B100 in low-density lipoprotein is disrupted at early stages of oxidation while neutral lipid core organization is conserved. *Biochemistry.* 37:938–944.

45. Eisenberg, S. 1983. Lipoproteins and lipoprotein metabolism. A dynamic evaluation of the plasma fat transport system. *Klin. Wochenschr.* 61:119–132.

46. Steinberg, D. 2002. Atherogenesis in perspective: hypercholesterolemia and inflammation as partners in crime. *Nat. Med.* 8:1211–1217.

47. Durrington, P. N., B. Mackness, and M. I. Mackness. 2001. Paraoxonase and atherosclerosis. *Arterioscler. Thromb. Vasc. Biol.* 21:473–480.

48. Kontush, A., S. Chantepie, and M. J. Chapman. 2003. Small, dense HDL particles exert potent protection of atherogenic LDL against oxidative stress. *Arterioscler. Thromb. Vasc. Biol.* 23:1881–1888.

Braz J Phys (2014) 44:753–764
DOI 10.1007/s13538-014-0273-z

GENERAL AND APPLIED PHYSICS

Structural Modifications and Clustering of Low-Density Lipoproteins in Solution Induced by Heating

Cristiano L. P. Oliveira · Andrea M. Monteiro · Antonio M. Figueiredo Neto

Received: 30 July 2014 / Published online: 21 October 2014
© Sociedade Brasileira de Física 2014

Abstract This work presents a systematic study of low-density lipoprotein (LDL) in solutions subjected to subtle temperature changes, monitored by small angle X-ray scattering. From the data analysis, information about the equilibrium aggregation of the particles, as well as changes on the internal structure of the lipoproteins, were observed. The electron density profiles of the LDL particles were retrieved with a recently developed deconvolution method. Our results indicate that LDL particles keep their structure in the temperature range from about 22 °C up to 60 °C. Moreover, the formation of aggregates and their evolution as a function of time were monitored. Interestingly, when the temperature is raised to 80 °C, the results indicate the rupture of the particle and unspecific aggregation.

Keywords Lipoproteins · Temperature · Aggregation · SAXS · Modeling · LDL

1 Introduction

Plasma lipoproteins are heterogeneous particles of different sizes, composition, and density, whose main function is the cholesterol transport. These particles are constituted of a non-polar core, composed of triglycerides and cholesterol esters, surrounded by a monolayer of phospholipids, free cholesterol, and apolipoproteins (apo). High levels of the low-density lipoprotein (LDL), known as "bad cholesterol," are associated with high risk in developing a cardiovascular disease. The LDL is a particle rich in cholesterol ester and poor in triglycerides and free cholesterol. Moreover, each LDL particle contains only one macromolecule of apolipoprotein B100 (apoB-100), which is responsible for the integrity of the particle and metabolism. The LDL structure is very sensitive to changes in the environment, and this may alter its function. The mechanism by which LDL in vivo is modified is not yet completely understood. In a recent publication [1], the changes on the internal structure of LDL and HDL, due to in vitro oxidation by Cupper, were described. Also, the apo-B100 structure has been shown to be highly sensitive to chemical modification, such as oxidation induced by free radicals, and to temperature changes [2]. Thereby, the conformation of apo-B100 could be modified at higher temperatures, which would affect its recognition by the LDL cell receptors [3].

Scattering methods allow the study of the particles directly in solution. Investigations on the LDL structure as a function of the temperature by using scattering methods were performed in the 1970s by the seminal works of Deckelbaum, Laggner, and Atkinson [4–6], and more recently by Laggner and co-workers [2]. However, in all these cases, the data analysis is limited due to the presence of aggregates (induced by the temperature increase) and also by the problems on the retrieval of trustful scattering-length density profile for the lipoproteins from the scattering data. In a recent work, Jayaraman and co-workers investigated the thermal stability of LDL by using different techniques including calorimetric, circular dichroism, fluorescence, turbidity, and electron microscopic [7]. Their data show that thermal disruption of LDL involves irreversible changes in the particle with the release of neutral lipid from LDL core which coalesce into droplets. Gursky and co-workers [8] made quantitative kinetic analysis of thermal stability of LDL suggesting that fusion of LDL is preceded by other structural changes.

In this work, we present a systematic study of the changes in the structure of native LDL induced by subtle changes in

C. L. P. Oliveira · A. M. Monteiro · A. M. F. Neto
Instituto de Física, Universidade de São Paulo, São Paulo, Brazil

C. L. P. Oliveira (✉)
Institute of Physics, University of São Paulo, P.O. box 66318, 05314-970 São Paulo, SP, Brazil
e-mail: crislpo@if.usp.br

the temperature. Synchrotron radiation small-angle X-ray scattering data was collected for a series of LDL samples, and by using advanced modeling methods [1], information about the formation of aggregates, changes on the internal structure of the LDL particle, and modifications on the APO B conformation were obtained.

2 Materials and Methods

2.1 Isolation of LDL

The purification of LDL particles was described elsewhere [1]. Shortly, blood was drawn from of healthy normolipidemic donors, and the plasma was obtained after centrifugation at 1,000×*g* at 4 ° C, for 15 min. Benzamidine (2 mM), chloramphenicol (0.25 %), pheny-methyl-sulfonyfluoride (0.5 mM), gentamicin (0.5 %), and aprotinin (0.1 U/ml) were added to the plasma. LDL (1.006 < d < 1.063 mg/dl) was isolated in a sequential ultracentrifugation [9] process at 10^5x*g* at 4 °C, using the rotor of an ultracentrifuge (Hitachi Ultracentrifuge—Japan). The obtained samples were dialyzed for 24 h at 4 °C against phosphate buffered saline (PBS), pH 7.4. Later, the samples were put through a filter with micrometer pore (Milipore—Germany) and the protein concentration was determined using bicinchoninic acid protein assay kit (Pierce, USA), with bovine serum albumin as standard. The final LDL concentration was 1.3 mg/ml.

2.2 SAXS

LDL SAXS measurements were performed at the Brazilian Synchrotron Light Laboratory at the SAXS1 beamline [10]. The sample holder [11], a cell with dimensions 1×4×8 mm^3, was placed in a device coupled to a water-circulating thermal bath, enabling LDL solution samples measurements at controlled temperature. The wavelength of the incoming monochromatic X-ray beam was λ=1.48 Å and the distance between the sample and the detector was set to 3,200 mm, providing a *q* (scattering-vector modulus) interval from 0.006 to 0.25 $Å^{-1}$, where $q=4\pi(\sin\theta)/\lambda$ and 2θ is the scattering angle. The 2D scattering data was collected on a Dectris Pilatus™ 300k detector, and the integration of the SAXS patterns and data treatment were done with the FIT2D software [12]. Error estimation and normalization to absolute scale were performed by using the SUPERSAXS package [Oliveira and Pedersen, unpublished]. A rectangular beam with dimensions 300×100 microns was used. This beam size is further convoluted with the detector resolution of 172 microns. The experimental setup provided a resolution in q values of $\Delta q=0.00042$ $Å^{-1}$.

Data were collected at the temperatures: 22 °C (room temperature), 42 °C, 60 °C, and 80 °C. For the measurement at room temperature only 5 frames were obtained since the sample was stable over time. For the experiments at higher temperatures, the data collection was performed as follows: after the system reaches the thermal equilibrium (which is measured directly on the sample holder and monitored remotely), a fresh LDL sample is injected inside the sample holder and the measurement is started immediately after injection. Several (up to 5) 1 min frames were collected at 0, 5, 10, 20, 40, 60, and 80 min after injection. In all the cases, the frames were compared and averaged in order to have a single dataset representing each temperature. After the measurement on a given temperature, the cell is clean and the PBS buffer is measured at the same conditions and temperature for a proper background subtraction. For each temperature, a new fresh LDL sample was used.

The series of treated data is shown in Fig. 1.

2.3 Initial SAXS Data Analysis and Decoupling of the Form and Structure Factors

The analysis of the SAXS data was performed in several steps. At first, the data was analyzed by the Indirect Fourier Transformation method—IFT [13], with a slightly different implementation [14, 15]. From these analyses, coarse information about the size, shape, and aggregation behavior are obtained. Even the fresh LDL solution sample at room temperature shows the presence of a small fraction of particle's aggregates. The number of aggregates was shown to increase for increasing temperatures. In order to correctly analyze the contribution from the isolated LDL particles and the aggregates separately, it is necessary to decouple the form factor and structure factor of the scattering data. This was possible by using the Generalized indirect Fourier Transformation Method—GIFT [14]. We used a theoretical function for the structure factor contribution, and by the simultaneous optimization of the $p(r)$ function (form factor) and structure factor parameters, it was possible to obtain the theoretical form factor (without the structure factor contribution) and also a reliable structure factor function. In this approach, the scattering intensity $I(q)$ and structure factor $S(q)$ are given by:

$$I(q) = P(q)S(q) \tag{1}$$

$$S(q) = 1 + S_C^{agg}\exp\left[-\frac{q^2 R_G^{agg\,2}}{3}\right] \tag{2}$$

The form factor $P(q)$ is described by a set of spline functions, which are related to the pair distance distribution function $p(r)$ of the single particle by a Fourier transform [13]. For the structure factor $S(q)$, several different models were tested, but the data series were reasonably described by a simple model, which assumes that, at low angles, there is a Guinier Law for a particle (or aggregate) with radius of gyration R_G^{agg}, as shown in Eq. 2. In this model, the scale factor S_C^{agg} gives an

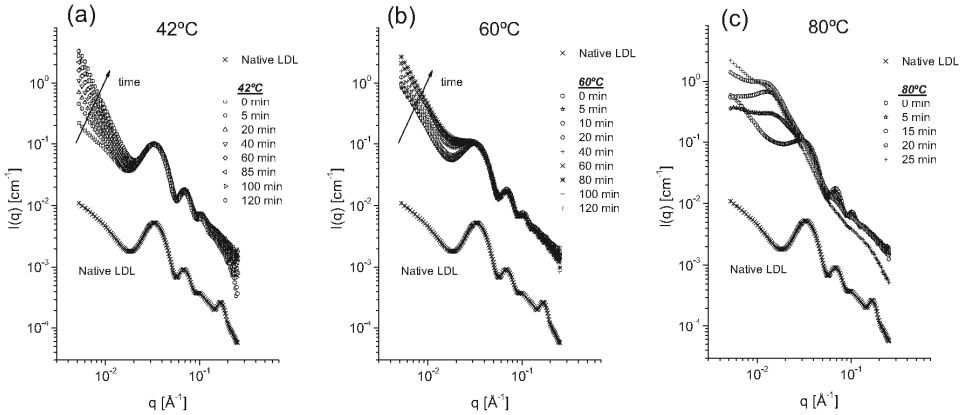

Fig. 1 SAXS data for the full series of measurements. **a** Data at 42 °C. **b** Data at 60 °C. **c** Data at 80 °C. In all the cases, the scattering data of the native LDL measured at 22 °C is shown for comparison. This *curve* is shifted for a better visualization

indication of the fraction of isolated particles and aggregates in the system, as described in the next section. As a result from these analyses, a good approximation for the form factor of the isolated particles and the structure factor of the aggregates were obtained.

2.4 Modeling of Aggregates and Evolution of the Aggregation Fraction

The description of the structure factor as an averaged radius of gyration for the aggregates allows the calculation of the "theoretical" scattering intensity of the aggregates by the simple extrapolation of the Guinier law to very small q values. From this curve, it is possible to obtain a pair-distance distribution curve, which may provide some general indications on the size and shape of the aggregates. Even though this procedure intrinsically assumes that the aggregates are globular, it provides some indications about the overall size and shape of the aggregates. Additionally, one can use an ab initio procedure to retrieve possible 3D shapes for the aggregates. This can be performed by the dummy atom modeling approach (Program DAMMIN [16]). Since one can assume that the aggregates are composed by isolated LDL particles, in this modeling, we used the radius of the dummy atoms similar to the average radius of the lipoproteins. In this framework, the obtained model for the aggregates is a direct indication of how the lipoproteins are arranged.

From the modeling results, it is also possible to follow the evolution of the fraction of aggregates in the sample. For this calculation, one can assume a simple two-component system: isolated LDL particles and aggregates. If there is only these two species in the sample, we have:

$$I(q)_{tot} = I(q)_{LDL} + I(q)_{Agg} \tag{3}$$

For a system of particles, the forward scattering is given by:

$$I(0) = c(\Delta\rho)^2 V^2 \tag{4}$$

where c is the concentration of particles, $\Delta\rho$ is the scattering length-density contrast, and V is the particle volume. Substituting Eq. 4 in Eq. 3, we have:

$$I(0)_{tot} = c_{LDL}(\Delta\rho)^2 V_{LDL}^2 + c_{agg}(\Delta\rho)^2 V_{agg}^2 \tag{5}$$

$$I(0)_{tot} = c_{LDL}(\Delta\rho)^2 V_{LDL}^2 \left(1 + \frac{c_{agg} V_{agg}^2}{c_{LDL} V_{LDL}^2}\right) \tag{6}$$

If one compares Eq. 6 with Eq. 2, one finds that:

$$S_C^{agg} = \frac{c_{agg} V_{agg}^2}{c_{LDL} V_{LDL}^2} \tag{7}$$

As demonstrated in the Appendix 1, it is possible to describe the numerical, volume, and intensity fraction of aggregates and isolated particles as a function of the scale factor S_C^{agg} and the radii of gyration of the isolated particles R_G^{LDL} and aggregates R_G^{agg}:

$$f_{LDL}^i = \frac{1}{1 + S_C^{agg}\left(\frac{R_G^{LDL}}{R_G^{agg}}\right)^{3\alpha}} \tag{8}$$

$$f_{agg}^i = \frac{1}{1 + \frac{1}{S_C^{agg}}\left(\frac{R_G^{agg}}{R_G^{LDL}}\right)^{3\alpha}} \tag{9}$$

So, we have for the numerical fraction i="num" and α=2, for the volume fraction i="vol" and α=1 and for the intensity fraction i="int" and α=0. The meaning of these fractions is related to the weighting of the calculation for each fraction.

The numerical fraction has no weighting, the volume fraction is weighted by the particle volumes, and the intensity fraction is weighted by the volume squared. The latter receives this name because the scattering intensity (Eq. 4) is weighted by the volume square, and therefore, this fraction provides the contribution to the final intensity.

Therefore, from the modeling (Eqs. 1 and 2) and estimations for the radius of gyration of the LDL particles and aggregates (which are also obtained from the fitting), one can retrieve the numerical, volume, and intensity fractions for the monomers and the aggregates for each dataset.

2.5 Modeling of LDL Single Particle

The complete description of the modeling procedure is found elsewhere [1]. In short, after having the form factors for each case, one can apply a deconvolution method, which fits the scattering data directly, allowing the inclusion of additional parameters as anisotropy and polydispersity, as well as to perform a simultaneous fitting of the background and other contributions. The particle is modeled as an ellipsoid of revolution with superimposed concentric shells of different electron densities. The parameters of these shells define the final radial profile. The polydispersity is included by integration of the form factor on a given size distribution. An additional term in the intensity is included in order to account for the contribution from flexible parts in the scatterers. The final expression that is used to fit the scattering data is given by:

$$I(q) = S_{C_1} P_{MOD}(q) + S_{C_2} P_{Deb}(q) + Back \quad (10)$$

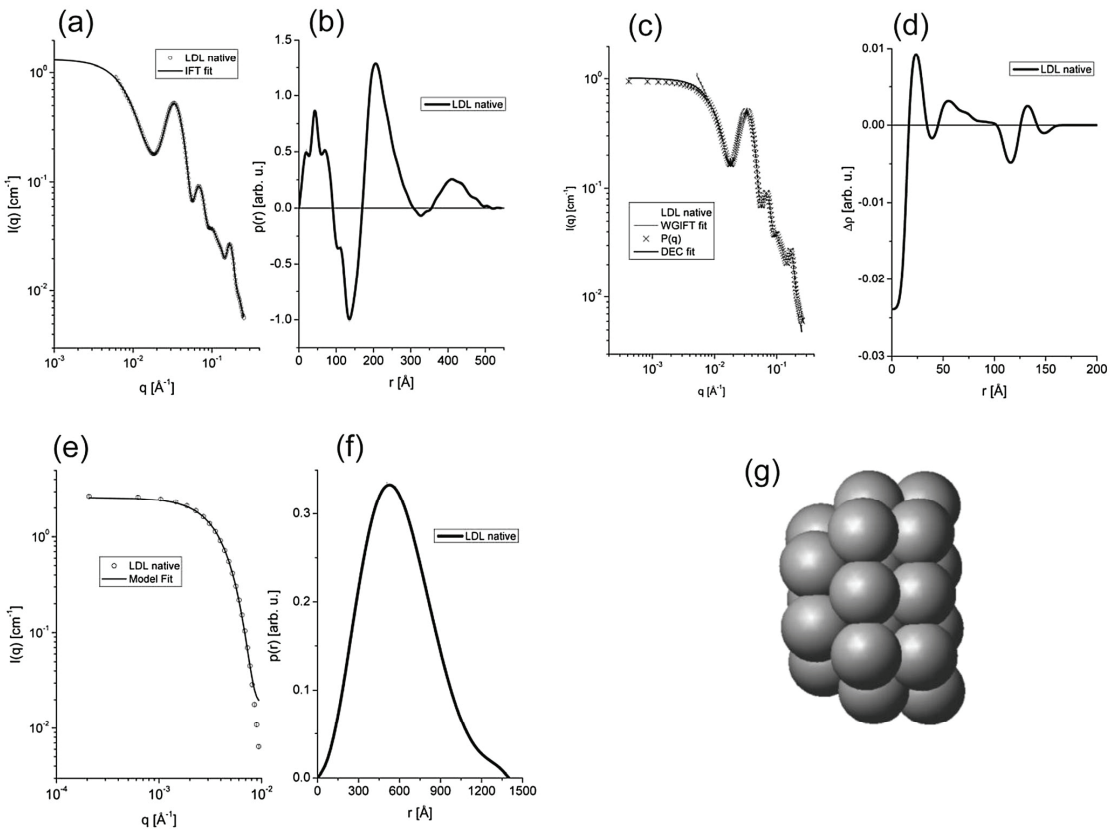

Fig. 2 Results for native LDL measured at 22 °C. IFT analysis: **a** experimental data (*circles*) and the IFT fit (*solid line*) and **b** pair distance distribution function $p(r)$. This *curve* indicates that the LDL nanoparticles have a diameter of ~310 Å ($p(r)$ curve approaching zero) and the maximum at round ~430 Å indicates the presence of a small fraction of aggregates. GIFT analysis: **c** GIFT fit (*dashed line*) and the calculated form factor (*crosses*). From this modeling, it is possible to obtain the structure factor and to estimate the size and shapes of the aggregates. The theoretical intensity for the aggregates is shown in **e** as *open circles* and the corresponding $p(r)$ curve in **f**. By using an ab initio modeling, it is possible to fit the data (*solid line* in **e**) and retrieve a 3D model for the aggregate, as shown in **g**. Note that the *spheres* in **g** have a diameter of 350 Å

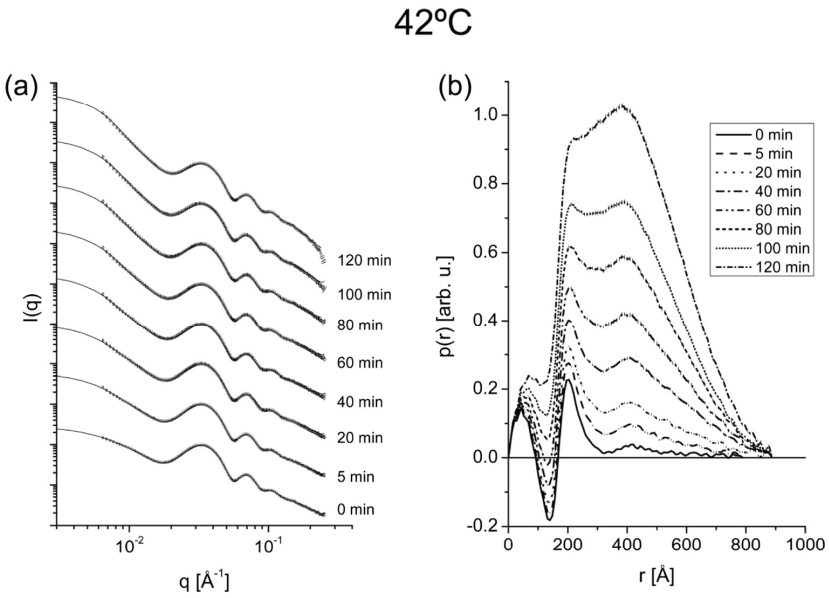

Fig. 3 IFT results for the LDL at 42 °C. **a** SAXS experimental data for different times (*open circles*) and theoretical fit (*solid lines*). **b** Pair distances distribution functions ($p(r)$). The increase of the height of the $p(r)$ curve for values larger than 300 Å indicates the increase of the contribution from the aggregates

In Eq. 10, the form factor $P_{\mathrm{MOD}}(q)$ is the normalized-intensity form factor for the ellipsoid of revolution composed of multiple shells [1], with maximum radius R and polydispersity σ_R. Sc_1 and Sc_2 are scale factors, *Back* is a constant background, and $P_{\mathrm{Deb}}(q)$ is the intensity form factor for the scattering from a flexible Gaussian chain with radius of gyration $R_{\mathrm{G}}^{\mathrm{Deb}}$ [17]. All values of the parameters are optimized by using a partially constrained least squares procedure [18].

3 Results

The analysis of LDL samples started with the use of the IFT method. The obtained pair-distance distribution function for the native LDL is shown in Fig. 2a,b and the pair-distances distribution functions for the different temperature series are shown in Figs. 3–5. As can be seen from these analyses, the samples at 42 °C and 60 °C presented an evolution of the

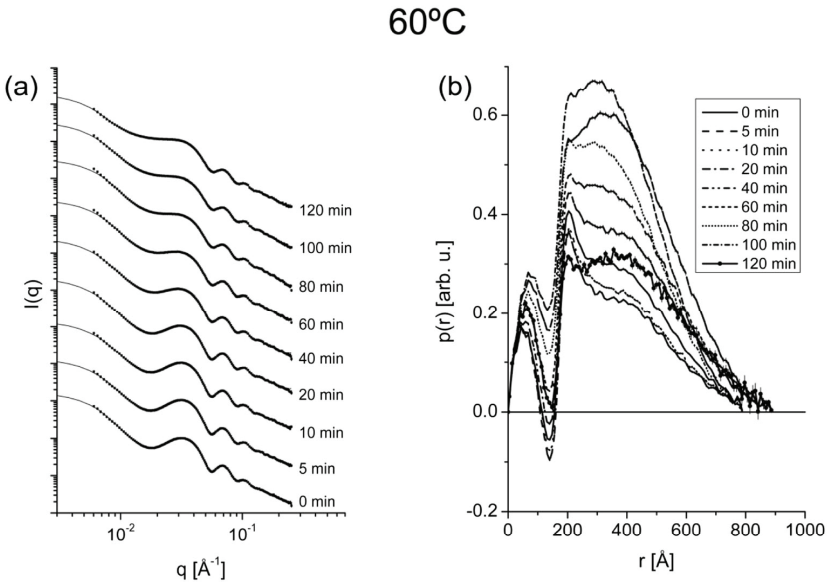

Fig. 4 IFT results for the LDL at 60 °C. **a** SAXS experimental data for different times (*open circles*) and theoretical fit (*solid lines*). **b** Pair distances distribution functions ($p(r)$). The increase of the height of the $p(r)$ curve for values larger than 300 Å indicates the increase of the contribution from the aggregates. For 120 min, one can see a decrease on the $p(r)$ height which can indicate either the breakage of the aggregates or precipitation of larger aggregates which effectively decreases the overall concentration of particle

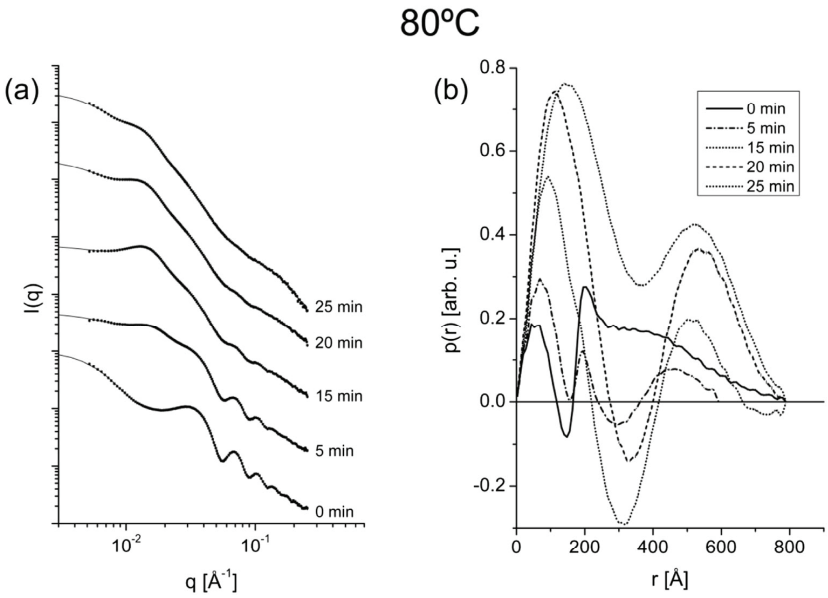

Fig. 5 IFT results for the LDL at 80 °C. **a** SAXS experimental data for different times (*open circles*) and theoretical fit (*solid lines*). **b** Pair distances distribution functions ($p(r)$). After the first $p(r)$ (at 0 min) which still resembles the overall shape of the LDL aggregates for the other samples (42 °C and 22 °C), the $p(r)$ curves completely change which can indicate the disruption of the LDL particles and the formation of different types of aggregates

fractions and types of aggregates over time. Interestingly, the lipoproteins seem to have an overall shape similar to that of the native (no modified) LDL. This can be inferred by the comparison of the initial part of the $p(r)$ functions in Figs. 3–5 and the Fig. 2b, which is the one of the native LDL at room temperature. These results and the systematic increase of the final region of the p(r) function for these temperatures indicate the formation of aggregates of LDL particles.

Table 1 Summary of results for the GIFT and Deconvolution methods for each dataset

Samples	Gift				Deconvolution			
	S_C^{agg}	R_G^{agg} [Å]	f_{LDL}^{num}	f_{agg}^{num}	Sc_2	R_G^{Deb}	R [Å]	σ_R [Å]
LDL 22 °C	1.5±0.6	329±5	0.997	0.003	0.19±0.1	54±1	155±1	14.4±0.3
LDL 42 °C 0 min	2.1±0.5	380±17	0.99	0.01	0.047±0.001	67±2	139±1	13.5±0.5
5 min	6.0±1.0	377±11	0.98	0.02	0.050±0.001	68±2	141±1	13.3±0.3
20 min	8.1±1.0	344±9	0.96	0.04	0.054±0.001	66±2	143±1	13.1±0.2
40 min	12.0±1.5	350±8	0.96	0.04	0.057±0.001	67±2	145±1	13.0±0.1
60 min	15.1±2.1	344±9	0.94	0.06	0.064±0.001	66±1	146±1	12.6±0.4
85 min	16.7±1.9	342±7	0.92	0.08	0.070±0.002	68±3	149±1	12.8±0.2
100 min	18.1±1.7	330±6	0.89	0.11	0.078±0.002	67±1	150±1	11.5±0.3
120 min	19.1±1.6	329±5	0.88	0.12	0.085±0.008	66±2	154±2	11.3±0.8
LDL 60 °C 0 min	9.0±0.5	327±4	0.94	0.06	0.15±0.02	147±2	161±3	15±2
5 min	8.2±0.5	329±5	0.94	0.06	0.13±0.01	117±8	162±2	16±2
10 min	8.1±0.6	339±5	0.94	0.06	0.16±0.02	132±8	167±2	14±2
20 min	9.1±0.7	328±5	0.93	0.07	0.21±0.03	136±7	167±3	16±2
40 min	8.0±0.8	346±6	0.93	0.07	0.44±0.03	178±7	170±4	15±2
60 min	8.1±0.7	337±6	0.91	0.09	0.71±0.05	190±9	170±15	16±3
80 min	7.1±0.5	349±5	0.89	0.11	1.16±0.08	240±11	171±11	14±5
100 min	6.8±0.5	352±5	0.91	0.09	0.96±0.05	224±7	172±20	15±6
120 min	6.0±0.3	377±4	0.96	0.04	0.45±0.02	167±4	167±3	16±2

The calculation of the numerical fractions for each sample is also presented (obtained with Eqs. 8 and 9, with α=2)

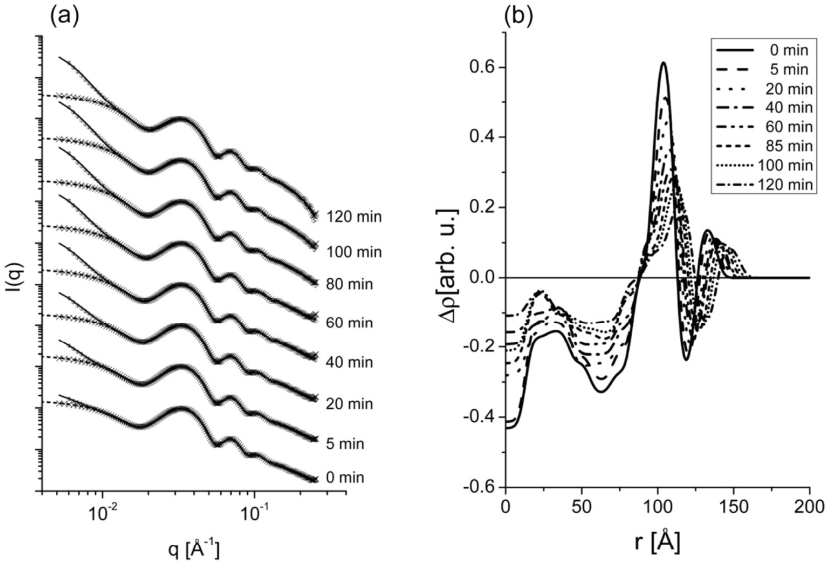

Fig. 6 GIFT and Deconvolution results for the LDL at 42 °C. **a** SAXS experimental data for different times (*open circles*), theoretical fits using Eq. 1 (*solid lines*), decoupled form factor (*crosses*), and the fit of the form factor by using the deconvolution procedure (*dash lines*). **b** Radial electron density profiles obtained for each temperature

For the sample at 80 °C, the first frame indicates that the LDL particles were assembled initially (maybe due to the heating of the sample inside the cell); but after 5 min, the SAXS profile and $p(r)$ curve changes drastically, probably indicating the disruption of the LDL particles and the formation of non-specific aggregates.

This initial analysis by using the IFT method suggested that, at the temperatures of 42 °C and 60 °C, the LDL lipoproteins (isolated and aggregated, but almost intact) are still present. However, the increase of the temperature may have changed its inner structure. In order to investigate this point, it was necessary to apply the GIFT method to decouple the particle's form factor and the system's structure factor. A summary of the results obtained with the GIFT method and deconvolution analysis is presented in Table 1. The fits by using the GIFT method are shown in Fig. 2 a, b, c for the native LDL at 22 °C, and in Figs. 6a and 7a for the data at 42 °C and 60 °C, respectively. As it can be seen, the fits by

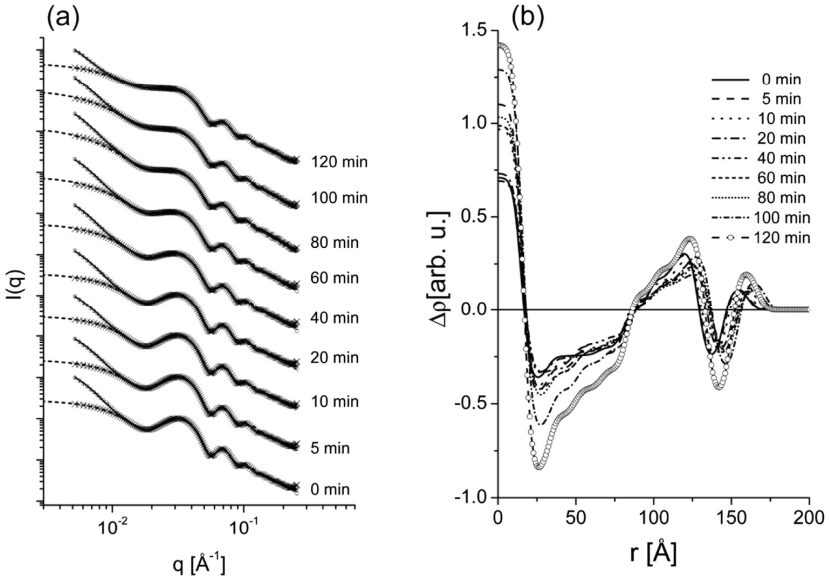

Fig. 7 GIFT and Deconvolution results for the LDL at 60 °C. **a** SAXS experimental data for different times (*open circles*), theoretical fits using Eq. 1 (*solid lines*), decoupled form factor (*crosses*), and the fit of the form factor by using the deconvolution procedure (*dash lines*). **b** Radial electron density profiles obtained for each temperature

using the proposed structure factor can describe the experimental data with high accuracy. Moreover, the corresponding form factor and structure factor for each dataset are obtained. From the structure factor, it was possible to obtain information about the aggregated state as well as the evolution of the corresponding fractions. In Fig. 2 a–f, the modeling of the form factor and structure factor, as well as the deconvolution procedure, is presented for the native LDL measured at 22 °C. In Figs. 8 a–f and 9 a–f, the aggregation results for the samples at 42 °C and 60 °C are shown. As it can be seen, it is possible to estimate the size of the aggregates (panels a, b) in each case and also obtain a representation of the shape of the aggregates (panel f). In addition, from the simple aggregation model described in section 2.4, one can calculate the evolution of the aggregates, i.e., their numerical fraction, volume fraction, and intensity fraction contributions (panels d–f). For the data at 42 °C (Fig. 8), one can see a monotonic increase of the forward scattering (panel c) indicating a continuous increase of the contribution of the aggregate. However, from Table 1, it is possible to see that the radius of gyration of the aggregate does not present a large variation; whereas, the scale factor S_C^{agg} shows a systematic increase. This can be converted in the aggregates numerical fractions, which are shown in panels d–f. It is interesting to note that even though the numerical fractions of the aggregates increases only up to 10 % (for 120 min at a constant temperature), the volume fractions of each population are similar at 60 min and the intensity fraction is dominated by the aggregates already from the first frame.

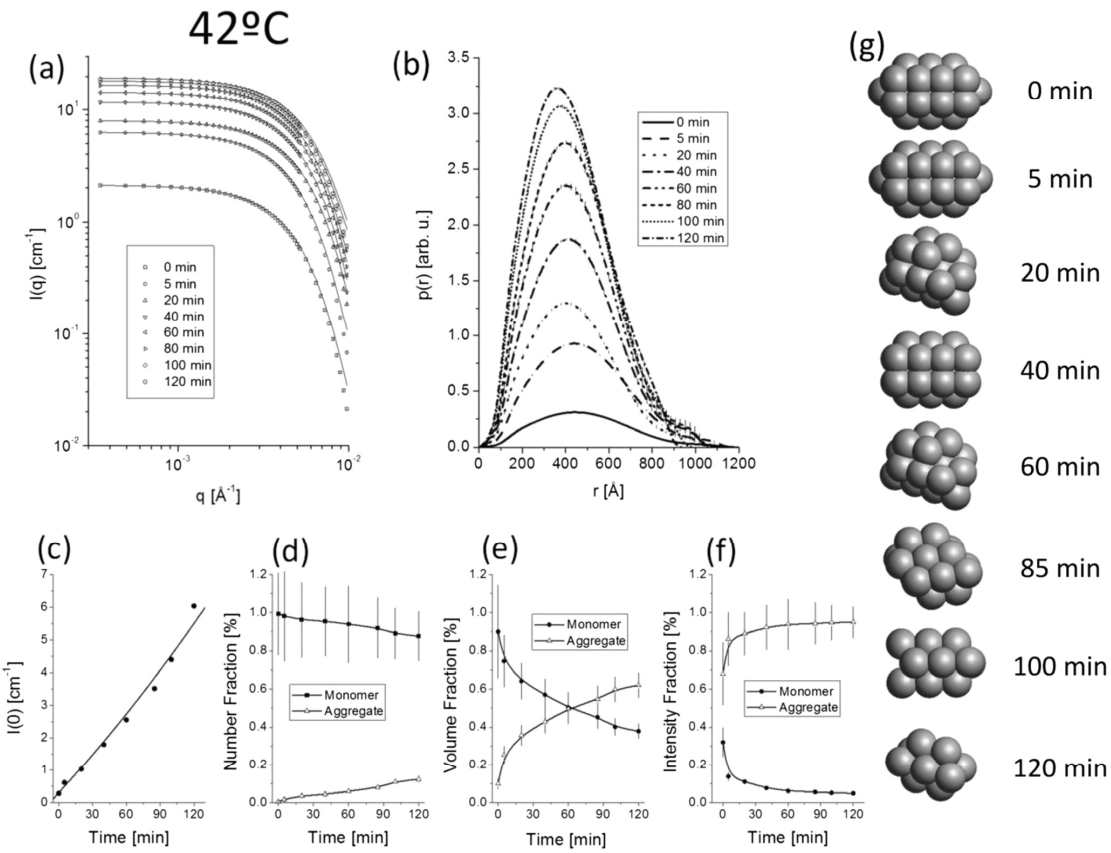

Fig. 8 Aggregation of LDL at 42 °C. IFT analysis: **a** Scattering intensity for the aggregates (*circles*) obtained from the GIFT method. The corresponding $p(r)$ function is shown in **b**. Calculation of the fractions: **c** forward scattering for the data collected at 42 °C (*circles*) indicating a monotonic increase of the intensity. This indicates a systematic increase of the contribution of the aggregates. In this graph, the line is for eye guiding. **d** Number fraction of monomers (*circles*) and aggregates (*open triangles*). **e** Volume fraction of monomers (*circles*) and aggregates (*open triangles*). **f** Intensity fraction of monomers (*circles*) and aggregates (*open triangles*). All fractions were calculated by using Eqs. 8 and 9 with the corresponding values for the exponent α. In these graph, the lines are for eye guiding. Modeling of the aggregates: by using ab initio modeling, it is possible to fit the data (*solid lines* in **a**) and retrieve a 3D model for the aggregates, as shown in **g** for each time. Note that the spheres in **g** have a diameter of 350 Å

Similar results were obtained for the data at 60 °C, as shown in Fig. 9. For this case, the numerical, volume, and intensity fractions of the isolated LDL and aggregates seem to be almost constant until 80 min. Differently from the data at 42°, the volume fraction of the isolated particles is always larger than the one of the aggregates. However, the intensity contribution is still dominated by that from the aggregates. The data after 100 min presents a strange behavior since the contribution from the aggregates seems to decrease. This can indicate the precipitation of the material due to formation of larger aggregates that are not visible by SAXS. This conclusion is also supported by the decrease of the $p(r)$ function height at larger values of r (Fig. 4b). All in all, the obtained results for the data at 60 °C presented more fluctuations than the one at 42 °C, which can be a consequence of the higher temperature of the system.

The fits from the deconvolution procedures and the corresponding electron-density profiles for each dataset are also presented. In Fig. 2 c,d, the results of the native LDL at 22 °C are shown. The modeling method provides a good fit to the experimental data (panel c) and the characteristic behavior for the electron-density profile [19]. It is interesting to analyze the differences induced by the temperature increase in the samples. When comparing the data at 22 °C and the ones at 42 °C and 60°, it is possible to see that the maximum at q~0.17 Å^{-1}, which is present at the room temperature SAXS data, disappears for the samples at higher temperature. This was already described in the literature as a phase transition of the lipidic content inside the lipoprotein, indicating a loss of the ordering [4–6, 19]. In a recent study, by using CryoEM, Molecular Dynamics, and SAXS [20, 21], it was shown that this maximum is

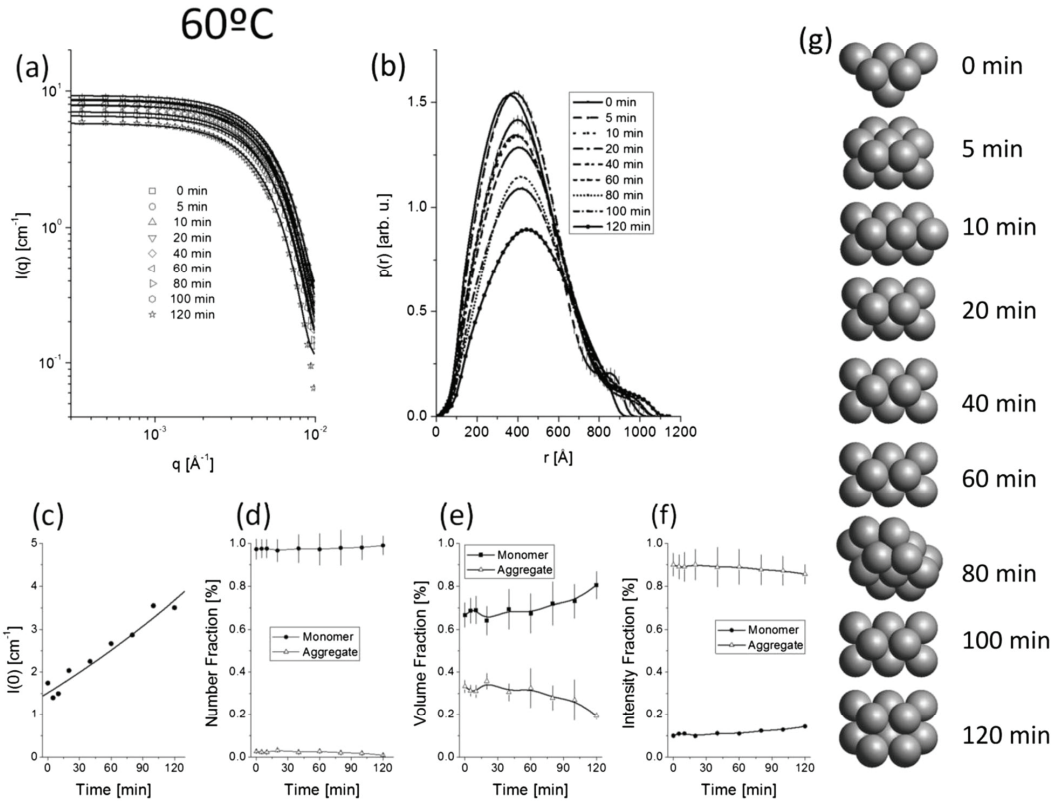

Fig. 9 Aggregation of LDL at 60 °C. IFT analysis: **a** scattering intensity for the aggregates (*circles*) obtained from the GIFT method. The corresponding $p(r)$ function is shown in **b**. Calculation of the fractions: **c** forward scattering for the data collected at 60 °C (*circles*) indicating a monotonic increase of the intensity. This indicates a systematic increase of the contribution of the aggregates. In this graph, the *line* is for eye guiding. **d** Number fraction of monomers (*circles*) and aggregates (*open triangles*). **e** Volume fraction of monomers (*circles*) and aggregates (*open triangles*). **f** Intensity fraction of monomers (*circles*) and aggregates (*open triangles*). All fractions were calculated by using Eqs. 8 and 9 with the corresponding values for the exponent α. In these graph, the lines are for eye guiding. Modeling of the aggregates: by using ab initio modeling, it is possible to fit the data (*solid lines* in **a**) and retrieve a 3D model for the aggregates, as shown in **g** for each time. Note that the *spheres* in **g** have a diameter of 350 Å

related to the ordering of the cholesterol molecules in the inner core of the LDL particle. This loss of ordering and "melting" of the inner core is clearly indicated by the electron density profiles, as shown in our experiment (see Figs. 6 and 7). By comparing the electron-density profile ($\Delta\rho$) obtained with the native LDL at room temperature (Fig. 2d) with those obtained at 42 °C and 60 °C (Figs. 6b and 7b), it is possible to see that the maxima in $\Delta\rho$ are broader in the experiments at higher temperatures. In the case of the native LDL, we observed a periodic behavior of the radial electron-density profile at small values of r. This indicates the existence of a local ordering and gives rise to the maximum in the scattering profile $I(q)$ at q~0.17 Å^{-1}. In the data acquired at 42 °C and 60 °C, this well-defined periodic behavior is lost, indicating the loss of ordering inside the particle. The electron-density profiles obtained for each temperature show remarkable differences, which may indicate important differences in the inner arrangement of the lipoproteins.

The contribution from flexible parts in the scatter system is also an interesting point. The radius of gyration of the Debye chain (R_G^{Deb}) obtained with the sample at 42 °C is slightly larger than the one obtained at 22 °C (Table 1). This indicates a small increase of the particle's shape fluctuation, and eventually, a signature of flexible parts on the particle. However, there is a systematic increase on the scale factor S_{C_2} , which indicates that these contributions become more and more important as time goes by. For the data at 60 °C, on the other hand, the parameters that characterize the flexible contribution to the scattering change drastically. Our results show an important and systematic increase on the R_G^{Deb} and also on S_{C_2} which indicates that the size of the flexible regions on the lipoprotein (probably the protein apoB on its surface) and its contribution to the total intensity increases as time goes by. A possible explanation for this result can be attributed to the detachment of some regions of the the apoB-100 from the particle, causing an important increase of the R_G^{Deb}. This effect is probably due to the effect of the high temperature.

4 Summary and Conclusions

In this work, it is presented a controlled and systematic study of LDL internal structure and particle's aggregation due to changes in the sample's temperature. A complete analysis and modeling procedure is proposed, permitting the retrieval of structural parameters for the LDL particles, shape and evolution of the aggregates, and also the fractions of the isolated and aggregated states. By the use of a decoupling procedure and the simple aggregation model, the evolution of the fraction of the two species (isolated particles and aggregates) could be retrieved as a function of temperature. The aggregates overall shapes could be obtained by the use of ab initio modeling of the scattering data. For the isolated particles, the use of the deconvolution modeling on the scattering data allowed the calculation of the corresponding radial electron-density profile, which is directly related to the particle's internal structure. The loss of internal ordering, which is associated to a phase transition on the cholesterol, occurred when varying the temperature from 22° to 42° (and above) and could be explained by the important change in the electron-density profiles. Also, by this analysis, it was possible to follow the changes in the LDL internal structure due to the increase of temperature. Finally, the use of the Debye chain in the model provided a direct indication of the degree of the flexibility and conformation of the apoB-100. The results demonstrated a remarkable and systematic increase on the degree of flexibility of the protein, probably due to structural changes induced by temperature.

The procedure presented in this work provides a general framework that can be used on the study of dynamical processes in lipoprotein systems, allowing the online and in situ monitoring and modeling of the system. Also, since the calculated electron-density profiles are a direct indication of the average distribution of the components inside the lipoproteins, they can be used to check and validate MD simulations for systems of lipoproteins. The size and shape of the aggregates, as well as the evolution of the fractions of each species, can be used as guide for aggregation models of lipoproteins.

Acknowledgments This study was supported by The National Council for Scientific and Technological Development (CNPq), São Paulo Research Foundation (FAPESP), and National Institute of Science and Technology of Complex Fluids (INCT-FCx). The authors acknowledge the Brazilian Synchrotron Light Laboratory for the SAXS data acquisition (proj. # SAXS1-10713). The authors thank Dr. Priscila R. Santos for the support on sample preparation and data acquisition.

Author Contributions The manuscript was written through contributions of all authors. All authors have given approval to the final version of the manuscript.

Appendix 1

a) Derivation of Eqs. 8 and 9

The scattering intensity for a system composed of two populations is given by:

$$I(0)_{tot} = c_{LDL}(\Delta\rho)^2 V_{LDL}^2 + c_{agg}(\Delta\rho)^2 V_{agg}^2 \quad \text{(a1)}$$

$$I(0)_{tot} = c_{LDL}(\Delta\rho)^2 V_{LDL}^2 \left(1 + S_C^{agg}\right) \quad \text{(a2)}$$

where,

$$S_C^{agg} = \frac{c_{agg} V_{agg}^2}{c_{LDL} V_{LDL}^2} \quad \text{(a3)}$$

The fraction of the particles in each population is the ratio between the number of particles in one population divided by the total number of particles weighted in a given way. For the number fraction, it is not necessary to use weighting, for the volume fraction one has to weight by the volume and for the intensity fraction the weighting function is the volume square. It is possible to write a single formula for the fractions if one uses as weighting function the volume to the power 2-α :

$$f^i_{LDL} = \frac{c_{LDL}(\Delta\rho)^2 V^{2-\alpha}_{LDL}}{c_{LDL}(\Delta\rho)^2 V^{2-\alpha}_{LDL} + c_{agg}(\Delta\rho)^2 V^{2-\alpha}_{LDL}}$$

$$f^i_{LDL} = \frac{c_{LDL}V^{2-\alpha}_{LDL}}{c_{LDL}V^{2-\alpha}_{LDL} + c_{agg}V^{2-\alpha}_{LDL}} = \frac{c_{LDL}V^{2-\alpha}_{LDL}/c_{LDL}V^{2-\alpha}_{LDL}}{\left(c_{LDL}V^{2-\alpha}_{LDL} + c_{agg}V^{2-\alpha}_{LDL}\right)/c_{LDL}V^{2-\alpha}_{LDL}} = \frac{1}{1+\frac{c_{agg}V^{2-\alpha}_{agg}}{c_{LDL}V^{2-\alpha}_{LDL}}} \tag{a4}$$

$$f^i_{LDL} = \frac{1}{1+S^{agg}_C\frac{V^2_{LDL}}{V^2_{agg}}\frac{V^{2-\alpha}_{agg}}{V^{2-\alpha}_{LDL}}} = \frac{1}{1+S^{agg}_C\left(\frac{V_{agg}}{V_{LDL}}\right)^{-\alpha}} \Rightarrow f^i_{LDL} = \frac{1}{1+S^{agg}_C\left(\frac{V_{LDL}}{V_{agg}}\right)^{\alpha}}$$

For the fraction of aggregates weighted by the volume to the power 2-α, simple algebraic operations lead to,

$$f^i_{agg} = \frac{1}{1+\frac{1}{S^{agg}_C}\left(\frac{V_{agg}}{V_{LDL}}\right)^{\alpha}} \tag{a5}$$

By inspection, one can show that $f^i_{LDL}+f^i_{agg}=1$.

If one assumes that the LDL particles and aggregates have a globular shape, the volume scales with the cube of the particle radius of gyration, so

$$f^i_{LDL} = \frac{1}{1+S^{agg}_C\left(\frac{\left(R^{LDL}_G\right)^3}{\left(R^{agg}_G\right)^3}\right)^{\alpha}} = \frac{1}{1+S^{agg}_C\left(\frac{R^{LDL}_G}{R^{agg}_G}\right)^{3\alpha}} \tag{a6}$$

$$f^i_{agg} = \frac{1}{1+\frac{1}{S^{agg}_C}\left(\frac{R^{agg}_G}{R^{LDL}_G}\right)^{3\alpha}} \tag{a7}$$

For the numerical fraction, i="num" and $\alpha=2$; for volume fraction, i="vol" and $\alpha=1$; and for the intensity fraction, i="int" and $\alpha=0$.

References

1. C.L.P. Oliveira, P. Santos, A. Monteiro, A.M. Figueiredo Neto, Effect of oxidation on the structure of human low and high density human lipoproteins. Biophys. J. **106**, 2595–2605 (2014)
2. R. Prassl, M. Pregetter, H. Amenitsch, M. Kriechbaum, R. Schwarzenbacher, J.M. Chapman, P. Laggner, Low density lipoproteins as circulating fast temperature sensors. Plos One **3**, e4079 (2008)
3. N.F. Galeano, M. Al-Haideri, F. Keyserman, S.C. Rumsey, R.J. Deckelbaum, Small dense low density lipoprotein has increased affinity for LDL receptor-independent cell surface binding sites: a potential mechanism for increased atherogenicity. J. Lipid Res. **39**, 1263–1273 (1998)
4. P. Laggner, G. Degovics, K.W. Muller, O. Glatter, O. Kratky, G. Kostner, A. Holasek, Molecular packing and fluidity of lipids in human-serum low-density lipoproteins. Hoppe-Seylers Z Physiol Chem **358**, 771–778 (1977)
5. D. Atkinson, R.J. Deckelbaum, D.M. Small, G.G. Shipley, Structure of human-plasma low-density lipoproteins—molecular-organization of central core. Proc. Natl. Acad. Sci. USA **74**, 1042–1046 (1977)
6. R.J. Deckelbaum, G.G. Shipley, D.M. Small, Structure and interactions of lipids in human-plasma low-density lipoproteins. J. Biol. Chem. **252**, 744–754 (1977)
7. S. Jayaraman, D. Gantz, O. Gursky, Structural basis for thermal stability of human low-density lipoprotein†. Biochemistry **44**, 3965–3971 (2005)
8. M. Lu, D.L. Gantz, H. Herscovitz, O. Gursky, Kinetic analysis of thermal stability of human low density lipoproteins: a model for LDL fusion in atherogenesis. J. Lipid Res. **53**, 2175–2185 (2012)
9. R.J. Havel, H.A. Eder, J.H. Bragdon, Distribution and chemical composition of ultracentrifugally separated lipoproteins in human serum. J. Clin. Invest. **34**, 1345–1353 (1955)
10. G. Kellermann, F. Vicentin, E. Tamura, M. Rocha, H. Tolentino, A. Barbosa, A. Craievich, I. Torriani, The small-angle X-ray scattering beamline of the brazilian Synchrotron Light Laboratory. J. Appl. Crystallogr. **30**, 880–883 (1997)
11. L.P. Cavalcanti, I.L. Torriani, T.S. Plivelic, C.L.P. Oliveira, G. Kellermann, R. Neuenschwander, Two new sealed sample cells for small angle X-ray scattering from macromolecules in solution and complex fluids using synchrotron radiation. Rev. Sci. Instrum. **75**, 4541–4546 (2004)
12. A.P. Hammersley, S.O. Svensson, M. Hanfland, A.N. Fitch, D. Hausermann, Two-dimensional detector software: from real detector to idealised image or two-theta scan. High Pressure Res. **14**, 235–248 (1996)
13. O. Glatter, A new method for the evaluation of small-angle scattering data. J. Appl. Crystallogr. **10**, 415–421 (1977)
14. C.L.P. Oliveira, M.A. Behrens, J.S. Pedersen et al., A SAXS study of glucagon fibrillation. J. Mol. Biol. **387**, 147–161 (2009)
15. J.S. Pedersen, S. Hansen, R. Bauer, The aggregation behavior of zinc-free insulin studied by small-angle neutron-scattering. Eur. Biophys J. Biophys. Lett. **22**, 379–389 (1994)

16. D.I. Svergun, Restoring low resolution structure of biological macromolecules from solution scattering using simulated annealing. Biophys. J. **76**, 2879–2886 (1999)
17. P. Debye, Molecular-weight determination by light scattering. J. Phys. Colloid Chem. **51**, 18–32 (1947)
18. C.L.P. Oliveira, B.B. Gerbelli, E.R.T. Silva, F. Nallet, L. Navailles, E.A. Oliveira, J.S. Pedersen, Gaussian deconvolution: a useful method for a form-free modeling of scattering data from mono- and multilayered planar systems. J. Appl. Crystallogr. **45**, 1278–1286 (2012)
19. P. Laggner, K.W. Muller, Structure of serum-lipoproteins as analyzed by X-ray small-angle scattering. Q. Rev. Biophys. **11** (1978)
20. G. Ren, G. Rudenko, S.J. Ludtke, J. Deisenhofer, W. Chiu, H.J. Pownall, Model of human low-density lipoprotein and bound receptor based on CryoEM. Proc. Natl. Acad. Sci. USA **107**, 1059–1064 (2010)
21. Y. Liu, D. Luo, D. Atkinson, Human LDL core cholesterol ester packing: three-dimensional image reconstruction and SAXS simulation studies. J. Lipid Res. **52**, 256–262 (2011)